How do seismic waves respond to fractures in rock? Evaluation of effective media versus discrete fracture representations.

Emmnaouil Parastatidis

School of Earth and Environment

University of Leeds

A thesis submitted for the degree of

Doctor of Philosophy

November 2019

Declaration

I confirm that the work submitted is my own and that appropriate credit has been given where reference has been made to the work of others. This copy has been supplied on the understanding that it is copyright material and that no quotation from the thesis may be published without proper acknowledgement

Acknowledgements

This work was funded by Natural Environment Research Council, Radioactive Waste Management Limited and Environment Agency through the Radioactivity and the Environment (RATE) programme, as part of the HydroFrame project, NE/L000660/1.

Firstly, I would like to express my sincere gratitude to my supervisor, Mark Hildyard, for his support, advice and encouragement, for creating a friendly research environment and being more than a supervisor over the last few years. I would like to thank Andy Nowacki who acted as a second supervisor and who has helped and encouraged my work over the last two years. The work in this thesis has been greatly improved by their contribution.

Besides my supervisors, I would like to thank Graham Stuart and Doug Angus for their insightful comments during the first part of my PhD, as supervisors.

My sincere thanks also goes to Will Flynn and Nicola Mathews from Itasca U.K., Suikkanen Johannes from Posiva and Noora Riihiluoma from Geofcon who gave access to survey data and provided me with the relevant technical reports. Without they precious support it would not be possible to conduct this research.

I thank Jim Hazzard and all Itasca team for providing training and technical support both remotely and during my time in the Itasca office in Minneapolis.

Particular thanks to colleagues in the University of Leeds for all the support - Hannah Bentham, John Martin, Chrysothemis Paraskevopoulou, Sam Parsons, Dave Price, Sofya Titarenko, James Woodman and especially Antonio Fuggi for moral and technical support.

Thanks to the friendship along these years: Antonio, Andreas, Giannis, Andrianno, Vasilis, who met in Leeds, Michalis, Savvas, Valia and Christina even though they were far they stand next to me, and my ex-wife Polina.

Last but not the least, I would like to thank my family: my parents and my brother and sister for supporting me throughout these years.

Abstract

The purpose of this study is to examine the wave propagation in a fractured medium using numerical models and to quantify their limitations and the range of applicability. This work is motivated by the needs of the industries to understand the physics of fractures and minimise uncertainties with the most efficient methods.

The finite difference code WAVE3D has been used to model wave propagation in fractured media. In this thesis I present a brief description of the background theory of the code and the theory of the three approaches for fracture representation; the explicit model, the Effective medium (EM) and the Localised effective medium (LEM). These three models are compared in this work.

A laboratory experiment with multiple parallel fractures under controlled conditions has been modelled using the above approaches creating synthetic waveforms. A methodology was first developed to invert the source from the experiment so that it could be applied to the numerical models. The performance of the models is evaluated for both uniform and for non-uniform fracture stiffness based on the background stress field. For the last case a new code has been developed to calculates stress dependent stiffness for the EM and LEM. The stress dependent models are a better approach to real data. Low-pass filter method is used to define the frequency range of applicability for the models.

The performance and flexibility of LEM is then examined against explicit and EM models to define the balance between maximum wave frequency, fracture stiffness and model's grid quality. Then I evaluate the performance of the fracture representations in media with complex fractures, using a Distinct Element Method code, and applying the effect of complex fractures to the LEM and EM models. I work on how to implement a dipping fracture

of the 3DEC numerical code with tetrahedral elements in the WAVE3D staggered grid by either pixelising the fracture or by using an equivalent discrete fracture medium.

Finally, based on the methodology developed earlier, I model a seismic cross-hole tomography survey for the EDZ of the GDF in Finland. Due to the non-controlled environment of the survey, the complexity of the studied area cannot be fully represented to the models, and the waveforms of the models are not expected to fully match the survey data. An optimisation process for fracture stiffness is applied to improve the model data for selected ray paths.

I reach a range of conclusions on the performance of the different fracture models, fracture stiffness and the techniques developed.

Abbreviations

AE	Acoustic Emission
DD	Displacement Discontinuity
DEM	Discrete Element Method
DFN	Discrete Fracture Network
EDZ	Excavation Damage Zone
EdZ	Excavation disturbed Zone
EDFM	Equivalent Discrete Fracture Medium
EM	Effective Medium
FDM	Finite Difference Method
FEM	Finite Element Method
FFT	Fast Fourier Transform
GDF	Geological Disposal Facility
HAW	High Activity Waste
HLW	High Level Waste
ILW	Intermediate Level Waste
LAW	Low Level Waste
LEM	Localised Effective Medium
LLW	Low Level Waste
NPP	Nuclear Power Plant

List of symbols

Symbol	Meaning	Units
ϵ	crack density	
λ	wavelength (not to be confused with Lamél's first parameter)	m
D	fracture density	m^-1
f	frequency	Hz
$\frac{1}{L}$	cracks per unit length	m^-1
K_n	Normal fracture stiffness	Pa/m
K_s	Shear fracture stiffness	Pa/m

Contents

List of Figures

LIST OF FIGURES

Chapter 1

Introduction

1.1 Nuclear waste repositories

In the late 1940's, the beginning of the 'Atomic Age' brought about the development and wide use of nuclear technology with applications in the energy sector, medicine, defence activities, industry, and research, which contributed to the rapid development of society (Sovacool, 2011). However, nuclear technology is associated with a cost that threatens the future generations. The by-products of the nuclear activity could remain radioactive and, as a result, harmful to any life form for up to hundreds of thousands of years. The terms 'radioactive waste' or 'nuclear waste' refers to these by-products. The majority of the radioactive waste comes from the energy sector and nuclear power plants (NPP) in particular. The nuclear reactors in the NPP use heat produced by the nuclear fission of uranium. Figure 1.1 shows the nuclear fuel cycle. After the uranium has been mined, enriched and fabricated, it fuels the nuclear reactor for up to five years. The fuel is then removed from the reactor, at this point its radio-toxicity is at its highest level (e.g., IAEA, 2016; NDA, 2015; SKB, 2010). About 95% of the spent fuel is uranium that can be reprocessed to be used as new fuel (SKB, 2010). The rest is treated as waste. The spent fuel needs to cool down in a neutron absorbing environment to avoid starting a chain reaction. Special water pools at the NPP sites are used for that purpose as an interim storage (Sovacool, 2011). Some radionuclides of the waste have a long half-life and it is dangerous to store it at the surface. Permanent storage with special man-made engineering and natural barriers is needed to keep the radioactive waste isolated from the biosphere for as long as the waste is considered

hazardous (SKB, 2010).
Based on their radio-toxicity, half-life, and the heat they produce, the radioactive waste can be divided into three main categories:

- **High level waste (HLW)** have long half-life and high level of radioactivity that increases their temperature. HLW has to be stored in a deep Geological Disposal Facility (GDF).
- **Intermediate level waste (ILW)** does not produce heat and may contain long-lived radionuclides. Could originate from the maintenance and operation of the reactor, such as water, filters etc. Must be stored in great depths in a GDF
- **Low level waste (LLW)** commercial or industrial waste, such as clothing, shoes etc (IAEA, 2016).

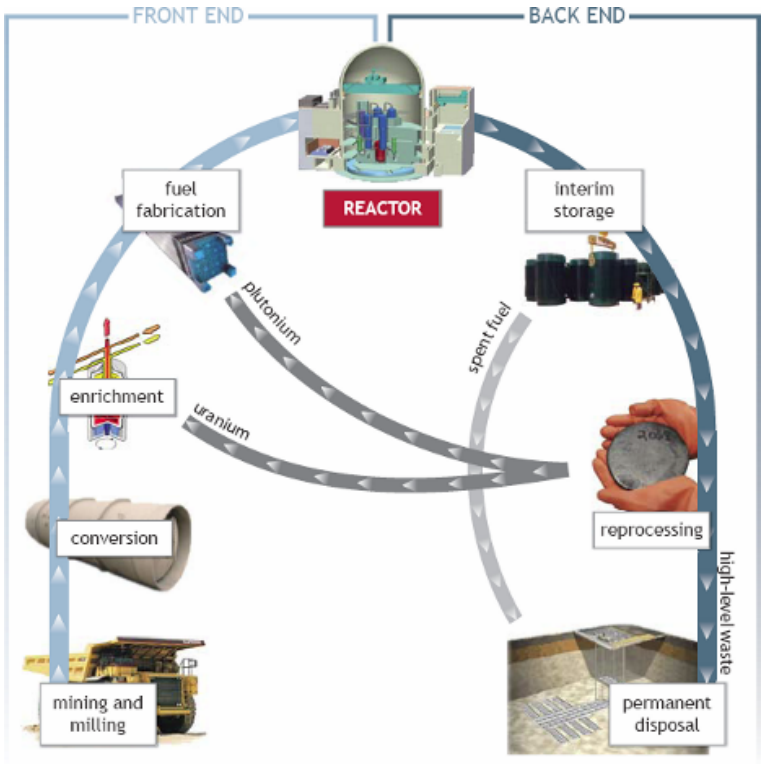

Figure 1.1: The nuclear fuel cycle (Sovacool, 2011)

HLW is about 3% of the total Radioactive waste, while the rest is categorised as ILW or LLW. Both ILW and LLW need to be stored in engineered facilities of shallow to intermediate depth. Many countries have already constructed and operate facilities for ILW and LLW (IAEA, 2016). Several solutions have been proposed for the final disposal of HLW. International conventions for radioactive waste have agreed on the following: each state is responsible for the safe disposal of generated waste, the problem should not be passed on to the future generation, and depositing the waste into the sea or on the seabed, in Antarctica or the icecap is prohibited. All of the studies carried out on the final disposal have concluded that the safest option is to store them at great depths in a stable geological formation (e.g., IAEA, 2016; NDA, 2015; Siren *et al.*, 2015a; SKB, 2010).

At the moment there is no such GDF operating anywhere in the world. However, most of the countries dealing with HLW have made progress on research in that direction. Finland is one step ahead in that direction, as in 2015 decided to start the construction of the GDF with plans to start disposal in the 2020's. Some of the leading countries in this research are Sweden, Finland, U.S.A., Canada, France, Japan, Belgium and Switzerland. By building an underground research lab (URL) and performing several tests on the possible future host rock, these countries concluded on the suitability of each rock type and the most efficient design for the GDF and engineering barriers (e.g., NDA, 2015; SKB, 2010).

The most common design for a GDF is the KBS-3 method (Figure 1.2). The depth of the KBS-3 is 400-700m and it consists of a network of tunnels. One of the major advantages of this method is the low level of exposure to radiation during the process of depositing the waste. This method has two engineering barriers and one natural barrier. The first is the cylindrical cooper canisters, where the spent fuel can be placed without prior processing. These canisters are about 5 m long, 1 m in diameter and 5 cm thick. They can carry up to two tonnes of spent fuel (SKB, 2010). The second barrier is the buffer, which consists of bentonite clay to prevent corrosion of the canister and absorb rock movements. Even in the event of a leaky canister the buffer will stop any radionuclide from escaping. Finally, the host rock, which is the natural barrier, provides a stable environment for a very long period and is not influenced by surface conditions (such as climate change). The canisters are placed either in vertical holes (KBS-3V) (Figure 1.2 left) or horizontal holes (KBS-3H) (Figure 1.2 right and 1.3)

surrounded by bentonite clay (e.g., Siren *et al.*, 2015a,b; SKB, 2010). The deposition holes must be separated by a safe distance due to the decay heat of the spent fuel and the thermal conductivity of the host rock. The tunnels will be backfilled when the fuel is deposited. This combination of engineering and natural barriers isolates the radioactive waste from the biosphere and is designed to further delay any release from the repository in case of a failed barrier.

A series of tests have taken place in the URLs to evaluate the properties and the construction limitation of each possible future host rock. Some of these tests are described in the next section and involve measuring the permeability in crystalline rock (e.g., David *et al.*, 2018; Wenning *et al.*, 2018), or the fractures and permeability increase due to the construction processes and the stress-state changes (e.g., Alejano, 2018; Hakala, 2018; Siren *et al.*, 2015a,b; Suikkanen, 2019; Tsang *et al.*, 2005, 2015). The behaviour of the rock during temperature increase is another research topic have been covered from different research groups (e.g., Lima *et al.*, 2019; Siren *et al.*, 2015a), the backfill have also been tested and modelled to evaluate the material properties and the long-term behaviour (e.g., Sinnathamby *et al.*, 2014; Tsang *et al.*, 2005).

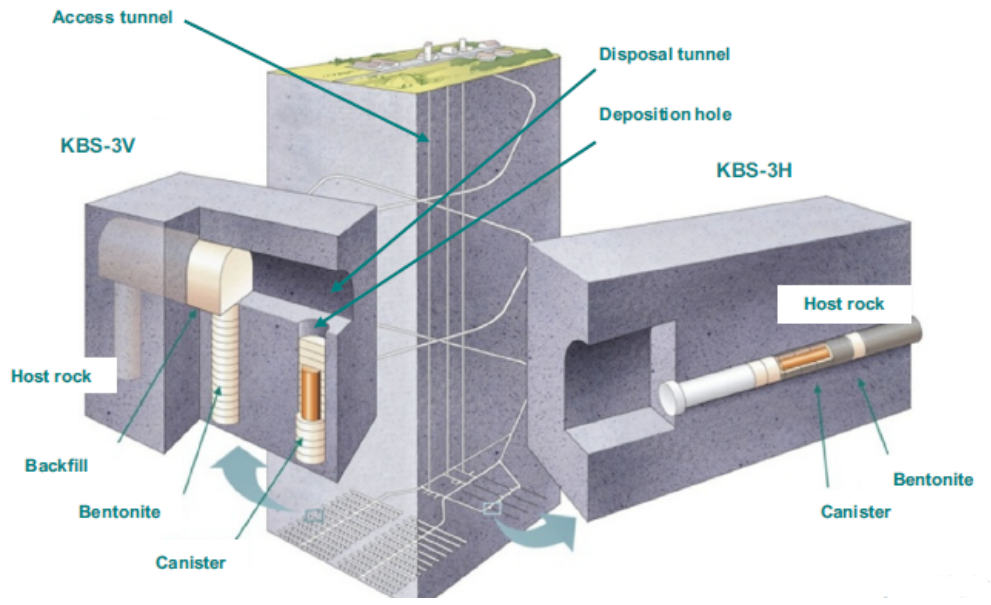

Figure 1.2: Design of radioactive waste deposition using the KBS-3V (left) and KBS-3H (right) methods (Sinnathamby *et al.*, 2014).

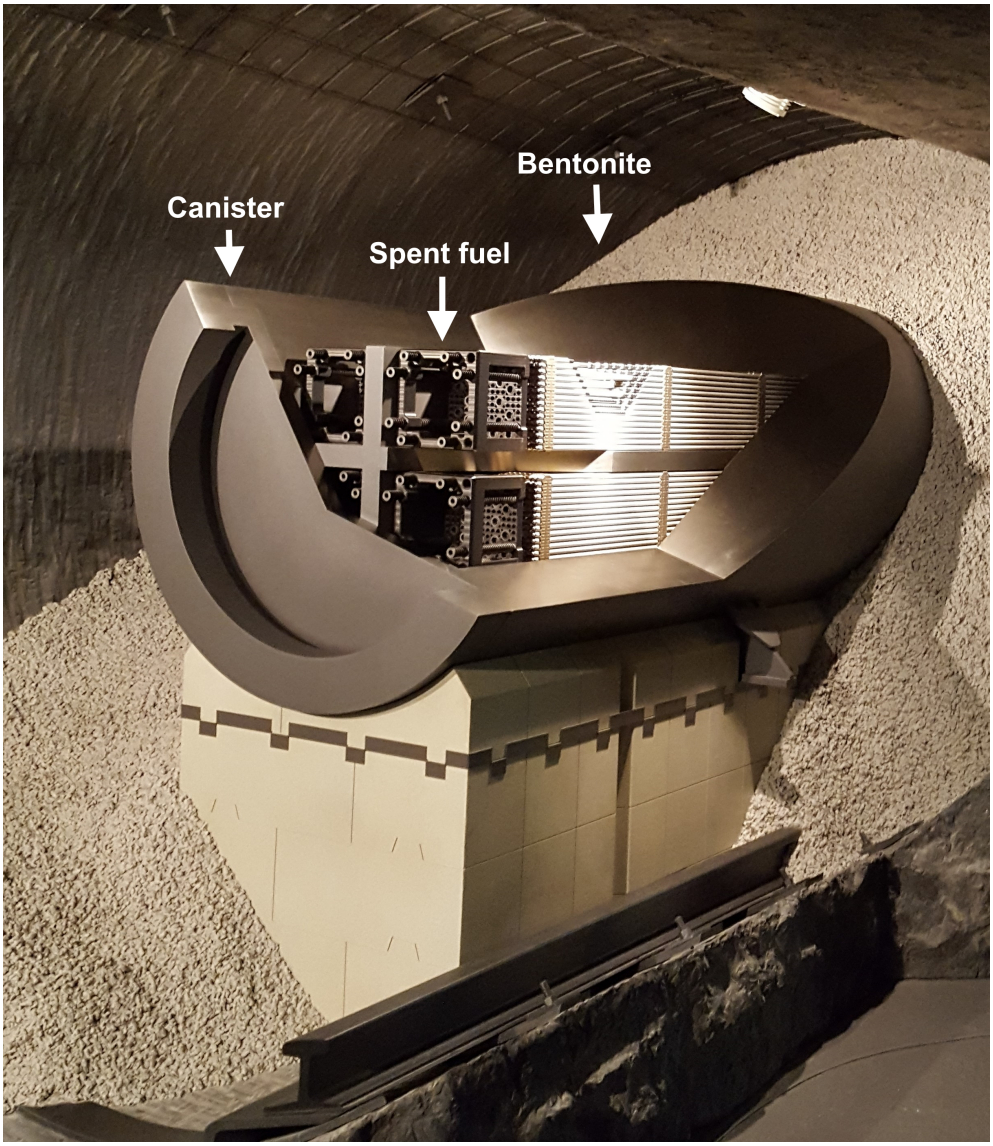

Figure 1.3: KBS-3H maquette in 1:1 scale size. Photo taken on visiting the Nagra's Grimsel URL in summer 2016. Nagra is the company designed and operating the URLs in Switzerland.

1.2 The importance of fractures

Spent fuel must remain isolated for a time frame of about hundreds of thousands of years in an oxygen-free environment to avoid canister corrosion and radionuclide mobility. During this time frame, significant changes in the climate may take place, which may affect the water chemistry around the repository. As a result, the hydro mechanical and geochemical evolution must be taken into account when choosing a suitable host rock (MacQuarrie & Mayer, 2005). Since the priority is to avoid contact with recharge water, the host rock should have very low porosity and permeability close to zero. Four rock types have been proposed as suitable for host rock for future GDFs. These are crystalline/granite, indurated or plastic clay, and salt (Tsang *et al.*, 2005). Even though the porosity and permeability in the rock matrix is very low, fractures could increase the fluid mobility.

Tsang *et al.* (2015) studied the hydrologic issues associated with each rock type in an overview study for a fractured crystalline rock, an unsaturated tuff and clay-rich formation. Each of the rock types has been studied for different hydrologic aspects. The focus for the crystalline rock is the solute transport through fractures for depths up to 500 m. This study concluded for the fractured crystalline rock that one of the major uncertainties, is the structure of the flow paths, which cannot be mapped with the used methods. Both lab and field techniques have been used to quantify the flow-wetted surfaces and the rock matrix properties which are responsible for the fluid movement. One of the barriers for nuclear waste repositories is to validate the model's prediction for solute transport with the in-situ traces tests, as a result of the long-term time frame, which is focusing. For the unsaturated tuff, the fluid flow occurs through a fracture-matrix system where layers of non-welded to welded tuff intersected by fractures creating fluid paths. Welded tuffs are low matrix porosity and permeability but highly fractured formations. Air injection tests in the welded tuff has confirmed that in partly saturated conditions, flow occurs only in the matrix, as the fractures filled with air. Finally, the study for the clays focuses on the coupled thermo-hydro-mechanical processes, since clays are characterised by very low permeability. The thermo-hydro-mechanical processes refers to changes in the water pore pressure due to changes in temperature or in-situ stress. Fractures in clays can change the permeability close to the tunnel surface due to excavation but these fractures are self-healed as the clay swells

when resaturated with water.

Fractures are discontinuities in the rock mass created during geological/tectonic events or human activity such as excavations. In both cases fractures are linked with changes in the stress field of the rock mass (Rutqvist, 2015). Natural fractures vary in size; they could be small in mm scale or up to hundreds of metres, and usually come in groups with the same orientation creating a network with new fluid paths (Lei *et al.*, 2017; Tsang *et al.*, 2015). The size of a fracture is in direct proportion to the opening of the fractures. Small fractures have smaller openings and large fractures have larger openings, which increase the permeability and allows the fluid to flow faster and finally reach underground water (Figure 1.4).

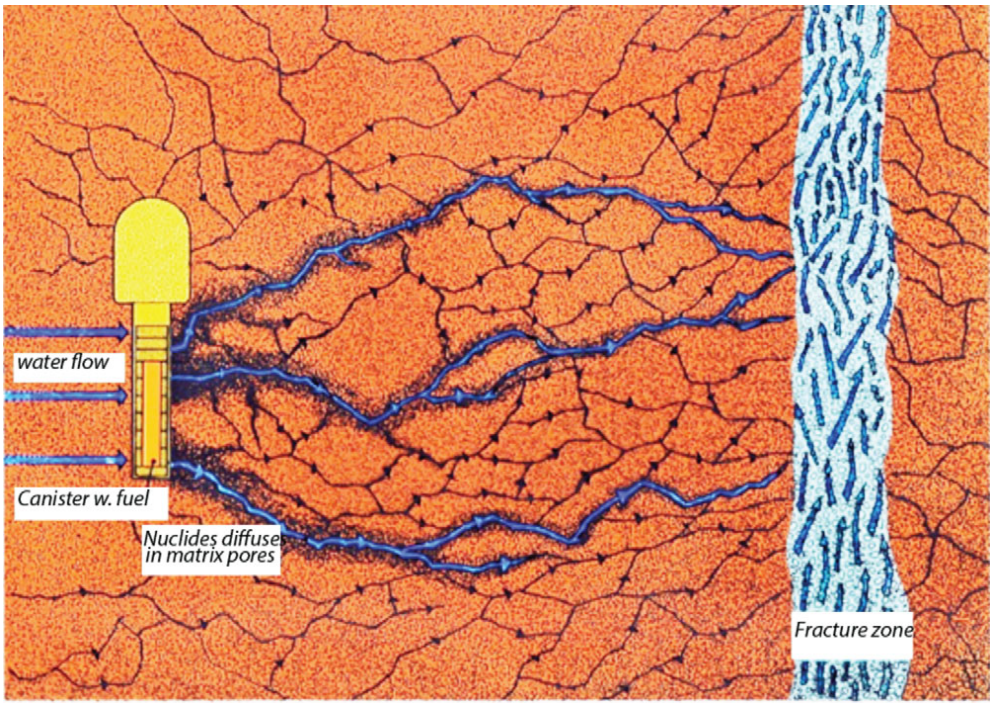

Figure 1.4: A model example of leaking in crystalline fractured rock in KBS-3V repository type (Tsang *et al.*, 2015)

Pores and/or fractures in the rock mass are an important property which must be characterised when studying fluid mobility. However, the geometry and the network of the pores and fractures are these parameters which characterise the permeability

of the rock, if the connection between pores and fractures is poor then fluid cannot easily flow in the rock matrix and permeability is low. Measuring permeability in tight rocks has proven to be challenging as these rocks are more sensitive to the methods used to measure permeability. David *et al.* (2018) worked on measuring and modelling permeability with different methods for the same single material, a low permeability granodiorite from Grimsel URL. For that purpose, twenty-four laboratories have been involved to compare results for different methods and analyse the factor of uncertainty for each method in order to provide a good practice for measuring permeability for such rock types. One of the first observations is that in the granodiorite rock mass the porosity is due to the microfractures in the rock matrix, and is about one percent, any larger microfracture opening between in-situ and lab samples might be linked to the stress release during drilling and sample preparation. They have used several methods, to characterise the microstructures, such as Micro-computerised tomography, Mercury injection capillary pressure (MICP) and nuclear magnetic resonance (NMR), in order to be used as input parameters for the modeling permeability. In this study they used five different modeling approaches, the statistical models, the pore network model, the percolation model, the free-fluid and the effective medium model. The statistical model uses porosity, fracture density and mean fracture aperture as input parameters, this model approach overestimates the permeability since heterogeneity of the fracture network is not considered. The pore network and percolation models which use MICP data successfully predicts permeability. The free-fluid model which uses NMR as input data, predicts permeability within the measured range, taking into consideration the higher pressure these values obtained. Since percolation, pore network and effective medium models have more input parameters such as aspect ratio, aperture, density and connectivity lead to more constraints on these parameters and make the models more relevant. This study concluded that MICP and advanced microscopy methods can offer valuable input data for estimating permeability. Finally, the foliation of the rock creates an anisotropy in permeability, with permeability values to be lower in the direction orthogonal to foliation and higher in direction parallel to that.

During the excavation process at the stage of constructing the GDF, the change in the stress and the mechanical excavation can create new fractures that could prove critical for the effectiveness of the GDF (Siren *et al.*, 2015b). These fractures linked with the excavation process create a zone around the tunnel called an excavation damage zone

(EDZ) and excavation disturbed zone (EdZ). The changes due to excavation lead to much higher permeability. Thus, the EDZ needs to be considered for the long-term effectiveness of the GDF (Tsang *et al.*, 2005).
Both natural and man-made fractures are an important factor to consider for the safety of the HLW. Use of numerical models and measurements to understand and evaluate the evolution of fractures and create a detailed map of existing fractures could help bridge the gap of uncertainty in the future construction of a GDF.

1.2.1 Excavation damage zone and other safety issues

The pre-existing fractures and microfractures in the rock matrix is an important topic of research for the effectiveness of the GDF. However, another important research topic, which attracts more attention in the last decades, is the development of fractures during the excavation process at the stage of constructing the GDF and their behaviour during the closing of the tunnels with the backfill material and the thermal loading from the spent fuel. The excavation process itself and the changes in the stress state of the rock mass are responsible for permanent and temporary changes in the geomechanical properties of the rock mass. This area around man-made openings are called Excavation damage zone (EDZ) and excavation disturbed zone (EdZ). Tsang *et al.* (2005) overview the hydromechanical processes linked with man-made opening and provide a definition and the evolution of the EDZ and the EdZ for all stages of the construction to long-term safety after closure of the GDF. This study examines all four rock types suggested as potential repositories (crystalline/granite, indurated or plastic clay and salt), based on experimental and modelling data from several Underground Research Laboratories (URL) (Tsang *et al.*, 2005).
For all the four rock types the EdZ is a zone away from the tunnel surface where the changes are stress related and are reversible having no negative effect on the GDF safety. For the crystalline rock and rock salt it is difficult to define the outer boundary of this zone. The EDZ for the crystalline rock is a region with irreversible changes and 'freshly opened' fractures, the thickness of the EDZ depends on the tunnel opening method. Rock salt's EDZ is characterised by microfractures and changes in the hydraulic properties. Similarly, EDZ for indurated clay is a region with weakly connected microfractures which is increasing the permeability by several orders of magnitude. Finally, plastic clay's EDZ is a region with geochemical and geomechanical changes with

possible negative effect on the GDF safety.

After the construction stage the EDZ is stable for the crystalline rock, in contrast with the other three rock types, where it is evolving under the new stress-strain conditions. During the early closing stage water from the rock will resaturate the EDF for clays and crystalline rocks, while the temperature from the spent fuel will have a dynamic impact on the behaviour of the EDZ. The EDZ fractures for all rock types will start closing as long as, the backfilling material will start swelling and applying pressure. At a later stage when backfill and EDZ will be fully saturated, the clays and the rock salt will self-heal. Tsang *et al.* (2005) concludes that the relatively high permeability of the EDZ must not be studied separately but as a total flow system. This is due to the fact that when the high permeability zone is surrounded by low permeability the water supply in the EDZ will be very poor.

Defining the characteristics of the EDZ and its evolution during different stages of GDF, for each rock type, is a useful tool for future research in that direction (Tsang *et al.*, 2005). However, more work needs to be done in defining the origin of that damage and how to minimise it. A more recent study, from Siren *et al.* (2015b), divides the EDZ into construction induced and stress induced EDZ. For the depth of the GDF the main damage in crystalline rocks, is induced during construction and depends on the opening method. When using a drill and blast (D&B) method the EDZ may extend between 0.1 m to 1.5 m while for the Tunnel Boring Machine (TBM) method is between 0.01 m to 0.03 m. In the Swedish hard rock laboratory (HRL) Aspo it is able to compare the construction induced damage in the same crystalline rock type for both TBM and D&B opening methods. The mean value of Young's modulus close to the tunnel surface is 10% higher for the TBM tunnel compared to the D&B tunnel. The Young's modulus is changing with depth by only 1% for the TBM and by 3% for the D&B, this difference in surface to depth values for the D&B are possibly linked with the construction method (Siren *et al.*, 2015b). The construction induced damage is notable over the whole tunnel surface while the stress induced damage is stronger in the stress peaks, usually in the roof and the floor of the tunnel. The damage in the rock due to stress are not visible, since the stresses are not high at that depth, however the measurements for porosity and wave velocities can prove the stress related damage Siren *et al.* (2015b).

Finland is a leading country in the research field of nuclear waste disposal. The Finnish

nuclear waste management company Posiva Oy has created the rock characterisation facility ONKALO in Olkiluoto and in 2015, after conducting a series of experiments over the last decades, moved forward from testing to construction stage of the future GDF. As part of this project I am going to model the velocity tomography EDZ experiment in Chapter 5. However, prior to that experiment, another one was testing the in-situ strength and failure mechanisms of the crystalline rock in ONKALO (Siren *et al.*, 2015a). The Posiva's Olkiluito Spalling Experiment (POSE) was mainly targeting on defining the in-situ strength of Olkiluito's gneiss, establishing the in-situ stress and using models to predict the experiment's outcome. It was divided in three phases, testing the pillar damage between two holes, pillar damage due to heating and heating damage for a single hole. Siren *et al.* (2015a) concluded that the fracture initiation strength is 40 MPa and the rock mass strength is 90 MPa while the mean uniaxial laboratory strength is 104 MPa for Olkiluito's gneiss. Based on these values for the vertical disposal (KBS-3V) new fractures will be created at some point after excavation, in contrast with the horizontal (KBS-3H) where no fractures are created after excavation. According to the calculations both designs will suffer fracture initiation 60 years after the fuel disposal but neither is going to have major failure, since secondary stress is lower than in-situ rock mass strength (Siren *et al.*, 2015a). Finally, the in-situ stress was not able to be confirmed by the experiment, while the models did not successfully predict the failure mechanism.

Another safety issue that needs to be considered on the risk assessment of a future GDF is how the temperature of the spent fuel is going to effect permeability. Lima *et al.* (2019) tested granite samples, for temperatures between $25-140°$C under normal stress of 5-25 MPa, and concluded that the hydraulic aperture of natural and artificial induced fractures, decreases while increasing the temperature by 20-75%. This decrease in aperture, linked with raising the temperature, is because of the dilation of the rock. When increasing the stress the thermal dilation is amplified by 10-30%. Lastly, this effect is more clear to samples with larger fracture aperture and larger spatial correlation.

As explained in the previous section, the host rock is the physical barrier to prevent any solute flow to ground water, in case the other engineering barriers fail. The other engineering barriers are equally important and laboratory and modelling studies conducted to prevent any future failure. One such study by Sinnathamby *et al.* (2014) is working

on how the buffer and backfill material are going to interact when the buffer material will start swelling due to water saturation and as a result pressure will increase. The density of the buffer must stay between 1950 kg/m^3 and 2050 kg/m^3. Lower density will end in corrosion of the cooper canisters and higher will increase pressure with possible rock movements. As a result the backfill must be designed in a way to absorb such forces created by buffer swelling.

Permeability of the rock, pre-existing fractures and EDZ, properties of the backfill and buffer material and system behaviour due to thermal loading are some of the safety issues which, must be considered when designing a GDF. Various geophysical methods have been used in order to, identify the above issues. Such methods include applications of seismic tomography velocity surveys, acoustic emission (AE) and microseismic monitoring both in-situ in URLs and in laboratory.

1.3 Fractures and seismicity

Passive seismic monitoring is a useful tool to detect and interpret the initiation and propagation of fracturing due to man made activities, such as the tunnel excavation for GDF construction. The location of the events, the source mechanism, the changes in P and S wave velocities are some of the information obtained when analysing the seismic data which are used to make conclusions about the damage in the rock (e.g., Carlson & Young, 1993; Collins *et al.*, 2002).

Over the last three decades several experiments are running, using passive and active seismic monitoring methods to understand rock damage. Some of these pioneering studies took place in the Canadian URL in Manitoba.

One of the first such studies was to monitor the rock displacement, during a large scale excavation. Carlson & Young (1993) used an active velocity survey prior to excavation and concluded that the rock is quite homogeneous. The majority of the AE data were located close to the tunnel surface and in depth up to 0.4 m. The wave velocities are 5-10% lower close to the tunnel surface and while moving to 0.75 m from the tunnel surface the velocities rise back to values measured prior to excavation. In terms of P-wave velocity anisotropy, it is higher for waves propagating orthogonal to the tunnel and weaker when propagating tangential to the tunnel (Carlson & Young, 1993).

After the excavation experiment and based on the same tunnel level in the Manitoba URL during a sealing experiment this time Collins *et al.* (2002) recorded AE and microseismic data in two different frequency systems in order to monitor rock failure. On these recordings Collins *et al.* (2002) observed that a sequence of AE events are recorded up to six hours prior, and one hour after each microseismic event. The locations of these AE events sequence help to interpret the slip direction of the microseismic event. The locations of the AE events are sub-parallel to the tunnel perimeter with a deviatoric mechanism. However, on each sequence of events there is at least one event classified as a tensile event and four events with a closure mechanism (Collins *et al.*, 2002).

The sensors from the above experiments were calibrated in the laboratory at a later stage in order to perform source parameter analysis of the AE and microseismic data from the above experiments. Goodfellow & Young (2014) concluded that AE and microseismic, from laboratory and in-situ measurements, in principal are linked with the

same rock behaviour. Changes in the wave velocities due to fractures are in the same level for in-situ and laboratory measurements providing a diagnostic tool for rock damage (Goodfellow & Young, 2014).

In similar manner Young *et al.* (2020) combines the AE data from POSE experiment described in previous section and AE data from laboratory triaxial testing to study the deformation, strength and AE during loading and unloading phases. The locations of the AE data from the POSE experiment shows that the fracture initiation and propagation is within the foliation zone. The tested area has two crystalline rock formations, the veined gneiss and a pegmatitic granite. Samples from both types have been tested in the laboratory. The study concludes that laboratory and in-situ data are in agreement. The veined gneiss is weaker than pegmatitic granite and the fracture initiation and propagation is parallel to the foliation of the first one, while peigmatitic granite needs higher principal stress for fracture initiation.

Passive monitoring can provide information about the rock deformation and fracture initiation during all stages of the GDF construction. However, a detailed knowledge of rock behaviour, the saturation of the buffer and EDZ healing during the post-closure time of the GDF without compromising the effectiveness of the GDF is necessary. The changes of the wave velocities over time can provide such information. Marelli *et al.* (2010) and Manukyan *et al.* (2012) have proposed that a full waveform seismic tomography can be used to monitor post-closure of the GDF. They performed cross-hole tomography experiments on the Grimsel and Mont Terri URLs in Switzerland establishing the limitation in coherent noise and the experimental repeatability required for the monitoring system. Modelling data suggests that changes such as water saturation of the buffer can be detected in the wave velocities and amplitude (Marelli *et al.*, 2010). This is in agreement with geophone data suggesting that EDZ sealing and water saturation measured in the waveforms (amplitude, velocities and polarities) (Manukyan *et al.*, 2012). Finally Manukyan *et al.* (2012) suggests that full waveform inversion can provide a more detailed velocity model but further algorithmic development is necessary.

Another study by Biryukov *et al.* (2016) examines the monitoring system for future GDF and concentrates on the attenuation of seismic waves in bentonite. In this study the synthetic data from numerical models compared against experimental traces while

they define the limitation of repository monitoring based on realistic geometries. Bendonite is tested and modelled for different temperatures and water saturation and concludes that waters has a major impact on its properties (Q-factor). About the monitoring system the geometry of source-receiver is important as, the closer to the GDF the more sensitive to viscoelstic parameter changes while, on the other hand the monitoring system must be in a safety distance from the GDF.
Velocity cross-hole tomography was also used as part of a series of experiments to map the EDZ of the niche's testing tunnel in ONKALO Finland. (Reyes-Montes & Flynn, 2015) performed the experiment and concluded that P-wave velocities range between 4800 m/s to 6500 m/s. The rock at depth higher than 0.5±0.1 m shows no significant changes in velocities. The first 0.15 m from tunnel surface is more damaged as velocities are lower. A more detailed description of this experiment is given in Chapter 5 where I model part of the experiment in order to reveal fracture properties.

1.3.1 Seismic waves and numerical modelling

As explained above passive and active seismic methods are widely used to help us interpret the fracture initiation and propagation due to man made activity. Seismic waves carry information about the medium they propagate through and fractures are one of these features that waves interact with (Schoenberg, 1980). The fracture acts like a boundary for the seismic waves. When the wave reaches the fracture, part of the energy of the wave is reflected and this results in attenuation of the transmitted wave. The reason for the reflection and attenuation is because of the change in the mechanical properties of the medium due to the fractures. Hence, seismic waves can provide information about the mechanical properties and the geometry of fractures. To interpret better the seismic waves, we first need to validate the theoretical models. One way is to use numerical models to try to achieve the same result as if using real data. The closer to the real waveforms, the more accurate the built model. The synthetic waves could match the experimental data in many ways: arrival time, frequency content, amplitude or the full waveform. The more parameters of the wave that match, the more accurate the information.
There are two main methods to model fractures. The first and the simplest is to consider an effective medium (EM) and map the properties of the fractures to the properties

of the medium (Crampin, 1981; Hudson, 1981). The second approach is to express the fracture explicitly within a homogeneous background medium (Hildyard, 2007b; Pyrak-Nolte *et al.*, 1990; Schoenberg, 1980). In addition to these two major methods, a third approach, which benefits from both methods, is to use EM but only local to the fracture area, in that way creating a localised effective medium (LEM) (Coates & Schoenberg, 1995).

In this project I examine all three approaches for fracture representation and compare their performance in order to define which fracture representation is more appropriate and under what conditions.

1.4 Objectives of the research and thesis outline

The ultimate goal of this project is to improve the characterisation of fracturing from seismic waves by defining the most accurate and efficient method. Specifically, I aim to prove that having appropriate representations of fracturing in numerical models, allows these models to be used in combination with seismic measurements, to refine our interpretation of fracturing and the underlying mechanical fracture properties. In order to achieve this, I work on the explicit and effective models for representing fracturing. The project works on experiments and numerical models with known fracture positions and links the conclusions from the wave propagation with the mechanical properties of the fractures. Finally, the findings of these models are used to increase the accuracy and improve the interpretation.

Firstly, in Chapter 2, I present the background theory and explain the implementation of the explicit and effective models. I also present the basic principles of the numerical modelling code WAVE3D (Hildyard *et al.*, 1995) and previous work in this field.

In Chapter 3, the explicit and effective fracture representations are used to model a laboratory experiment with multiple parallel fractures (Pyrak-Nolte *et al.*, 1990). After a source inversion the synthetic waveforms of the effective and explicit models are compared against each other and against the experiment. To improve the result of the models, I then introduce stress-dependence into the models through stress-dependent fracture stiffness. In the last part of this chapter I determine the appropriate frequency range of application for each model.

After comparing the models against experiment data, I examine the performance of a special case of effective fracture models; the Localised Effective Medium (LEM), which have been applied in the previous part as well. I create numerical experiments with parallel fractures to define the boundaries between explicit, effective and LEM and scale the experiment for larger size. Using the outcome from that numerical experiments, I design and run numerical experiments, using a commercial numerical code 3DEC (Itasca Consulting Group, 2019), with complex fracture geometries using Discrete Fracture Networks (DFN). At first, wave propagation is tested in explicitly expressed DFN using different fracture densities and the stress-dependence stiffness approach is applied. At the end of this section I express the DFN in the two effective representations of the fractures and compare the result and the applicability of such a model in a case with

complex fractures.

Finally, I use the outcome of modelling a laboratory experiment and the numerical experiments with parallel and complex fractures to improve the understanding and interpretation of a real engineering problem. Posiva is the leading organisation in Radioactive waste management in Finland. As part of the research into the GDF in Finland, Posiva designed and executed a series of studies and experiments related to the EDZ. One of those experiments was an insitu ultrasonic velocity tomography survey for the EDZ on the testing site in the Finnish URL. I use the detailed fracture model which has been designed for the survey area and the velocity survey to model the experiment using the different fracture representations. In that way I can examine the performance of the models in a non-controlled environment and understand how much of the reality each model could show.

Chapter 2

The theory behind the numerical models

This section describes briefly the background theory of the methods used for representing fractures as implemented in numerical modelling code WAVE3D. The implementations of fractures that I am going to use are the explicit fracture representation, effective medium (EM) and localised effective medium (LEM). A description of the numerical implementation of these fracture models will be given along with previous work which has been carried out on each fracture implementation and its limitations.

2.1 Introduction

Physically, fractures are discontinuities in a continuous rock mass and can vary in size, geometry and origin. Numerically, the fractures are described with mechanical parameters such as normal and shear stiffness, friction angle and cohesion. There are several different numerical methods available under commercial and open source codes. In this project I use WAVE3D which was written by Cundall & Hart (1992) and developed to the current version by Hildyard (2001); Hildyard *et al.* (1995) and Hildyard (2007b). WAVE3D uses a staggered finite difference grid, which is widely used to numerically solve wave propagation both in elastodynamics and electrodynamics. Figure 2.1 presents the positions of the grid variables for a three dimensional unit cell in the WAVE3D mesh as designed by Cundall & Hart (1992) and Hildyard (2001, 2007b); Hildyard *et al.* (1995). Each grid variable is computed at a different position in space.

The stresses are calculated from the velocities using :

$$\sigma_{ij} = \delta_{ij}\big(K - \frac{2}{3}\mu\big)\epsilon_{kk} + 2\mu\epsilon_{ij}, \tag{2.1}$$

and the velocities are given by

$$\rho\frac{\partial \dot{u}_i}{\partial t} = \frac{\partial \sigma_{ij}}{\partial x_j}, \tag{2.2}$$

where σ_{ij} is the stress tensor, δ_{ij} is the Kronecker delta, K is the bulk modulus, μ is the shear modulus, ϵ_{ij} is the strain tensor, ρ is the density and u_i is velocity.
Wave dispersion due to the finite difference method (FDM) is a common problem where wave speed is a function of frequency (Hildyard, 2001). Practically, this means that there is a threshold maximum frequency for a given element size or a maximum element size for a given frequency to avoid numerical dispersion. WAVE3D solves a fourth-order wave equation to increase accuracy, increasing the frequency range for a given element size and leading to less numerical dispersion. The coefficients for the grid points are obtained by considering their Taylor series expansions (Hildyard, 2007b).
Based on the WAVE3D methodology, the background medium has no intrinsic attenuation but it has extrinsic attenuation due to the fractures. Due to the basic principals of WAVE3D described above, the element size and the source frequency are coupled parameters (Hildyard, 2007a). Therefore, to avoid dispersion the size of the element in the model must follow the rule for 2^{nd} and 4^{th} order wave equation (Hildyard, 2001):

$$\begin{aligned} \Delta x &< \frac{1}{10}\Big(\frac{c_{min}}{f}\Big) \quad \text{2nd order,} \\ \Delta x &< \frac{1}{5}\Big(\frac{c_{min}}{f}\Big) \quad \text{4th order,} \end{aligned} \tag{2.3}$$

where Δx is the element size, c_{min} is the minimum wave velocity and f is the frequency of the wave.

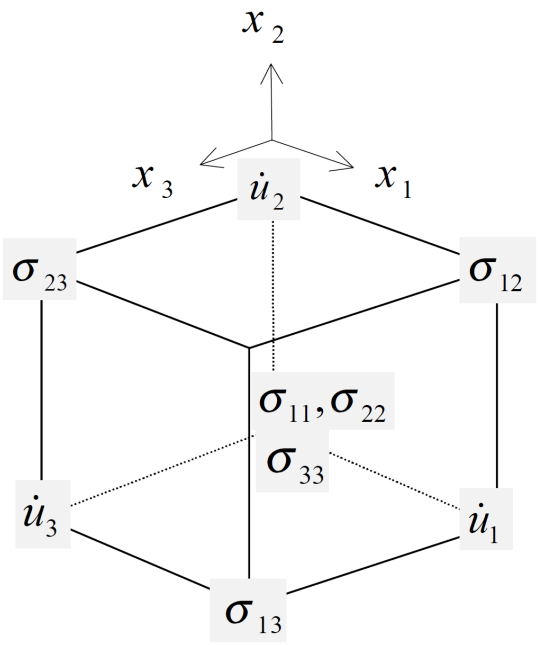

Figure 2.1: 3D unit cell in the staggered grid of WAVE3D (Hildyard, 2001)

Since the purpose of this project is not developing a numerical modelling code I do not present full details. An extended technical description of the methods those can be described by Cundall & Hart (1992), Hildyard (2001, 2007b); Hildyard *et al.* (1995) and Hildyard & Young (2002). However code developments were required particularly for encapsulating stress-dependence in the fracture models and these are explained in detail in Section 3.6.2.

All the models used in this project are three dimensional. The reason for using only 3D models is because the waveforms are compared against real data where the source surface is relatively large but finite compared to the size of the model. The source cannot be described as a plane wave and 2D modelling is inappropriate.

2.2 Theory

There are two main methods for representing fractures in numerical models. The first is to use an effective medium (EM) which combines the effect of the fractures and the rock into a single medium. The second is to use displacement discontinuities to represent discrete fractures within a background medium. This leads to three models studied in this project for representing fracturing. The first is an explicit implementation of the displacement discontinuity with explicit fracture surfaces. The second is an EM of a transversely isotropic material. The third is a hybrid of the two methods with 'localised effective medium' (LEM).

2.2.1 Explicit fractures

A discrete representation of a fracture would typically use a displacement discontinuity (e.g., Chichinina *et al.*, 2009a; Fan & Sun, 2015; Gu *et al.*, 1996; Hildyard, 2007b; Nakagawa *et al.*, 2002; Perino *et al.*, 2010; Pyrak-Nolte *et al.*, 1990; Schoenberg, 1980; Shao *et al.*, 2015). This considers two elastic homogeneous and isotropic spaces in a non-fixed contact of zero thickness connected by linear or non-linear spring (Figure 2.2) which is expressed by normal and shear fracture stiffness, K_n and K_s respectively.
The definition of the displacement discontinuity is the difference in the displacement of the two opposite sides of the fracture for a continuous stress across:

$$\begin{aligned} u_n^t - u_n^b &= \tau_n / K_n, \\ u_s^t - u_s^b &= \tau_s / K_s, \\ \tau_n^t &= \tau_n^b = \tau_n, \\ \tau_s^t &= \tau_s^b = \tau_s, \end{aligned} \tag{2.4}$$

where τ_n and τ_s are the normal and shear stress, u_n and u_s are the normal and the shear displacement of the fracture respectively, the superscript *(t)* and *(b)* indicate the top and bottom surfaces of the fracture (Pyrak-Nolte *et al.*, 1990). When the wave hits the two surfaces with zero thickness, part of the energy is reflected and that part of the energy transmitted is reduced in amplitude and filtered in frequencies based on the stiffness of the fracture. It is clear from the equations that as the stiffness tends to infinity, the displacement discontinuity approaching the behaviour of a continuous

medium. In contrast, when the stiffness tends to zero the displacement reaches maximum value, behaving as a free surface open fracture. This model gives us a discrete representation of a fracture where the surfaces of the fracture are represented explicitly. Figure 2.3 shows the effect in wave propagation for a medium with a single fracture modelled as explicit fracture against a solid continuous medium when the wave propagates perpendicular to the fracture. The above description considers the fracture to be infinite. However, the fractures are normally finite in size and continuity must be restored at the fracture edges. To achieve that the fracture must not extend till the edge of the block and leave at least two grid points from the edges.

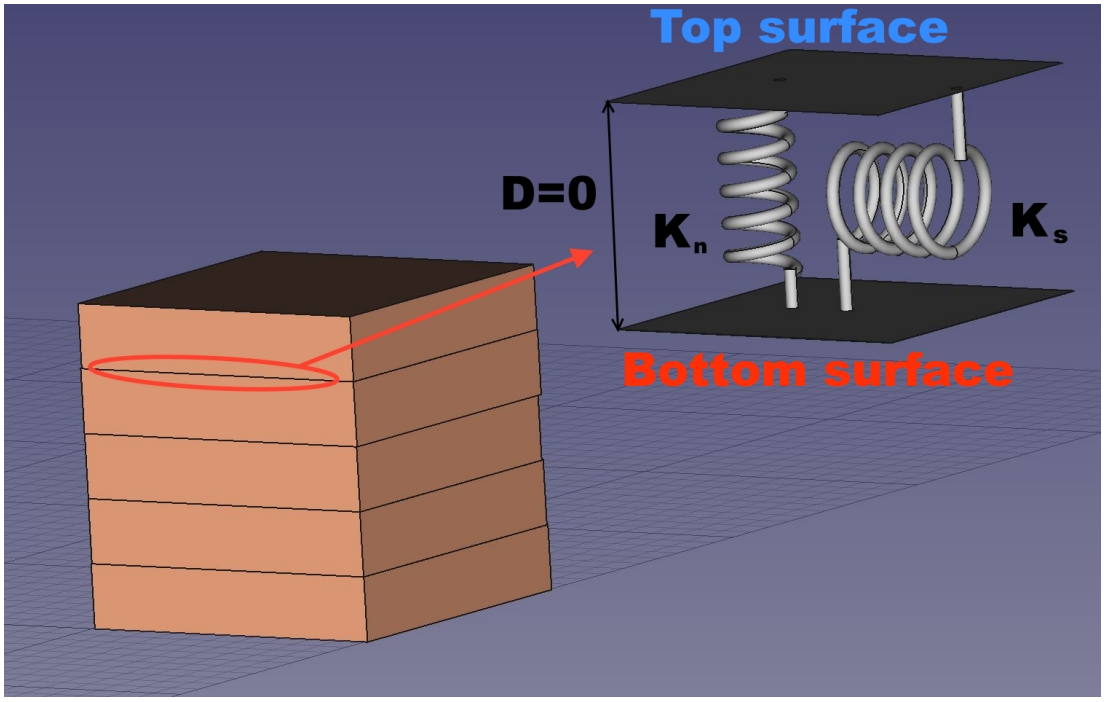

Figure 2.2: The linear spring contact for the displacement discontinuity model. D is distance between the surfaces, K_n and K_s are normal stiffness and shear stiffness (Parastatidis *et al.*, 2017).

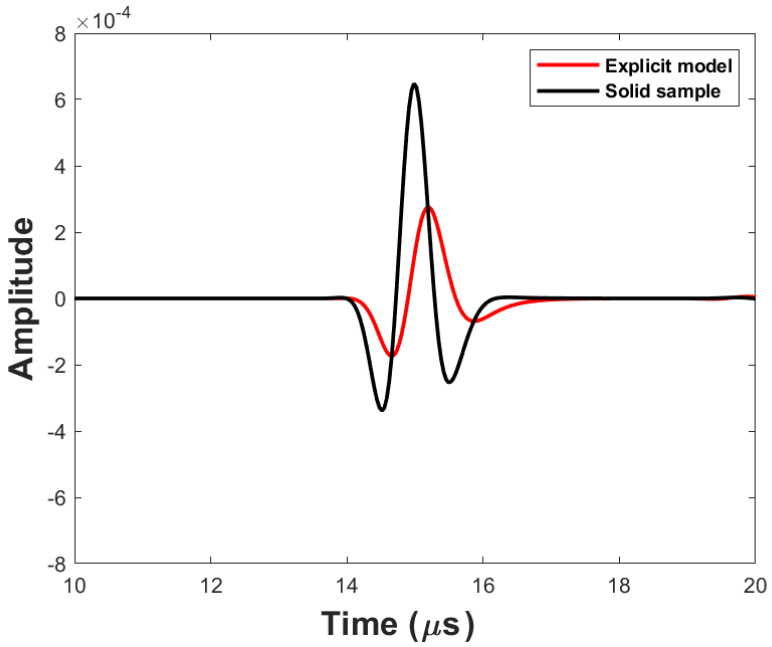

Figure 2.3: Example of a Ricker wave source propagating through a medium with a single explicit fracture (red) and a solid continuous medium (black). The geometry of the solid model is a cube with side 0.09 m, the model with the fracture has the same size and the fracture cuts through the block in two equal pieces. The source and receiver distance is fixed at 0.09 m and are aligned vertical to the fracture. The material properties used are in Table 3.1.

2.2.2 Effective Medium

In modelling seismic waves, a common approach for fracture representation is an effective medium model (EM) (e.g., Crampin, 1981; de Figueiredo *et al.*, 2013; Ding *et al.*, 2014; Hudson, 1981; Kawai *et al.*, 2006; Majer *et al.*, 1988; Rathore *et al.*, 1995; Schoenberg, 1983; Tillotson *et al.*, 2011, 2014). If a medium contains a single set of parallel fractures, this leads to the simplest effective medium which can be described by five elastic constants (equation 2.5),provided the wavelength is sufficiently larger (at least an order of magnitude larger) than the size of the fractures. This case of a single set of parallel fractures creates a transversely isotropic medium. An example of such a transversely isotropic medium is presented in Figure 2.4. When the P-wave propagates parallel to the fractures, the properties are equivalent to the homogeneous

isotropic medium. On the other hand, when the wave propagates perpendicular to the fractures, the properties are different causing anisotropy and attenuation in wave velocities. Figure 2.5 shows an example of a medium with a single fracture modelled as the effective medium against a solid continuous medium when the wave propagates perpendicular to the anisotropy, the parameters, of the mapped fracture, are the same as in the explicit example 2.3. The effect of the fractures is mapped into the five elastic constants losing the discreteness of the fracture and leading to a model which is less sensitive to frequency and amplitude effects due to the presence of fractures.

$$\begin{bmatrix} \sigma_{11} \\ \sigma_{22} \\ \sigma_{33} \\ \sigma_{44} \\ \sigma_{55} \\ \sigma_{66} \end{bmatrix} = \begin{bmatrix} C_{11} & C_{11}-2C_{66} & C_{13} & 0 & 0 & 0 \\ C_{11}-2C_{66} & C_{11} & C_{13} & 0 & 0 & 0 \\ C_{13} & C_{13} & C_{33} & 0 & 0 & 0 \\ 0 & 0 & 0 & 2C_{44} & 0 & 0 \\ 0 & 0 & 0 & 0 & 2C_{44} & 0 \\ 0 & 0 & 0 & 0 & 0 & 2C_{66} \end{bmatrix} \begin{bmatrix} \epsilon_{11} \\ \epsilon_{22} \\ \epsilon_{33} \\ \epsilon_{44} \\ \epsilon_{55} \\ \epsilon_{66} \end{bmatrix} \tag{2.5}$$

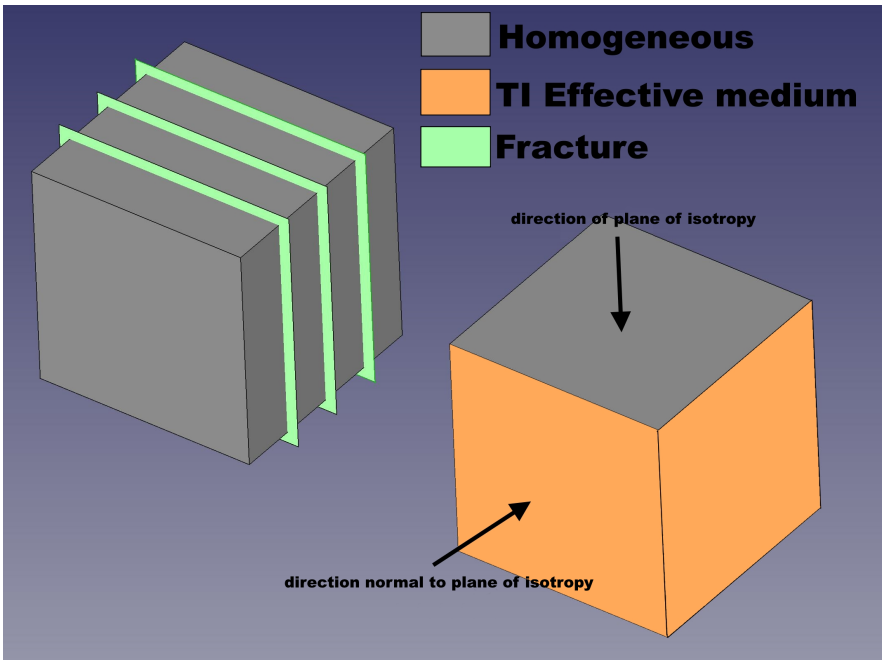

Figure 2.4: In an effective medium the fractures are mapped into the material properties of the medium (Parastatidis *et al.*, 2017). The material properties in direction perpendicular to the fractures has an anisotropic behaviour and the properties parallel to fractures are isotropic.

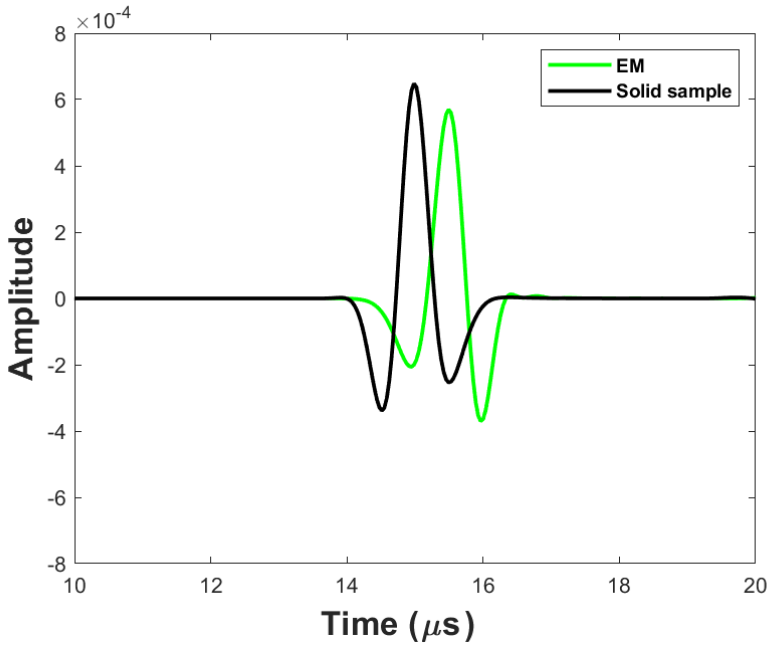

Figure 2.5: Example of a Ricker wave propagates through an effective medium with the same parameters as in the explicit case 2.3 (green) and a solid continuous medium (black). The geometry of the solid model is a cube with side 0.09 m, the model with the fracture has the same size. The source and receiver distance is fixed at 0.09 m and are aligned vertical to the direction normal to isotropy. The material properties used are in Table 3.1.

2.2.3 Localised Effective Medium

The localised EM model (LEM) uses the same stiffness matrix as the EM (equation 2.5). The major difference between EM and LEM is that, in the case of EM the fractures in the stiffness matrix represented as a sum of all the fracture areas in the modelled volume (see next section 2.3 equation 2.9). In contrast, the LEM solves the five constant effective medium moduli only local to the predefined fractures. Where its fracture is represented as zone with material properties of an EM the stiffness matrix calculated separately for each zone (Coates & Schoenberg, 1995; Li *et al.*, 2010; Vlastos *et al.*, 2003; Wu *et al.*, 2005; Zhang & Gao, 2009) as presented in Figure 2.6. This model can be considered a hybrid between the displacement discontinuity and effective medium models, as it introduces explicit fracture regions into the medium and vice

verse. This highlights the extra flexibility of this model as it can perform either close to the explicit model or close to the EM model depending on the the density of fractures and the resolution of the model. Figure 2.7 shows an example of a medium with a single fracture modelled as localised effective medium against a solid continuous medium when the wave propagates normal to the plane of isotropy, the parameters, of the mapped fracture, are the same as in the explicit example 2.3.

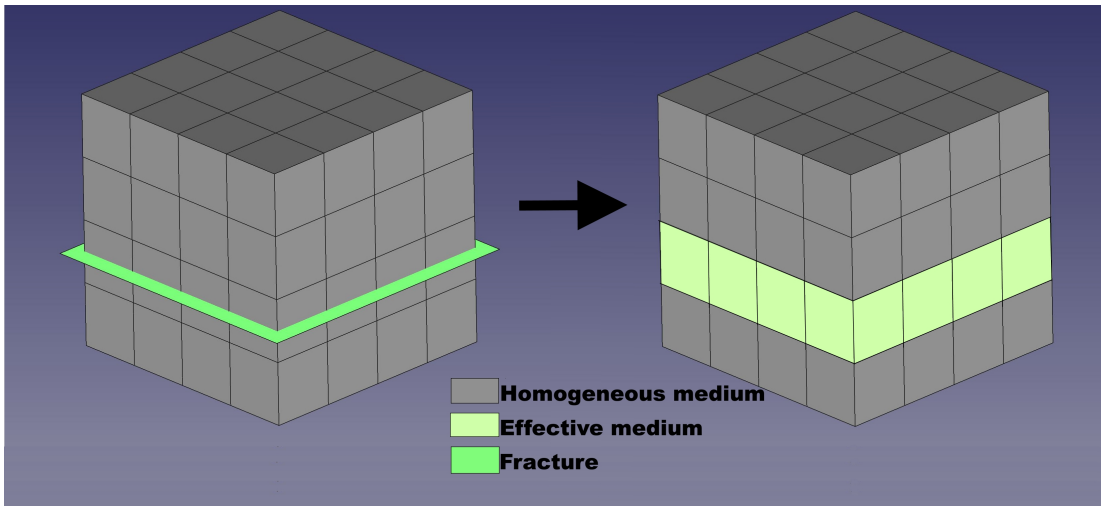

Figure 2.6: The zones close to the predefined fracture position are anisotropic while the rest are the background medium (Parastatidis *et al.*, 2017). The finer the mesh of the model the thinner the LEM layer and the closer to the explicit model.

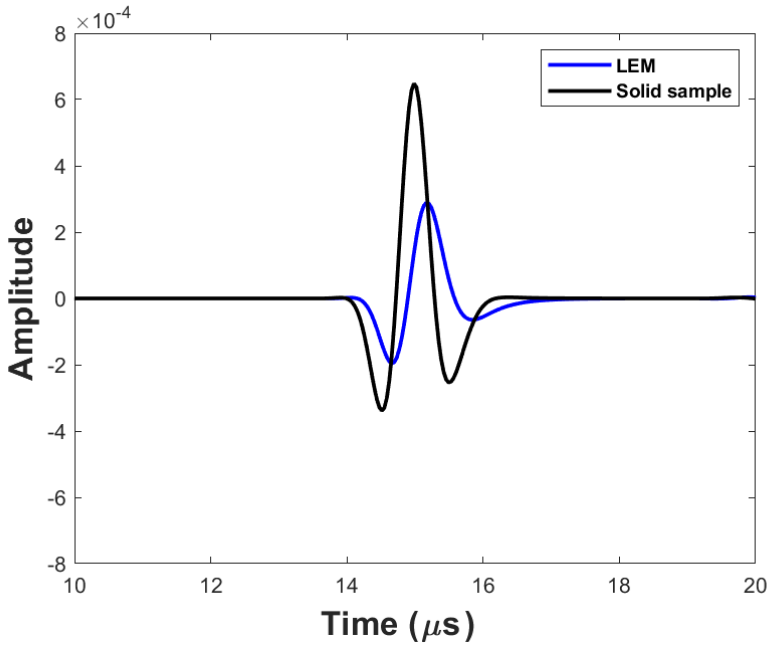

Figure 2.7: Example of a Ricker wave propagates through a localised effective medium with the same parameters as in the explicit case 2.3 (blue) and a solid continuous medium (black). The geometry of the solid model is a cube with side 0.09 m, the model with the fracture has the same size and the layer of LEM cuts through the block in two equal pieces. The source and receiver distance is fixed at 0.09 m and are aligned vertical to the fracture. The material properties used are in Table 3.1.

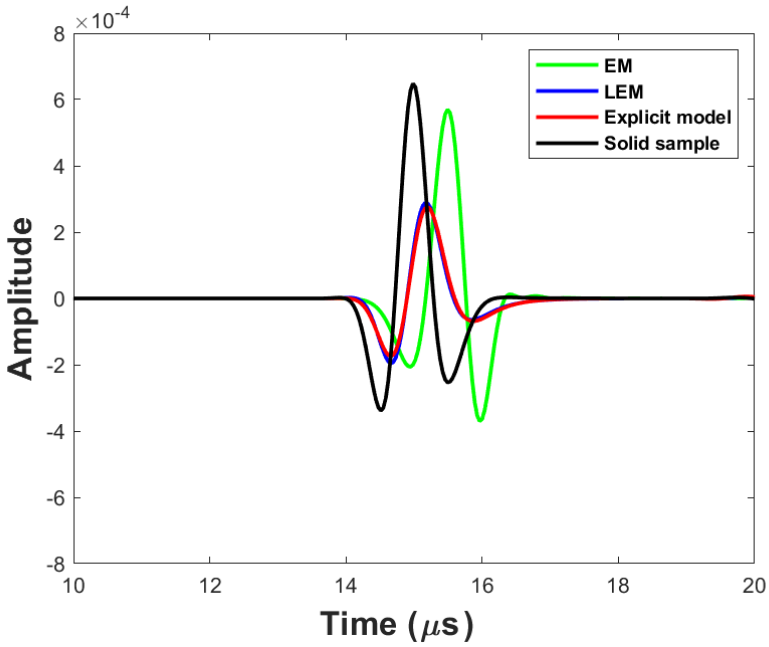

Figure 2.8: Example of a Ricker wave propagates through a medium with a single fracture modelled as an explicit fracture model(red), effective medium (green) and a localised effective medium (blue) and a solid continuous medium (black).

2.3 Crack density vs cracks per unit length

Before describing the numerical implementation of the models, it is necessary to define the differences between the two values describing the fracture population in the medium, to avoid confusion.

The first is 'crack density', ε, introduced by Budiansky & Oconnell (1976), which considers dry disk-shaped fractures linking the surface of the fracture with volume providing a dimensionless value of fracture density. This is given by

$$\epsilon = \frac{2N}{\pi}\left\langle \frac{A^2}{P} \right\rangle, \tag{2.6}$$

where brackets denote an average of the crack area A divided by the crack perimeter P and N the number of cracks per unit volume. For circular cracks:

$$\epsilon = \frac{1}{V}\sum a^3 = N\langle a^3 \rangle, \tag{2.7}$$

where V in the volume, α is the crack radius and N is cracks per unit volume.
In WAVE3D cracks are rectangular and Hildyard (2007b) gives the crack density for rectangular cracks as:

$$\epsilon = \frac{1}{\pi V} \sum \frac{A^2 B^2}{A + B}, \tag{2.8}$$

where V is the volume A and B are the sides of the rectangle.
The second value to describe the fracture population is the 'cracks per unit length' $\frac{1}{L}$. The cracks per unit length is used in the EM and LEM as an input value to the stiffness matrix (see next section 2.4 equation 2.12). The cracks per unit length refers to the total surface of the fractures over the total volume of the area the fractures are:

$$\frac{1}{L} = \frac{\sum (A \times B)}{V}, \tag{2.9}$$

where V is the volume A and B are the sides of fractures. The cracks per unit length, in contrast with the crack density, is not dimensionless and its units are m^{-1}.
A way to convert crack density ε to cracks per unit length $\frac{1}{L}$ and vice versa as

$$\frac{1}{L} = \epsilon \times \frac{(A + B)\pi}{AB} \Leftrightarrow \epsilon = \frac{AB}{(A + B)\pi} \frac{1}{L}. \tag{2.10}$$

In the next sections both crack density and cracks per unit length are used to describe the fracture population and in all cases conversion from an explicit model crack density to EM and LEM cracks per unit length is necessary in order to be able to compare the results from the different fracture representations.

2.4 Numerical implementation of the models

The numerical implementation of explicit fractures based on the displacement discontinuity model is presented in Figure 2.9. Some variables are continuous and some have to be calculated independently for the different positions of the upper and the lower fracture surface. It is clear from the definition of the displacement discontinuity model that the normal stress $\sigma_{22}{}^{u} = \sigma_{22}{}^{l}$ since the stress is continuous. The stress $\sigma_{11}{}^{u}$, $\sigma_{11}{}^{l}$ and velocity $u_1{}^{u}$, $u_1{}^{l}$ are discontinuous and have dual values. The values of normal and shear displacement can be calculated, assuming that they are coupled to the normal and shear stress with the K_n and K_s values respectively. Further description of the numerical implementation of the displacement discontinuity model along with the equations solutions are presented in Hildyard (2001).

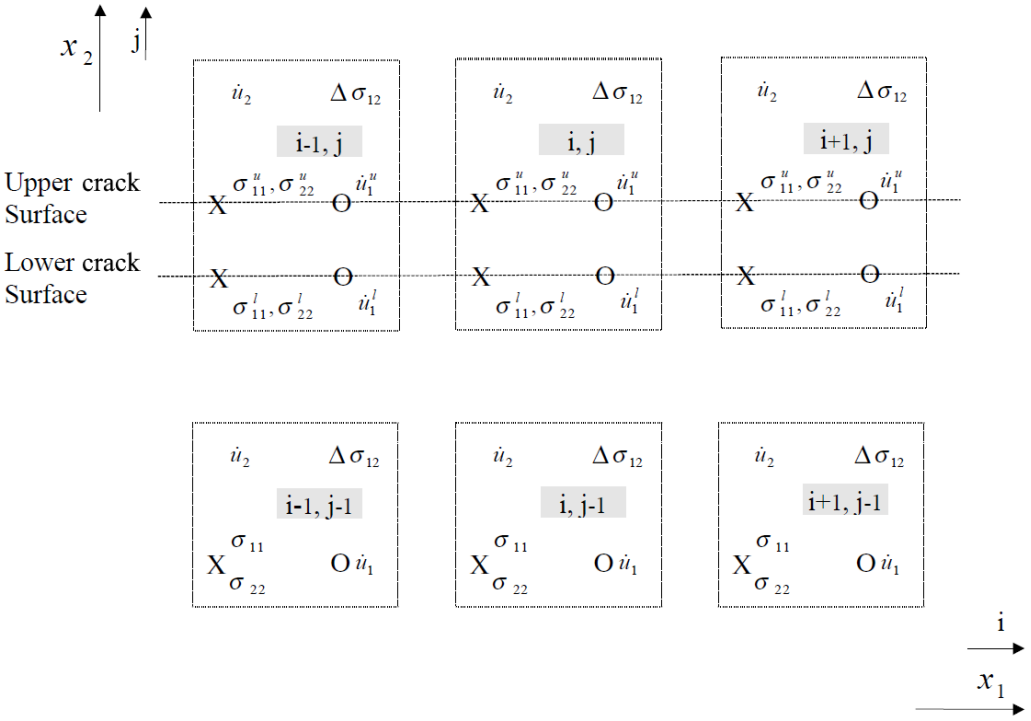

Figure 2.9: Variable positions in a two dimension fracture in staggered grid modified from Hildyard (2001). The X and O symbols are the position of the pointed variables in the grid.

As explained in the previous section, EM theory uses five elastic constants to apply the

effect of a single set of parallel fractures in the medium. The stiffness matrix in equation 2.11 has a general representation of these five elastic constants. For this project, I use the Coates & Schoenberg (1995) approach for an effective medium, linking cracks per unit length *(1/L)* and crack stiffness *(Kn, Ks)* with elastic constants (equations 2.12). For the EM, the cracks per unit length is calculated as presented in equation 2.10 taking into account the *total* number of fractures and the *total* volume of the studied area.

$$C = \begin{bmatrix} (\lambda+2\mu)(1-r^2\delta_N) & \lambda(1-r\delta_N) & \lambda(1-\delta_N) & 0 & 0 & 0 \\ \lambda(1-r\delta_N) & (\lambda+2\mu)(1-r^2\delta_N) & \lambda(1-\delta_N) & 0 & 0 & 0 \\ \lambda(1-\delta_N) & \lambda(1-\delta_N) & (\lambda+2\mu)(1-\delta_N) & 0 & 0 & 0 \\ 0 & 0 & 0 & \mu(1-\delta_T) & 0 & 0 \\ 0 & 0 & 0 & 0 & \mu(1-\delta_T) & 0 \\ 0 & 0 & 0 & 0 & 0 & \mu \end{bmatrix}, \quad (2.11)$$

$$r = \frac{\lambda}{\lambda+2\mu} = \frac{\nu}{1-\nu},$$

$$\delta_T = \frac{K_s^{-1}\mu}{L + K_s^{-1}\mu}, \quad (2.12)$$

$$\delta_N = \frac{K_n^{-1}(\lambda+2\mu)}{L + K_n^{-1}(\lambda+2\mu)},$$

where λ is Lamé's first parameter, μ is the shear modulus (Lamé's second parameter), ν is Poisson's ratio and *1/L* is the cracks per unit length. On the other hand, the LEM applies the equation's 2.11 stiffness matrix locally to the fracture. Therefore, the cracks per unit length *(1/L)* is calculated as follows (equation 2.13).

$$\frac{1}{L} = \frac{A \times B}{A \times B \times h} = \frac{1}{h}, \quad (2.13)$$

where A and B are the sides of the fracture and h is the thickness of the LEM layer. Usually h is equal to the element size Δx to provide maximum discreteness. However, various values of thicker h are also considered in Chapter 4 to examine the flexibility of this model.

2.5 Previous studies

A great number of studies have been carried out on wave propagation for all the three models described above. Some of these studies have been validated using laboratory experimental measurements, in comparison with analytical or numerical modelling solutions based on the theories of the three models (e.g., Chichinina *et al.*, 2009a,b; de Figueiredo *et al.*, 2013; Ding *et al.*, 2014; Huang *et al.*, 2014; Li *et al.*, 2010; Molero & IturraranViveros, 2013; Mollhoff & Bean, 2009; Perino & Barla, 2015; Perino *et al.*, 2012; Rathore *et al.*, 1995; Tillotson *et al.*, 2011, 2014; Yil *et al.*, 1997). On the other hand, some of the research studies are at a purely theoretical level, for either analytical or numerical model solutions, introducing new implementations for the models or making conclusions for fracture properties and wave propagation (e.g., Li *et al.*, 2010; Mollhoff & Bean, 2009; Perino & Barla, 2015; Perino *et al.*, 2012; Vlastos *et al.*, 2003; Yil *et al.*, 1997).

An analytical solution of the displacement discontinuity model using the method of characteristics to produce the transmission ratio in a singly or multiply fractured medium has been examined by Huang *et al.* (2014), who compare the theoretical values with experimented data. Another study (Carcione *et al.*, 2012) working on the analytical solution of a localised effective medium model and on the numerical solution of a displacement discontinuity model, examined the phase velocity and dissipation factor for dry and saturated conditions, using experiments from Chichinina *et al.* (2009a) and Chichinina *et al.* (2009b). This work concluded that the models are in qualitative agreement with the experimental data and attenuation is linked with the fracture viscosity.

Studies on the numerical implementation of the effective medium model have introduced a new technique to create synthetic rock samples with fractures (Rathore *et al.*, 1995), in which the effective medium model theories by Thomsen (1986) and Hudson (1981) for wave velocity in dry and saturated condition are validated, and concluded that both approaches agree well for dry case. However the Thomsen theory predicted better velocities for the fluid saturated case.

Rathore *et al.* (1995) and Tillotson *et al.* (2011) showed the fluid dependency of shear wave splitting, based on experimental measurements and on the effective medium model output for velocity and Thomsen anisotropy. A second experiment by Tillotson *et al.*

(2014) using more realistic synthetic sandstone and lower frequencies compared to their previous experiment, measured propagation along four different angles of incidence to give Thomsen anisotropy parameters. Studies using synthetic samples by Ding *et al.* (2014) measured velocities and compared the experimental data with the theoretical Hudson (1981) model, concluding that the model data overestimates the P-wave velocity due to the model limitation for fluid saturated conditions. Schubnel & Gueguen (2003) and Schubnel *et al.* (2003) have studied the validation of crack density for effective medium in lab and field data with high and low frequencies respectively, for both dry and wet cracks. The effect of cracks is stronger for the dry cracks. The comparison with the experiment have proven that for total crack densities up to 0.5 the models are valid. de Figueiredo *et al.* (2013) worked on wave propagation in synthetic samples, examining samples varying from homogeneous isotropic to anisotropic, where the discontinuities were created using rubber. Working on the frequency changes and attenuation for different cracks, they observed that the Thomsen parameters vary with the frequency and size of the fractures. Lastly, on the effective medium model Molero & IturraranViveros (2013) studied the velocity in 2D anisotropic media comparing the model results with laboratory experiments, which have good agreement. The size of the fractures and the wavelength of the signal is very crucial for the effective medium model. Shuai *et al.* (2018) used the effective medium to model the wave velocities for an experiment with a synthetic sample to study how wavelength and fracture diameter ratio (λ/d) affects the wave velocity dispersion. They concluded that as the wavelength decreases the scattering caused by fractures creates velocity dispersion. When $\lambda/d > 14$ for P and $\lambda/d > 4$ wave velocities can be described by effective medium and equivalent medium respectively while Hudson theory is not predicting velocities accurately for small fracture diameter.

For the displacement discontinuity model, experiments have been done to validate the model for velocity, attenuation and scattering amplitude. Hildyard (2007b) modelled Pyrak-Nolte *et al.* (1990) experiment and in-situ monitoring from the underground research laboratory (URL) in Canada, using the displacement discontinuity model in the numerical code WAVE3D, where he directly compared the modelled and real waveforms. He studied the frequency dependent fracture stiffness of the wave speed and amplitude for various fracture sizes and concluded that the fracture stiffness has a significant effect

on wave velocity, amplitude attenuation and frequency content, and established the importance of stress dependence on wave propagation. He also studied random fractures assemblies with different crack densities, fracture sizes and crack stiffness deriving their frequency depend, velocity and attenuation behaviour. Working on laboratory experiments using a layered sample of plexiglass, under 2 and 4 MPa load for ultrasonic surveys, utilizing on various angles of propagation Chichinina *et al.* (2009a) and Chichinina *et al.* (2009b) examined the attenuation and velocity for dry and oil saturated conditions. In addition, they used the displacement discontinuity method to model the experiment and concluded that attenuation and velocity anisotropy are linked. Another experiment using Resonant Column Apparatus Test for Aluminium and soft rock samples performed by Perino & Barla (2015) to estimate the shear modulus and shear wave velocity based on the resonant frequency, the results from the test have been successfully compared with the 3DEC model (Itasca Consulting Group, 2019). Working on the displacement discontinuity model Blum *et al.* (2011) used experimental data from a plastic cylinder with a single fracture to produce an analytical expression of the scattered amplitude of a plane fracture of arbitrary size under Born approximation. The method for acquiring data was with a non-contacting source-receiver (laser), using two different source positions giving angles of 0^o and 50^o. A similar experiment performed by Blum *et al.* (2014) introduced uniaxial stress, with the source-receiver position fixed and the sample being rotated.

Although laboratory experiments have been as reformed to validate the displacement discontinuity model, many studies are theoretical, analysing for example, the transmission coefficient and velocity behaviour and the effect of fracture stiffness on seismic waves. Mollhoff & Bean (2009) used analytical and numerical solutions for a displacement discontinuity to model a former experiment, on a granite sample where they studied the transmission coefficient behaviour. Another theoretical study on the displacement discontinuity model examines dispersion as a function of frequency (Nakagawa *et al.*, 2002). They worked on the Pyrak-Nolte *et al.* (1990) experiment to examine the effect of fracture stiffness on the dispersion of the waves, using the dispersion of lower order symmetric mode, concluding that the normal fracture stiffness can be determined. Yil *et al.* (1997) study wave propagation in multiple parallel fractures, examining the frequency-related amplitude and velocity anisotropy. In this work the effective medium

model is compared with the displacement discontinuity model, concluding that the effective medium may underestimate the velocities and the amplitude anisotropy due to the frequency-dependent nature of the fractures. Finally, an analytical solution of the scattering matrix method is described by Perino *et al.* (2012) where they successfully compare the results for the transmission and reflection coefficients with the distinct element method (DEM) using 3DEC.

Experiments have also been done to validate the localised effective medium model. Groenenboom & Falk (2000), using data from a triaxial laboratory experiment and a numerical model based on a localised effective medium in order to examine scattering phenomena like guided waves and concluded that diffracted arrival times can be used to determine the size of the fractures. Fang *et al.* (2014) used the fracture transfer function from surface seismic scattered waves to detect fracture direction, to model laboratory measurements for parallel fractures in different azimuths.

There has been a significant amount of work at a purely theoretical level for the localised effective medium model examining velocity, transmission coefficient and scattering attenuation. Vlastos *et al.* (2003) comparing theoretical travel times with the synthetic waveforms of the localised effective medium model for three cases to validate the method. The first case concentrates, on different spatial distributions, which produce different wave field characteristics and shows the importance of spatial distribution. The second case studies the effect of fracture length variation where high clustering does result in increasing local fracture densities causing energy trapping. The last case examines how fractures with a fractal distribution of size affects the wave field and concludes that frequency-dependent seismic scattering depends on spatial distribution. A study for scattering attenuation for different stages of fracture growth was made by Vlastos *et al.* (2007) using a localised effective medium. Synthetic seismograms generated for each stage of the fracture growth computing multiple scattering attenuation as a function of frequency and they concluded that scattering attenuation is strongly frequency dependent. Using this method of scattering attenuation the fracture properties can be characterised and dominant scale lengths of the fractures identified. Li *et al.* (2010) introduced a viscoelastic medium model with equally spaced parallel joints, creating a new localised effective medium model using the assumption of a virtual wave source. Comparing velocities with the displacement discontinuity model, Li *et al.* (2010) show that the virtual wave source model is equally as good as displacement

discontinuity model results with the new model accurately predicting the transmission coefficient. Synthetic waveforms for displacement discontinuity and localised effective medium numerical models have been compared for numerical experiments on propagation in single and multiple parallel fractures by Zhang & Gao (2009), where they concluded that both models agree well.

Another model for wave propagation in fractured rock replaces the fracture with a thin layer with different properties from the surrounding material. Wu *et al.* (2005) compared the thin layer model with the localised effective medium method for full waveforms, for a single fracture, for a viscoelastic material and concluded that both methods agree very well one another, although the localised effective medium is more efficient in terms of computational time. Furthermore, the thin layer model has a very slow fluid-guided wave which is the major difference on the results of the two methods.

Finally, a study by Perino *et al.* (2012) which compares three different approaches of analytical solutions for the displacement discontinuity model with the analytical solution of a virtual wave source implementation of a localised effective medium as described above. The first three models which are based on the displacement discontinuity model are: the Method of Characteristics, Virtual wave source and Scattering matrix method. The fourth method is based on an equivalent medium and a virtual wave source. Examining the particle velocities and transmission coefficient they conclude that the four methods agree well.

Most of the previous work on wave propagation in a fractured medium only compares individual characteristics, such as velocity, attenuation and transmission coefficients of recorded and modelled waveforms Chichinina *et al.* (2009a,b); de Figueiredo *et al.* (2013); Ding *et al.* (2014); Huang *et al.* (2014); Li *et al.* (2010); Molero & Iturraran-Viveros (2013); Mollhoff & Bean (2009); Perino & Barla (2015); Perino *et al.* (2012); Rathore *et al.* (1995); Tillotson *et al.* (2011, 2014); Yil *et al.* (1997) and Perino *et al.* (2010)). None of these studies compare full synthetic waveforms with the recorded. There is also much recent work validating the models, as described previously. As a result the models produce a theoretical arrival, transmission coefficient or attenuation (Li *et al.*, 2010; Molero & IturraranViveros, 2013; Perino & Barla, 2015; Perino *et al.*, 2012; Vlastos *et al.*, 2003; Yil *et al.*, 1997) using either analytical or numerical solutions without outputting full waveforms.

A small number of papers have published waveforms from experiments (Fang *et al.*

(2014); Groenenboom & Falk (2000); Rathore *et al.* (1995) examining the arrival time), (Tillotson *et al.* (2011) compare the time delay between water and glycerine saturation), (Perino *et al.* (2010) publishing frequency-amplitude data measured from an experiment and from a 3DEC model) but none compares the experiment fully.
Some recent work compares the displacement discontinuity model with the localised effective medium model where the two models agree well (Li *et al.*, 2010; Perino *et al.*, 2012; Wu *et al.*, 2005)).
In contrast, Hildyard (2001) does compare full waveforms with data. However this work exclusively studied the displacement discontinuity model and not effective medium (EM) or localised effective medium (LEM) models.
The seismic waveform recorded from a laboratory experiment or in-situ, contains information from the medium. Models are used in comparison with real data, so as to better understand the properties and the discontinuities of the medium. However, often only a small amount of information from the waveform is being used such as first arrival, when the work is concentrated on individual wave characteristics such as velocity and attenuation. Another limitation that arises in these cases, is the non-uniqueness of the model interpretation, a limitation which can be minimised when more parts of the waveforms was used. Such a method which is widely used, both on regional seismology and on laboratory scale is the coda wave which is the later part of the seismogram. Coda wave is the result of multiple reflections of the wave energy as it propagates through medium with heterogeneities and can be used to estimate fracture parameters (e.g., King *et al.*, 2017; Napolitano *et al.*, 2019; Wang *et al.*, 2017). However, in this project I am going to match the full waveform of experimented and modelled data without using any phase velocity peaking and examine the total length of the waveform.
Using numerical models to create synthetic waveforms in order to compare and match them may improve the model and can minimise the gap between modelled fractures and reality. The more parts of the waveform matches with the real data the better understanding we have for the fracture properties. Finally, there is a need to define which of the three models is most accurate and what is the range of applicability of each model. In addition to the above it is necessary to study how to create reliable models and at the same time, computational efficient models by using alternative methods to represent fractures.

Chapter 3

Modelling seismic wave propagation in medium with parallel fractures

I am using an effective medium approach, an explicit representation of fractures and a localised effective medium to model fractures. In this chapter I examine how waves propagate through a block with multiple parallel fractures using the three models for fracture representation. I then compare their performance against each other and against the experimental data. To match the experiment I need to include the stress field which I do by implementing stress dependent fracture stiffness in all three models.

3.1 Introduction

Many studies (e.g., Crampin (1981), Hudson (1981), Majer *et al.* (1988), Rathore *et al.* (1995) Kawai *et al.* (2006), Tillotson *et al.* (2011), de Figueiredo *et al.* (2013), Ding *et al.* (2014), Tillotson *et al.* (2014)) have assumed that the response of a large number of fractures can be mapped into the overall effective behaviour of the medium, by linking the elastic constants with the fracture density and orientation, leading to anisotropy in the wave velocities (effective medium modelling). Another widely used approach is discrete fracture representation using displacement discontinuities. The model was introduced for seismic wave propagation by Schoenberg (1980) and has been studied by numerous authors, (e.g., Pyrak-Nolte *et al.* (1990), Nakagawa *et al.* (2002), Hildyard

(2007b), Chichinina *et al.* (2009a), Perino *et al.* (2010), Fan & Sun (2015), Shao *et al.* (2015)). A third case which is a hybrid of the other two approaches comes out when considering the area close to the predefined fractures as an effective medium while the rest of the medium is treated as homogeneous isotropic (Coates & Schoenberg (1995), Wu *et al.* (2005), Vlastos *et al.* (2003), Zhang & Gao (2009), Li *et al.* (2010)).

Pyrak-Nolte *et al.* (1990) examined the displacement discontinuity model for elastic wave propagation through multiple parallel fractures, in an experiment using laminated steel plates to simulate natural fractures. Hildyard (2007b) then showed that an explicit representation of the fractures could match the experimental recorded waveforms but only if the effect of a non-uniform loading on fracture stiffness was included. In this chapter I am modelling this experiment on laminated steel block (Pyrak-Nolte *et al.*, 1990), using the numerical modelling code WAVE3D (Hildyard *et al.*, 1995) to demonstrate the resulting changes to seismic waveforms for both effective and discrete fracture models. I do this to establish under what conditions each representation is most appropriate and how close the models are to producing real effects on waveforms. Part of this work has been presented in the 51st U.S. Rock Mechanics/Geomechanics Symposium (Parastatidis *et al.*, 2017). The discontinuities on this experiment are parallel and there are two acquisition geometries, with waves perpendicular and parallel to the fractures. I first describe a source inversion process used in order to have a comparable result with the experiment. Next, I examine the performance of the models against one another assuming that the stress is uniform and consequently that the fracture stiffness is uniform along all the fractures. Later, I introduce the stress dependent fracture stiffness so that I can mimic the experimental conditions and compare the waveforms from the models against the waveforms from the experiment. Finally, to better understand the nature of these three fracture representations, I filter the model data to lower frequencies in order to define the frequency range where the three approaches match and perform in a similar way.

3.2 Setup of laboratory experiment

Pyrak-Nolte *et al.* (1990) recorded ultrasonic waves through multiple parallel fractures created by stacking and bolting together 31 steel plates of 2.92 mm thickness. The result is a 90.6 mm sided cube (Figure 3.1). The surfaces of the steel plates were sandblasted to create a rough surface closer to real fractures. The sample was loaded biaxially with 30 kN, perpendicular to the plates to hold them together and one direction parallel to the plates as shown in (Figure 3.1). A P and two polarisations of S wave were transmitted and recorded from a transducer-receiver couple, first orientated perpendicular to the fractures and then parallel. The transducer-receiver couple were loaded in series to create a good coupling. The same procedure was repeated for a solid steel cylinder sample of 99mm height and 102 mm diameter. The steel material properties are published and are shown in (Table 3.1). Hildyard (2007b) modelled the experiment using the finite difference numerical code WAVE3D (Hildyard *et al.*, 1995) with numerically implemented displacement discontinuities representing the fractures to study the effect of the fracture stiffness on the waveforms and the stress-dependence on the wave propagation.

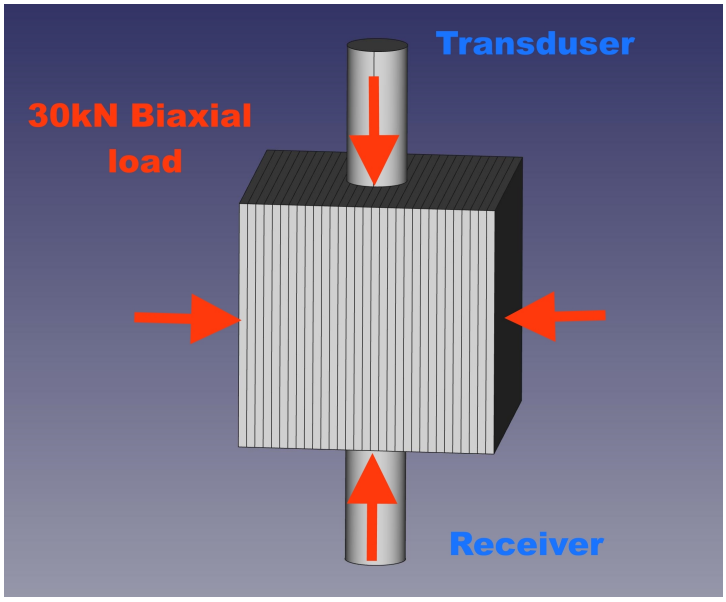

Figure 3.1: Original experiment (90mm cube sample) loaded biaxially (red arrows) (Parastatidis *et al.*, 2017).

Property	Value
Shear modulus	82.15 GPa
Density	7750 kg/m^3
Poisson's ratio	0.3
P-wave Velocity	6023 m/s
S-wave Velocity	3254 m/s

Table 3.1: Material properties of laminated steel sample (Pyrak-Nolte *et al.*, 1990).

3.3 Model design

The geometry and size of the models depend on the original experiment and the frequency content of the waveforms. The predominant period for the P-wave based on the frequency of the waveform from the solid sample is 1.2 μs, which is the same as the S-wave. The element size must be small enough as the waveform will also include frequencies higher than the dominant frequency. Hence, the size of the elements for the P-wave based on the wave velocity from the solid sample should be a maximum of 1.4 mm and for the S-wave it should be no more than 0.78 mm (equation 2.3).
The size of the element for the S-wave is smaller than the P-wave due to the wave speed being slower. In order to make the models consistent in terms of geometry, the same element size was used for both models. As a result, the maximum size of the element should be no larger than 0.78 mm. However, because the thickness of each plate is 2.92 mm, in the model the space between the discontinuities should be an integer number of elements and, at the same time, smaller than the maximum element size. It was decided to have 6 elements between each discontinuity, and this gives an element size of 0.4871 mm leading to a 3D model with 187 elements on each side and a total number of approximately 6×10^6 elements.

3.3.1 Source inversion

The source described in the original paper is a 1 kV spike with a 0.3 μs duration and as this signal propagates through the transducer it changes due to the transducer material and geometry. The receiver has a similar effect on the waveform. As a result, if a 0.3 μs spike is used as the source, the waveforms from the modelling will not match the experiment as it does not implement the effect of the transducers. The

model could be made to include the receiver-transducer material and geometry, but this adds unnecessary complexity. Instead, one way to overcome this problem is to add together the transfer function of the receiver, transducer and the source itself and use the solid sample system transfer function to invert the source, hence importing their effect into the source of the model (Hildyard (2007b), Parastatidis *et al.* (2017)). The solid sample is homogeneous, the material properties are presented in Table 3.1. The numerical model for the solid sample uses the same material properties, at this stage I assume that the system transfer function of the solid sample is equal for the model's transfer function ($h_m(t)$) and the laboratory experiment ($h_e(t)$). Using the definition of the convolution, in time domain, between source *s(t)* and system transfer function *h(t)* for the recorded wave *o(t)*:

$$o(t) = s(t) * h(t), \tag{3.1}$$

the effective source can be inverted.
Applying an arbitrary test source within the model and taking the Fourier transforms of equation 3.1

$$O(\omega) = S(\omega) \times H(\omega), \tag{3.2}$$

where ω is angular frequency. From equation 3.2 divide the experiment data $O_e(\omega)$ by the model $O_m(\omega)$:

$$\Rightarrow \frac{O_e(\omega)}{O_m(\omega)} = \frac{S_e(\omega)}{S_m(\omega)} \times \frac{H_e(\omega)}{H_m(\omega)}, \tag{3.3}$$

where $H_e(\omega)$ is the system transfer function for the experiment and $H_m(\omega)$ is the system transfer function for the model, assuming that $H_e(\omega)=H_m(\omega)$ from equation 3.3 find:

$$\Rightarrow S_e(\omega) = \frac{O_e(\omega)}{O_m(\omega) + e} \times S_m(\omega), \tag{3.4}$$

where e is added to $O_m(\omega)$ to make sure the denominator will always have a non zero value.
The required source can be derived from equation 3.4 after applying an inverse Fourier

transform. The inverted source can then be imported into the WAVE3D model as a table.

Figure 3.2a (top) presents the arbitrary test source $s(t)$ applied to the WAVE3D model and Figure 3.2b (top) the recorded system transfer function $s_m(t)$ along with the recorded waveform from the experiment $o_e(t)$ for P-wave propagation. Similarly, Figure 3.2a (bottom) shows the S-wave arbitrary test source, and Figure 3.2b (bottom) shows the recorded system transfer function $o_m(t)$ and the experiment data $o_e(t)$. The model source for P and S wave has been designed based on the predominant period of the experiment data in order to produce a wave close to the experiment. For that reason, the source consists of two pulses with opposite polarity and the time between the two pulses is again due to the time difference of the peaks of the wave.

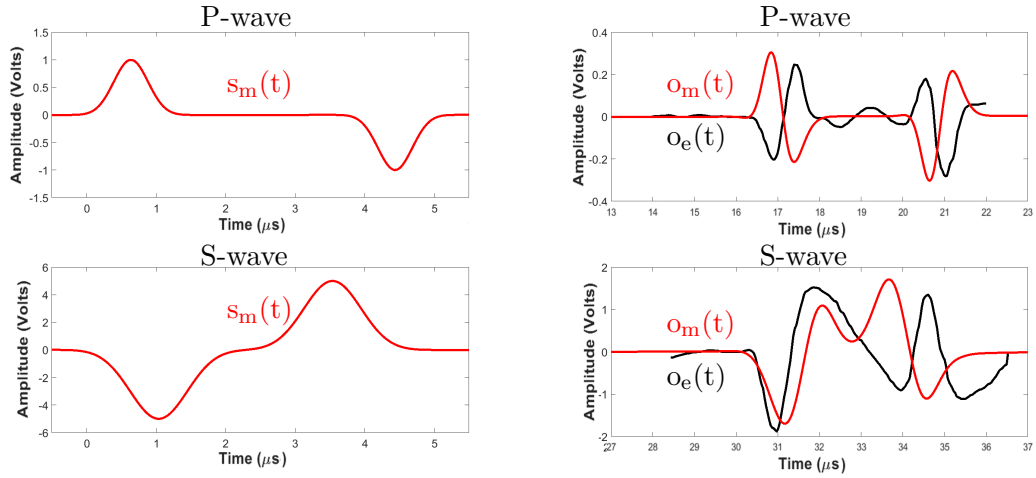

(a) (b)

Figure 3.2: Source inversion (a) arbitrary P and S wave sources applied from the transmitter (blue), (b) P and S wave for the experiment (black) and for the arbitrary model source (red)

Figure 3.3a and 3.3c show the source derived from the inversion process using equation 3.4 as described previously.

In the experiment the transducer and receiver surface is circular with a 22 mm diameter. Because WAVE3D is a rectilinear staggered grid, the source is represented as a square surface with the same area as the circle in the experiment and it has 40 elements on each side.

In the source inversion process I have used two different sources for P and S waves; the first is a stress source and the second a velocity source. Figure 3.3a and 3.3c depict the P and S wave source after the inversion process respectively. In the experiment the amplitude of the waveforms is in Volts. To avoid confusion and make comparison with the experiment easier, all the presented result will be in Volts. The conversion between voltage, stress and velocity is arbitrary, where 1 Volt = 1 MPa = 1 mm/s. The recorded waveforms from the solid steel models are shown in Figure 3.3b and 3.3d. As shown in the comparison with the data in Figure 3.3b and 3.3d the results of the inverted source match the experimental data very well, however the velocity source is closer to the experiment data, especially for the S-wave. This source function is then assumed to be the same for the fractured experiments.

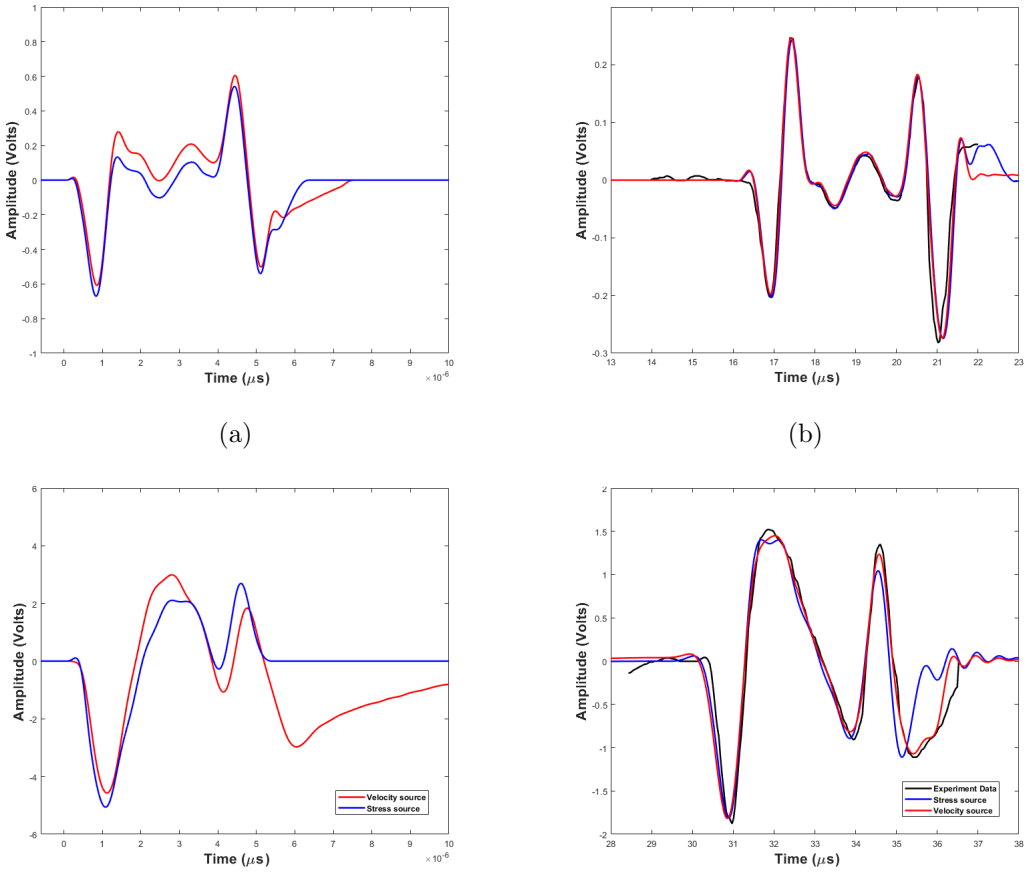

Figure 3.3: (a and c) P and S wave stress and velocity source after inversion. (The units on the experiment records are in Volts, for the models the equivalent units are 1 Volt to 1 MPa to 1 mm/s). (b and d) WAVE3D output for P and S wave stress and velocity in comparison with experiment data. (Units are 1Volt = 1 MPa = 1 mm/s)

3.3.2 Experiment Data and Thomsen parameters

The waveforms from the experiment are presented in Figure 3.4, as published in the original work (Pyrak-Nolte *et al.*, 1990). Figure 3.4a is for the P-wave in the solid steel sample (Figure 3.4a black), propagating parallel to the fractures (Figure 3.4a blue), and propagating perpendicular to the fractures (Figure 3.4a red). Figure 3.4b is for the S-wave with the solid steel sample (Figure 3.4b black), propagating parallel to the fractures and polarised horizontal to the fracture surface SH (Figure 3.4b blue),

propagating parallel to the fractures and polarised vertical to the fracture surface SV (Figure 3.4b green), and propagating perpendicular to the fractures (Figure 3.4b red). The solid steel block is 8.4 mm longer than the discontinuous block. Due to that fact, the waveform from the solid sample for P- and S- wave has a delayed arrival compared with when the wave propagates parallel to the fractures, as shown in Figure 3.4. Figure 3.5 presents the P- and S- waveforms from the solid block model using the inverted velocity source, as presented in Figure 3.3a and 3.3c. In order to avoid any confusion for wave velocities and arrival time between the waveform in the solid sample and the waveforms in the fractured case, I have created two recording positions in the model, one for the original length of the solid sample (0.990 mm) and one at the length of the fractured sample (0.906 mm). The waveforms in red are recorded in length the same as the original solid sample 0.990 mm, while the waveforms in blue are recorded in the same length as the fractured block 0.906 mm. This makes a clear point on the time delay and the attenuation of the waveforms for the solid block due to the extra length and gives an idea of how different the waveform would have been if the two blocks had the same length. In Figure 3.6 I present the frequencies of the P and S experiment waveforms for the solid sample to be used as a reference when comparing frequency changes in experimental and modelled data for wave propagation parallel and perpendicular to the fractures. The table 3.2 below summarises the arrival time and the calculated velocities for the P and S wave. The velocities for wave propagation perpendicular to the fractures are approximately 35% lower than the wave velocities for propagation parallel to the fractures, for both P and S wave. This difference in the wave velocities means the the anisotropy of the fractured sample is very high. Even though, the Thomsen anisotropy parameters (Thomsen, 1986) applies only to materials with weak elastic anisotropy I calculate the parameters in table 3.3 in order to mention the size of anisotropy of the sample used in the experiment.

Property	Arrival time (μs)	Velocity (m/s)
Sample length 99.0 mm		
P-wave Solid sample	16.44	6022
S-wave Solid sample	30.42	3254
Sample length 90.6 mm		
P-wave parallel to fractures	15.36	5898
P-wave perpendicular to fractures	23.54	3848
SH-wave parallel to fractures	27.67	3274
SV-wave parallel to fractures	27.58	3285
S-wave perpendicular to fractures	44.02	2058

Table 3.2: Measured velocities calculated based on the arrival time from the Pyrak-Nolte *et al.* (1990) experiment.

Property	Value
ϵ	0.674
γ	0.765
δ	-0.437
δ^*	0.037

Table 3.3: Thomsen parameters based on the calculated velocities.

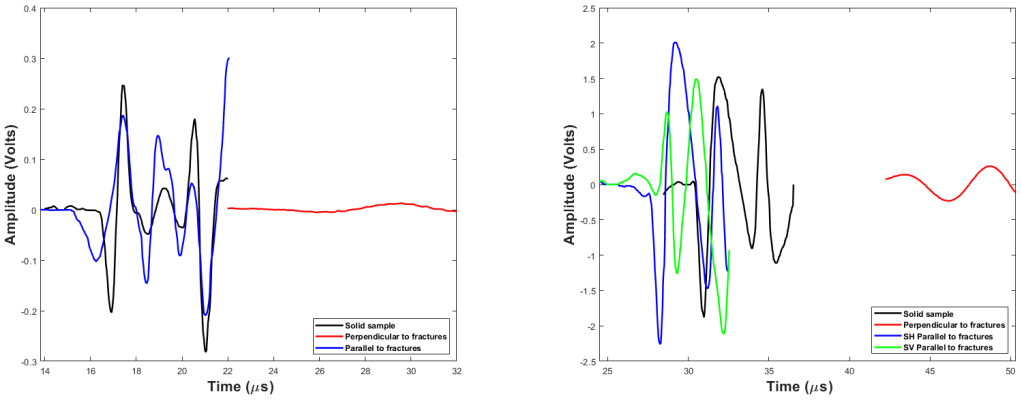

(a) (b)

Figure 3.4: a) P-wave experiment data for solid steel (black), propagation parallel to fractures (blue), propagation perpendicular to fractures (red). b) S-wave experiment data for solid steel (black), SH propagation parallel to fractures (blue), SV propagation parallel to fractures (green), propagation perpendicular to fractures (red). (Data from Pyrak-Nolte *et al.* 1990)

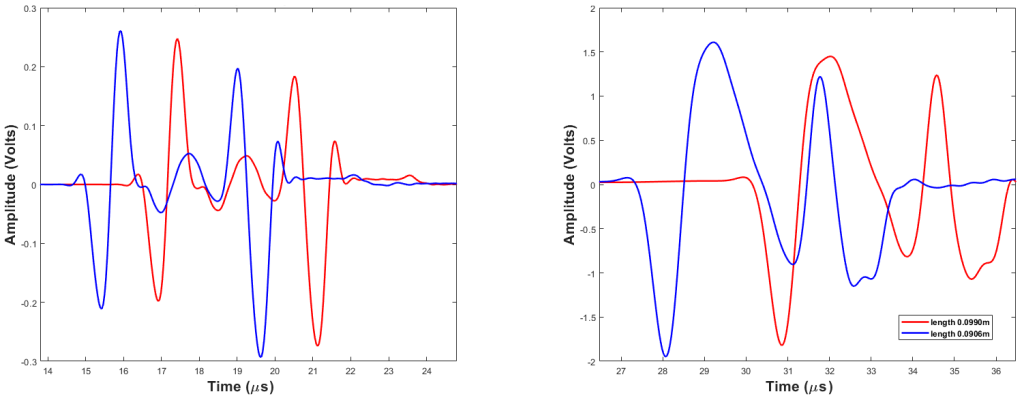

(a) (b)

Figure 3.5: P and S wave modeled data for solid steel for sample length equal to the original size 99.0 mm (red) and for length equal to the fractured sample 90.6 mm (blue).

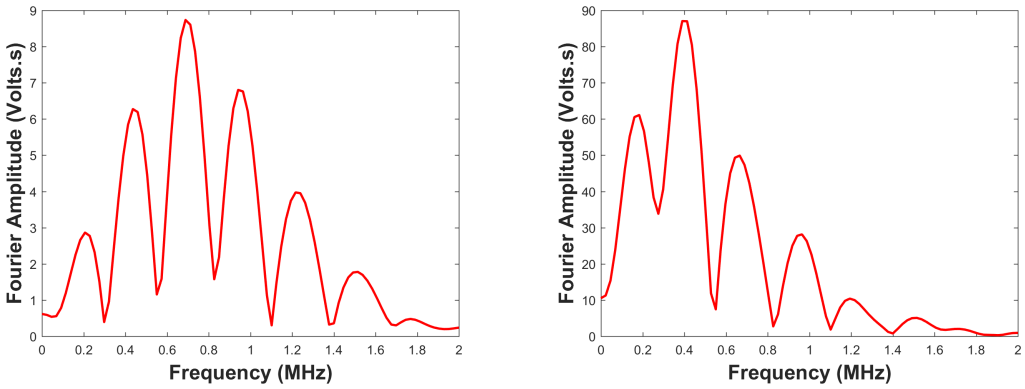

(a) (b)

Figure 3.6: Frequency of P 3.6a and S 3.6b wave experiment data for solid steel.

3.3.3 Fracture representation

There are two main methods for representing fractures in wave propagation models. The first is to use an effective medium which combines the effect of the fractures and the rock into a single medium. The second is to use displacement discontinuities to represent discrete fractures within a background medium. These lead to three models for representing fracturing, which are studied here. The first is an effective medium of a transversely isotropic material. The second is an explicit implementation of the displacement discontinuity with explicit fracture surfaces. The third is a hybrid of the two methods with a localised effective medium.

In modelling seismic waves, a common approach for fracture representation is an Effective Medium model (EM) (e.g., Crampin (1981), Hudson (1981), Majer *et al.* (1988), Rathore *et al.* (1995) Kawai *et al.* (2006), Tillotson *et al.* (2011), de Figueiredo *et al.* (2013), Ding *et al.* (2014), Tillotson *et al.* (2014)). In this case I consider the stiffness matrix from equation 2.2 and the effect of the fractures is calculated based on the equation 2.1 as described in section 2.2.2 cracks per unit length $\frac{1}{L}$ is calculated as $\frac{1}{L} = 331\ m^{-1}$.

A discrete representation of a fracture would typically use a displacement discontinuity (e.g., Pyrak-Nolte *et al.* (1990), Nakagawa *et al.* (2002), Hildyard (2007b), Chichinina *et al.* (2009a), Perino *et al.* (2010), Fan & Sun (2015), Shao *et al.* (2015)), which considers two surfaces in a non-fixed contact of zero thickness connected by a linear or

non-linear spring (Figure 2.2) which is expressed by normal and shear fracture stiffness, K_n and K_s respectively.

The definition of the displacement discontinuity is the difference in the displacement of the two opposite sides of the fracture for a continuous stress across it. This model gives us a discrete representation of a fracture where the surfaces of the fracture are represented explicitly.

The Localised EM model (LEM) uses the same equations as the EM, but is applied only locally around the predefined fractures providing a heterogenous anisotropic medium (Coates & Schoenberg (1995), Wu *et al.* (2005), Vlastos *et al.* (2003), Zhang & Gao (2009), Li *et al.* (2010)). This model implements a displacement discontinuity with a localised effective medium. The rest of the medium is treated as homogeneous isotropic. For further details concerning the implementation of the fracture models see section 2.4, cracks per unit length $\frac{1}{L}$ is now calculated as 2061 m^{-1} for a zone size in the model of 0.4871 mm thick for each of the fractures.

The crack density for the effective medium is ϵ=4.7 (using equation 2.8) while for LEM is ϵ=29.6 for each zone. The dominant frequency for the solid sample is 0.68 MHz for P and 0.40 MHz for S wave (Figure 3.6) with wavelength-to-fracture diameter ratio λ/d=0.1 for P and 0.09 for S waves. Based on previous studies (e.g., Schubnel & Gueguen, 2003; Schubnel *et al.*, 2003; Shuai *et al.*, 2018) the crack density is an order of magnitude higher and the λ/d is more than an order of magnitude lower in order to make the effective medium model to work and avoid dispersion in wave velocities. As a result I expect that the EM model will not agree with the experiment data when wave propagates perpendicular to the fractures. However, the reason for presenting the EM model for this experiment is to compare the result with the LEM models and highlight the different results these models can produce even though both of them based on the same background theory but different implementation.

3.4 Previous modelling

The modelling performed by Hildyard (2007b) in reproducing the experiment by Pyrak-Nolte *et al.* (1990) was limited by the computation power of that time. It was necessary to follow some assumptions about the size and number of the elements in the model. This led to some small differences in the geometry of the model. The element size for the P-wave was 1 mm and for the S-wave 0.5 mm. This leads to a smaller spacing between the fractures as it is rounding the fracture spacing from 2.92 mm by fitting three or six elements between fractures, for P and S waves respectively. The slightly smaller fracture spacing could end in small differences in the high frequency content. Some of the main conclusions are presented.

Firstly, a source inversion process has been developed while modelling the experiment, where the same technique is used for the current models. Since the element size and the geometry is slightly different, the previous inverted source could not be used and a new source inversion process is needed, resulting in a similar but different source.

Hildyard (2007b) highlighted the importance of the fracture stiffness in modelling waves through fractures. The fracture stiffness affects the wave propagation, causing delay, changes in amplitude and frequency which results in a completely different waveform when considering fractures as either open or closed.

Another output was that the non-uniform stress field is linked to non-uniform fracture stiffness, and this stiffness may vary along a single continuous fracture. Hence, the fracture stiffness is stress dependent, which has an important application in modelling fractures around fields with complex stress such as mining and tunnelling. As a result, the stress state can significantly affect wave propagation, and it is important to consider the coupled problem of the in-situ stress together with the seismic loading, when a non-uniform stress distribution is expected.

Changes in stiffness can result in the attenuation of high frequencies and amplification of lower frequencies. In addition, for P-waves the amplitudes of the first arrivals are dependent on both the normal fracture stiffness and the shear fracture stiffness.

Finally, large amplitude waves have a non-linear behaviour as a wave with a large amplitude changes locally the stress state while the wave propagates, and this results in fracture stiffness changes.

3.5 Uniform-stress and uniform fracture stiffness models

The experiment has been modelled for the P-wave source, using explicit fractures represented by displacement discontinuities; as an EM material; and as a third model using the approach of the LEM described previously. In this stage, the models are assumed to have a uniform stress and the effect of the biaxial load is not considered and hence all the fractures are identical. The normal fracture stiffness is $K_{\mathrm{n}} = 6 \times 10^{13}$ Pa/m and the shear fracture stiffness is $K_{\mathrm{s}} = 2 \times 10^{13}$ Pa/m, these stiffness values have been calculated by Pyrak-Nolte *et al.* (1990) using the wave velocities of the experiment. The material properties used for the models shown in Table 3.1.

The EM model (Figure 3.7b) was relatively simple to build as it does not contain individual fractures. In contrast, the LEM (Figure 3.7c) and explicit model (Figure 3.7a) have predefined positions for the heterogeneities and fractures respectively. One of the first conclusions from the snapshots of the wave propagation for the three models (Figure 3.7) is that wave propagation perpendicular to the fractures (Figure 3.7 left) is significantly slower than the one propagating parallel (Figure 3.7 right) as expected. The three models seem to synchronise very well on the travel time for both propagation parallel and perpendicular to the fractures. The attenuation of the amplitude is higher for all three approaches when wave propagates perpendicular to the fractures. The strong attenuation for the perpendicular case is due to the discontinuities which reflect back part of the waveform energy.

In this stage where the stiffness is uniform, I do not expect the models to match the experiment which had an non-uniform stress state and therefore non-uniform fracture stiffness. All three models in this stage assume the same uniform fracture stiffness across all fractures or stiffness matrix. I therefore compare the EM and LEM model against the explicit model rather than against experimental waveforms. The Fourier analysis presented in this section considers a wide time window of 20 μs with tapering and zero padding applied to all of the model waveforms. The Fourier analysis of the experiment data is not presented here because the time window of the experiment waveforms are limited to 8 μs, as a result the longer period part of the waveform is not included and could lead to inaccurate comparisons with the model waveforms.

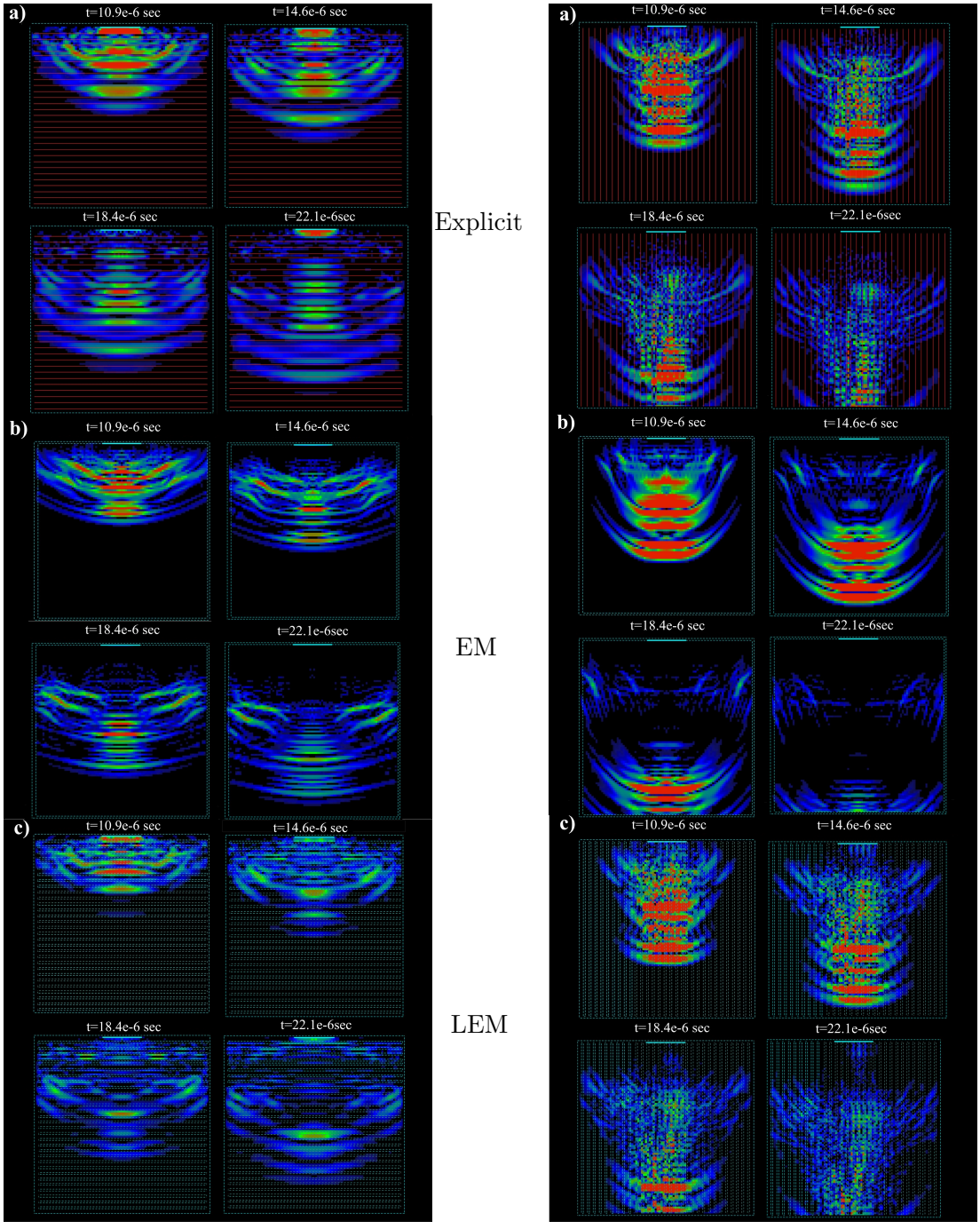

Figure 3.7: Snapshots from P-wave propagation perpendicular (left) and parallel (right) to fractures at t=10.9 μs, t=18.4 μs, t=25.8 μs and t=33.3 μs respectively, for the a) EM model b) explicit and c) LEM. (Red represents the peak amplitude, and all snapshots are on the same scale).

3.5.1 P-wave comparisons

For all three models, the waveforms are more delayed and attenuated when the wave propagates perpendicular to the fractures compared to propagation parallel to the fractures. The explicit model is almost identical to the experimental data for propagation parallel to the fractures (figures 3.8a and 3.9a) and matches the experimental waveforms in terms of wave shape, frequency and arrival time.

Performance of EM model

Waveforms for the EM model do not mimic waveforms from the explicit model or the experiment for propagation parallel to the fractures, but they match in terms of the first arrival. The amplitude of the EM model is two times higher than the explicit model for the P-wave parallel case; this is visible in the snapshots in Figure 3.7 in which the EM model has a large area marked in red representing the high amplitude. The shape of the EM waveform is very similar to the waveform from the solid block (Figure 3.8a). In terms of the frequency content of the waveform, there are three large notches at 0.3 MHz, 0.5 MHz and 0.8 MHz (Figure 3.8b). The two models perform the same for frequencies up to 0.6 MHz.

For propagation perpendicular to the fractures, the explicit model is very different from the experimental data (Figure 3.8c). The explicit model produces significant attenuation and slowing of the wave, but it does not produce the degree of attenuation and slowing observed in the experiment. However, the amplitude for the EM model is nine times higher than the explicit model for the P-wave. The predominant period of the explicit model is three times shorter than that for parallel propagation, while the predominant period for the EM model is similar to parallel propagation. The explicit model shows a major reduction in frequencies higher than 0.4 MHz for propagation perpendicular to fractures, whereas the EM model have a wider frequency content from that of the explicit model. The frequency content of the EM is similar for both directions of propagation (figure 3.8c 3.8d).

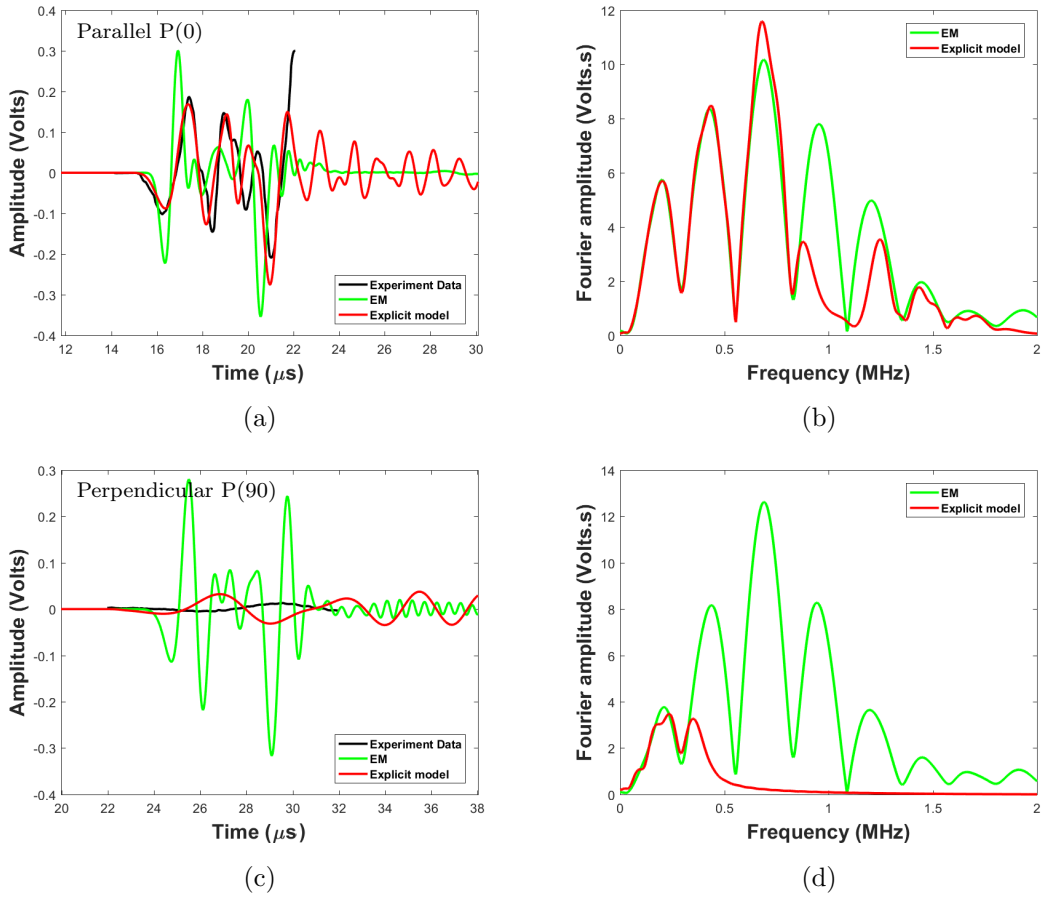

Figure 3.8: Comparison of the P-wave recording for the Explicit and EM uniform stress models and the experimental data in time (3.8a and 3.8c) and frequency (3.8b and 3.8d) for propagation parallel P(0°) (3.8a and 3.8b) and perpendicular P(90°) (3.8c and 3.8d) to the fractures.

Performance of LEM model

The LEM model is close to the explicit model results, for both cases of the P-wave propagation (Figures 3.9), with similar amplitudes and predominant periods. The first arrival for the parallel case is the same and the frequency content for both cases is almost identical for frequencies up to 0.8 MHz (Figure 3.9b). However, the amplitude in the propagation parallel (Figure 3.9a) to the fracture is about 5% higher for the LEM waveforms compared to the explicit model.

Similarly, to the previous analysis, waveforms for wave propagation perpendicular to

the fractures (Figure 3.9c) are very different from the experimental data. However, the two models, explicit and LEM, have a similar result with a reduction in amplitude of about an order of magnitude and a three times lower period, when compared to the waveforms propagating parallel to the fractures. The two models match in terms of frequency (Figure 3.9d), and amplitude (Figure 3.9c and 3.7). However, the LEM waveform is 0.5 μs delayed compared to the explicit model.

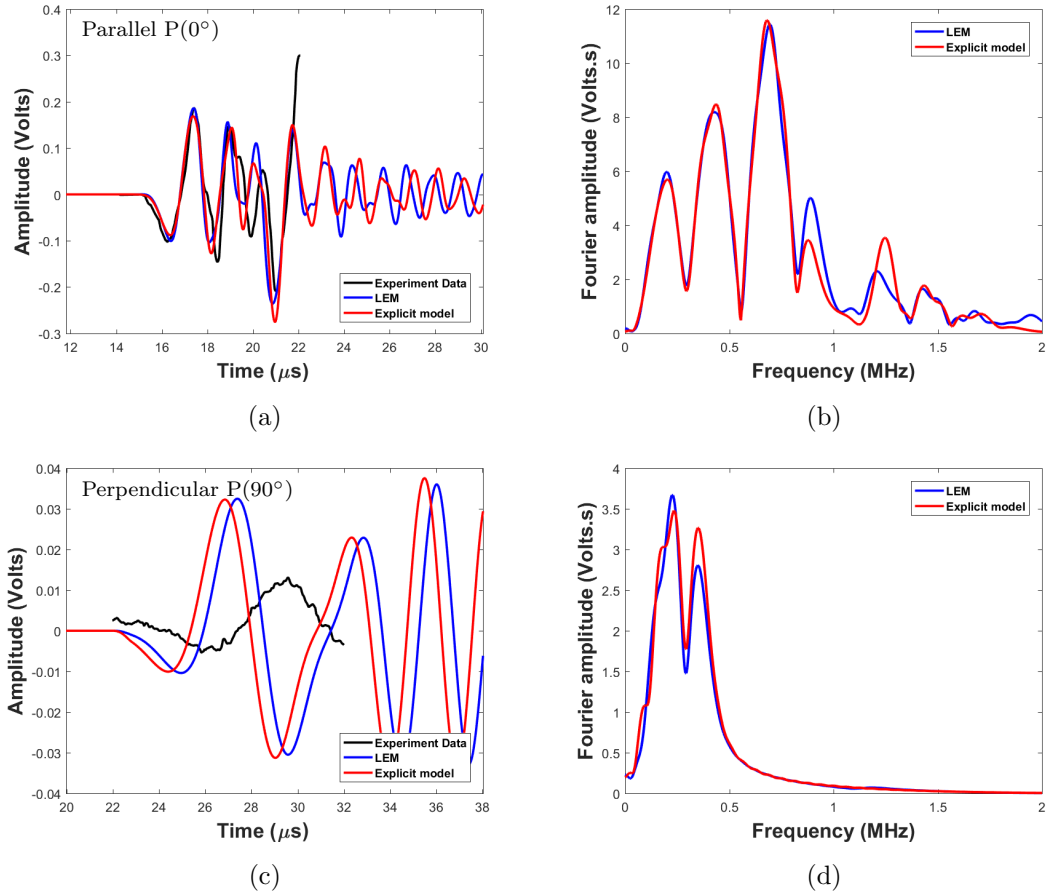

Figure 3.9: Comparison of the P-wave recording for the Explicit and LEM uniform stress models and the experimental data in time (3.9a and 3.9c) and frequency (3.9b and 3.9d) for propagation parallel P(0°) (3.9a and 3.9b) and perpendicular P(90°) (3.9c and 3.9d) to the fractures.

In order to quantify the performance of each model against the experimental data, I have calculated the cross-correlation maximum coefficient along with the lags for each

case. Table 3.4 summarises the values for maximum cross-correlation and the lag in μs. The maximum correlation appears on the solid model and wave propagation parallel (0°) to the fractures for the explicit and LEM model as expected.

	Max. coefficient	**Time μs**
Solid	0.9699	-0.0363
Explicit P(0°)	0.8953	0.109
EM P(0°)	0.7052	0.472
LEM P(0°)	0.8856	0.145
Explicit P(90°)	0.6583	2.69
EM P(90°)	0.1407	2.58
LEM P(90°)	0.6698	2.14

Table 3.4: Cross-correlation between experiment and models for P-wave propagation.

3.5.2 S-wave comparisons

Similar to the P-wave, more delayed and attenuated waveforms are expected when propagating perpendicular to the fractures, compared to propagation parallel to the fractures. Again, the explicit model is very close to the experimental data for propagation parallel to the fractures (Figure 3.10a, 3.10c, Figure 3.11a and 3.11c) for both SH and SV waves and matches the experimental waveforms in terms of wave shape, frequency (Figure 3.10b, 3.10d, Figure 3.11b and 3.11d) and arrival time.

Performance of EM model

The EM model correlates very well with the waveforms from the explicit model and the experiment for the SH-waves propagating parallel to the fracture (figure 3.10a). The maximum cross-correlation coefficient, between experiment and EM model data, is 0.95 while for explicit model is 0.94 (Table 3.5). This is to be expected since the fractures have little affect on this wave and the waveform is comparable to the waveforms in a solid sample. Both the explicit and the EM model match the experiment in first arrival, predominant period and shape, but peaks and troughs are different amplitudes and the maximum amplitude is 30% higher. The Fourier transform for both models is almost identical (Figure 3.10b). The SV-wave for the EM model is significantly slower (delay

of 14μs) compared to the explicit model and the experimental data (Figure 3.10c) very different. The explicit model performs very close to the experiment in arrival, amplitude and shape. For the EM model, the peak amplitudes in the frequency domain are 10% lower than the explicit model (Figure 3.10d). Even though the two models do not match each other in terms of arrival and wave shape, the dominant frequencies are the same. Continuing on to propagation perpendicular to the fractures results are similar to the P-wave and both the explicit and the EM model are very different from the experimental data. The waveforms for the explicit model are attenuated and have a delayed arrival, but not as much as in the experimental data (Figure 3.10e). As mentioned previously, this is likely due to the non-uniform stress field of the experiment. The maximum amplitude for the EM is 60% higher than the explicit model and in both models it is higher than the experimental data. The arrival time of the EM model matches the explicit, but they do not agree with the experiment where both models have an approximately 3 μs earlier arrival (Figure 3.10f). The EM model has a broad frequency range while the explicit model, shows significant attenuation of high frequencies (above 0.2 MHz) (Figure 3.10f).

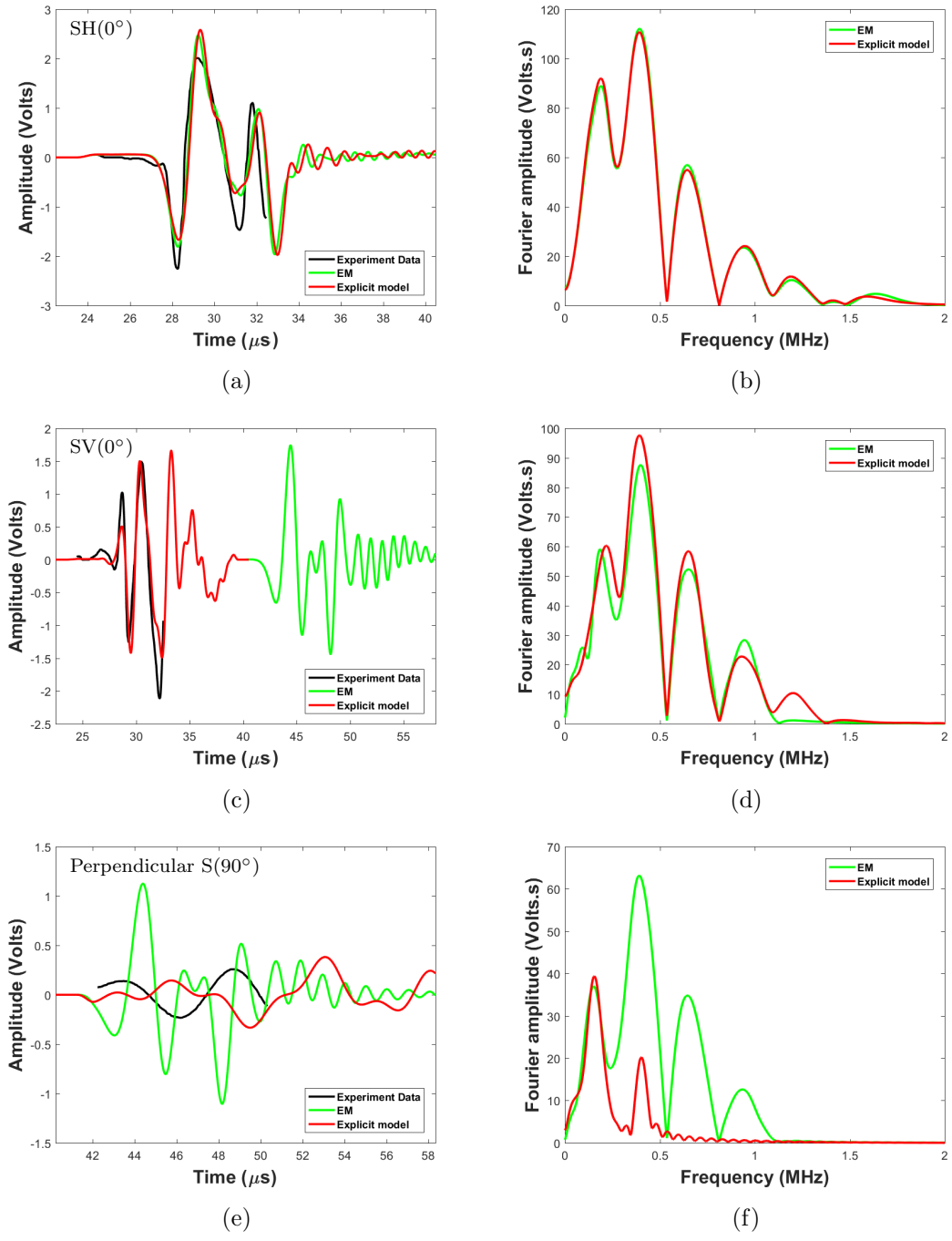

Figure 3.10: Comparison of the S-wave recording for the Explicit and EM uniform stress models and the experimental data in time (3.10a, 3.10c and 3.10e) and frequency (3.10b, 3.10d and 3.10f) for parallel SH(0°) (3.10a and 3.10b) and SV(0°) (3.10c and 3.10d), and perpendicular S(90°) (3.10e and 3.10f) to the fractures.

Performance of LEM model

For the S-wave, the LEM waveforms perform similarly to the explicit model as was the case for the P-wave. The SH-wave is similar compared to the explicit model (Figure 3.11a) and, as a result, to the EM model and experiment as described previously. The LEM model performs slightly better than the explicit, though in terms of amplitude it reaches the same maximum and minimum amplitudes as the experiment data but is 20% lower than the explicit model waveforms. The frequency content of the waveforms are almost identical between the explicit and the LEM (Figure 3.11b). For the SV-wave, the localised EM model has a 0.8 μs delayed arrival time compared to the explicit model and the experimental data (Figure 3.11c). Apart from the delay, the amplitude and the shape and the predominant period of the waveform is close to the explicit model. The frequency response is the same for both models for frequencies up to 1.1 MHz (Figure 3.11d). Finally, for S-wave propagation perpendicular to the fracture (Figure 3.11e), the LEM model has 0.5 μs earlier arrival times and predominant period as the explicit model, but slightly earlier compared to the experiment. Both models have higher amplitude compared to the experiment data with the explicit model having 20% higher amplitude compared to the LEM model and 35% higher against the experiment data. The frequency range as shown in the Fourier analysis (Figure 3.11f) is the same for both models for frequencies above 0.4 MHz.

Table 3.5 presents the values for maximum cross-correlation and the lag with maximum correlation on the solid model and the SH wave (0°) for all three models in contrast to the minimum value for the EM S-wave propagation perpendicular to the fractures (90^o).

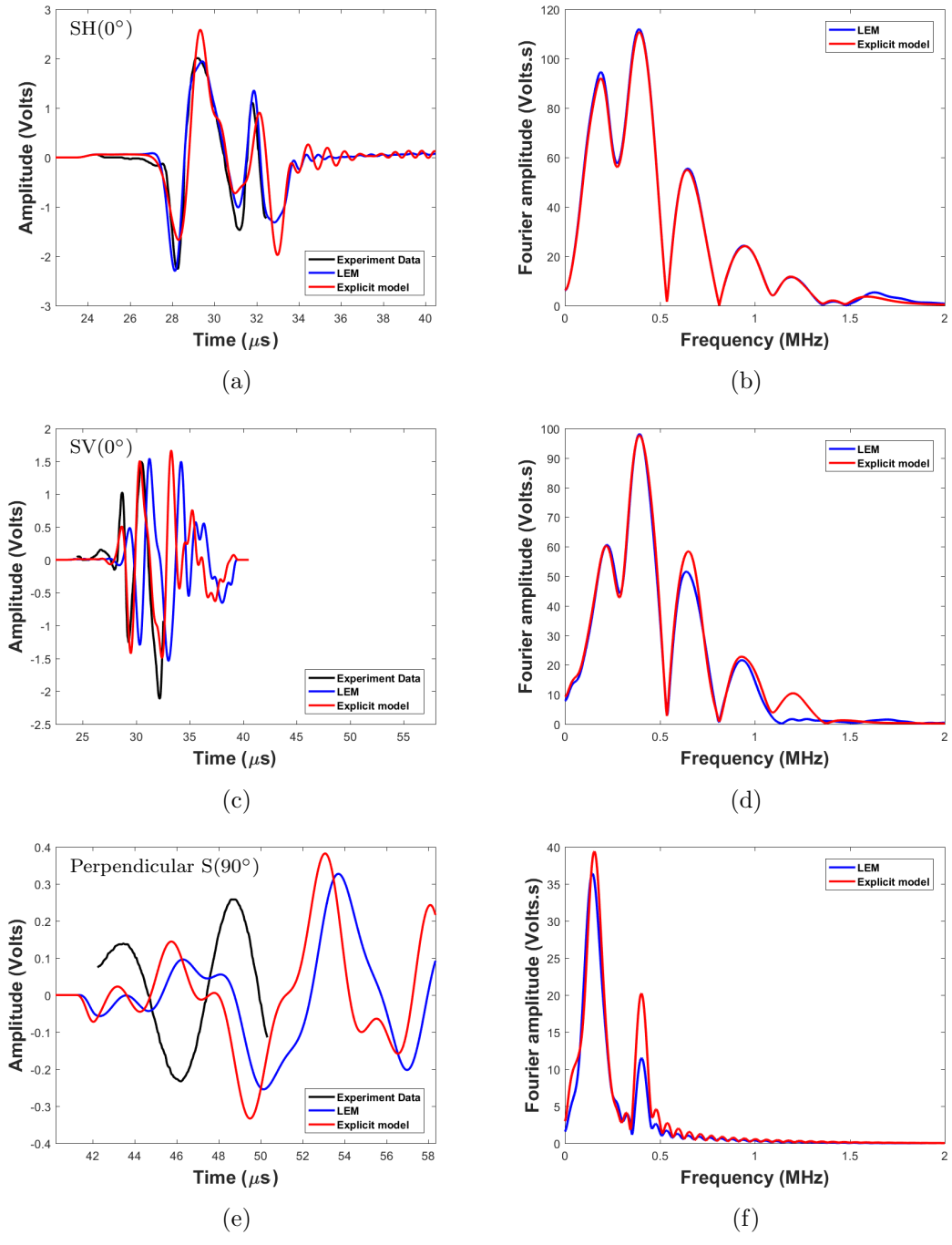

Figure 3.11: Comparison of the S-wave recording for the Explicit and LEM uniform stress models and the experimental data in time (3.11a, 3.11c and 3.11e) and frequency (3.11b, 3.11d and 3.11f) for propagation parallel SH(0°) (3.11a and 3.11b) and SV(0°) (3.11c and 3.11d), and perpendicular S(90°) (3.11e and 3.11f) to the fractures.

	Max. coefficient	**Time μs**
Solid S	0.9848	0.0363
Explicit SH(0°)	0.9368	-0.145
EM SH(0°)	0.9505	-0.072
LEM SH(0°)	0.9672	0.036
Explicit SV(0°)	0.7464	-0.109
EM SV(0°)	0.5627	-13.7
LEM SV(0°)	0.7613	-0.908
Explicit S(90°)	0.6378	-3.09
EM S(90°)	0.3544	4.39
LEM S(90°)	0.6025	-3.52

Table 3.5: Cross-correlation between experiment and models for S-wave propagation.

3.6 Models using stress dependence fracture stiffness

In the previous section, I examined the performance of the EM and LEM approaches against the explicit representation when I considered the stress to be uniform and hence the fracture stiffness to be uniform. When comparing the model results with the experimental waveforms, it becomes clear that wave propagation parallel to the fractures matches very well with the experiment for the explicit model and the LEM for both P and S waves. The EM does not perform as well as the other two models apart from in the case of SH-wave, where it matches. On the other hand, none of the models correlate well with the experiment when the wave propagates perpendicular to the fractures. The amplitude of the models are much higher than the experiment, and the arrival time and the predominant period are also different.

This big difference between parallel and perpendicular wave propagation is due to the fracture stiffness. When the wave propagates parallel to the fracture, the stiffness has low impact, because the wave travels through the intact part of the medium. However, when the wave propagates perpendicular to the fractures, the stiffness leads to changes in amplitude, frequency and arrival time. If the stiffness is low, then the attenuation is high, the waveform is delayed significantly and the high frequencies suppressed. If the stiffness approaches infinity, the attenuation due to the fractures is close to zero, and the arrival time and frequency contents approach the homogeneous case.

In a previous study (Hildyard, 2007b) different values for uniform fracture stiffness were used to trying match the model results with the experiment. No consistent match was found for uniform stiffness and this study concluded that since the steel block is stress loaded, the fracture stiffness cannot be uniform due to the non-uniform stress field. In this case, it is necessary to use a non-linear solution which links stiffness with stress. In this section, three models of fracture representation are compared against the experimental waveforms in a non-uniform stress field.

3.6.1 Laboratory experiment loading

Based on the description of the experiment, the sample with the steel plates is loaded biaxially with 30 kN. Force is applied in a circle-shape area of 50 mm diameter leading to a stress equal to 14.8 MPa. However, in WAVE3D it is simpler to apply the stress over a square area of similar size to the circular area. The sides of the square were

40 mm, thus the stress applied is 17.8 MPa. The figures below (Figure 3.12) show the stress state of the three models for the vertical stress (S22) and horizontal stress (S11) at the given loading with a scale from 15 MPa to 0 MPa. The fracture stiffness is related to the coupling between the two surfaces of the fracture. The better the contact between the surfaces, the higher the fracture stiffness and the lower the slowing and attenuation. As a result, compression increases the stiffness and different values of stress along a fracture lead to different values of stiffness along the same fracture. Due to the variation in stress, as shown below in Figure 3.12, we expect to have similar variations in stiffness.

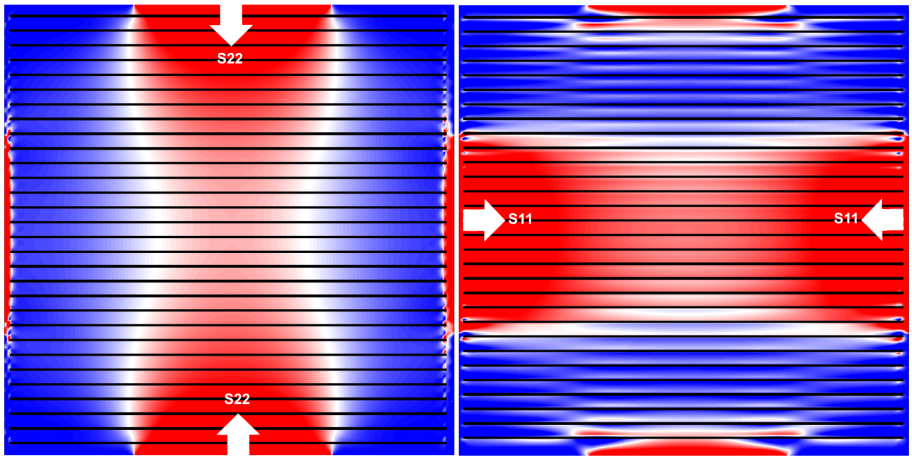

(a) Explicit fractures stress state

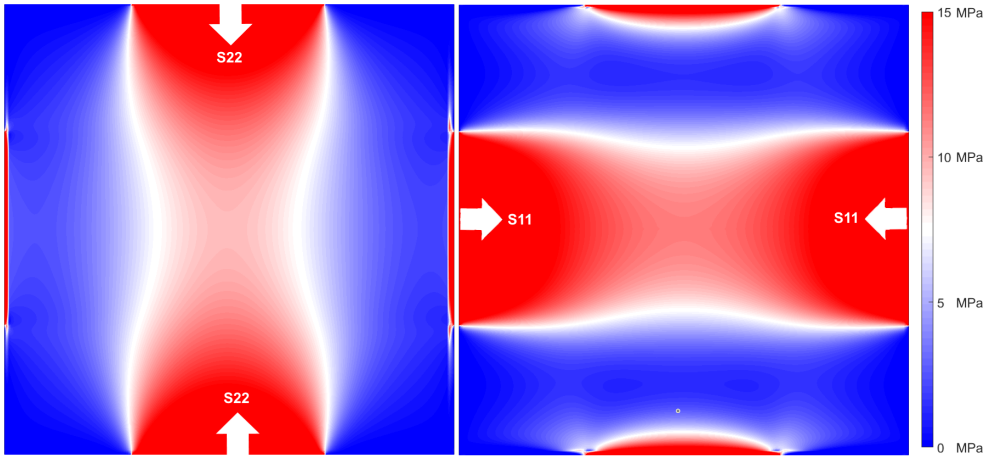

(b) Effective medium fractures stress state

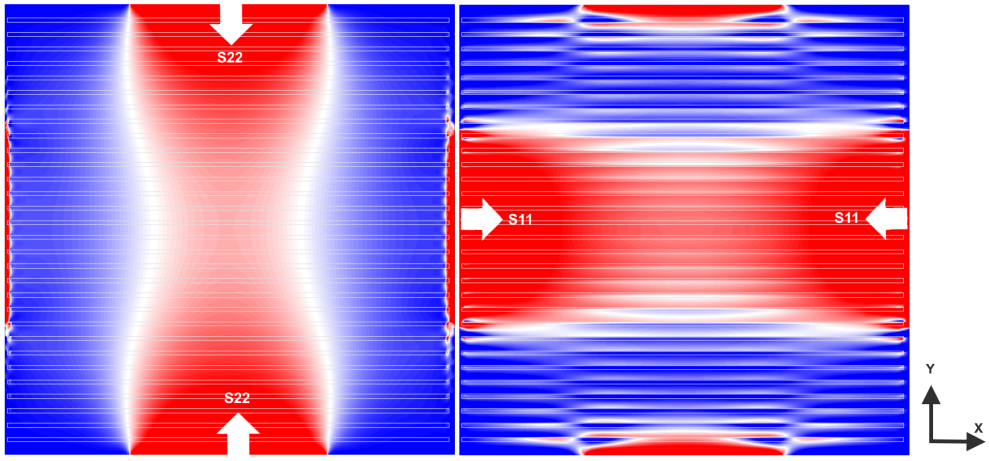

(c) Localised effective medium fractures stress state

Figure 3.12: 2D cross-section through the centre of the block showing the stress state for (a) explicit model (b) EM and (c) LEM for the S22 (vertical stress, left) and S11 (horizontal stress, right) due to the biaxial load (scale from 15 MPa red to 0 MPa blue).

3.6.2 Stress dependent fracture stiffness theory

The stress field for this experiment as described is not uniform (Figure 3.12). Stress is linked with fracture stiffness (Bandis *et al.*, 1983) and the non-uniform stress causes non-uniform fracture stiffness. Using Bandis *et al.* (1983) equations (equation 3.5 and 3.8) for the given stresses from the stress model (Figure 3.12), the K_{n} and K_{s} is defined for each different value of stress as:

$$K_n = \frac{(1 + b\sigma_n)}{\alpha}, \tag{3.5}$$

where

$$\alpha = \frac{1}{K_{ni}}, \tag{3.6}$$

$$b = \frac{\alpha}{u_{n(max)}}, \tag{3.7}$$

and

$$K_s = c \times K_n, \tag{3.8}$$

$u_{n(max)}$ is the maximum possible closure of a fracture, K_{ni} is the initial fracture stiffness at zero normal stress, σ_n is the normal stress, c is a fixed parameter linking the ratio of shear to normal fracture stiffness.

The normal stress is linked to fracture stiffness in both directions, creating a coupled case. This means that once the initial stiffness has been recalculated using the above equations, the stress state changes slightly. As a result, the calculation of fracture stiffness at a given stress is not a single-pass process. The first stage of applying the stress dependent stiffness involves the use of a static model, that will go back and forth several times, in an iterative calculation for the coupled stress and stiffness. This process continues until the static model reaches equilibrium with the maximum velocity from the noise caused due to changes in stress and stiffness, becoming lower than 10^{-7} m/s. All the three models run for 40,000 cycles to reach that equilibrium point. Finally, the static model is switched to dynamic and the source wavelet is applied and propagated as previously.

In the case of the explicit fracture model, the application of the above equations is simple. Since the fractures are expressed explicitly in the model, each contact between

the two elements of the fracture plane has a stiffness parameter. The value of the stress between these two contacts is used to calculate the stiffness with the process described above.

In the effective medium there are no defined fractures and no surface contacts as in the explicit model. The properties of the fractures are mapped to the properties of the material, as shown previously (Section 2.2.2 and 2.4). In equivalent medium stiffness matrix (equation 2.2) the values of K_n and K_s are constant. The stress dependent application of the EM and LEM needs to calculate the stiffness matrix for each element for every cycle. To apply the stress dependent stiffness for the EM and LEM models, a new function has been developed. The function calculates K_n and K_s for every single element equations 3.5 to 3.8 at the given stress. The code for EM and LEM stress dependent stiffness was implemented in WAVE3D and is listed in Appendix A.1 A similar process to that of the explicit case is followed for the EM and LEM models. First of all, I run a static model to reach equilibrium and then apply the source in a dynamic mode. In the effective medium however, there is no fracture closure to calculate the b value. In this case, the same theoretical values of α, b and c used for the explicit fractures models will be considered for the EM and the LEM.

For the stress dependent static models, three cases for the values of a, b and c are used (Table 3.6). All three cases consider the initial stiffness as: $K_{ni} = 1 \times 10^{13}$ Pa/m such that $\alpha = 1 \times 10^{-13}$ m/Pa. In the first case b=1.5 $\times$ 10^{-7} Pa^{-1}, c=0.5. The second case has a lower b=1.0 $\times$ 10^{-7} Pa^{-1} and c=0.5. Finally, the third case uses b=1.0 $\times$ 10^{-7} Pa^{-1} and c=0.33. The values for a, b and c were based on previous work (Hildyard, 2001) in which these values show better correlation with the experiment result. I adjusted these values to the new models, including the LEM and EM stress dependent models. The graph below presents the K_n and K_s variations due to normal stress, creating a hyperbolic relationship (Figure 3.13 and table 3.6) as described in equations 3.5 and 3.8.

The stiffness variations as a result of the applied stress which are linked with the equation 3.5 and 3.8 are presented in Figures 3.14, 3.15 and 3.16 below. As expected, the higher values of stiffness are close to the areas of high stress and lower values are in the centre and on the edges of the block where the stress is lower. From Figure 3.13, it is clear that the higher the b parameter, the higher the normal stiffness and, as a consequence, the higher the shear stiffness as well. This assumption is confirmed when

comparing the normal and shear stiffness cross-section for case 1 (Figure 3.14a, 3.15a and 3.16a) and case 2 (Figure 3.14b, 3.15b and 3.16b). The variations in normal and shear stiffness are similar for the explicit, EM and LEM models when using the same three cases (Figures 3.14, 3.15 and 3.16).

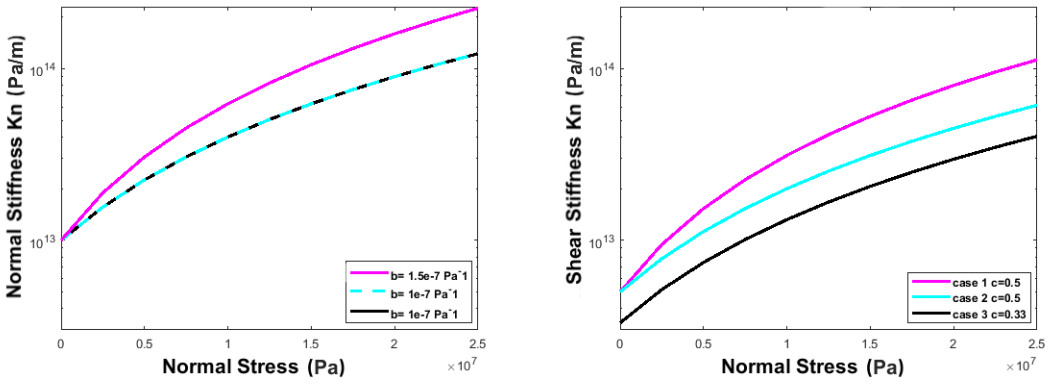

(a) (b)

Figure 3.13: Relationship of fracture normal stiffness 3.13a and shear fracture stiffness 3.13b to normal stress given by equation 3.5 and 3.8 for the three cases of b and c parameters. Case 1, b=1.5 $\times$ 10^{-7} Pa^{-1} c=0.5, case 2, b=1.0 $\times$ 10^{-7} Pa^{-1} c=0.5, case 3, b=1.0 $\times$ 10^{-7} Pa^{-1} c=0.33 (parameter $a = 1 \times 10^{-13}$ m/Pa is kept constant).

	α (Pa/m)	b (Pa^{-1})	c
Case 1	1×10^{-13}	1.5×10^{-7}	0.5
Case 2	1×10^{-13}	1.0×10^{-7}	0.5
Case 3	1×10^{-13}	1.0×10^{-7}	0.33

Table 3.6: Stress dependent parameters for the relationship of fracture normal and shear fracture stiffness to normal stress given by equation 3.5 and 3.8 for the three cases.

Using the output of the static models as described previously, we end up with nine stiffness models; three for each fracture representation model (Figures 3.14, 3.15 and 3.16). The next step is to use the stiffness models in a dynamic mode as previously done with the uniform stiffness. Some of the results of the dynamic models are presented below (Figure 3.17). The selection of the two cases, for propagation perpendicular to the fracture for P- and S-waves, is because in the previous section for uniform stress,

these were the two cases with a higher mismatch between the experiment and the models.

As expected, the higher b values (case 1) cause higher stiffness and as a result earlier arrivals compared to the other two cases (Figure 3.17). The lower values for shear stiffness K_s due to lower c value in case 3, result in higher amplitudes for the P-wave and an earlier arrival compared to the case 2 (Figure 3.17a, 3.17c and 3.17e). On the other hand, the lower K_s works the opposite way for the S-wave causing higher attenuation and delayed arrival (Fig. 3.17b, 3.17d and 3.17f). In the next part, the experiment is compared with the models, using the case 3 stiffness model.

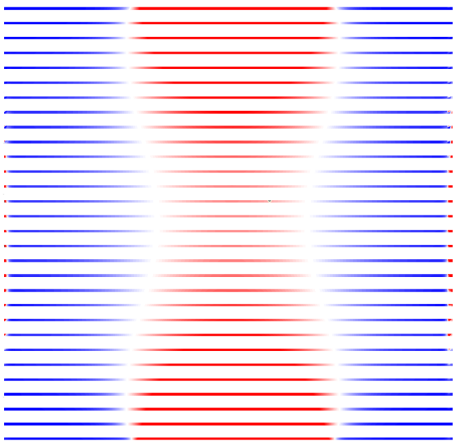

(a) K_n cross-section case 1

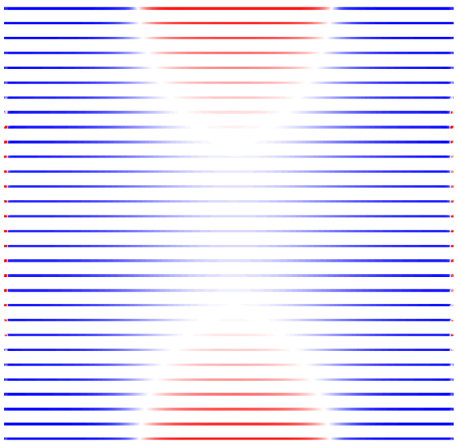

(b) K_n cross-section case 2

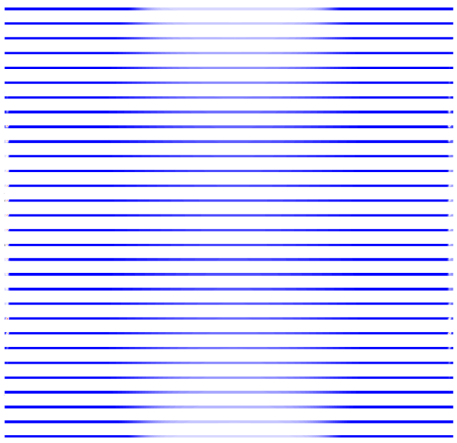

(c) K_s cross-section case 2

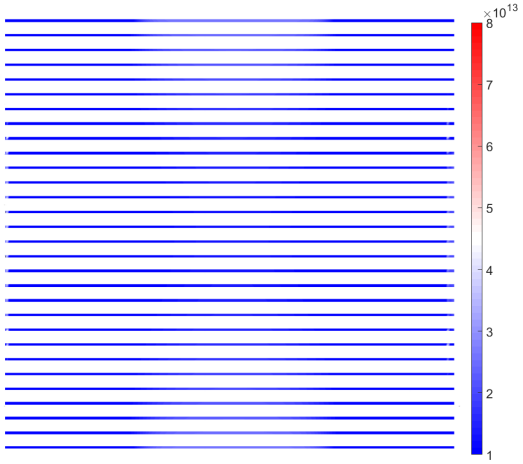

(d) K_s cross-section case 3

Figure 3.14: Cross-section for Stress dependent fracture stiffness on EM, for the three cases of b and c parameters, A) K_n cross-section case 1, b=1.5 $\times$ 10^{-7} Pa^{-1} c=0.5, B) K_n cross-section case 2, b=1.0 $\times$ 10^{-7} Pa^{-1} c=0.5, C) K_s cross-section case 2, b=1.0 $\times$ 10^{-7} Pa^{-1} textitc=0.5 D) K_n cross-section case 3, b=1.0 $\times$ 10^{-7} Pa^{-1} c=0.33.

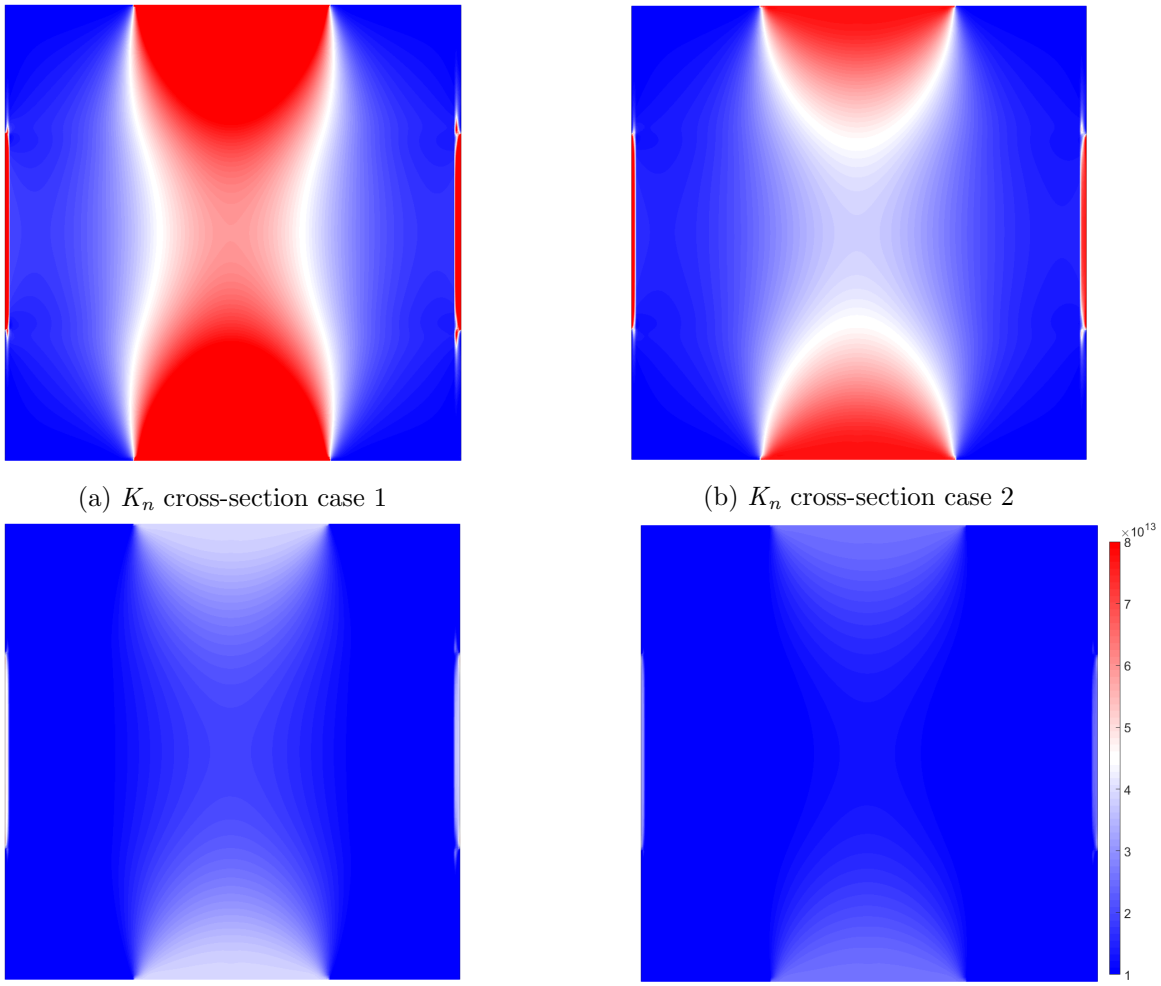

(a) K_n cross-section case 1

(b) K_n cross-section case 2

(c) K_s cross-section case 2

(d) K_s cross-section case 3

Figure 3.15: Cross-section for Stress dependent stiffness distribution on EM, for the three cases of b and c parameters, A) K_n cross-section case 1, b=1.5×10^{-7} Pa^{-1} c=0.5, B) K_n cross-section case 2, b=1.0×10^{-7} Pa^{-1} c=0.5, C) K_s cross-section case 2, b=1.0×10^{-7} Pa^{-1} textitc=0.5 D) K_n cross-section case 3, b=1.0 × 10^{-7} Pa^{-1} c=0.33.

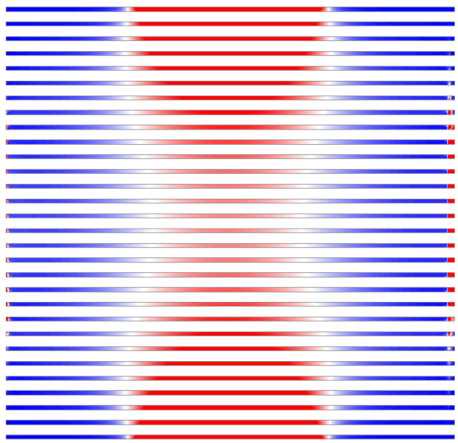

(a) K_n cross-section case 1

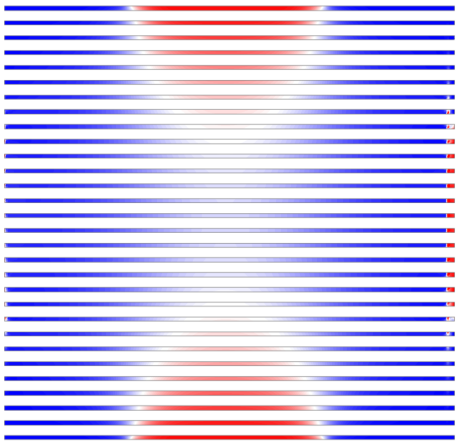

(b) K_n cross-section case 2

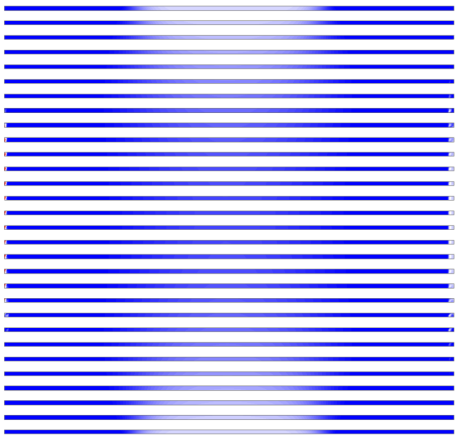

(c) K_s cross-section case 2

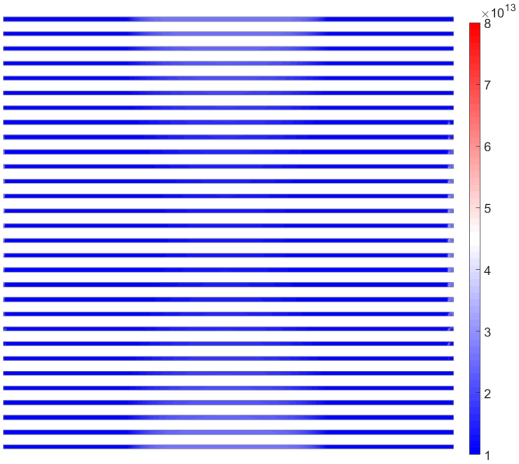

(d) K_s cross-section case 3

Figure 3.16: Cross-section for Stress dependent stiffness distribution on LEM, for the three cases of b and c parameters, A) K_n cross-section case 1, b=1.5×10^{-7} Pa^{-1} c=0.5, B) K_n cross-section case 2, b=1.0×10^{-7} Pa^{-1} c=0.5, C) K_s cross-section case 2, b=1.0×10^{-7} Pa^{-1} textitc=0.5 D)) K_n cross-section case 3, b=1.0 × 10^{-7} Pa^{-1} c=0.33.

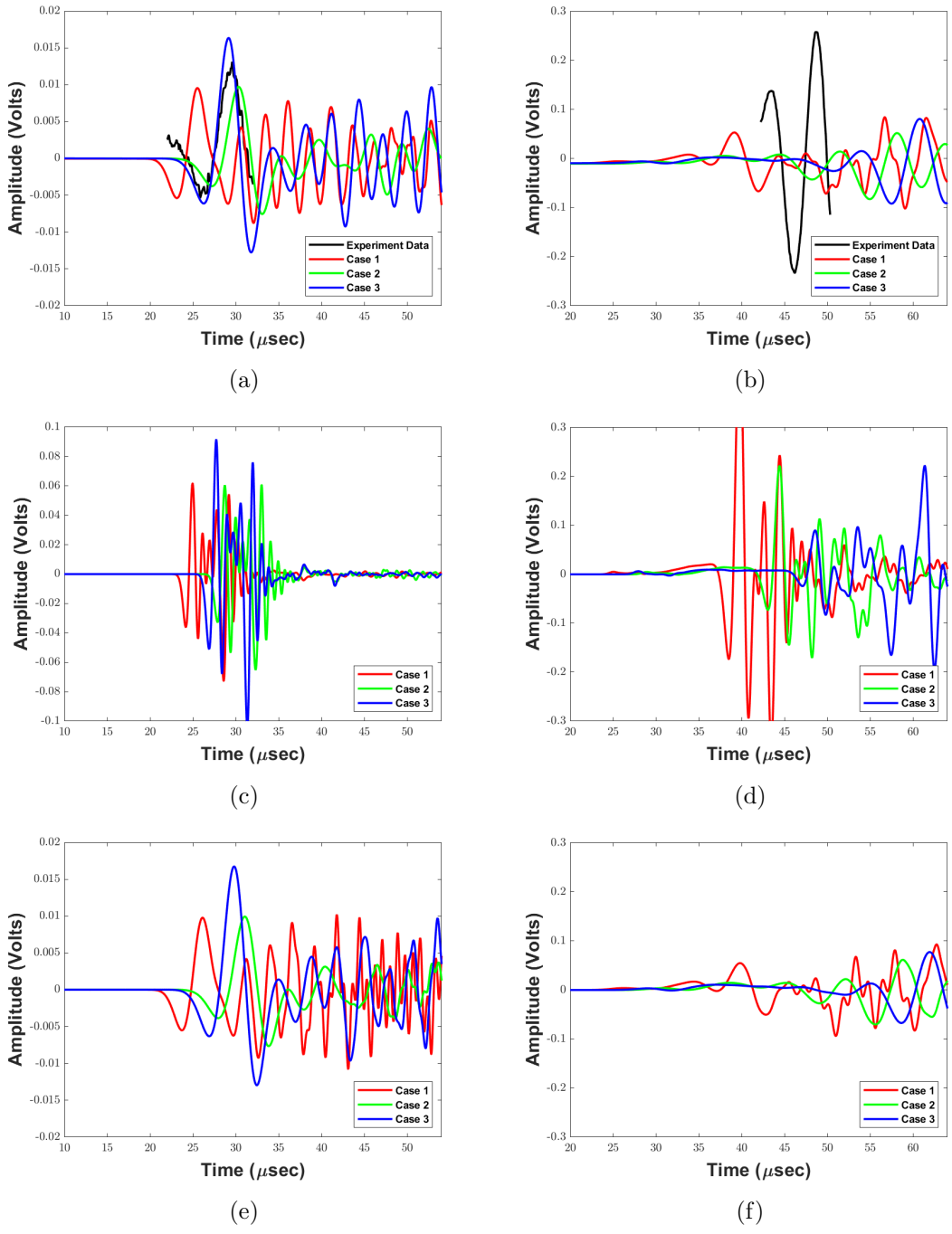

Figure 3.17: The waveforms from the three stiffness models (case 1,b=1.5 $\times$ 10^{-7} Pa^{-1} c=0.5, case 2 b=1.0$\times$10^{-7} Pa^{-1} c=0.5, case 3, b=1.0$\times$10^{-7} Pa^{-1} c=0.33) for propagation perpendicular to the fractures for P- and S- waves a) explicit model P-wave and b) S-wave propagation perpendicular to the fractures, c) EM model P-wave and d) S-wave propagation perpendicular to the fractures, e) LEM model P-wave and f) S-wave propagation perpendicular to the fractures.

3.6.3 P-wave comparisons

The results of the stress dependent explicit model for P-wave propagation are shown in Figure 3.18 and 3.21 (red), where for propagation parallel to the fracture (Figure 3.18a and 3.21a (red)) the stress dependent case has a small delay of 0.47 μs, the amplitude is 10% lower than the uniform stress model, the shape and the predominant period agree with the experiment. In addition, in comparison with the uniform stress model, the last one matches better with the experimental data with cross-correlation coefficient equal to 0.89 against 0.73 for stress-dependent case (Tables 3.4 and 3.7). More specifically, the amplitude and the frequency range for the stress dependent model and the experiment is almost 20% higher amplitude than the experimental data for frequencies up to 0.22 MHz and 40% lower for frequencies higher 0.57 MHz.
In this stage, where the models are compared against the experiment, the Fourier analysis for the modelled data uses the same time window as the experiment of 8-10 μs, both the experiment and the modelled data are tapered, and zero padding is added. As a result, the differences in the Fourier analysis between the uniform stress models and the current stress dependent will not only be due to the changes in the waveforms, but also due to the different time window used in the two cases.
The stress dependent explicit model waveform for perpendicular propagation agrees very well with the experiment, as shown in Figure 3.18b and 3.21c with 7% higher cross-correlation coefficient (Tables 3.4 and 3.7). The amplitude is 50% lower than the uniform stress case due to the variable fracture stiffness. The explicit model has similar frequency contents to the experiment with 20% higher amplitude (Figure 3.21d (red)). The stress affects the wave propagation in a way that higher K_n causes less attenuation to the waveform. Since the biaxial stress is applied to a limited surface, the values of K_n at the edges are lower than the value used in the uniform case, leading to increased scattering. The results of the stress dependent EM model for P-wave propagation are shown in Figure 3.19 and 3.21 (green). For propagation parallel to the fracture (Figure 3.19a and 3.21a (green)) the stress dependent case has a small delay of 0.3 μs and the amplitude is about 2% higher compared to the uniform case, and the shape and the predominant period agree with the uniform stress case. In comparison with the experiment, none of the EM models, uniform stress or stress dependent match the experimental data. The EM model for propagation parallel to the fractures performs

similarly to the experiment and the other two models for frequencies up to 0.5 MHz and has a wider range of frequencies, reaching up to 1.5 MHz (Figure 3.21b (green)).

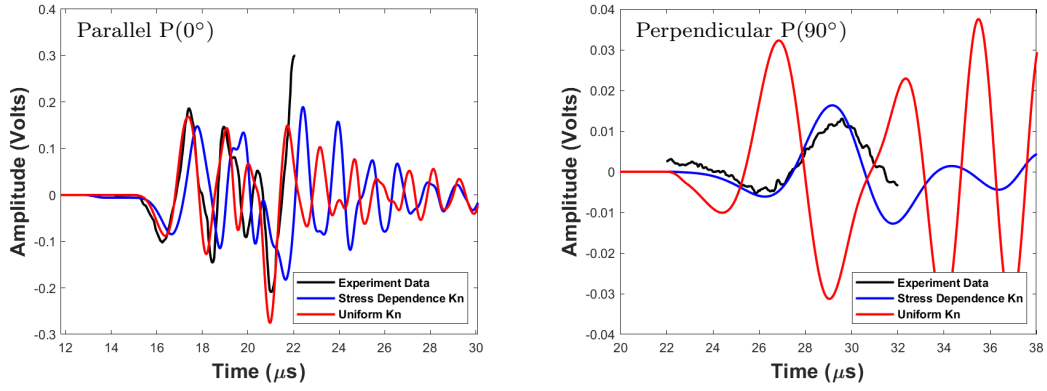

(a) (b)

Figure 3.18: Comparing the recording of the P-wave from the experiment and the explicit model using uniform and stress-dependent fracture stiffness for propagation a) parallel P(0°) and b) perpendicular P(90°) to the fractures.

The stress dependent EM model waveform for P-wave perpendicular propagation (Figure 3.19b and 3.21c (green)) has three times smaller amplitude and approximately a 3 μs delay compared to the uniform stress EM model. The predominant period though is the same for both cases. Even though the amplitude has been reduced significantly, it still does not match the amplitude of the experiment data neither in time domain (Figure 3.19b and 3.21d (green)) nor in frequency domain (Figure 3.21d (green)). The EM model for perpendicular propagation has a four times wider frequency range compared to the experiment and the other two models (Figure 3.21d (green)).
The stress dependent LEM P-wave shown in Figure 3.20 and 3.21 performs similar to the explicit model. The P-wave propagation parallel to the fracture (Figure 3.20a and 3.21a (blue)) for the stress dependent case has a small delay of 0.22 μs and the amplitude is about 20% lower compared to the uniform case and the experiment, the shape and the predominant period agree with the uniform stress case. When comparing with the experiment, both match the experimental data with the uniform stiffness model to perform 7% closer (Tables 3.4 and 3.7). The amplitude and the frequency range for the stress dependent model and experiment is almost identical (Figure 3.21d (blue)) but

about 20% higher amplitude than the experimental data for frequencies up to 0.22 MHz and 20% lower for frequencies higher 0.57 MHz (Figure 3.21d (blue)).

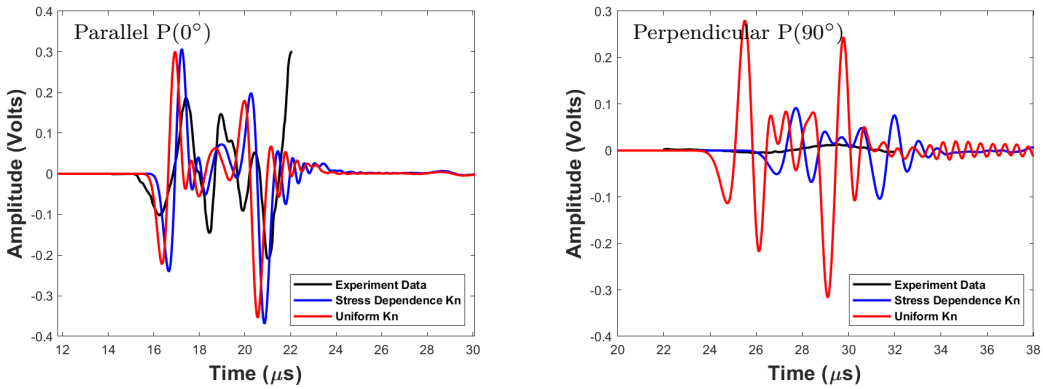

(a) (b)

Figure 3.19: Comparing the recording of the P-wave from the experiment and the EM model using uniform and stress-dependent fracture stiffness for propagation a) parallel P(0°) and b) perpendicular P(90°) to the fractures.

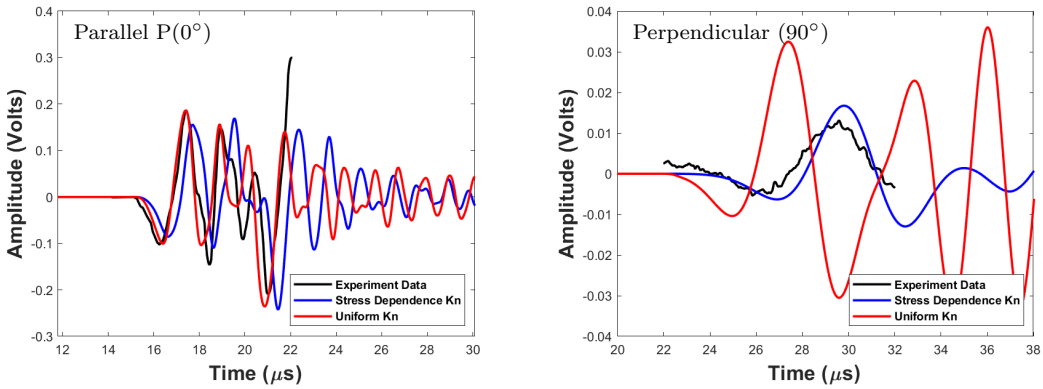

(a) (b)

Figure 3.20: Comparing the recording of the P-wave from the experiment and the LEM model using uniform and stress-dependent fracture stiffness for propagation a) parallel P(0°) and b) perpendicular P(90°) to the fractures.

The stress dependent LEM model waveform for perpendicular propagation has a higher cross correlation coefficient of 0.78 with the experiment as shown in Figure 3.20b and 3.21c (blue) and Table 3.7. The amplitude is 50% lower than the uniform stress case

due to the variable fracture stiffness. The arrival time though is 0.4 μs later than both the explicit and the experiment data and a similar delay was observed in the uniform stress waveform for the same acquisition (Figure 3.9c). The frequency range is the same as the experiment and the explicit model, with 15% higher amplitude compared to the experiment (Figure 3.21d (blue)).

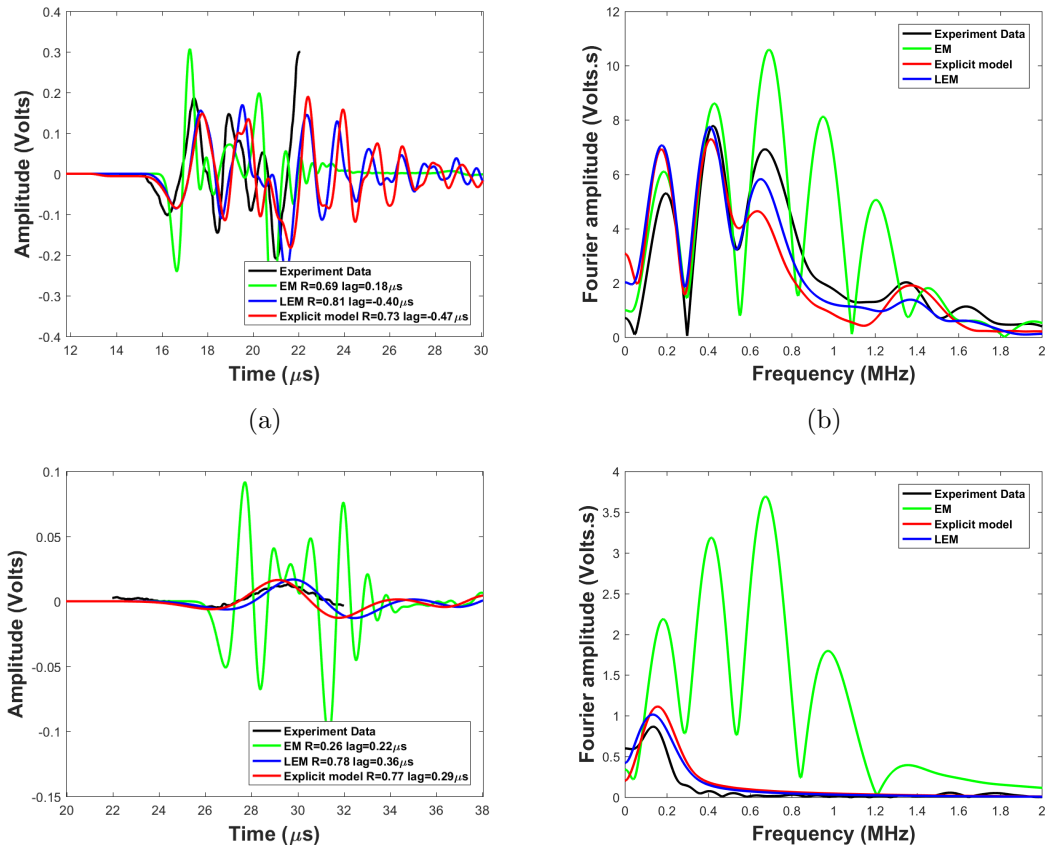

Figure 3.21: Comparing the P-wave recordings of the three models a) and c) and the Fourier analysis b) and d) for Explicit, EM and LEM models against the experiment for the stress dependent fracture stiffness case for propagation a) and b) parallel P(0°) and c) and d) perpendicular P(90°) to the fractures along with the cross-correlation coefficient R and the lags between the experiment and modelled data.

To sum up for the P-wave stress dependent models, the explicit and the LEM approaches perform similar to the experiment with an average cross correlation coefficient

above 0.75 for all cases (Figure 3.20, 3.21 and Table 3.7) and time lag variations lower than 0.5 μs. The EM model is very different from the experiment for propagation perpendicular to the fractures, but it has similar frequency content for parallel to the fractures propagation (Figure 3.20 and 3.21).
Table 3.7 presents the values for maximum cross-correlation, where the values for wave propagation perpendicular to the fractures (90^o) have increased for Explicit and LEM model but decreased further for the EM.

	Max. coefficient	**Time μs**
Solid	0.9699	-0.0363
Explicit P(0°)	0.7321	-0.472
EM P(0°)	0.6858	0.182
LEM P(0°)	0.8099	-0.399
Explicit P(90°)	0.774	0.290
EM P(90°)	0.2574	0.218
LEM P(90°)	0.7826	0.363

Table 3.7: Maximum cross-correlation coefficient between experiment and models for P-wave stress dependent stiffness

3.6.4 S-wave comparisons

The stress dependent explicit model for S-wave propagation is presented in Figure 3.22. The SH-wave propagation parallel and polarised parallel to the fracture surface (Figure 3.22a) for the stress dependent case performs almost identically to the uniform stress model and both match well with the experimental data in time (Figure 3.22a) and frequency domain (Figure 3.25b). The SV-wave (Figure 3.22b) has a 1 μs earlier arrival compared to both the experiment and the uniform stress model (Figure 3.22b). From the Fourier analysis, the experiment and the model share a similar frequency range for frequencies up to 0.85 MHz, but the stress dependent model has 20% higher amplitude and 12% lower dominant frequency (Figure 3.25d).
The stress dependent explicit model waveform for S-wave perpendicular propagation (Figure 3.22c) is attenuated and delayed significantly compared to the uniform stress model. The amplitude is four time smaller than the previous model. The frequency range from the Fourier analysis is incomparably small against the experiment (Figure

3.25f).

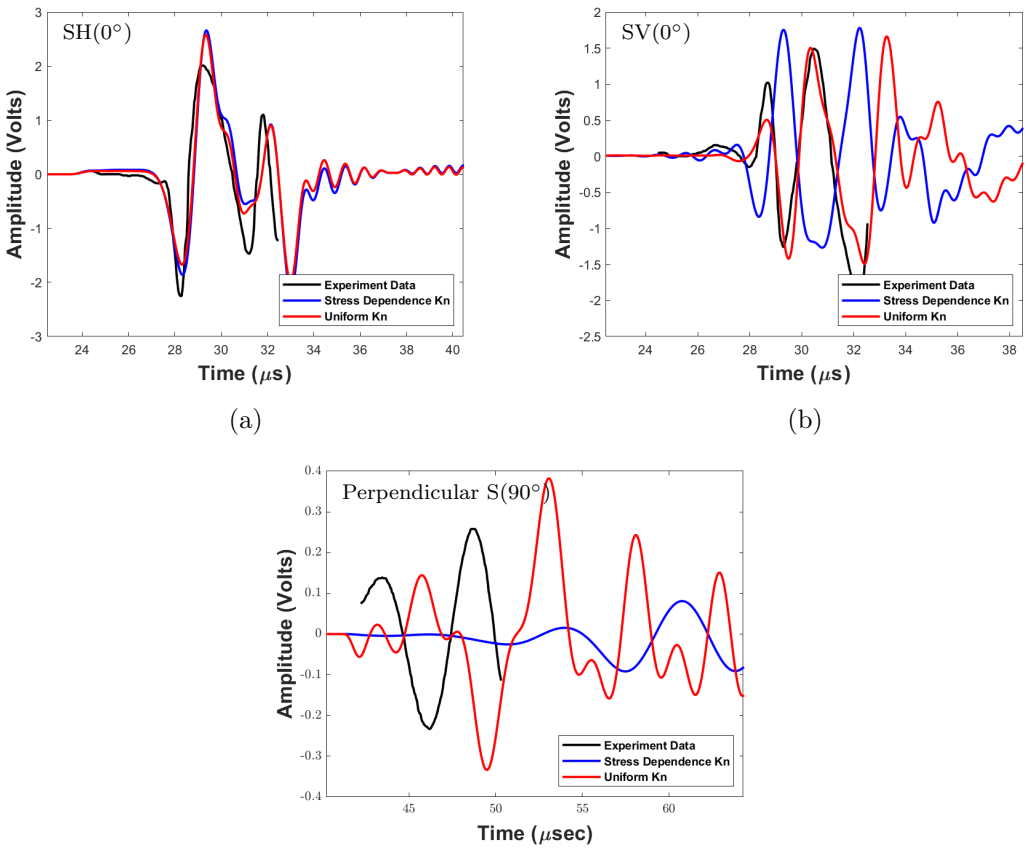

Figure 3.22: Comparing the recording of the S-wave from the experiment and the explicit model using uniform and stress-dependent fracture stiffness for propagation parallel a) SH(0°) b) SV(0°) and c) perpendicular S(90°) to the fractures.

Figure 3.23 presents the result waveforms for the EM stress dependent model for S-wave. The SH-wave (Figure 3.23a) for the stress dependent model performs similar to the uniform stiffness model in terms of amplitude, arrival time and frequency (Figure 3.25b) with the later to have 13% better match with the experiment based on the cross correlation coefficient (Tables 3.5 and 3.8).

SV-wave propagation parallel the fracture surface (Figure 3.23b) has a massive delay of 33 μs compared to the experiment and a 18μs delay compared to the uniform stress

case, the amplitude is 20% lower compared to the uniform model. In the frequency domain, it performs similar to the experiment for frequencies up to 0.3 MHz (Figure 3.25d).

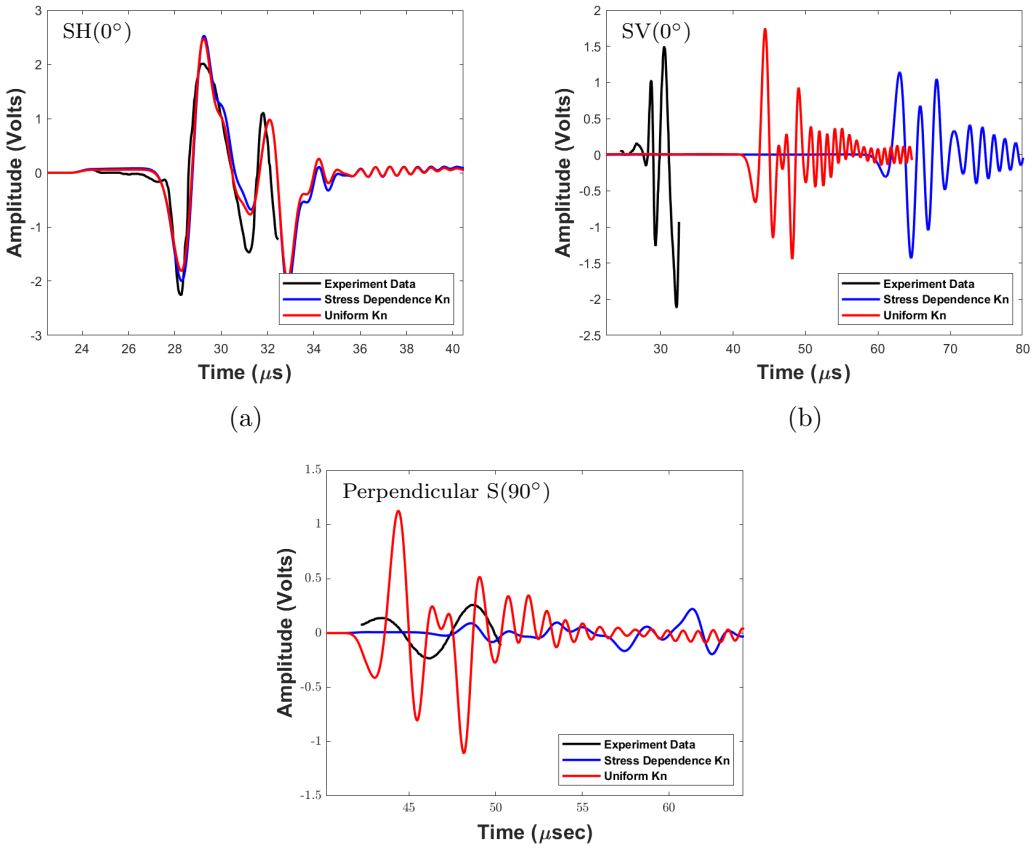

Figure 3.23: Comparing the recording of the S-wave from the experiment and the EM model using uniform and stress-dependent fracture stiffness for propagation parallel a) SH(0°) b) SV(0°) and c) perpendicular S(90°) to the fractures.

For the S-wave propagation perpendicular to fractures, the stress dependent EM model (Figure 3.23c) is 4 μs later than the uniform stress model. The amplitude is highly suppressed to five times lower than the uniform stress but one third of the experiment waveform. Similar to the explicit model, the Frequency range is different from the experiment for low frequencies (Figure 3.25f).

Finally, the LEM model for stress dependent S-wave propagation is shown in Figure 3.24 The stress dependent case for the SH-wave (Figure 3.24a) resembles the uniform model and the experiment data in amplitude, shape and frequency (Figure 3.25b). In comparison with the other two models, the latter correlates better with the experimental data but once again similar to the previous cases the stress dependent SH-wave for LEM correlates 12% less compared to the uniform stress case.

The SV-wave propagation (Figure 3.24b) has a slightly higher amplitude and predominant period compared to the uniform stress model. In terms of arrival and phase, the stress dependent matches better with the experiment. In the frequency domain, the model performs similarly with 9% lower amplitude to the experiment for frequencies up to 0.6 MHz (Figure 3.25d).

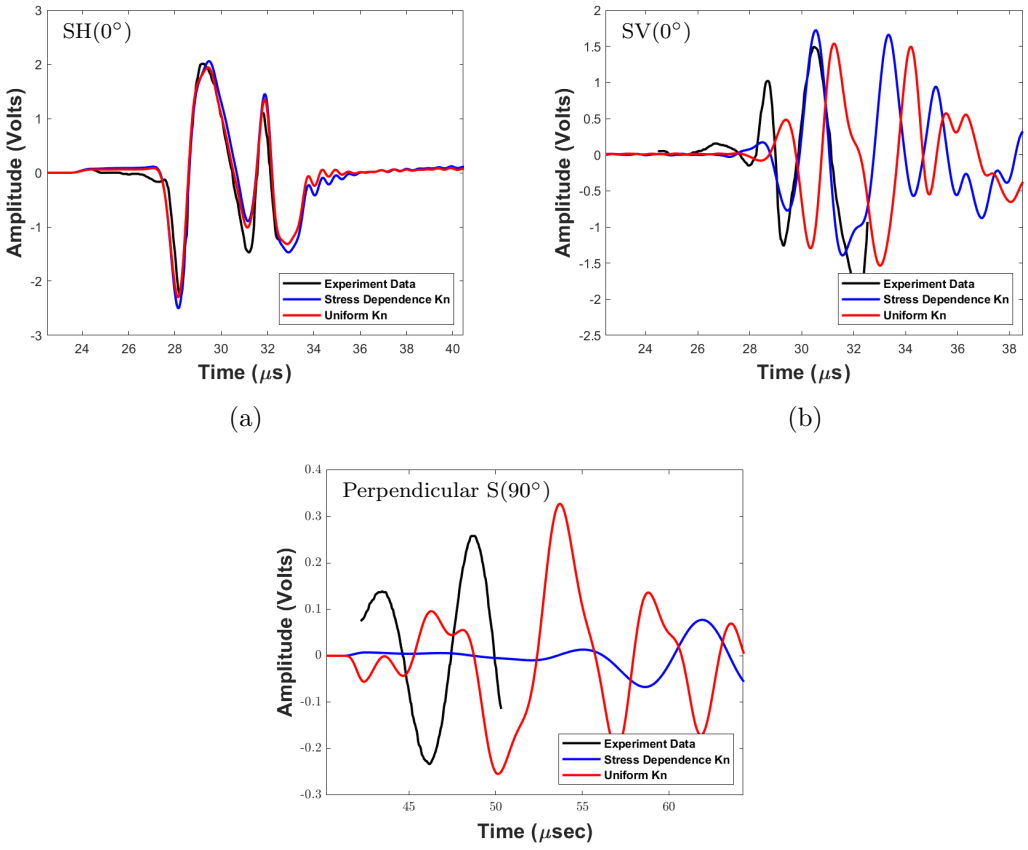

Figure 3.24: Comparing the recording of the S-wave from the experiment and the LEM model using uniform and stress-dependent fracture stiffness for propagation parallel a) SH(0°) b) SV(0°) and c) perpendicular S(90°) to the fractures.

The stress dependent LEM model waveform for S-wave perpendicular propagation (Figure 3.24c) has a 65% lower amplitude compared to the experiment waveform and the first arrival looks significantly delayed. The amplitude has attenuated massively compared to the uniform stress model, a drop of 80% of the uniform stress model. The LEM frequency range is very limited to low frequencies (Figure 3.25f).
None of the three models (explicit, EM and LEM) (Figure 3.25e) have managed to perform close to the experimental data for S-wave propagation perpendicular to the fractures. All the three models have failed in arrival time with delays on models reaching up to 12 μs with an average cross correlation coefficient below 0.60. The SH-wave

(Figure 3.25a) for all three models matches the experiment data up to 85% however in all three cases is a lower matching compared to the uniform stress cases. The SV (Figure 3.25c) is close to the experiment for the explicit model and the LEM with some delay in the latter, but is not realistically modelled for the EM model.
Comparing the cross-correlation values from uniform stress against stress dependence for the S-wave (3.5 and 3.8) the S-wave for Uniform-stress has higher values.

	Max. coefficient	**Time μs**
Solid S	0.9848	0.0363
Explicit SH(0°)	0.8011	-0.182
EM SH(0°)	0.8169	-0.109
LEM SH(0°)	0.8513	0.0
Explicit SV(0°)	0.6672	-1.20
EM SV(0°)	0.5703	-32.50
LEM SV(0°)	0.6757	0.0
Explicit S(90°)	0.5846	-11.20
EM S(90°)	0.5582	-10.9
LEM S(90°)	0.6592	-11.90

Table 3.8: Maximum cross-correlation coefficient between experiment and models for S-wave

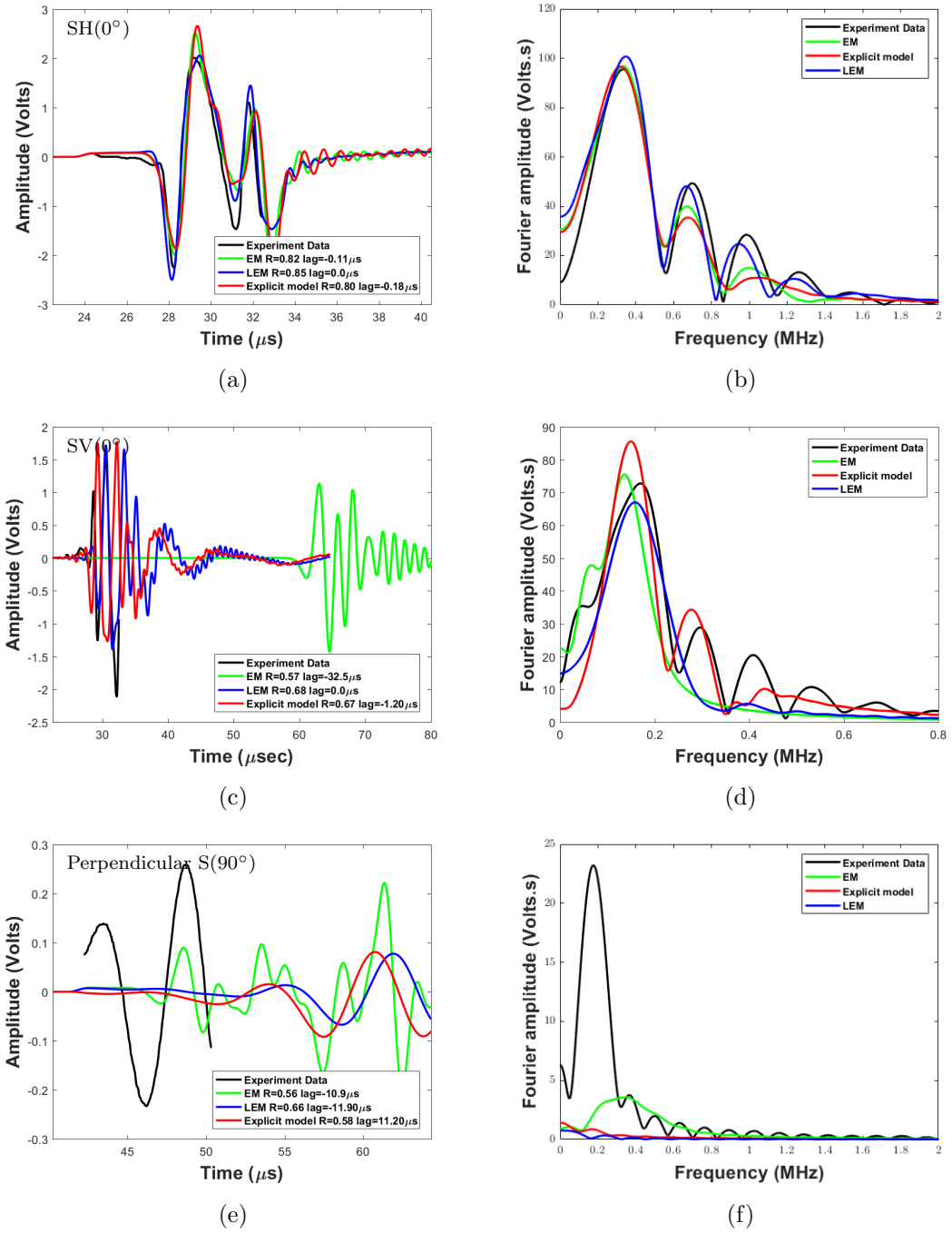

Figure 3.25: Comparing the recording of the three models and the Fourier analysis (Explicit, EM and LEM) against the experiment for the S-wave of the stress dependent fracture stiffness case for propagation parallel a) and b) SH(0°), c) and d) SV(0°) and e) and f) perpendicular S(90°) to the fractures along with the cross-correlation coefficient R and the lags between the experiment and modelled data.

3.7 How do the models and the experiment respond to different frequencies

In the previous section I observed that the explicit and the LEM model waveforms matching one the other between 87% to 97% and with time differences of 0.07 to 1.19 μs (Table 3.9). On the other hand, the EM is very different from the other two models and in some cases it does not even match on arrival time, such as with the SV wave with time differences more than 33 μs as shown in Table 3.9.

cross correlation between explicit and LEM waveforms				
	Uniform stress		**Stress dependent**	
	Max. coefficient	**Time μs**	**Max. coefficient**	**Time μs**
P(0°)	0.89	0.07	0.89	0.11
P(90°)	0.97	-0.51	0.99	-0.62
SH(0°)	0.94	0.18	0.94	0.18
SV(0°)	0.96	-0.87	0.94	-1.19
S(90°)	0.89	-0.76	0.87	-1.01
cross correlation between explicit and EM waveforms				
	Uniform stress		**Stress dependent**	
	Max. coefficient	**Time μs**	**Max. coefficient**	**Time μs**
P(0°)	0.68	0.33	0.41	0.51
P(90°)	0.11	0.07	0.26	0.07
SH(0°)	0.99	0.07	0.99	0.07
SV(0°)	0.54	-15.90	0.63	-33.79
S(90°)	0.39	-1.41	0.55	0.07
cross correlation between LEM and EM waveforms				
	Uniform stress		**Stress dependent**	
	Max. coefficient	**Time μs**	**Max. coefficient**	**Time μs**
P(0°)	0.70	0.29	0.57	0.51
P(90°)	0.11	0.69	0.26	0.69
SH(0°)	0.95	-0.11	0.95	-0.11
SV(0°)	0.54	-15.10	0.63	-32.59
S(90°)	0.32	1.99	0.61	1.34

Table 3.9: Maximum cross-correlation coefficient between explicit and LEM models, explicit and EM and LEM and EM models for P- and S-wave.

However, there is one case though where all three models for fracture representation agree very well and match the experimental data with correlation coeffiecient $\geqslant 0.94$. This case is the SH-wave propagation parallel to the fractures and polarised horizontal to the surface of the discontinuities. According to the Fourier analysis (Figure 3.25b) of the waveforms, the frequency content of the experiment data is the same as the data from the three cases. This leads to a conclusion that there might be a threshold frequency for each case where the models will start to perform the same below that frequency, and will match each other and the experiment. From the Fourier analysis above we can see that the waveforms have a bandwidth up to 1 MHz with higher amplitudes concentrated below 0.5 MHz. The idea then is to use a low-pass filter on the waveforms with a cutoff frequency based on the results of the Fourier analysis.
Unfortunately the short time window of the experimental data (8-10 μs), makes it difficult to accurately filter the data, and so I first compare how the filtered data from the models perform against each other. At this stage I use the waveforms from the models with the uniform stress and the experiment data are filtered only to be used as a reference point and to to be directly compared with the models.
The filter method applied is a zero-phase low-pass time domain Butterworth filter of second order, using WVPLOT software (Hildyard, 2007b).

3.7.1 Filtering out high frequencies

The EM results for P-wave propagation parallel to the fractures has a shape similar to the waveform from the solid sample. On the Fourier analysis (Figure 3.8b), it is clear that the frequency contents of the EM and the explicit model, and, as a result, the LEM, are similar, however the EM has higher amplitudes at higher frequencies and lower amplitude between 0.73-0.65 MHz. The first cutoff frequency then is 0.65 MHz (Figure 3.26a) where the explicit model and LEM agree as expected and the EM model is closer to the other two with only small differences. As the cutoff frequency gets lower, the cross correlation coefficient between EM and the other two models increases to $\geqslant 0.98$ (Table 3.11) for frequencies below 0.6 MHz (Figure 3.26c)

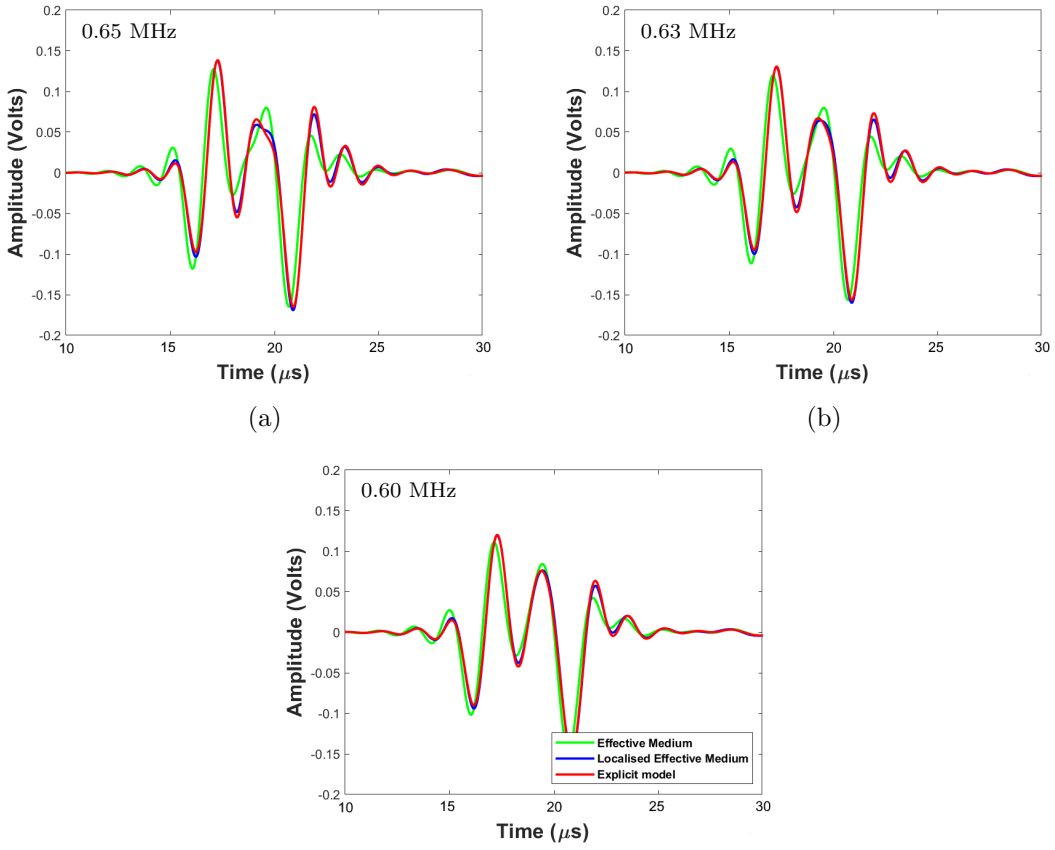

Figure 3.26: Filtering the results of the three models with uniform stiffness, for the P-wave propagation parallel to the fractures, for a) 0.65 MHz, b) 0.63 MHz and 0.60 MHz.

Continuing with P-wave propagation perpendicular to the fracture. The explicit model and the LEM perform similarly with a small delay (0.51 μs) on arrival for the LEM waveform, but the EM model is very different, the correlation with explicit or LEM is equal 0.11 (Table 3.9). The Fourier analysis of the LEM and explicit (Figure 3.9d) are identical for frequencies below 0.35 MHz and the frequency bandwidth is up to 0.46 MHz. The EM bandwidth is very different as it goes up to 2 MHz and much higher amplitude from the other two for frequencies between 0.46 MHz to 0.35 MHz (Figure 3.8d). The first cutoff frequency is 0.35 MHz and the result of the EM is closer to the other two models but still not matching completely (Figure 3.27a). Reducing the cutoff frequency to 0.27 MHz, the shape of the waveform is almost the same as the

other two models, but the amplitude is 10% higher (Figure 3.27b). Finally, using as a cutoff frequency 0.2 MHz, the shape of the wave gets close to the explicit model as the LEM has a small time shift of 0.22 μs between explicit and EM and 0.79 μs between LEM and EM(Figure 3.27c and Table 3.11).

For the SV-wave propagation parallel to the fractures polarised vertical to the fractures. Both LEM and EM are delayed with EM delayed for more than 15 μs. The shape of the waveforms between the LEM and explicit model are similar up to 96%. Since the frequencies bandwidth is similar for all models, the amplitude is used as a guide for the cutoff frequency (Figure 3.10d and 3.11d). When the cutoff frequency is 0.8 MHz, the result is similar to the non-filtered data (Figure 3.28a). Using a much lower cutoff frequency of 0.15 MHz, the waveforms still do not match (Figure 3.28b). Finally, the waveforms perform alike with correlation coefficient been between 0.81 to 0.85 (Table 3.11) when the cutoff frequency gets as low as 0.1 MHz (Figure 3.28c).

Lastly, S-wave propagation perpendicular to the fractures on the Fourier analysis the two models match in frequencies above 0.33 MHz (Figure 3.11f), the frequency bandwidth for the LEM and explicit model is the same, but the explicit has higher amplitude for frequencies above 0.33 MHz. The EM frequency bandwidth is up to 1 MHz and it starts matching with the explicit for frequencies above 0.22 MHz (Figure 3.10f). The first cutoff frequency used is 0.2 MHz where all three models perform better, but the cutoff frequency needs to be reduced even further (Figure 3.29a). Next, on the 0.15 MHz cutoff frequency the shape of the waveform for the LEM and explicit model are close with a time delay of 0.94 μs for the LEM model (Figure 3.29b). Finally, when reducing the cutoff frequency to 0.1 MHz, the three models perform the same with correlation coefficient between 0.95 to 0.97 (Figure 3.29c and Table 3.11).

The Table 3.10 summarises the wavelength of the cutoff frequencies with the best results for the EM models as described above. Due to the values in the Table 3.10 the EM will start perform similar to the other two models when the wavelength will be at least ten times larger than the fracture spacing which is 2.92 mm.

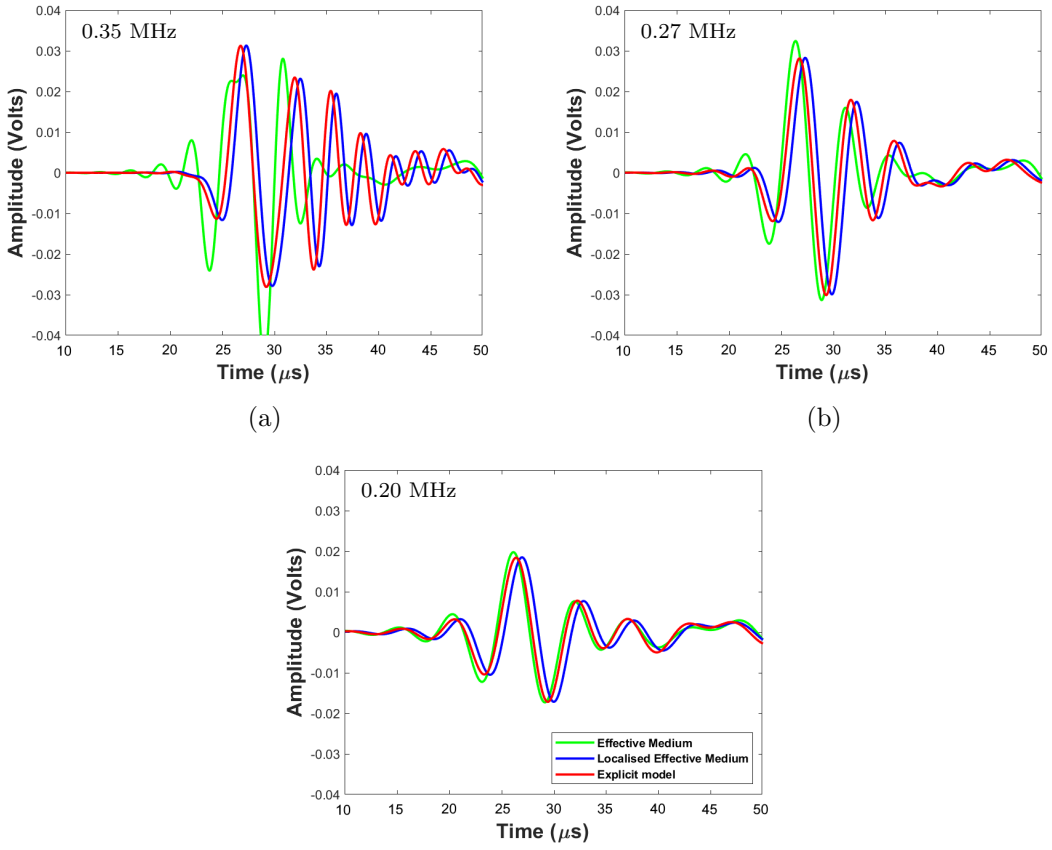

(a) (b) (c)

Figure 3.27: Filtering the results of the three models with uniform stiffness, for the P-wave propagation perpendicular to the fractures, for a) 0.35 MHz, b) 0.27 MHz and c) 0.20 MHz.

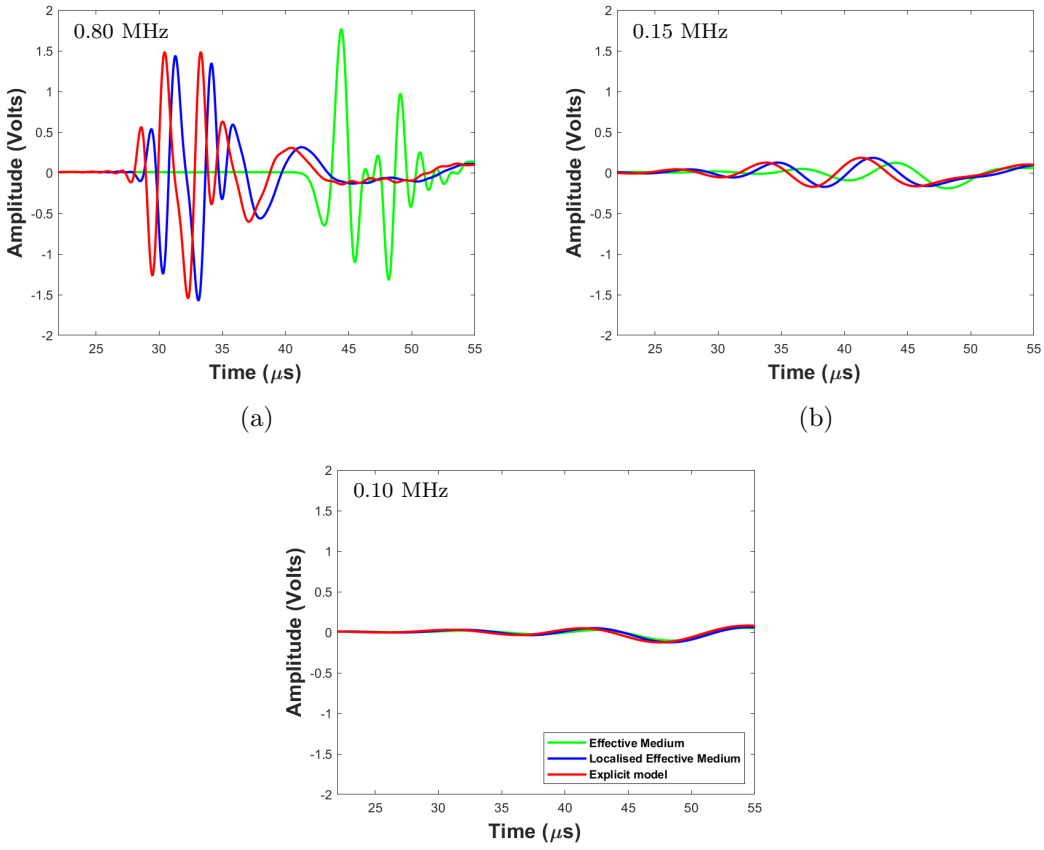

Figure 3.28: Filtering the results of the three models with uniform stiffness, for the S-wave propagate parallel to the fractures, for a) 0.80 MHz, b) 0.15 MHz and c) 0.10 MHz.

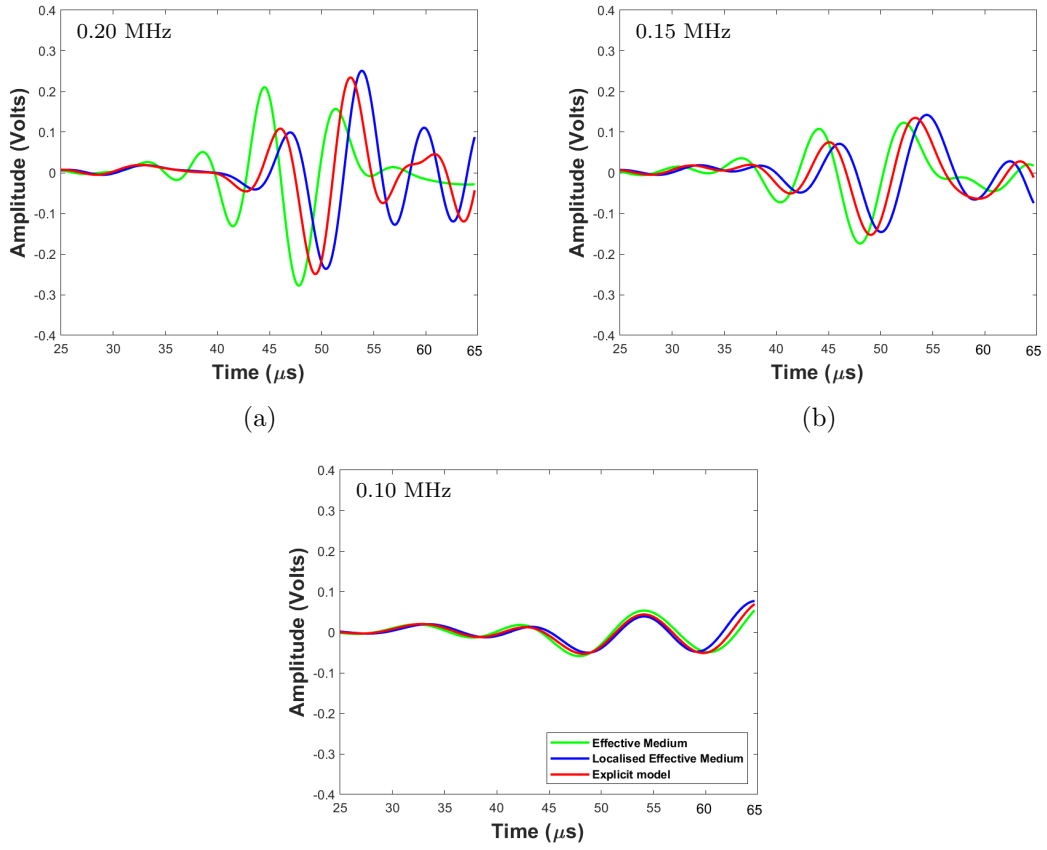

Figure 3.29: Filtering the results of the three models with uniform stiffness, for the S-wave propagation parallel to the fractures, for a) 0.20 MHz, b) 0.15 MHz and c) 0.10 MHz.

	Cutoff frequency (MHz)	**Wavelength (mm)**
P-wave parallel (0°)	0.60	10
P-wave perpendicular (90°)	0.20	30
SV-wave (0°)	0.10	32
S-wave perpendicular (90°)	0.10	32

Table 3.10: Wavelength for the cutoff frequency filtering. The space between the fractures is 2.92 mm.

cross correlation between explicit and LEM waveforms		
	Max. coefficient	**Time μs**
P(0°)	0.99	0.0
P(90°)	0.99	-0.58
SV(0°)	0.92	-0.22
S(90°)	0.95	0.0
cross correlation between explicit and EM waveforms		
	Max. coefficient	**Time μs**
P(0°)	0.98	0.11
P(90°)	0.98	0.22
SV(0°)	0.85	0.0
S(90°)	0.95	0.0
cross correlation between LEM and EM waveforms		
	Max. coefficient	**Time μs**
P(0°)	0.99	0.11
P(90°)	0.98	0.79
SV(0°)	0.81	0.0
S(90°)	0.97	0.0

Table 3.11: Maximum cross-correlation coefficient between explicit and LEM models, explicit and EM and LEM and EM models for the lowest cutoff frequency of the P and S modelled waveforms.

3.8 Discussion

For all three uniform stress models, wave propagation parallel to the fractures are closer to the experiment data, the effect of the fractures is low for the experiment data and the models. The difference in velocities between P-waves propagating in the solid sample and parallel to the fractures is only 124 m/s. Comparing the frequency contents of the solid sample and that of the P-waves propagating parallel to the fractures, it is clear that the high frequencies above 0.63 MHz suppressed and the low frequencies above 0.1 MHz are strengthened (Figures 3.6 and 3.9b). The explicit and the LEM model have the same frequency suppression as the experiment data while the EM model is frequency independent (e.g., de Figueiredo *et al.*, 2013; Pyrak-Nolte *et al.*, 1990; Yil *et al.*, 1997) and the result is similar to the wave from the solid sample (Figure 3.8b). Similarly for the SH waves propagating parallel to the fractures the frequency and the arrival time is in a good agreement for all three models with higher amplitudes for frequencies between 0.2 to 0.4 MHz compared to the waveform form the solid sample (Figure 3.5, 3.10b and 3.11b). On the other hand, the SV waves propagating parallel to the fractures the signal for all the three models follow the experiment suppression of frequency lower than 0.4 MHz but the EM fails to predict the arrival time. When wave propagates perpendicular to the fractures the attenuation is frequency dependent for the explicit and LEM models (Hildyard, 2001; Pyrak-Nolte *et al.*, 1990; Vlastos *et al.*, 2003, 2007) but not for the EM as mentioned above. The explicit model and LEM has higher frequency suppression when the wave propagates perpendicular to the fractures. This is because the surface of the fractures and the fracture spacing filter the wave, allowing only the lower frequencies to pass through. Explicit and LEM are in a good agreement one to the other as expected from previous studies (Li *et al.*, 2010; Zhang & Gao, 2009).

For the stress dependent explicit and LEM models show 18% better matching between model and experiment waveforms. This is in agreement with previous studies such as Chichinina *et al.* (2009a,b); Perino & Barla (2015) that the explicit model is in qualitative agreement with experiment data. As mentioned in Chapter 2 the LEM creates equally good results as the explicit models (Li *et al.*, 2010; Zhang & Gao, 2009). Stress dependent model works better for P-waves propagating perpendicular to the fractures because the wave propagates faster and more strongly in the centre of the

block since the stiffness is higher (Figure 3.14 and 3.16) leading to greater scattering and dispersion of the wave, similar to what Hildyard (2001) has shown for the explicit stress dependent model.

In contrast when wave propagates parallel to the fractures the explicit and LEM models have a up to 15% lower correlation and up to 1 μs delay (Tables 3.4, 3.5, 3.7 and 3.8) for all P and S (SH and SV) cases. This difference in the data maybe caused by the lower stiffness values created at the edges of the block due to the biaxial compression and especially due to lower K_s values since the c parameter for the stress dependent model is only 0.33 of the K_n. Hildyard (2001) has previously modelled this experiment for explicit fractures and concluded that lower uniform K_n and K_s values leads to a result similar to what we see on the stress dependent when the wave propagating parallel to the fractures (P(0°), SH(0°) and SV(0°)). Similarly, the S-wave propagates perpendicular to the fractures for the stress dependent explicit and LEM models, have delayed arrival, lower amplitude and suppressed frequencies compared to the experiment data. Again the low K_s values might be responsible for that mismatch. A further parameter search is necessary in order to balance the values of a, b and c for the stress dependent models and create better results for S-waves propagating perpendicular to fractures as well as to create as good results, for waves propagating parallel to fractures as the uniform stress models did.

As explained in section 3.3.3 the EM model is not expected to match the experiment data since the crack density is as high as 4.7 while the threshold value to make EM work based on previous studies (Schubnel & Gueguen, 2003; Schubnel *et al.*, 2003) is about 0.5 and the λ/d ratio is more than an order of magnitude lower than the required (Shuai *et al.*, 2018). Filtering the data makes the EM work closer to the other two models when the wavelength of the signal gets more than ten times the fracture spacing as summarised in table 3.10, this can be useful for future modelling applications of the EM since fracture spacing for large fractures is another limitation for EM.

EM and LEM are based on the same background theory and using the same stiffness matrix (e.g., Coates & Schoenberg, 1995; Crampin, 1981; de Figueiredo *et al.*, 2013; Ding *et al.*, 2014; Vlastos *et al.*, 2003), the major difference is the way the effective medium is implemented. In the LEM the EM properties are applied only local to the fractures. This alternation between EM and homogeneous material, in the LEM model, is responsible for the frequency dependent scattering attenuation similar to the

explicit model. The flexibility of the LEM model and how close to the EM or explicit representation it is performing, based on the resolution of the model, will be tested further in the next Chapter 4.

Finally, a model apart from being accurate has to be efficient as well in terms of computational time. In table 3.12 below I have summarised the run time for each of the three models for uniform and stress dependent fracture stiffness. For running the models I have used a Linux computer with total memory 256 GB and base CPU frequency at 2.4 GHz. Since WAVE3D code is not parallel a single core was used each time and 1% of the memory. Code optimisation has not been applied neither for the EM and LEM approaches, nor for the newly developed stress dependent code for EM and LEM. As a result the run-time of these models is up to 4 times more for the uniform stress models and up to 13 times more for stress dependent models. Overall, stress dependent models need more time to run because the time per cycle is higher and the number of cycles needed to reach equilibrium is 20 times more than the dynamic run time. In the next chapter 4 I am going to use another numerical modelling code (3DEC) as well and a reference of the models run-time is necessary.

	Uniform stress models	
	Time per cycle (s)	**Total run time (min)**
Explicit model	0.57	17.1
LEM model	0.91	27.3
EM model	2.22	66.6
	Stress dependent models	
	Time per cycle (s)	**Total run time (min)**
Explicit model	0.97	646.7 (static) + 29.1 (dynamic)
LEM model	3.32	2213.3 (static) + 99.6 (dynamic)
EM model	13.69	9126.7 (static) + 410.7 (dynamic)

Table 3.12: Run-time of the models for uniform stress and stress dependent for each model run in Linux computer from faculty of environment in the University of Leeds.

So far the three models have been tested for a medium with parallel fractures. In nature though fractures are not always parallel and waves may propagate in various angles rather than parallel and perpendicular to the fractures. There is a need then to

examine the performance of the models in a medium with fractures of various angles for uniform and stress dependent stiffness.

3.9 Summary and conclusions

I have used three approaches for fracture representation (EM, an explicit model, and a LEM model), to model the experiment from Pyrak-Nolte *et al.* (1990). In order to understand the physics of the experiment, I first considered uniform stiffness to compare the performance of these different representations against the experimental data.

For P-wave propagation parallel to the fractures, the waveforms from the EM model does not match the other two. The waveform from the explicit model matches closely that of the experiment with correlation coefficient be 0.89. The waveform from the LEM model is reasonably similar to that of the explicit model (correlation coefficient 0.88), and certainly matches in arrival, predominant period, frequency content, and the experiment in amplitude (Figure 3.9). While the waveform for the EM model is 0.4 μs slower and it does not match with the experiment (correlation coefficient 0.70) with differences in period, and significantly higher amplitudes and high frequency content.

For wave propagation perpendicular to the fractures, none of the models properly correlate with the experimental waveform. All models come close to matching the significant delay in arrival observed in the experiment, and the explicit model and LEM model produce a significant reduction in period to about half, which mimics the experiment. The EM model does not cause a reduction in period and its high frequency content is a significant departure from the experimental behaviour. Waveforms from all three models have much lower amplitudes compared to wave propagation parallel to the fractures, but not the same amplitude reduction as the experiment. The reason the models, with wave propagation perpendicular to the fractures, fail to produce the same result as the experiment is because of the uniform stiffness and as a consequence uniform stress, consideration. Since the experimental waveforms was recorded under biaxial stress the stiffness is expected not to be uniform.

Similarly, for SH-wave propagation parallel to the fractures the three models agree and correlates (up to 0.97 Table 3.5) with the experiment data in arrival time, frequency content, predominant period, with a small variation in amplitude. The SV-wave for the explicit and LEM model is close to the experiment apart from a small time delay (0.91 μs) for the latter. The SV-wave for EM is completely different from the experiment and significantly delayed. Finally, S-wave propagation perpendicular to the fractures is a big mismatch for all three models, even though the amplitude is reduced, by almost

an order of magnitude, and the wave is delayed of about 3 μs due to the presence of the fractures. Similar to the P-waves propagating perpendicular to the fractures the uniform stiffness is not suitable for modelling the experiment for S-waves propagating perpendicular to the fractures too.

The goal of this work, is to use different approaches for fracture representations (explicit, LEM and EM) using numerical models and generate waveforms comparable to the experimental one. The differences between experimental and modelled waveforms in the case of propagation perpendicular to the fractures leads us to conclude that the fracture stiffness cannot be uniform in an environment where the stress is not uniform. As a consequence the stress state is crucial to match the experiment with the model waveforms. For that reason I have implemented stress dependent behaviour for the EM and LEM models in the WAVE3D code (Appendix A.1). The stress-field has been modelled in all three models in conjunction with stress dependent fracture stiffness, to create a coupled case where the waveforms agree very well with the experimental data for the full waveform. The key outcomes of the stress dependence models are that for wave propagation perpendicular to the fractures, the amplitude is reduced by half and for the P-wave, the explicit and the LEM models agree very well with the experimental data increasing the correlation coefficient up to 0.78.

P-wave propagation parallel to the fractures is similar to the uniform stress case and all three approaches have a small time delay. The SH-wave performs almost identically with the uniform stiffness model for EM, explicit and LEM models. However, the SV-wave is delayed significantly compared to the uniform case for the EM. For the LEM and explicit model the arrival is early.

I then studied whether the EM model was consistent with the explicit at least at low frequencies and obtained frequency ranges for which it was an appropriate representation. For the P-wave parallel to the fractures the frequency is 0.6 MHz while for the perpendicular case it is 0.2 MHz. For the S-wave, the two cases which do not match are the SV and the perpendicular to the fractures one. In both of these cases, when the frequencies drop below 0.1 MHz, the models match to a level with up to 85% for SV(0$\circ$) and 97% for S(90$\circ$) based on cross correlation.

The conclusions come out of modelling this experiment with parallel fractures are as following:

- Overall the explicit and the LEM models capture the physics of the waveforms observed in the experiment for most cases. They match in terms of wave-speed, period, frequency, amplitude and indeed the full waveforms.
- Uniform fracture stiffness cannot explain the recorded experimental waveforms, propagating perpendicular to the fractures.
- I have developed and implemented versions of the EM and LEM models in which the stiffness is dependent on the stress state. These models alters the waveforms as expected, in wave-speed, period, frequency and amplitude.
- The waveforms from the stress dependent LEM model performs as well as the stress dependent explicit fracture model.
- Even though the stress dependent EM model has been improved compared to the uniform stiffness, it is still no matching the experimental results for the given frequencies.
- On the other hand the stress dependent LEM performs similar to the stress dependent explicit fracture model. The two models with non-uniform stiffness successfully explains the experimental data for the P-wave for parallel fractures.
- The three cases of stress dependent parameters a,b and c did not successfully match the experimental data for the S-wave as I did with the P-wave. In future, further parameter search, for a,b and c may needed to improve the model's response.
- The LEM model is promising in matching fully explicit parallel fractures for wave propagation parallel and perpendicular to the fractures.
- Filtering the high frequency content of the waveforms, the EM model starts approaching the other two models when the wavelength is at least ten times larger than the fracture spacing.

Chapter 4

Flexibility of the Localised Effective Medium model for parallel fractures and for more complex fracture networks

For wave propagation in fractures medium, the localised effective medium (LEM) model can perform close to the explicit model or close to an effective medium (EM) model depending on the geometry of the model, resolution and the frequency content of the wave. In this chapter, I work on defining the limits of the LEM model in terms of frequency, normal stiffness, and fracture geometry complexity. To examine wave propagation in complex fracture geometries, I use WAVE3D and the distinct element method (DEM). I run the models for different wave frequencies and normal stiffness, and again study stress dependent fracture stiffness. I then develop and evaluate a method to convert dipping fractures from a tetrahedral to an orthogonal staggered grid for the explicit and the LEM models. In most cases the waveforms propagating in the LEM match very well with the explicit model when adjusting the cracks per unit length parameter (1/L) and the wave frequency. Part of this work has been presented in the 2nd International Discrete Fracture Network Engineering Conference (Parastatidis *et al.*, 2018).

4. FLEXIBILITY OF THE LOCALISED EFFECTIVE MEDIUM MODEL FOR PARALLEL FRACTURES AND FOR MORE COMPLEX FRACTURE NETWORKS

4.1 Introduction

Seismic waves can give information about fractures. The discontinuity in the rock mass created by the fracture affects seismic wave propagation (e.g., Schoenberg, 1980). Part of the energy of the wave is reflected back and the transmitted wave is attenuated. The energy loss and attenuation depends on the geometry and the mechanical properties of the fracture and is frequency dependent. As a result the recorded waveform carries information about the fractures and can be used as a diagnostic tool. Using numerical models to simulate the wave propagation in the rock mass and compare the full waveform with recorded experimental waveforms allows us to both improve the model and to improve interpretation of the fractures.

In the previous chapter I presented a model for a medium with parallel fractures to match experimental waveforms (e.g., Hildyard, 2001, 2007b; Parastatidis *et al.*, 2017; Pyrak-Nolte *et al.*, 1990). Finite difference modelling code WAVE3D (Hildyard *et al.*, 1995) was used to examine three different approaches to fracture representation - explicit representation of discontinuities, a transversely isotropic effective medium, and a localised effective medium - in order to define the limitations and the applicability of each model. In addition the stress state of the medium can lead to a non-uniform fracture stiffness and modify waveforms. Introducing stress dependent fracture stiffness to the previous models showed that the explicit and the LEM model can closely approach waveforms recorded in a laboratory experiment for high frequencies with multiple parallel fractures (Hildyard, 2001, 2007b; Parastatidis *et al.*, 2017). A further step is to examine the performance of LEM for parallel fractures and how its behaviour changes along with the changes in of the cracks per unit length. It is necessary to examine the performance of the three approaches in fracture networks with more complex geometries closer to real rock fractures.

In this chapter I examine how flexible as a model the LEM approach is, by comparing the waveforms of an explicit case with parallel fractures, the EM approach and five cases for the LEM with different cracks per unit length and different thicknesses of the effective medium layers. Next, I compare the waveforms from the three approaches, scaling the element size and the stiffness and the frequency of the models from mm to m.

The next part of my work is on validating the models for complex fracture networks

using a commercial code 3DEC. Initially I examine the wave propagation for the explicit fracture representation using a discrete fracture network (DFN). That creates a set of planar disk shape fractures with finite size and random position and orientation. I compare the wave propagation for varying fracture densities and varying fracture stiffness. I then examine how the stress affects the fracture stiffness and as a consequence the wave propagation in this media with complex explicit fractures. I have developed a method to apply the DFN output to the LEM and EM approach, and use this to evaluate the LEM and EM models for complex fractures.

The DEM 3DEC is efficient in working with relatively low wave frequencies but it needs much longer run-times for models with a fine mesh and high wave frequencies compared to WAVE3D. As a result I need a method to convert the dipping fractures of the tetrahedral grid to the WAVE3D staggered grid. In the last part of this chapter I evaluate two such methods, the pixelised dipping fractures and the equivalent discrete fracture medium (EDFM). The output of these two methods will be used in the last chapter to model fractures on the EDZ seismic tomography velocity survey.

4.2 The flexibility of the Localised Effective Medium model

From the definition of the implementation of the LEM, it is clear that the finer the mesh of the models and the thinner the LEM layer, the closer it is to the explicit model. As previous work in Chapter 3 has shown, the LEM model performs close to the explicit when the wavelength is much larger than the element size and relatively larger than the fracture spacing. The question then is how the thickness of the LEM layer changes the result, and whether there is a balance between stiffness, frequency and LEM thickness, where the LEM performs close to the explicit model or is approaching the EM model.

4.2.1 Models with parallel fractures

To better understand the flexibility of the LEM, a set of numerical experiments with various LEM thickness and for different source frequencies and fracture stiffness were designed. In order to maximise computational efficiency and the parameter space to search, the models are relatively small in terms of size. The element size is 0.5 mm and the size of the model is 120 elements on each side, giving a model with 1.7 million elements. The block has been cut through by five parallel fractures with 5 mm spacing. The material properties for this set of models have been kept the same as the previous steel experiment (Chapter 3, table 3.1). The source is a double ricker wavelet, the area the source is applied to is a 10 mm×10 mm square shape area and I use five different source frequencies. Based on the method for maximum frequency linked with the element size, described above (Chapter 3), the predominant frequencies of the sources and the wavelength λ are summarised in Table 4.1, the largest wavelength (19.30 mm) for the lower frequency is almost four times larger than the fracture spacing. In addition, three values for K_n and K_s have been applied for the fracture stiffness of the explicit case and for the stiffness matrix of the EM and LEM models. The values for stiffness are in Table 4.2. Since the material properties are the same as in Chapter 3 and the whole model structure is similar, the first values for fracture stiffness is the same as the values for uniform stiffness used in Section 3.5.

Frequency (MHz)	**Wavelength λ (mm)**
0.625	9.64
0.500	12.04
0.416	14.48
0.357	16.87
0.312	19.30

Table 4.1: The five frequencies used in the models and the wavelength λ in mm based on the P-wave velocity (6022 m/s).

	case 1	**case 2**	**case 3**
$\mathbf{K_n}$	6×10^{13} Pa/m	3×10^{13} Pa/m	1×10^{14} Pa/m
$\mathbf{K_s}$	2×10^{13} Pa/m	1×10^{13} Pa/m	5×10^{13} Pa/m

Table 4.2: The three cases for fracture stiffness (K_n and K_s) used in the models to evaluate the performance of LEM against the explicit and EM models.

LEM thickness (mm)	LEM layer spacing (mm)	**1/L ($\mathbf{m^{-1}}$)**
0.5	5.0	2000
1.0	4.5	1000
1.5	4.0	667
2.0	3.5	500
2.5	3.0	400

Table 4.3: The five sub-cases for LEM thickness in mm and the calculated 1/L m^{-1} used in the models to evaluate the performance of LEM against the explicit and EM models.

The acquisition is again perpendicular and parallel to the fractures. This creates in total fifteen cases (five source frequencies and 3 sets of fracture stiffness) for parallel and fifteen for perpendicular propagation. There are then seven different implimentation of these models. The explicit model, EM model, and five sub-cases of the LEM model, resulting in 105 models for parallel and 105 models for perpendicular propagation. These five sub-cases vary the thickness of the LEM layer around a fracture (Table 4.3). The thickness of the LEM layer surrounding the fracture affects the

cracks per unit length parameter (1/L) of the LEM model. The first sub-case has one element thickness 0.5 mm and as a result the cracks per unit length parameter (Chapter 2) 1/L=2000 m^{-1} (Figure 4.1c), next double the thickness with two elements 1/L=1000 m^{-1} (Figure 4.1d), continuing with three elements 1/L=667 m^{-1} (Figure 4.1e), four elements 1/L=500 m^{-1} (Figure 4.1f), finally increase the thickness to five elements 1/L=400 m^{-1} (Figure 4.1g).

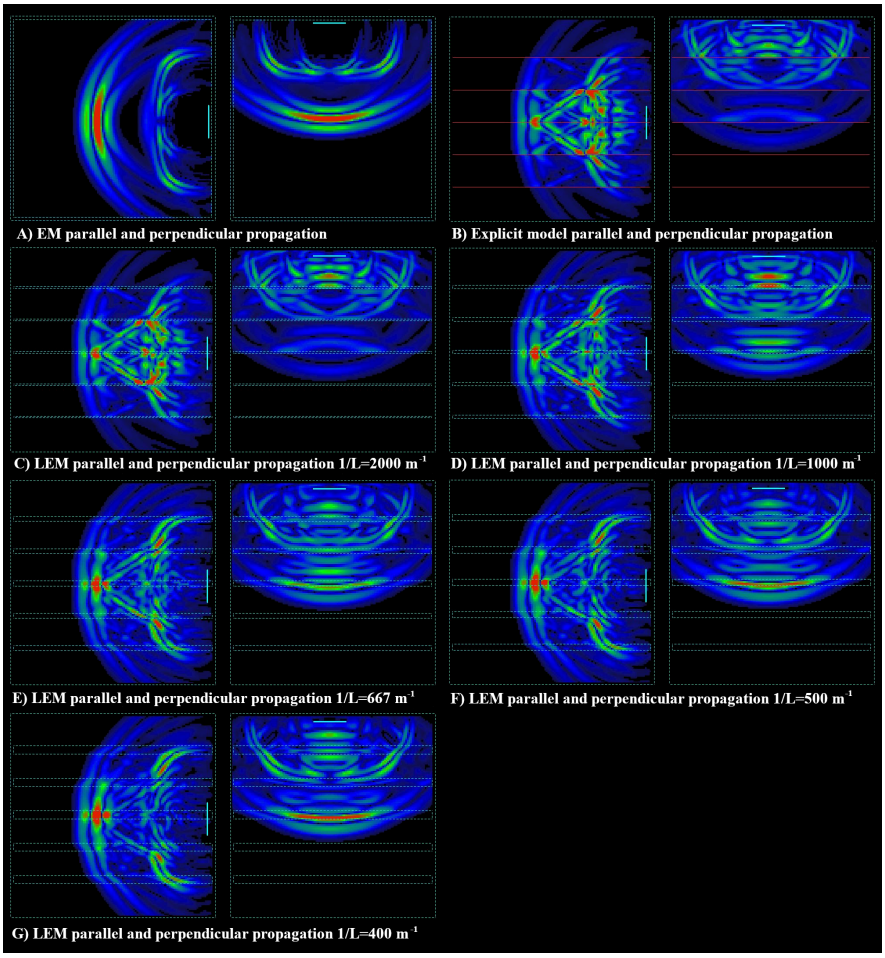

Figure 4.1: Snapshots from P-wave propagation perpendicular (left) and parallel (right) to fractures at $t = 6.7$ μs a) EM model b) explicit and c) localised effective medium 1/L=2000 m^{-1} d) localised effective medium 1/L=1000 m^{-1} e) localised effective medium 1/L=667 m^{-1} f) localised effective medium 1/L=500 m^{-1} g) localised effective medium 1/L=400 m^{-1}. (Red represents the peak amplitude, and all snapshots are on the same scale).

Wave propagation parallel to fractures

In this section I examine wave propagation parallel to the fractures. Firstly, I examine the fractures with stiffness with the same values used in the previous chapter regarding the steel plates for uniform stiffness K_n=60000 GPa/m. In general, as the frequency of the source gets lower, the different thickness LEM models start to produce the same results. More specifically, in Figure 4.2a the higher 1/L, the higher the attenuation and the closer to the explicit model for the highest frequency. As shown in Figure 4.5a the cross-correlation coefficient between explicit and LEM models increases as the 1/L goes higher, the correlation coefficient gets maximum values for lower frequencies. On the other hand, as the cracks per unit length parameter decreases and, the thickness of the LEM layers increases, the waveform has lower attenuation and is close to the EM model (Figure 4.5b). When the frequency and the cracks per unit length are at their highest values (Figure 4.2a) it is possible that, at time 13 μs and 16 μs reflections from the fractures above and below the source point (Figure 4.1). However, when 1/L gets below 667 m^{-1} these reflections become smoother in frequency and amplitude. It seems that all of the five LEM cases have captured some of the complexity that the waveform of the explicit model has. In the next step where the frequency of the source is 0.5 MHz (Figure 4.2b), all of the LEM cases which did not previously match with the explicit one, approach the second case (1/L=1000 m^{-1}) to perform the same as the first case (1/L=2000 m^{-1}), increasing the correlation coefficient from 0.85 to 0.94 (Figure 4.5a). Reducing the source frequency further (Figure 4.2c, 4.2d and 4.2e), more LEM cases with lower 1/L value start to perform in a similar manner. The correlation coefficient increasing gradually above 0.9 for all the five LEM cases when source frequency is 0.31 MHz . In Figure 4.2c for the first three LEM models the correlation coefficient is above 0.9 with time shifting lower than 0.1 μs. In Figure 4.2d four of the LEM models have correlation coefficient above 0.9. As a result, a first conclusion concerning wave propagation parallel to the fractures is that the LEM can perform similar to the explicit model at lower frequencies when the wavelength is more than five times higher than the spacing of the LEM layers (Tables 4.3 and 4.3), no matter the thickness of the LEM layer and the 1/L value, but at high frequencies the LEM has to be thin and the 1/L value very high.

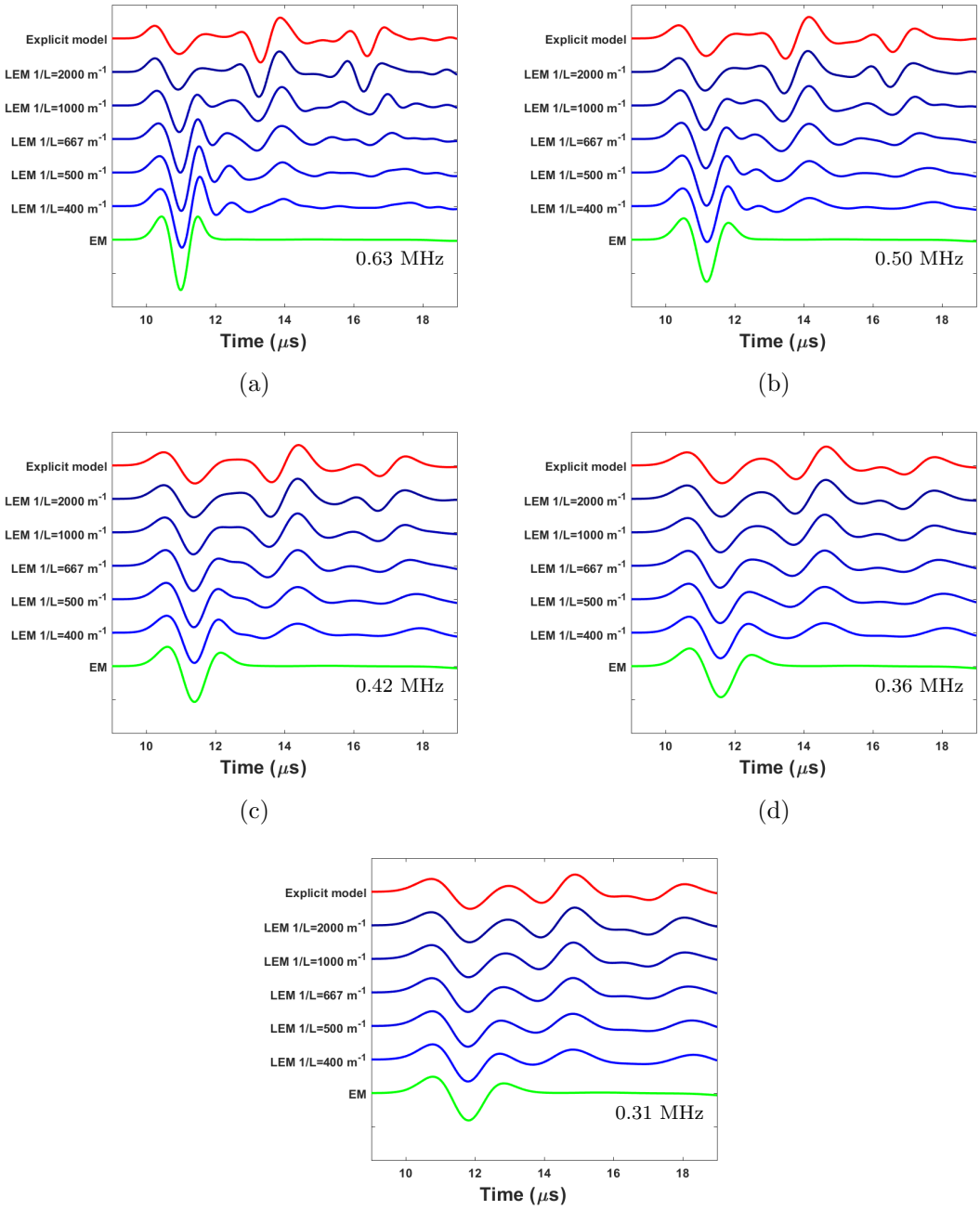

Figure 4.2: Comparison of P-wave propagation parallel to the fractures for the Explicit, EM and the 5 cases of LEM, with K_n=60000 GPa/m and with source frequencies of 4.2a 0.63 MHz , 4.2b 0.5 MHz , 4.2c 0.42 MHz ,4.2d 0.36 MHz and 4.2e 0.31 MHz.

The second case (Figure 4.3) is similar to the previous case but with increased fracture stiffness from 60000 GPa/m to 100000 GPa/m. As expected, the higher the stiffness the less amplitude attenuation for the waveforms. The waveforms from the LEM models now start to correlate better with values between 8-28% higher than before (Figures 4.5a and 4.5c) at even higher frequencies compared to the case with K_n=60000 GPa. In Figure 4.3a the waveform of the second LEM model (1/L=1000 m^{-1}, maximum correlation=0.92) is already closer to the first (1/L=2000 m^{-1}, maximum correlation=0.97) compared to the previous case (1/L=1000 m^{-1}, maximum correlation=0.85 and 1/L=2000 m^{-1}, maximum correlation=0.97). The reflections from the fractures above and below (at the points 13 μs and 16 μs) the source, have a lower amplitude due to the higher stiffness that allows more wave energy to pass through. However, as mentioned in the previous case, the lower the 1/L value, the closer to the EM model and the higher the amplitude of the direct wave, as maximum correlation values shows in Figure 4.5d. Reducing the frequency of the source to 0.5 MHz (Figure 4.3b) and 0.42 MHz (Figure 4.3c) the second and third LEM models perform the same as the first, which is identical to the explicit model (Figure 4.5c). Finally, when the frequency drops (Figure 4.3d and 4.3e) further, the reflections almost disappear even for the explicit model and the direct wave for all five LEM models are the same as both the EM and explicit models. The low amplitude for the reflection part of the wave as the frequency gets lower is due to the fact that the wavelength of the wave gets higher relative to the fracture spacing.

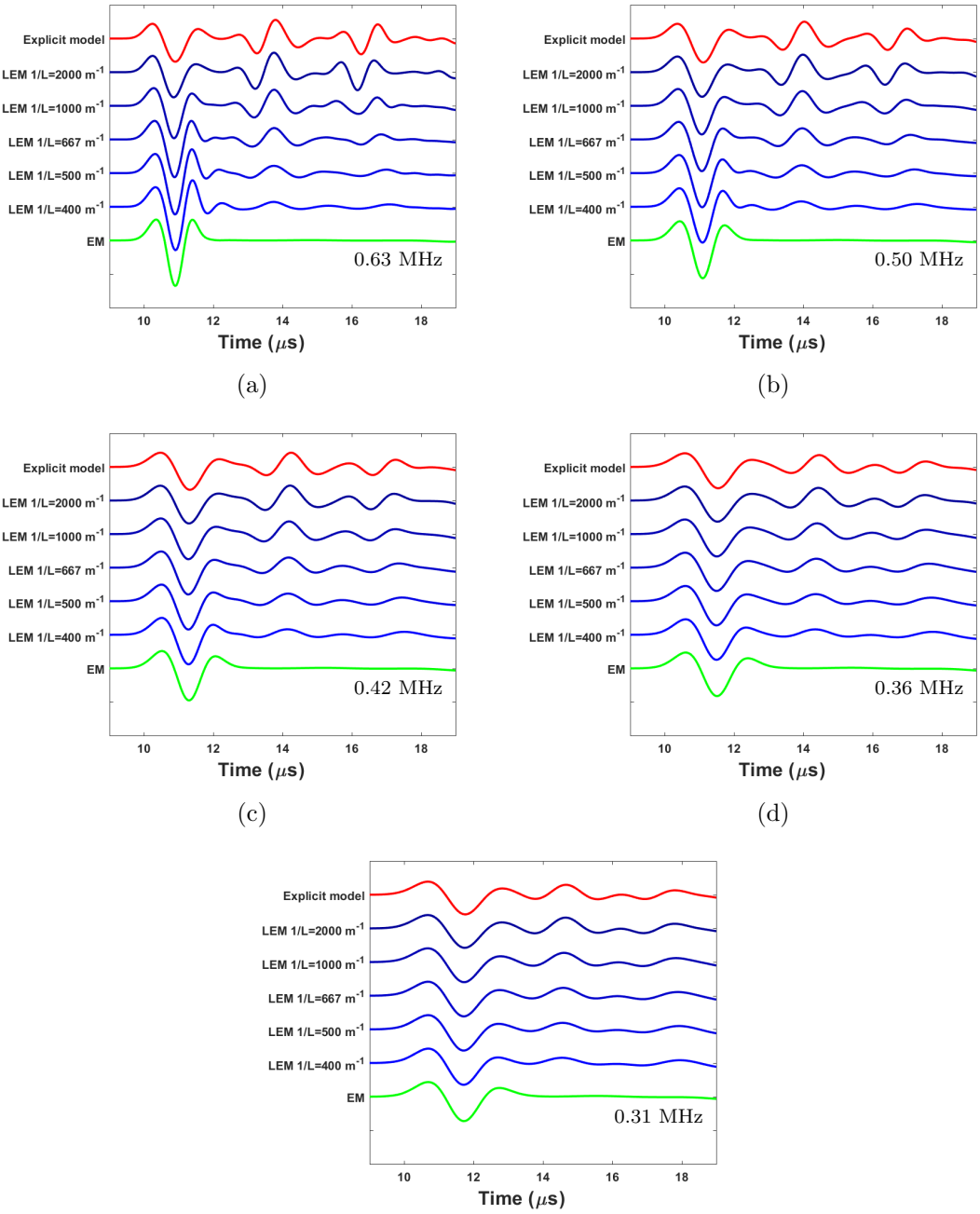

Figure 4.3: Comparison of P-wave propagation parallel to the fractures for the Explicit, EM and the 5 cases of LEM, with K_n=100000 GPa/m and with source frequencies of 4.3a 0.63 MHz , 4.3b 0.5 MHz , 4.3c 0.42 MHz ,4.3d 0.36 MHz and 4.3e 0.31 MHz.

Finally, the lower the normal stiffness, the higher the attenuation of the wave (Figure 4.4). In all of the five frequencies, the amplitude of the direct wave is significantly lower compared to the two previous cases and the amplitude of the reflected wave is higher as more energy is trapped between the fractures (Figure 4.1). The first two LEM models start to perform similarly, with correlation coefficient above 0.90, for lower frequencies below 0.42 MHz (Figure 4.4c and 4.4e). In Figure 4.4a only the LEM with 1/L=2000 μs value correlates to 0.94 with the explicit model and as the source frequency decreases, the second LEM model approaches the result of the explicit model (Figure 4.4b, 4.4c and 4.5e). In contrast with the previous cases with higher normal stiffness, the models with lower 1/L value do not match the EM model as much for the high frequencies (Figure 4.4a, 4.4b and 4.5f). When the source frequency gets even lower (Figure 4.4d and 4.4e), the LEM models with lower 1/L (500 and 400 m^{-1}) tend to mimic the explicit and the first LEM model, with maximum correlation values 0.90 and 0.86 respectively performing better than in Figure 4.4b 4.4c and 4.5e.

To sum up, for wave propagation parallel to the fractures, for high stiffness and higher frequencies the LEM models with 1/L=667 m^{-1} and above perform closer to the explicit model and the models below that 1/L value are closer to the EM model. However, when the stiffness is low and the source frequency is also low (with wavelength more than six times the spacing between LEM layers, as in Tables 4.3 and 4.1), the LEM model with 1/L=500 m^{-1} and 400 m^{-1} is closer to the explicit model and not to the EM model.

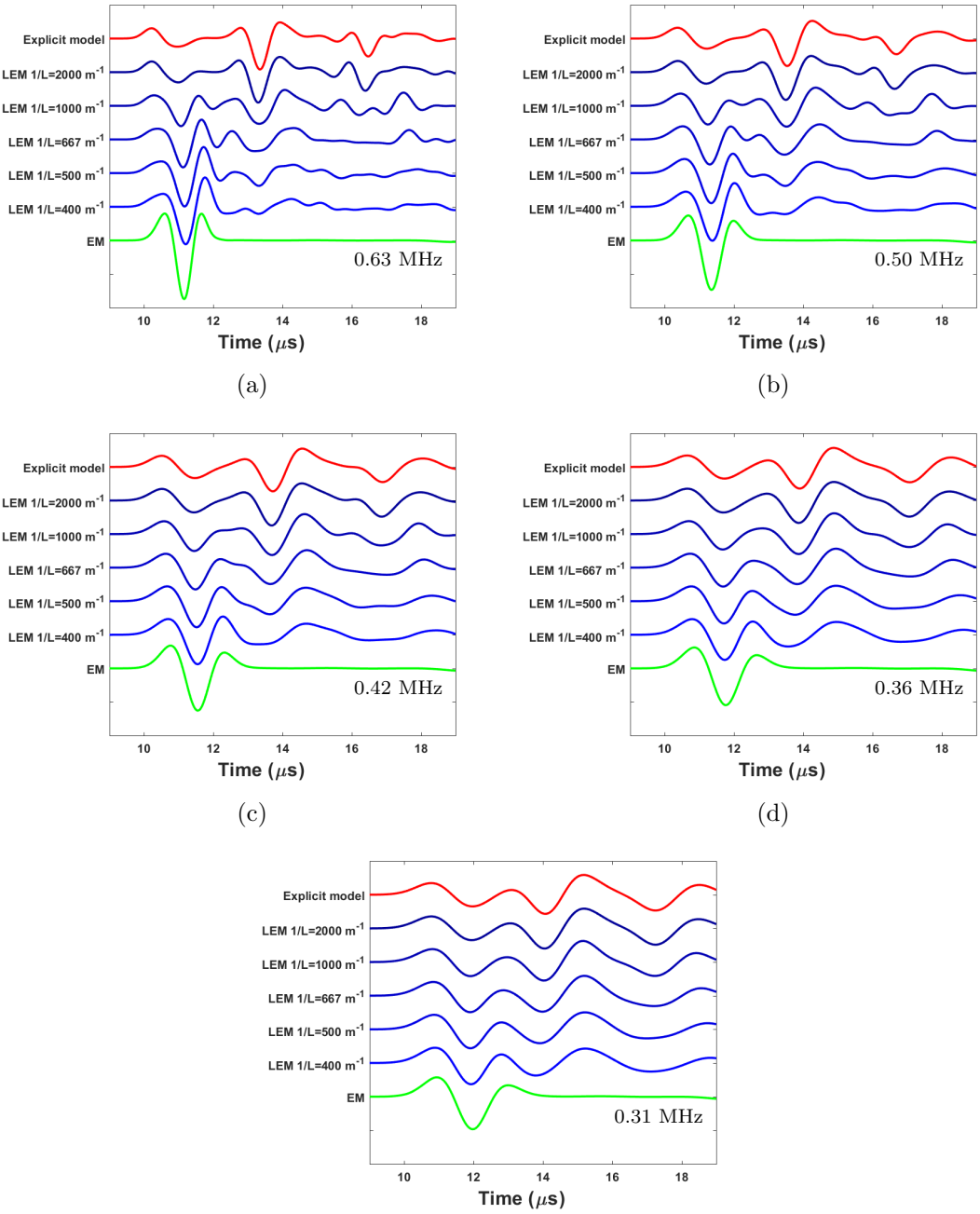

Figure 4.4: Comparison of P-wave propagation parallel to the fractures for the Explicit, EM and the 5 cases of LEM, with K_n=30000 GPa/m and with source frequencies of 4.4a 0.63 MHz , 4.4b 0.5 MHz , 4.4c 0.42 MHz ,4.4d 0.36 MHz and 4.4e 0.31 MHz.

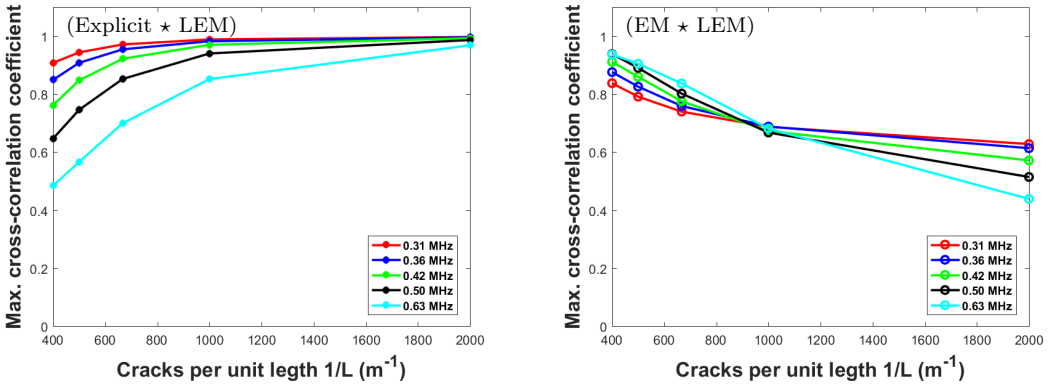

(a) K_n=60000 GPa/m (b)

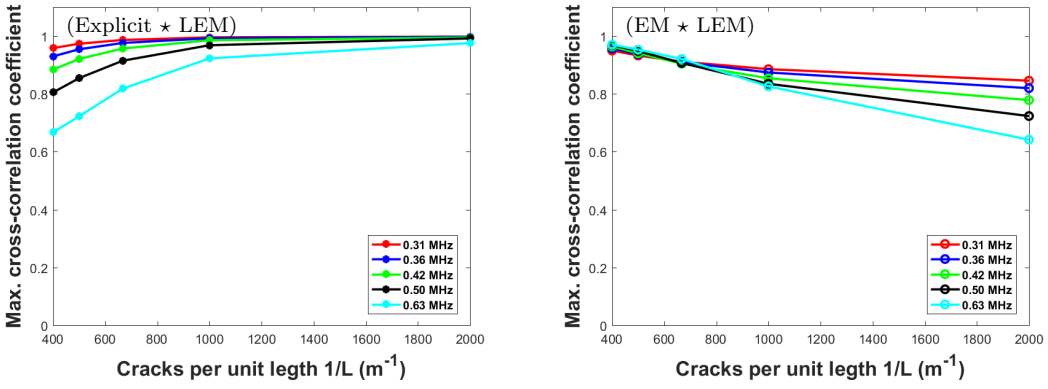

(c) K_n=100000 GPa/m (d)

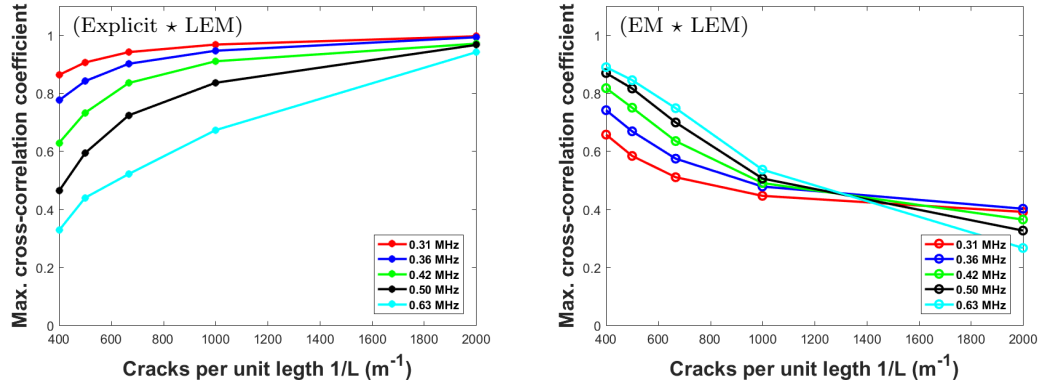

(e) K_n=30000 GPa/m (f)

Figure 4.5: Maximum cross correlation coefficient for wave propagation parallel to fractures between explicit and LEM 4.5a, 4.5c and 4.5e, EM and LEM 4.5b, 4.5d and 4.5f, versus the different LEM cracks per unit length. As for the five different source frequencies, with K_n=60000 GPa/m 4.5a and 4.5b, K_n=100000 GPa/m 4.5c and 4.5d and K_n=100000 GPa/m 4.5e and 4.5f.

Wave propagation perpendicular to the fractures

In this part, the source and receiver are aligned perpendicular to the fractures (Figure 4.1). As expected, similar to the previous Chapter 3, the amplitude is significantly lower for all models compared to wave propagation parallel to the fractures.
In contrast with the previous section, the waveforms from the last four LEM cases are a lot different from the first and the explicit one for K_n=60000 GPa/m. This is due to the lower 1/L values which do not create as strong reflection surfaces as the first model. More energy of the wave passes through the thicker LEM layers resulting in waveforms with up to ten times higher amplitude (Figure 4.6a LEM 1/L=400 m^{-1}). Moreover, the first arrival is different in all of the models with a slowing arrival up to 0.18 μs (Figure 4.6a and 4.6b). The predominant period of the waveforms for the last three models is similar to the EM model and only the first LEM model has the same first arrival and predominant period as the explicit model with correlation coefficient value above 0.9 (Figure 4.9a). The EM model has higher amplitude and later first arrival. When the frequency of the source goes below 0.42 MHz (Figure 4.6c), the LEM model with half the 1/L value (1/L=1000 m^{-1}) and double the thickness of the LEM layers compared to the original case (1/L=2000 m^{-1}) starts to look closer to the explicit model in first arrival and predominant period with correlation 0.87 (Figure 4.9a). The amplitude is lower than in the previous frequencies (Figure 4.6a and 4.6b) but not as low as with the explicit model. As in the previous case with wave propagation parallel to the fractures, the higher the frequency (0.63 MHz) and the lower the 1/L,(1/L=400 m^{-1}) the closer to the EM model, with correlation coefficient close to 0.90 (Figure 4.9b). Finally, for source frequency 0.36 MHz (Figure 4.6d and 4.6e) the first two LEM models matching increase by 8%. The other three cases, even though they have the same predominant period and arrival time closer to the explicit, the amplitude is still higher than the other models.

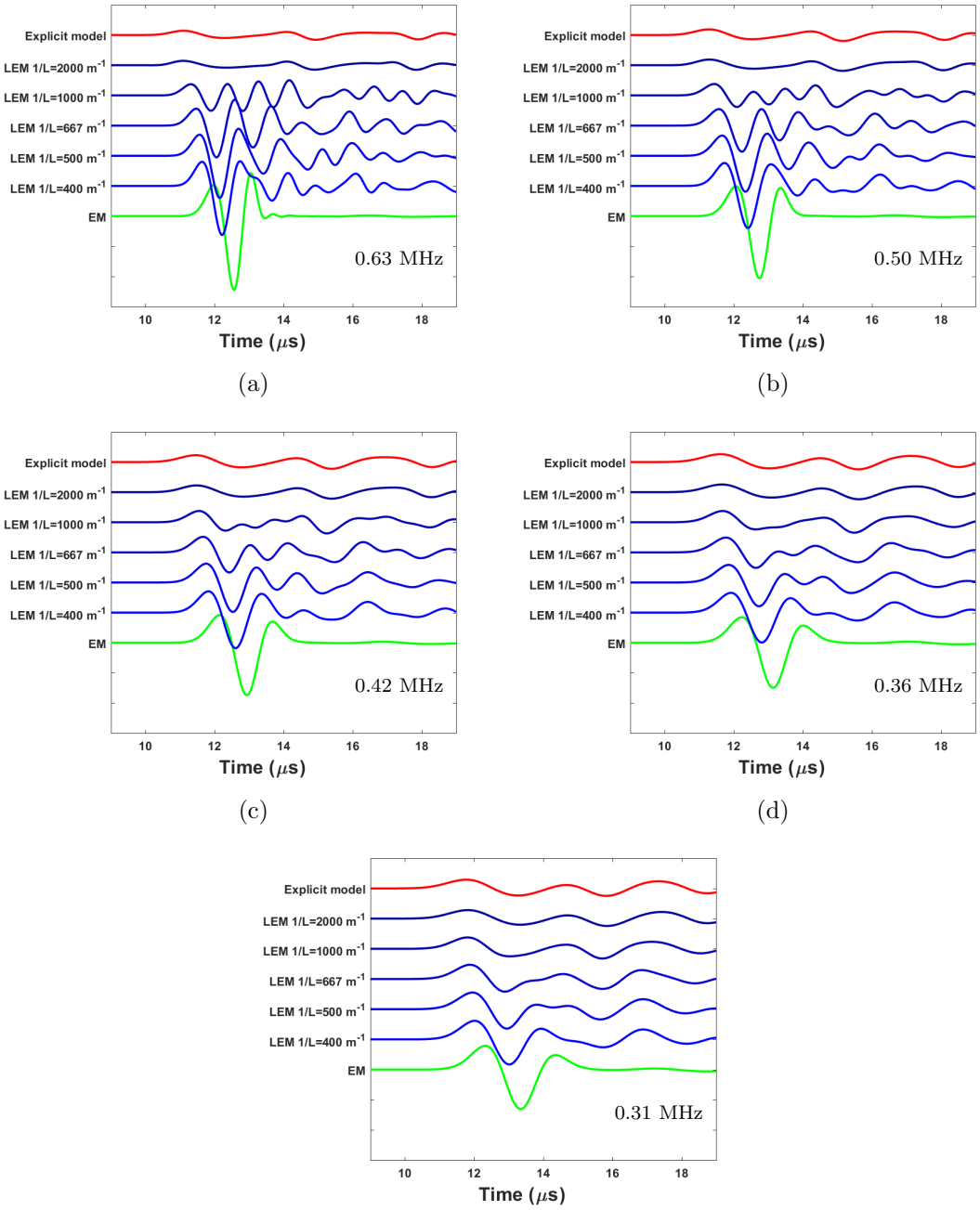

Figure 4.6: Comparison of the P-wave propagation perpendicular to the fractures for the Explicit, EM and the 5 cases of LEM, with K_n=60000 GPa/m and with source frequencies of 4.6a 0.63 MHz , 4.6b 0.5 MHz , 4.6c 0.42 MHz ,4.6d 0.36 MHz and 4.6e 0.31 MHz.

As for wave propagation parallel to the fractures when increasing the normal stiffness to 100000 GPa/m, the amplitude of the recorded waveforms is higher (Figure 4.7). In the higher source frequency model (Figure 4.7a) only the first case of LEM matches the explicit model. The other four cases have high amplitude comparable to the EM model with correlation coefficient between 0.70 to 0.95 (Figure 4.9d), but are different in arrival time as they have earlier arrival compared to it. When the frequency is reduced as in Figure 4.7b, the second LEM model approaches the first and the explicit in amplitude arrival time and predominant period, the correlation coefficient increases by 27% (Figure 4.9c). The third LEM model (1/L=667m^{-1}) tends to match the explicit model for frequency below 0.42 MHz (Figure 4.7c), while for the same frequency the second case fully matches the explicit (with maximum correlation coefficient 0.96 and 0.87 respectively). As the source frequency gets lower (Figure 4.7d and 4.7e) all of the LEM models gets closer to the explicit model in arrival time, predominant period and have a comparable amplitude range. Thus, the higher the normal stiffness and the lower the source frequency, the LEM performs close to the explicit model increasing the correlation by up to 83%, (Figure 4.9c) no matter the thickness and the 1/L value.

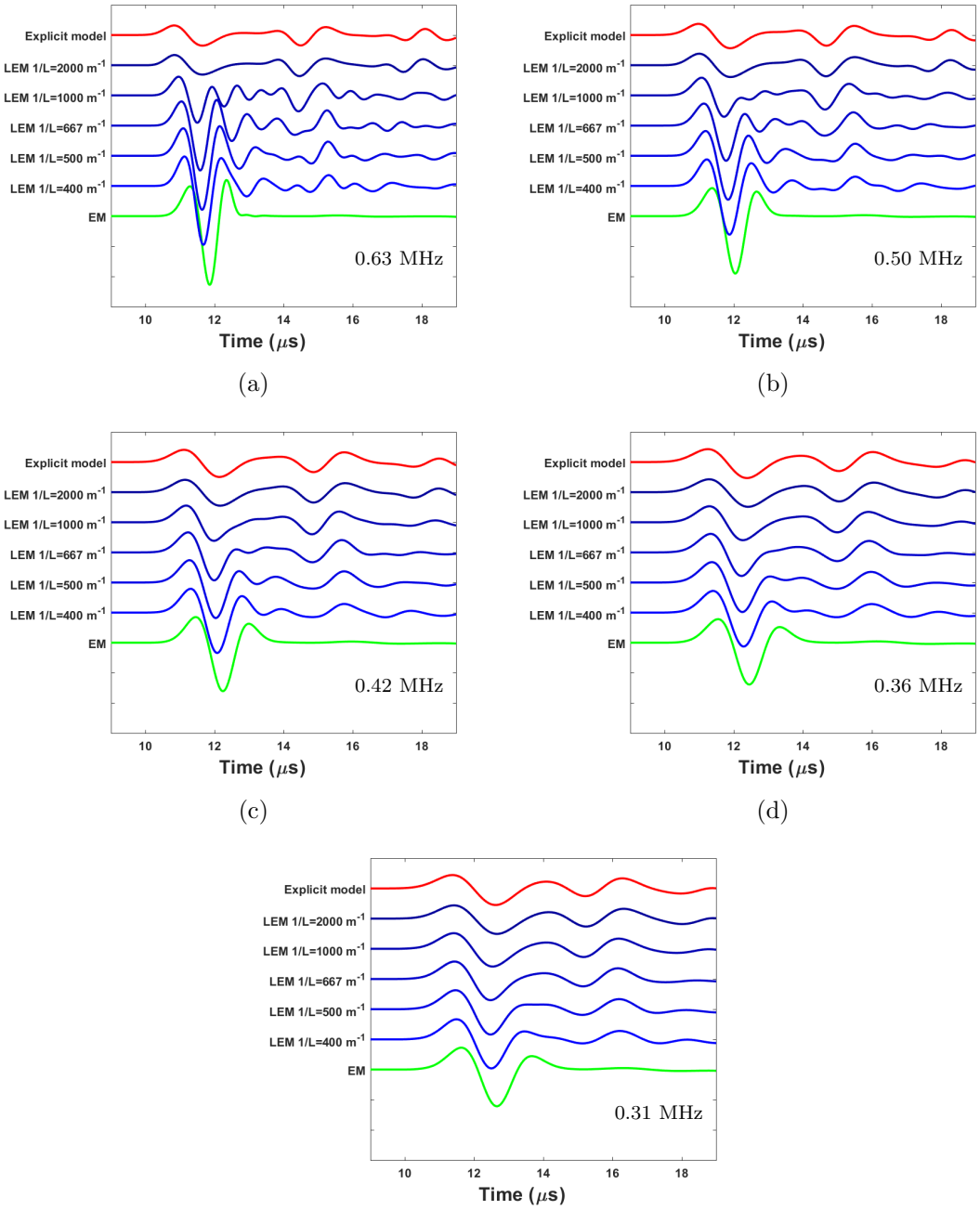

Figure 4.7: Comparison of the P-wave propagation perpendicular to the fractures for the Explicit, EM and the 5 cases of LEM, with K_n=100000 GPa/m and with source frequencies of 4.7a 0.63 MHz , 4.7b 0.5 MHz , 4.7c 0.42 MHz ,4.7d 0.36 MHz and 4.7e 0.31 MHz.

Finally, a lower stiffness of 30000 GPa/m is used as in the previous section for wave propagation parallel to the fractures (Figure 4.8). The amplitude of the explicit model and the first LEM model are very low compared to the other models for source frequency 0.63 MHz (Figure 4.8a). In the previous cases with higher stiffness and high frequencies, the last three models match each other (Figure 4.6a and 4.7a). However, in the case where the stiffness is low, none of them is equal to the other two. The arrival time is delayed compared to the previous scenarios. Dropping the source frequency, the last three models start to have the same predominant period but not the same amplitude (Figure 4.8b and 4.8c). The amplitude of the last two LEM models reach the same level for frequencies below 0.36 MHz (Figure 4.8d and 4.8e). In order for the second LEM model to start to match the first and the explicit with correlation coefficient above 0.8 (Figure 4.9e), the source frequency has to drop below 0.31 MHz (Figure 4.8e). For wave propagation perpendicular to the fractures, it is harder to match the waveforms of the five LEM models. As the 1/L value reduces and the thickness of the LEM layers increases, the LEM becomes a smoother reflector allowing more energy of the wave to pass through for high frequencies creating this mismatch. For the four LEM cases with 1/L between 1000 and 400 m^{-1} the correlation coefficient between explicit and LEM models never reaches a value above 0.90 even for the lower frequency (Figure 4.9e). In contrast the correlation is higher between EM and LEM models especially for the higher frequencies (Figure 4.9f). When the frequency is low, the wavelength is high relative to the fracture spacing, and when the stiffness is high the LEM models start to match.

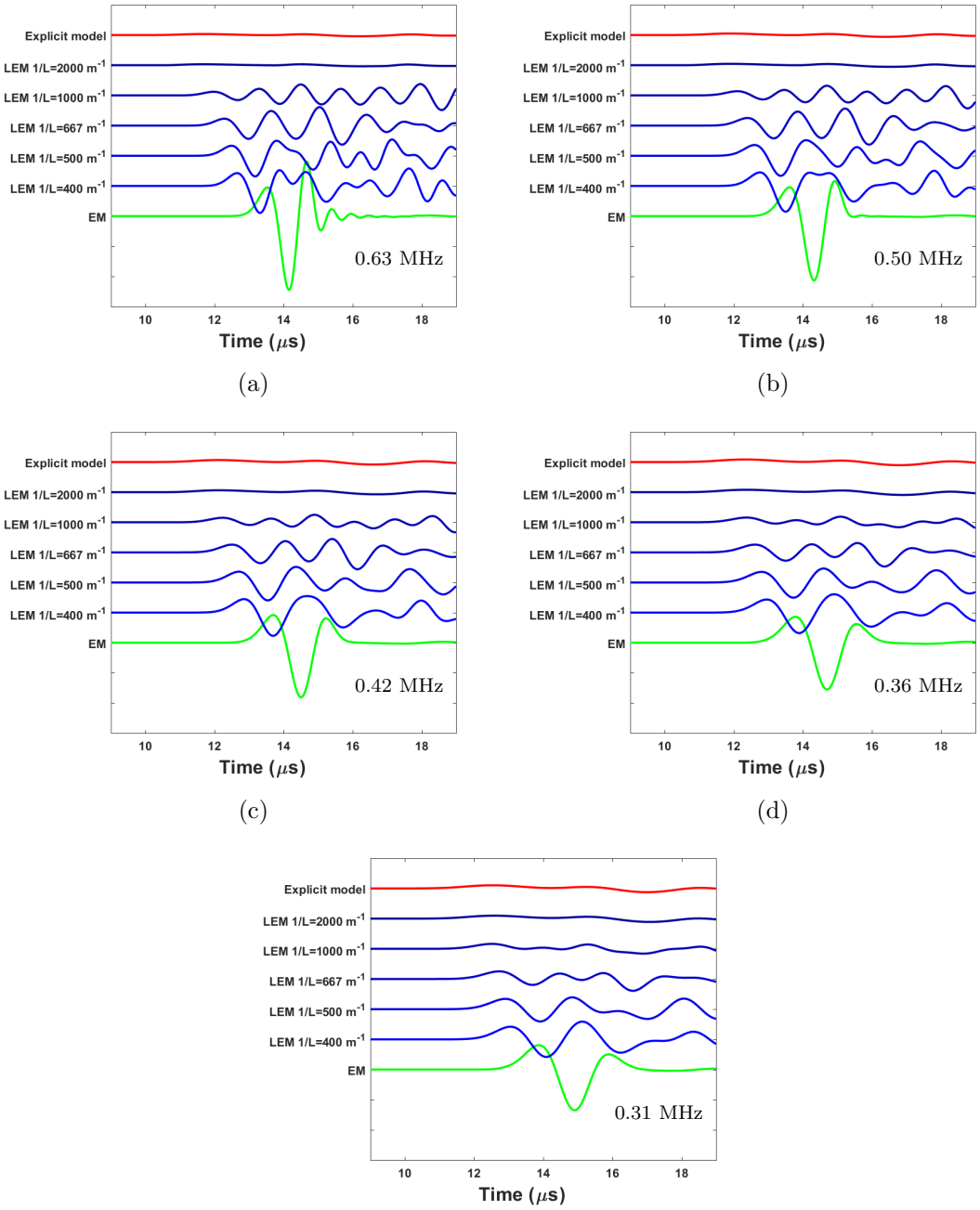

Figure 4.8: Comparison of the P-wave propagation perpendicular to the fractures for the Explicit, EM and the 5 cases of LEM, with K_n=30000 GPa/m and with source frequencies of 4.8a 0.63 MHz , 4.8b 0.5 MHz , 4.8c 0.42 MHz ,4.8d 0.36 MHz and 4.8e 0.31 MHz.

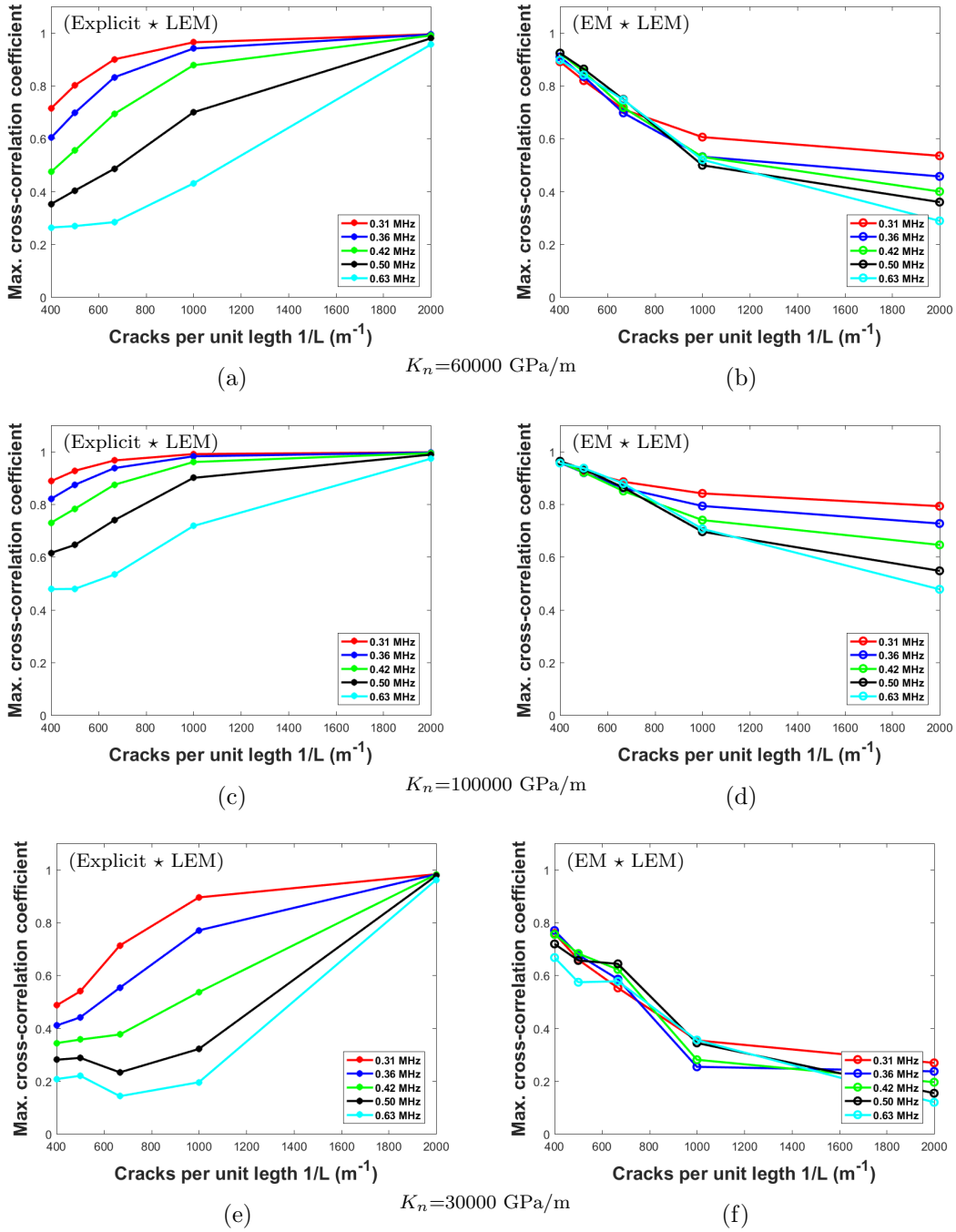

Figure 4.9: Maximum cross correlation coefficient for wave propagation perpendicular to fractures between explicit and LEM 4.9a, 4.9c and 4.9e, EM and LEM 4.9b, 4.9d and 4.9f, versus the different LEM cracks per unit length. As for the five different source frequencies, with K_n=60000 GPa/m 4.9a and 4.9b, K_n=100000 GPa/m 4.9c and 4.9d and K_n=100000 GPa/m 4.9e and 4.9f.

4.2.2 Scaling the models to larger size

From the previous work described above, I concluded that when increasing the thickness of the LEM model and decreasing the 1/L value, the model loses the ability to match with the explicit fracture model for high frequencies, but as the frequency drops the model finally tends to match the explicit model. As explained in section 2.4 the maximum 1/L value depends on the element size when using the thinner LEM option (equation 2.13). Now I examine how the LEM model works when the element size is larger than the previous models by scaling the previous experiment by a factor of ten for three cases. In the first case, the element size is the same as in the previous models 0.5 mm and 1/L=2000 m^{-1} (Figure 4.10a and 4.10b) the second is 5 mm and 1/L=200 m^{-1} (Figure 4.10c and 4.10d) and finally 50 mm and 1/L=20 m^{-1} (Figure 4.10e and 4.10f) (Table 4.4). In this stage, I use only one value for normal stiffness and one source frequency per model which is scaled by a factor of ten and I examine the wave propagation parallel and perpendicular to the fractures. For all three cases, the maximum frequency for the source has been used, as calculated using the method described previously, to avoid dispersion.

	Dx=0.5 mm	**Dx=5 mm**	**Dx=50 mm**
K_n	60000 GPa/m	600 GPa/m	60 GPa/m
Time step	3.68×10^{-8} sec	3.68×10^{-7} sec	3.68×10^{-6} sec
Frequency	630kHz	63kHz	6.3kHz
1/L	2000 m^{-1}	200 m^{-1}	20 m^{-1}

Table 4.4: Scaling the experiment for larger element size to test the performance of the LEM model for larger element size and lower 1/L value.

The first conclusion related to these models concerns wave shape. In all three scaled cases, the wave shape is the same for both parallel (Figure 4.10a, 4.10c and 4.10e) and perpendicular (Figure 4.10b, 4.10d and 4.10f) to the fractures propagation. When comparing the explicit model (red waveform) with the LEM model for the smallest element size 0.5 mm and 1/L=2000 m^{-1}, both parallel (Figure 4.10a) and perpendicular (Figure 4.10b), look identical. As the size increases to 5 mm with 1/L=200 m^{-1} (Figure 4.10c and 4.10d) and 50 mm with 1/L=20 m^{-1} (Figure 4.10c and 4.10d) the LEM models mimic the explicit models. While we expect this result from the laws of scaling,

this leads to the conclusion that it is the alternation of the LEM layer and homogeneous isotropic layers in between that creates an "explicitness" of the LEM model and not the actual value of the 1/L. However, the rule for matching the explicit model with the LEM with a low 1/L value was to use the highest frequency source with the highest possible 1/L value with as thin as possible LEM layers. As shown in a previous section, when the LEM layer is thicker than the element size and lower 1/L values for high frequencies are used, the models perform differently when the frequency goes lower.

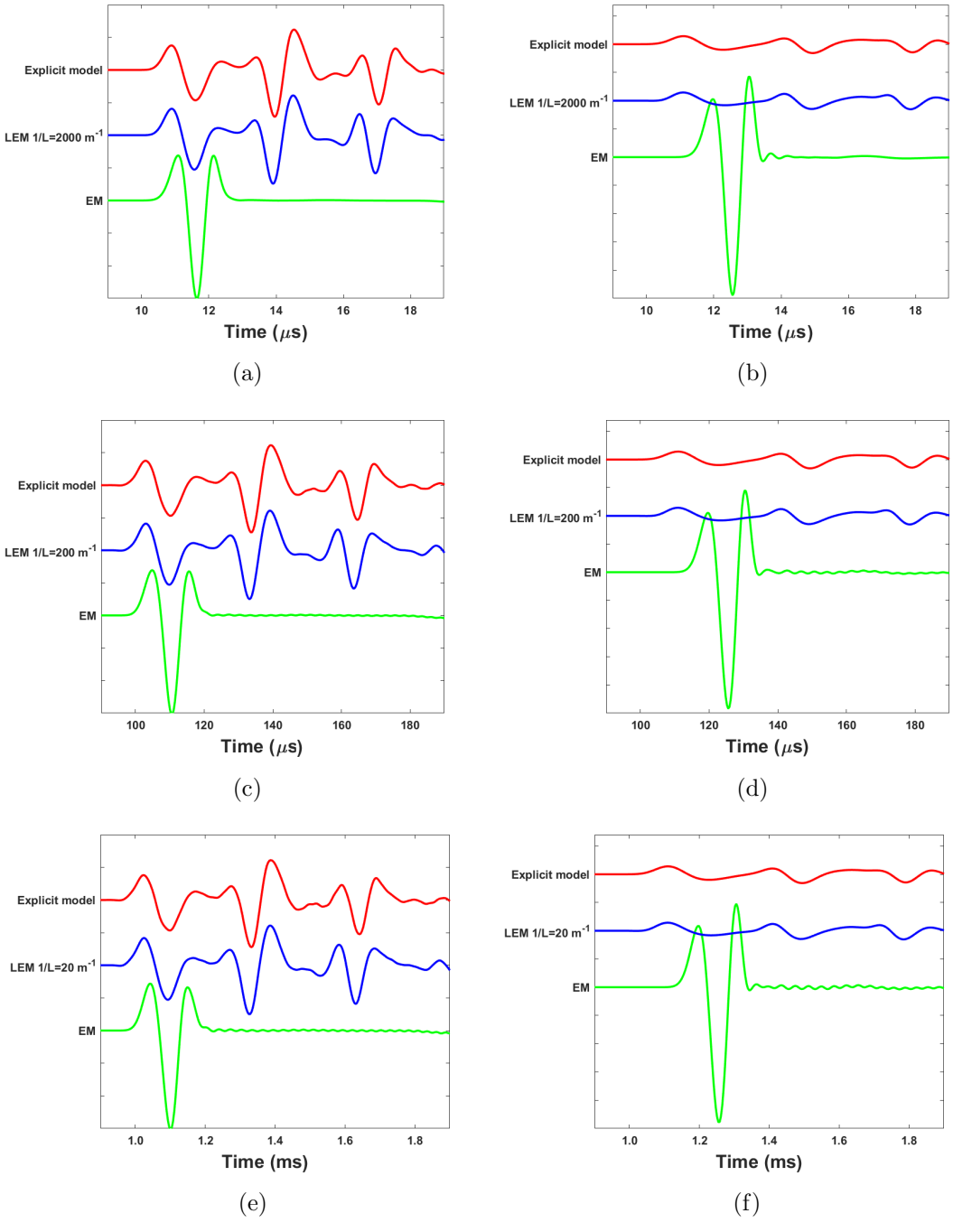

Figure 4.10: Comparison of P-wave propagation parallel and perpendicular to the fractures for the Explicit, EM and the LEM (4.10a and 4.10b) the element size is 0.5mm and 1/L=2000m^{-1}, (4.10c and 4.10d) element size is 5mm and 1/L=200m^{-1} and (4.10e and 4.10f) element size is 50mm and 1/L=20m^{-1} the explicit model consists of 5 fractures

4.2.3 Discussion

In this section I am testing the limits of the LEM model by changing the layer thickness and as a consequence the value of 1/L for various frequencies and fracture stiffiness. Vlastos *et al.* (2007) concluded that for the LEM model the scattering attenuation is frequency dependent. Similarly, the explicit model is frequency dependent too (e.g., Pyrak-Nolte *et al.*, 1990). The two models produce similar results, as shown previously in chapter 3, when the LEM layers are as thick as the element size and 1/L is at its maximum value (see section 2.4). The question then is, how thin the LEM layers has to be in order to produce comparable results to the explicit model and what are the frequency and stiffness limits.

It is clear from the Figures 4.2 to 4.9 that as the frequency goes lower and stiffness higher, the value of 1/L is less important to match the explicit and LEM models. On the other hand as the frequency increases the models with lower 1/L start to behave like the EM model. As the 1/L decreases the thickness of the LEM layers increases and as a result the spacing between the LEM layers is reduced (see Table 4.3). Cai & Zhao (2000) studied the effects of multiple parallel explicit fractures on wave attenuation as a function of spacing and number of fractures and show that the dependence of the transmission coefficient on the number of fractures and the fracture spacing is controlled by $\xi = \frac{\Delta x}{\lambda}$ the ratio of fracture spacing (Δx) to wavelength (λ). The transmission coefficient $|T_1|$ of the P-wave for a single fracture is:

$$|T_1| = \left[\frac{4\left(\frac{k}{z}\right)^2}{4\left(\frac{k}{z}\right)^2 + \omega^2}\right]^{1/2}, \tag{4.1}$$

where k is the normal stiffness, ω is the angular velocity and $z{=}\rho V_P$ is the seismic impedance for given density ρ and P-wave velocity V_P. For N number of fractures the transmission coefficient is $|T_N| = |T_1|^N$ (Cai & Zhao, 2000; Pyrak-Nolte *et al.*, 1990). However this is only a simple approximation and it doesn't consider multiple reflections and waveform conversions which is something expected to have in the explicit and the very thin LEM models. Figure 4.11 summarise $|T_5|$ as a function of ξ for the three stiffness values used in the models and five fracture spacing values (see Table 4.3). Based on the calculation in Figure 4.11 it is expected that the $|T_5|$ will be almost double for higher stiffness value (100000 GPa/m) and close to zero for the lower one (30000 GPa/m). Table 4.5 summarise the upper and lower limit of $|T_5|$ for each of the

stiffness value. From table 4.5 it is concluded that for explicit fractures $|T_5|$ will be the same for the same frequency and different fracture spacing (e.g., for ξ=0.16, Δx=3 mm, λ=19 mm and K_n=60000 GPa/m $|T_5|$=3.15 and for ξ=0.26 Δx=5 mm, λ=19 mm and K_n=60000 GPa/m $|T_5|$=3.15) creating a frequency dependence of fracture spacing and $|T_5|$. However, the LEM models with 1/L other than the maximum (2000 m^{-1}) do not behave like that. Based on the models presented above, when the LEM layer starts to become thicker the model starts losing its frequency dependence for high frequencies, behaving closer to the EM model which is frequency independent. One rule which needs further testing might be that the LEM is frequency dependent as long as the wavelength of the source is 19 times higher than the LEM layer thickness for wave propagation perpendicular to the fractures. For example the LEM with 1/L=2000 and 1000 m^{-1} (thickness is 0.5 and 1 mm respectively) reaches maximum correlation (0.89 to 0.99) with the explicit model when the source frequency is lower than 0.625 MHz (λ=9.64 mm) for the first and 0.312 MHz (λ=19.30 mm) for the second for all the different values of stiffness (Figure 4.9). Lower frequencies with 19 times higher wavelength from the other LEM models need to be tested to confirm the above statement. Finally, transmission coefficient $|T_N|$ of the LEM need to be tested as a function of layer spacing and layer thickness, in order to test if there is any relationship similar to the one for the explicit model.

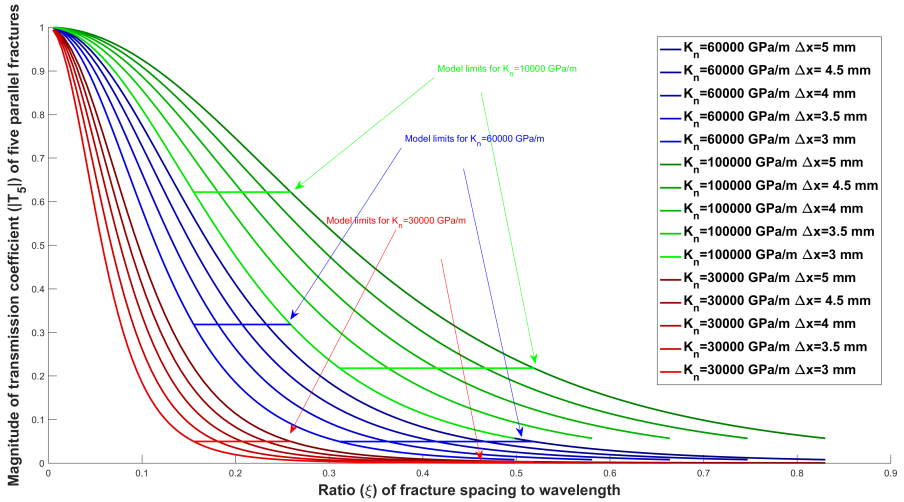

Figure 4.11: Magnitude of transmission coefficient for 5 fractures $|T_5|$ as a function of ξ for different values of normal stiffness K_n and fracture spacing Δx.

	$\xi = 0.16$	$\xi = 0.26$	$\xi = 0.33$	$\xi = 0.56$
$\|T_5\|$ **for** $\mathbf{K_n}$**=60000 GPa/m**	0.315	0.315	0.049	0.049
$\|T_5\|$ **for** $\mathbf{K_n}$**=100000 GPa/m**	0.622	0.622	0.218	0.218
$\|T_5\|$ **for** $\mathbf{K_n}$**=30000 GPa/m**	0.050	0.050	0.003	0.003

Table 4.5: $|T_5|$ values for the upper and lower xi limit for each stiffness value.

4.3 3DEC distinct element method theory

While WAVE3D is very efficient and accurate, it can only work with orthogonal geometries. For modelling complex fracture geometries I use a DEM code 3DEC which is widely used to solve problems in industries such as civil engineering, mining, hydraulic fracturing and nuclear waste disposal (Itasca Consulting Group, 2019).

In this section I use 3DEC to simulate wave propagation in a medium with different Discrete Fracture Networks (DFN) and compare the waveforms with those from a solid sample with the same rock properties and with parallel fractures with the same fracture density.

3DEC is a three-dimensional distinct element code using polyhedral solid blocks to model engineering problems. The blocks can be inflexible or fully deformable (Damjanac & Cundall, 2016). The assembly of blocks fit tightly approximating a fractured rock mass with the contacts between the blocks representing rock joints and fractures. The contacts can deform elastically or inelastically, resulting in opening or slip, governed by fracture stiffness and a Coulomb slip law (Damjanac & Cundall, 2016). 3DEC can also create a DFN template (Itasca Consulting Group, 2019) which is a group of planar, curved polygons or disks, where each element is termed a fracture and holds a list of fracture properties. The code then creates a mesh based on the DFN template. Using the disks from the template a number of cuts are made though the block to create the fracture set. Each cut must extend from the boundary or a fracture to another boundary or a fracture. The result is that the large block consists of a number of smaller pieces which then the tetrahedral elements are fitted into those pieces during the meshing process. Only parts of these contacts correspond to fracture positions. The parts which are "non-fractures" are given a very high contact stiffness of 5000 GPa/m to simulate solid material. This value of stiffness has been tested, for the same model size and source frequency, and the waveform is identical to the solid model, as a result that value of stiffness is sealing the "non-fractures" part of the DFN. Appropriate values of fracture stiffness, based on the size of the fractures (Worthington & Lubbe, 2007), are set for the contacts that do form parts of real fractures, as shown in the Table below.

The fracture density for the DFN is defined as the area of fracture per unit volume (Itasca Consulting Group, 2019):

$$D = \frac{1}{V}\sum(\pi \times r^2), \tag{4.2}$$

where D is fracture density, V is the volume and r is the radius of the disk (fracture). The fracture density described above is a geometrical approach of the fracture density used by the DFN tool and it is important to note that this is different from the quantity of crack density which describes equivalent material behaviour through energy considerations (Budiansky & Oconnell, 1976; Schubnel & Gueguen, 2003; Schubnel *et al.*, 2003; Shuai *et al.*, 2018) which is defined in Chapter 2.

4.3.1 Wave propagation in explicitly represented fractures

As mentioned previously granite is a low permeability igneous rock which is considered a good option as a host rock for a nuclear waste disposal facility. For that reason the mechanical properties from Bohus granite rock on the Swedish west coast (Saadati *et al.*, 2014) have been used for the models (Table 4.6) in this project. The material properties presented below (Table 4.6) are from static measurements.

Property	**Value**
Young's modulus	52 GPa
Density	2630 kg/m^3
Poisson's ratio	0.15
P-wave velocity	4569 m/s
S-wave velocity	2931 m/s

Table 4.6: Mechanical properties of Bohus granite rock (Saadati *et al.*, 2014) from static measurements. Wave velocities have been calculated from the measured elastic parameters.

I first model waveforms for a solid block of granite without the presence of discontinuities to create a reference for the behaviour of the medium. The size of the block is 1 m^3 with 1 m length each side. The size of the tetrahedral elements is 0.05 m. To avoid numerical dispersion in the recorded velocities the minimum wavelength (λmin) should be ten times larger than the size of the elements (equation 2.3). Taking λmin=0.5 m and using the P-wave velocity gives a maximum frequency of around 9 kHz. I therefore choose the predominant frequency of our P-wave Ricker wavelet source to be 4 kHz.

	Normal stiffness K_n (GPa/m)	**Shear stiffness K_s (GPa/m)**
Case 1	1000	300
Case 2	100	30
Case 3	60	18

Table 4.7: Values of normal and shear fracture stiffness used in the DFN models and the model with parallel fractures, the value of normal and shear stiffness used for the intact part of the DFN is K_n=40000 GPa and K_s=20000 GPa.

The same model size and source is used for all models.
I next calibrate behaviour with the case of parallel fractures, with the block cut into six equal size pieces to create five parallel fractures with equal spacing between the fractures (0.16 m) (Figure 4.12 a and b). The source and receiver are aligned perpendicular to the fractures on the bottom and top of the block respectively. For the DFN model I used a template with the same fracture density (D=5 m^{-1}) and with fracture size varying from 0.2 m to 2 m (Figure 4.12 c and d).

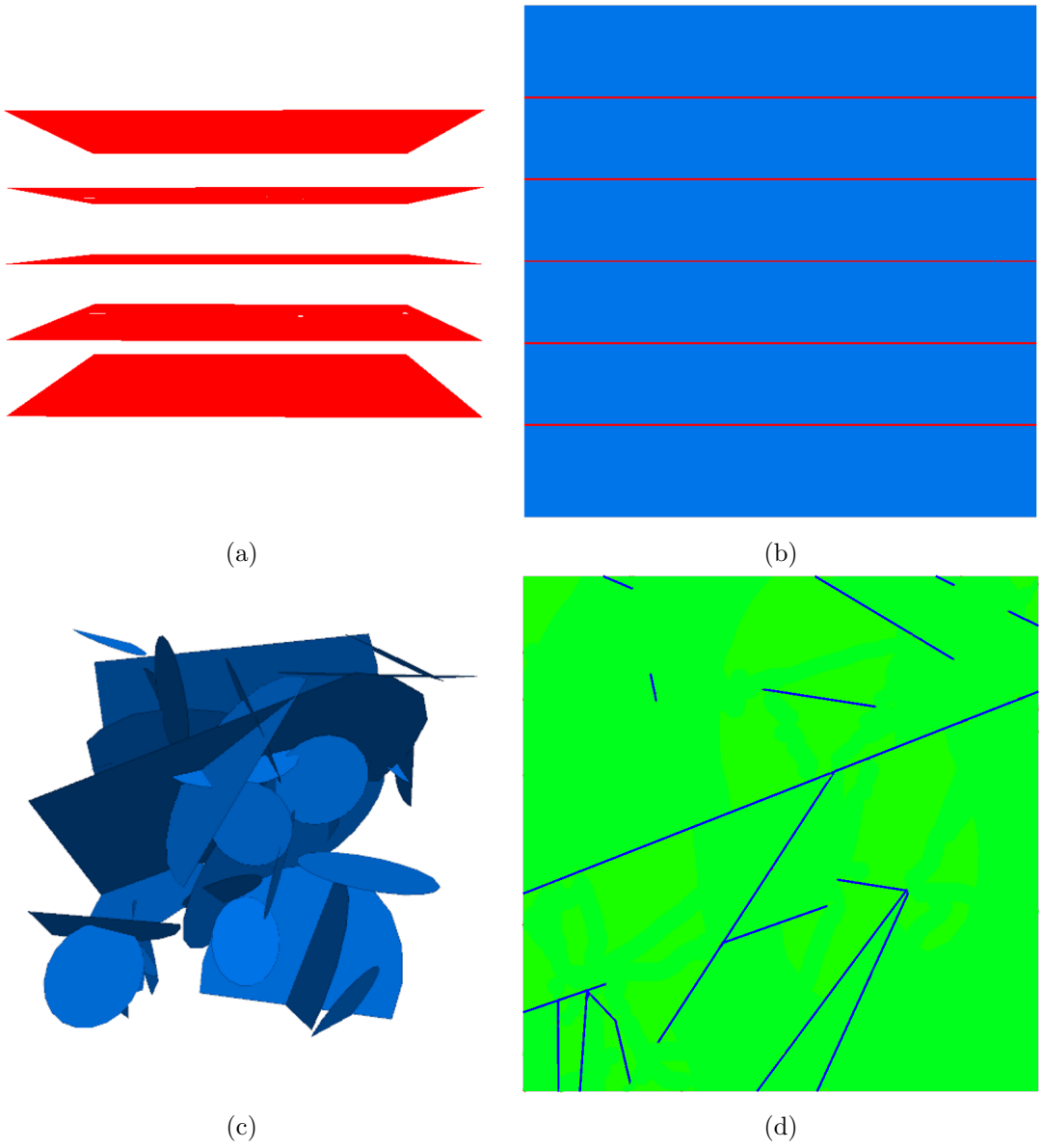

(a) (b)

(c) (d)

Figure 4.12: Model Geometry 4.12a 3D view of the block with parallel fractures 4.12b 2D cross section of the same block. 4.12c 3D view of the DFN model used in comparison with parallel fractures 4.12d 2D cross section of the DFN through the centre of the model (Z-X plane).

Fracture stiffness typically scales with fracture size (Worthington & Lubbe, 2007). Three cases of fracture stiffness were chosen based on our sizes of fractures as shown in Table 4.7. In the first case the fracture stiffness is in the lower limit 60 GPa/m, the

next is the maximum 1000 GPa/m and the third value is 100 GPa/m (Worthington & Lubbe, 2007).

As expected the waveforms for all cases of fracture stiffness show velocity and amplitude changes compared to those from the solid block (Figure 4.13).

For the stiffest fractures (K_n=1000 GPa/m) waveforms have similar first arrivals and little attenuation or even amplification compared to the solid model (Figure 4.13a). The amplitudes in the DFN are similar to the solid case but amplitudes are 36% higher for the case with the parallel fractures. From the Fourier amplitude spectra (Figure 4.13b), I can see that for DFN, and to a lesser extent the parallel fractures, there are higher amplitudes for frequencies between 6 and 8 kHz (Parastatidis *et al.*, 2018).

On the other hand, considering the lowest value of fracture stiffness (K_n=60 GPa/m), the amplitude for parallel fractures is almost halved while the amplitudes from the DFN are less attenuated and 30% larger than those of the parallel fractures (Figure 4.13e). High frequencies have been suppressed, and the frequency range has shifted to lower frequencies by 13% for the DFN case and 37% for the case with the parallel fractures (Figure 4.12). The arrival time is delayed by 32% for the DFN and 72% for the parallel fractures (Figure 4.13f).

The intermediate case of fracture stiffness (K_n=100 GPa/m) also exhibits arrival delay and attenuation but to a lesser degree than the low stiffness case (Figure 4.13c and 4.13d). More specifically, amplitudes for the DFN are similar to the solid sample while the case with parallel fractures is 20% lower. Frequencies are shifted to lower frequencies by 21% (Figure 4.13c and 4.13d).

Comparing the DFN with parallel fractures we can clearly conclude that the waveforms for the DFN are attenuated and delayed less even though the fracture density is the same in the two cases. This is due to the fact that in the DFN medium the fractures have various angles and do not reflect most of the energy on the opposite direction of the propagation (Parastatidis *et al.*, 2018).

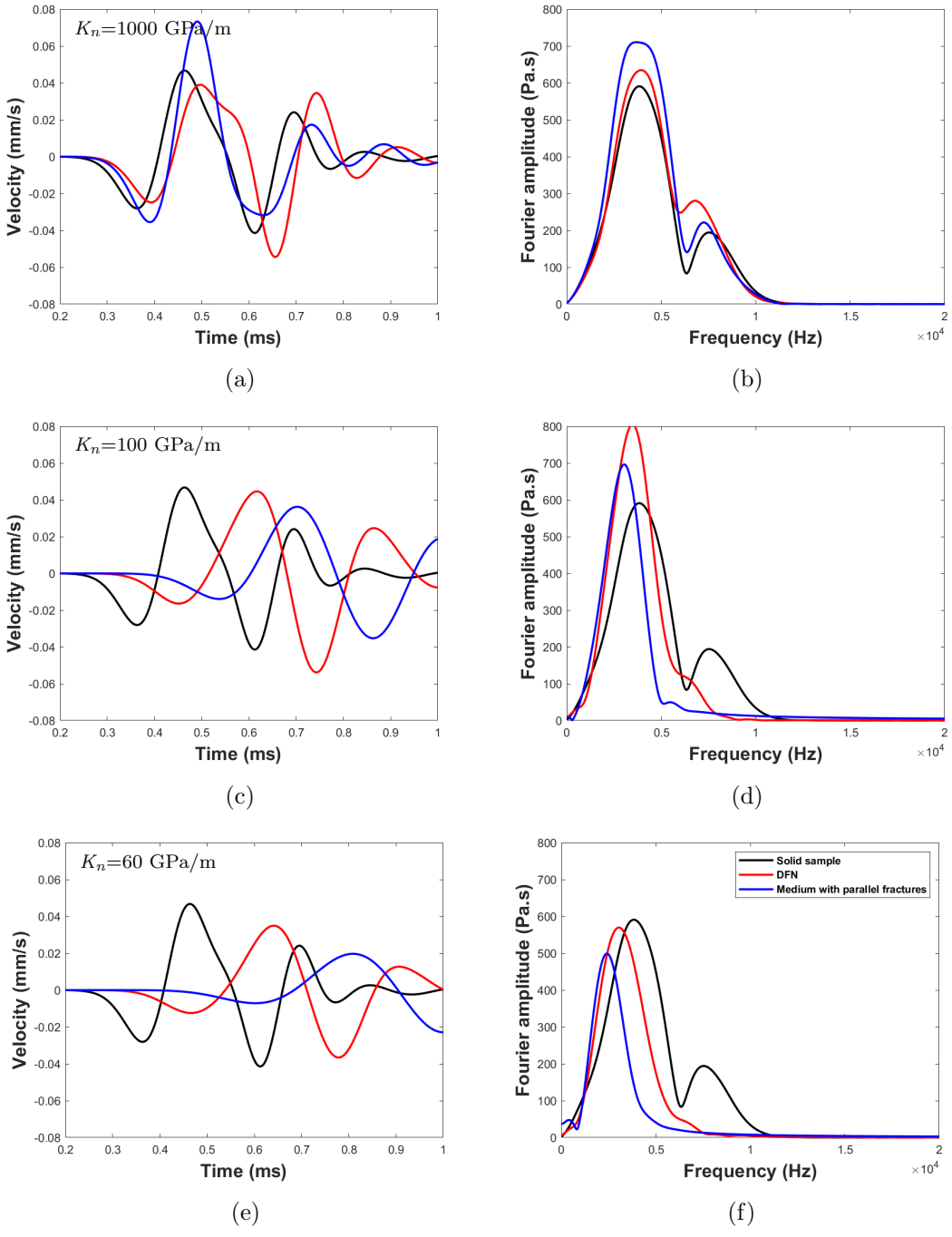

Figure 4.13: Comparison of waveforms for the solid model (black), parallel fracture model (blue) and the DFN model (red) for 4.13a K_n=1000 GPa/m and Fourier amplitude spectra for waveforms 4.13b, 4.13c and 4.13d K_n=100 GPa/m, 4.13e and 4.13f K_n=60 GPa/m.

Comparing DFN with different fracture densities

I now create different DFN, to study the effect of fracture size and fracture density on the waveforms. The first DFN case is the one which has already been shown in the previous section with fracture size from 0.2 m to 2 m and fracture density D=5 m^{-1} (Figure 4.12). The second case has a lower density (D=3 m^{-1}) and same range for size while the third DFN has the lowest density (D=1 m^{-1}) and fracture sizes from 0.2 m to 0.5 m.

As mentioned previously for low normal stiffness (60 GPa/m) the waveforms in case 1 is delayed, the amplitude attenuated, and the high frequencies suppressed relative to solid sample (Figure 4.14e and 4.14f). For case 2 where the range of fracture sizes are the same as case 1 but the density is smaller (D=3 m^{-1}), I can see a small delay and about 15% attenuation in amplitude (Figure 4.14e). In terms of frequencies it has a 20% wider range. For the case 3 where the fractures are smaller than the wavelength and the density is smaller (D=1 m^{-1}), there is no attenuation or delay in the arrival and the shape of the waveform looks almost identical to the waveform from the solid case (Figure 4.14).

Increasing the normal stiffness to 100 GPa/m reveals that all the three cases match well in the frequency spectrum (Figure 4.14d). Case 1 has greater attenuation. Cases 2 and 3 appear not to be affected by the increased fracture stiffness (Figure 4.14c).

Finally, with the highest fracture stiffness 1000 GPa/m the waveform for DFN 2 approaches that of DFN 3 and looks almost identical to the solid case waveform (Figure 4.13 and 4.14). DFN 3 has a smaller delay and the amplitude and frequency range is identical to the other two cases and the solid case (Figure 4.13 and 4.14). The more the fracture stiffness increases, and the fracture size goes smaller than the wavelength, the more it is approaching the non-fractures solid case.

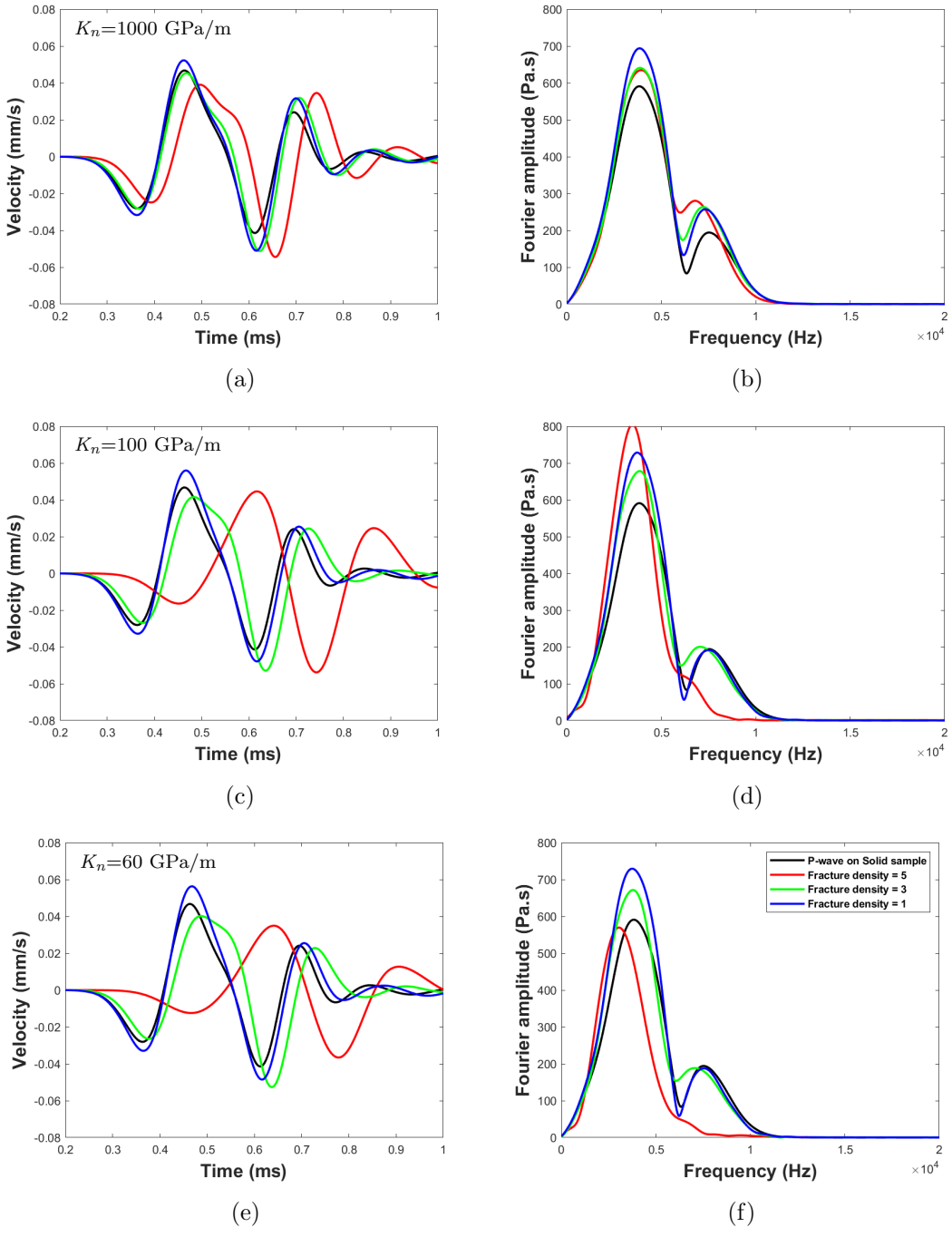

Figure 4.14: Comparison of the P-wave velocities of the waveforms for DFN models with different fracture densities and sizes for 4.13a K_n=1000 GPa/m and Fourier amplitude spectra for waveforms 4.14b, 4.14c and 4.14d K_n=100 GPa/m, 4.14e and 4.14f K_n=60 GPa/m.

Wave propagation with stress dependent fracture stiffness for DFN models

Using a constant fracture stiffness for all the fractures and throughout the whole length of the fracture does not represent reality, as due to the presence of stress in the rock mass causes the fracture stiffness to vary. Bandis *et al.* (1983) has proposed a formula, linking the normal stress (or closure) of the fracture with the normal stiffness (K_n). Further details on the theory and the equations used to apply stress dependent stiffness is provided in section 3.6.2 and equations 3.5 and 3.8, including definition of the parameters *a, b* and *c*.

These equations were implemented in a numerical modelling code WAVE3D to match waveforms with the waveforms from a laboratory experiment using steel plates to simulate fractures (Hildyard, 2001). In extension to previous work the same method has been successfully used in Chapter 3 and implemented in the EM and LEM approach. The code considers an initial value for Kn and Ks and starts to apply stress to the block. As the normal stress changes it calculates new values for Kn and Ks. The new values of Kn and Ks affect the stress state in the block, it recalculates Kn and Ks with the newest stress values, and this iteration proceeds, creating a coupled case between stress and stiffness until an equilibrium is reached.

The same process has been applied to 3DEC as a FISH function (Appendix A.2) in order to test the DFN case for stress dependent stiffness. The DFN template with a fracture density D=5 (Figure 4.14c) was used to create three models with different b values (case 1 $a = 2 \times 10^{-11}$ m/Pa, $b = 2 \times 10^{-7}$ Pa^{-1}, $c = 0.3$, case 2 $a = 2 \times 10^{-11}$ m/Pa, $b = 7 \times 10^{-7}$ Pa^{-1}, $c = 0.3$, case 3 $a = 2 \times 10^{-11}$ m/Pa, $b = 2 \times 10^{-6}$ Pa^{-1}, $c = 0.3$) as shown in Table 4.8 and there were compared with the compare the three cases with uniform stiffness shown previously (Figure 4.14).

	α (Pa/m)	b (Pa^{-1})	c
Case 1	2×10^{-13}	2×10^{-7}	0.3
Case 2	2×10^{-13}	7×10^{-7}	0.3
Case 3	2×10^{-13}	2×10^{-6}	0.3

Table 4.8: Stress dependent parameters for the relationship of fracture normal and shear fracture stiffness to normal stress given by equation 3.5 and 3.8 for the three cases.

In all the three models a triaxial compression force of 2160 kN over a surface of 0.4 $m \times 0.4$ m has been applied (stress of 13.5 MPa).
For the lowest value of $b = 2 \times 10^{-7}$ Pa^{-1} the waveform has a delayed first arrival by 36% compared to the highest b value and 9% with the intermediate case (Figure 4.15) and frequencies are shifted to lower frequencies by 16% (Figure 4.16b). In comparison with the uniform stiffness models, the waveform is in between the two cases of K_n=60 GPa/m and K_n=100 GPa/m. This can be explained better by considering the range of normal stiffness I expect to have with different values of stress as shown in Figure 4.15. More specifically the first arrival is similar with the two cases (Figure 4.16c), the frequency range is the same as the lowest uniform stiffness case and in the amplitude spectra it is approaching the intermediate value of K_n=100 GPa/m (Figure 4.16d).

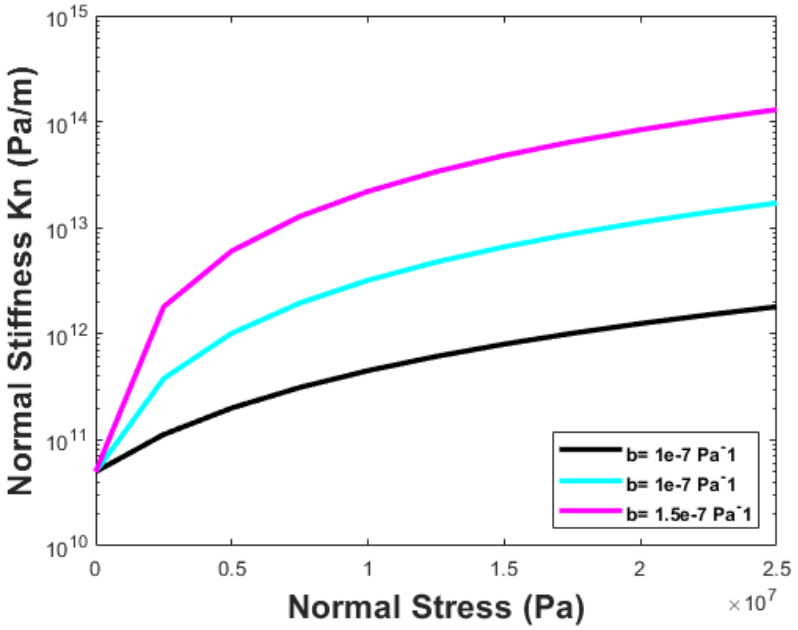

Figure 4.15: The response of stress dependence fracture stiffness (equation 3.5) on different values of stress for the three models with different b values.

The highest b value is expected to have the highest stiffness and as a result lower attenuation and earlier first arrival. For the two cases with higher b values the first arrival is 24% delayed for the intermediate case of $b = 7 \times 10^{-7}$ Pa^{-1} (Figure 4.16a). The

frequency range is almost the same, and in the amplitude spectra the highest b is 30% lower for the frequencies between 200 Hz and 600 Hz, and 142% higher for frequencies up to 1 kHz compared to the intermediate case (Figure 4.16b).
In comparison with the uniform stiffness models, waveforms from the highest b value and highest stiffness model (black and green 4.16c) are approaching one another very well in terms of wave shape, first arrival and frequencies (Figure 4.16c and 4.16d). The intermediate case for the stress dependent stiffness has an earlier first arrival by 6% compared to the case of uniform fracture stiffness K_n=100 GPa/m and 10% delayed with the case of highest uniform stiffness (Figure 4.16c). In the frequency domain the case of K_n=100 GPa/m and $b = 7 \times 10^{-7}$ Pa^{-1}have the same range of frequencies, but in the amplitude spectra the uniform stiffness model has 9% higher amplitudes.

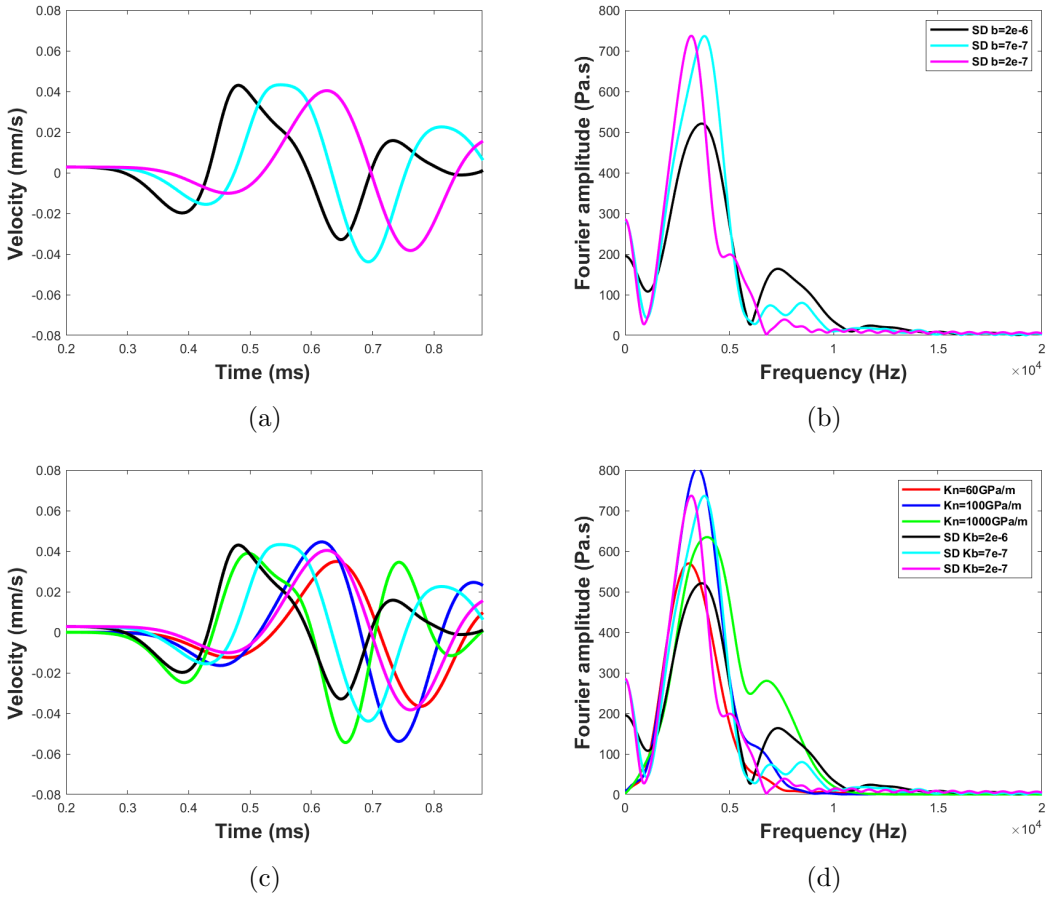

(a) (b)

(c) (d)

Figure 4.16: Comparison of the P-wave recordings and frequency domain for the (4.16a and 4.16b) stress dependente models and (4.16c and 4.16d) stress dependent models vs uniform stress models.

4.4 Simulating the DFN for effective medium (EM) and localised effective medium (LEM) representations

So far, I have examined the performance of the LEM model against the explicit and the EM ones in media with parallel fractures for various thickness of the LEM layers, at different frequencies, normal stiffness and element size, for wave propagation parallel and perpendicular to the fractures. Also I have examined the wave propagation in a medium with randomly orientated fractures (DFN) for the explicit model for uniform and stress dependent fracture stiffness. In this section, the performance of the LEM and the EM models is examined in a medium with more than one fracture orientation. For this part, 3DEC code is used (Itasca Consulting Group, 2019) to create the DFNs and model wave propagation. In the previous section, a fully randomly orientated DFN was used. However, in this section, in order to avoid the huge complexity on the EM and LEM models, the fractures are a combination of three sets of DFNs, each set has a given dipping and azimuth angle, creating three sets of fractures with a range of fracture sizes.

The motivation for this work comes from the need to create more efficient and at the same time accurate models. In 3DEC, where the elements are tetrahedral, the meshing is based on the geometry of the DFN. This can lead to flat, very thin elements with acute angles when the DFN is very complex and dense. These thin elements along with the value of fracture stiffness need a very small time step, increasing the run time of the model significantly. Because neither the EM nor the LEM have physical fracture surfaces to create this thin elements are able to run in larger time steps.

For the LEM model, the implementation of the DFN effect was relatively simple. Using the same output from the explicit DFN template I create zones around the DFN disks. These zones then call the stiffness matrix (Chapter 2) to create an LEM layer around the DFN disks with the same angles for dip direction (azimuth) and dip, the rest of the material is homogeneous isotropic.

The implementation of the DFN effect in the effective medium was more complex. Based on Schoenberg & Sayers (1995) approach for multiple fracture systems, at first I calculate the stiffness matrix C for each fracture system as described previously (Chapter 2). Then I invert the stiffness matrix C to get the compliance matrix S as:

$$S_i = C_i^{-1}, \tag{4.3}$$

and rotate the matrices for each fracture set to the global coordinate system Sg using the angles for azimuth and dip:

$$S_{gi} = R_i C_i^{-1} R_i^{-1}, \tag{4.4}$$

i=1, 2, 3 for the three DFNs.

Finally, the sum of the three compliance matrices is obtained and the compliance tensor S_{iso} of the un-fractured background material is added and the material properties coming from the final matrix applied to the whole block as an orthotropic material:

$$S = S_{iso} + \sum_{i=1}^{3} S_{gi}. \tag{4.5}$$

Two DFN templates are created with three different sets for each. The fracture orientation for the two DFNs is the same (Table 4.9, Figure 4.17), however on the second DFN the set-l fractures are larger, and the density is different for the three sets. Finally, in terms of normal fracture stiffness, all of the models have the same values of K_n for all the three sets of fractures.

DFN 1						
	Dip	**Azimuth**	**size**	**Number**	**Density ϵ**	**Density D m^{-1}**
Set 1	60°	85°	0.25-1 m	17	0.26	1.38
Set 2	20°	35°	0.25-1 m	20	0.16	0.99
Set 3	40°	170°	0.25-1 m	21	0.27	1.43
DFN 2						
Set 1	60°	85°	1-2 m	9	0.29	1.21
Set 2	20°	35°	1-2 m	10	0.19	1.05
Set 3	40°	170°	1-2 m	10	0.64	1.60

Table 4.9: Geometrical properties of the fracture sets for each DFN case.

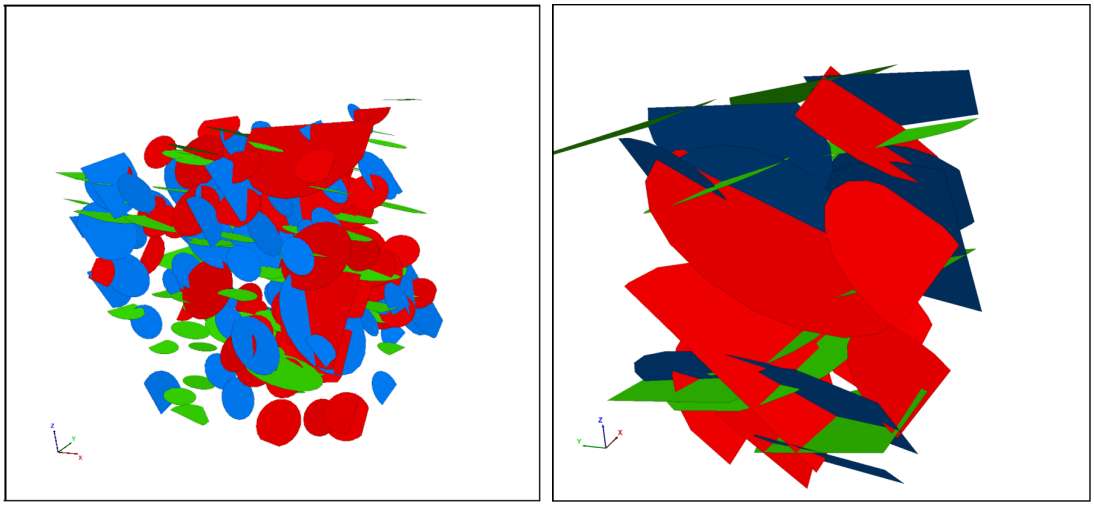

(a) (b)

Figure 4.17: a) DFN Type 1 uses the same ratio on all the three sets b) DFN Type 2 uses larger fractures.

In order to make the models efficient in terms of computational time, the element size used is 0.04 m and the block size is 1 m × 1 m × 1 m. The source is a ricker wavelet at frequency 7.5 kHz, the material properties are the same as the experiment with the steel plates (Table 3.1 Chapter 3).

The first DFN (case 1) has a large population of medium and small fractures relative to the size of the block (Table 4.9). The same normal stiffness is applied to all three sets of fractures for case 1, starting with K_n=200 GPa/m (Figure 4.18a and 4.18b). The LEM and the explicit model have the same arrival time with explicit model to have almost half the amplitude of the LEM for the first cycle. The predominant period is similar for all three models (Figure 4.18a). The EM model has almost five times higher amplitude than the LEM and explicit and is 2.5 ms delayed (Figure 4.18a).

The next set of models use K_n=100 GPa/m. As the stiffness goes lower, the amplitude for explicit and LEM models are getting closer the first arrival matching again for these two models, but again EM has higher amplitude and is delayed (Figure 4.18c). The explicit and LEM models are almost the same for frequencies up to about 6 kHz, for higher frequencies the explicit model has higher amplitude drop (Figure 4.18d).

The third set of models for case 1 DFN is considered a lower value for normal stiffness, K_n=50 GPa/m. As in the previous models, the arrival of the explicit and LEM model

match, but not the EM same as in the previous cases. However, as the stiffenss drops the amplitude of the EM model is more comparable with the other two models. The explicit and the LEM models are similar for up to 7.5 kHz (Figure 4.18f). Overall, the explicit and the LEM models are performing similarly as the stiffness goes lower they match better.

For the next case of DFN (Table 4.9), larger fractures are used for all the three sets, with sizes ranging from 1-2 m and using the same values for normal stiffness. For K_n=200 GPa/m the amplitude of the EM is the same as in the previous case, the amplitude of the explicit is reduced compared to the LEM model similar to the previous case (Figure 4.19a). The arrival time for the last two models is the same and the explicit model is phase shifted compared to the LEM (Figure 4.19a). The explicit and LEM model match well for frequencies up to 9 kHz, as shown in the frequency spectrum, (Figure 4.19b).

When the stiffness is reduced by half to (K_n=100 GPa/m) the waveform of the LEM and explicit model is attenuated, and the amplitude drops up to ten times the previous model (Figure 4.19c). The EM model has a slightly lower amplitude too but only by 20% compared to the previous case. The LEM and explicit model are not as closely matched as before in terms of amplitude (Figure 4.19c) however the two models still match in the arrival time. As the normal stiffness is reduced, the explicit model has a smaller frequency range, as it allows only the energy of low frequencies to pass through and the higher frequencies are suppressed (Figure 4.19d).

Finally, for lower fracture stiffness (K_n=50 GPa/m), the amplitude of the explicit model is five times lower than the LEM. For the EM model the amplitude is less than half to the previous case (Figure 4.19e). The arrival matches again but the first pick for explicit model is three times lower the LEM. In Figure 4.19f the Fourier analysis of the LEM has higher energy compared to the explicit model which is significantly suppressed.

When the fractures of the DFN are small as in case 1, the LEM and the explicit match better. When the fractures are large, as in case 2, the two models get a closer response only for high values of fracture stiffenss. However, due to the various angles of the fractures, the higher frequencies in the explicit model are attenuated which does not occur in the LEM model. More specifically, when the wave propagates parallel or perpendicular to the fractures the response in time and frequency domain of LEM and explicit model is similar. When the fractures are at an angle other than orthogonal, the

numerical implementation of the models do match but under specific conditions such as fracture size and fracture stiffness.

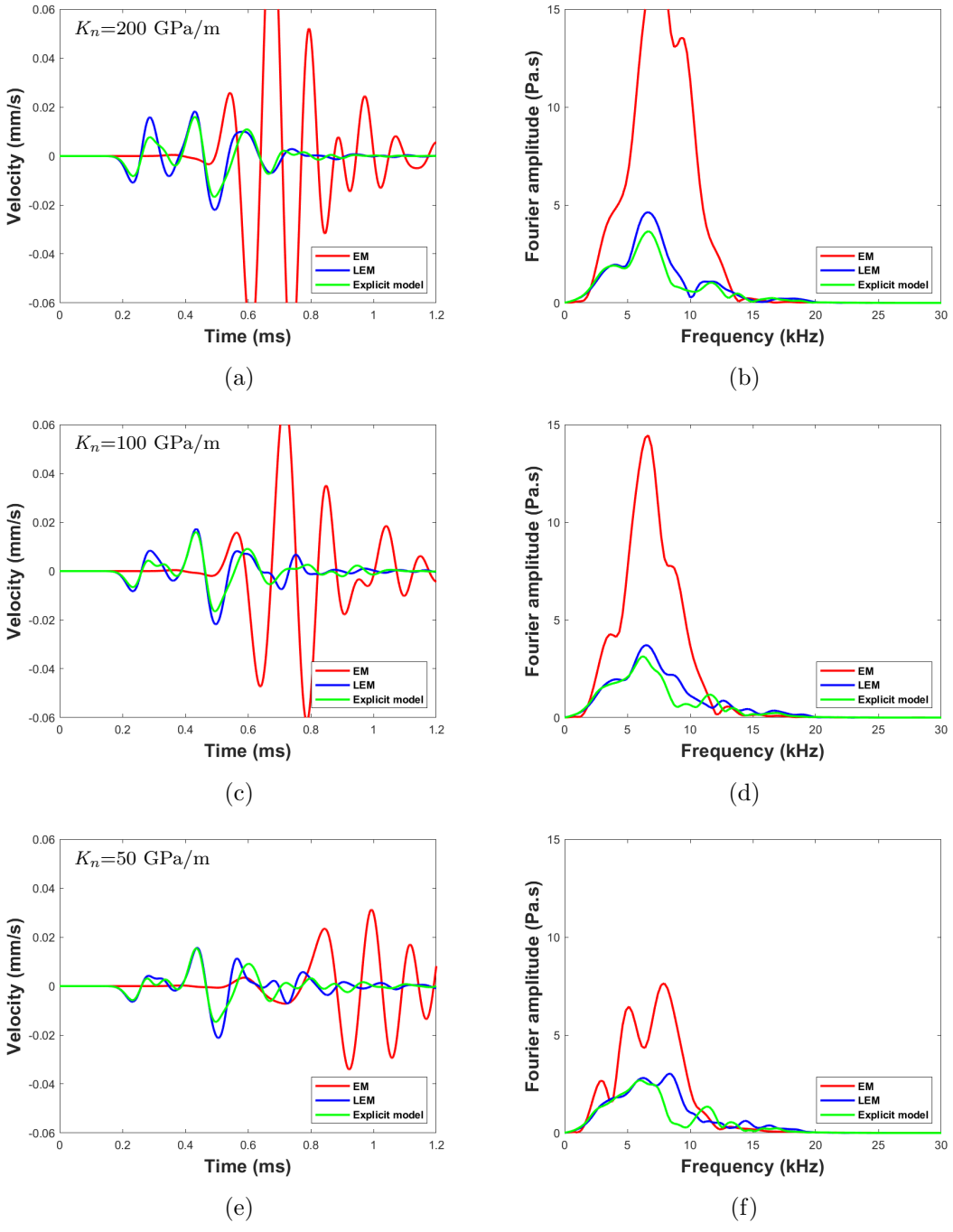

Figure 4.18: Comparison of the P-wave recordings for DFN case 1 represented explicitly, as LEM, and EM, for K_n=200 GPa/m (4.18a and 4.18b), K_n=100 GPa/m (4.18c and 4.18d) and K_n=50 GPa/m (4.18e and 4.18f).

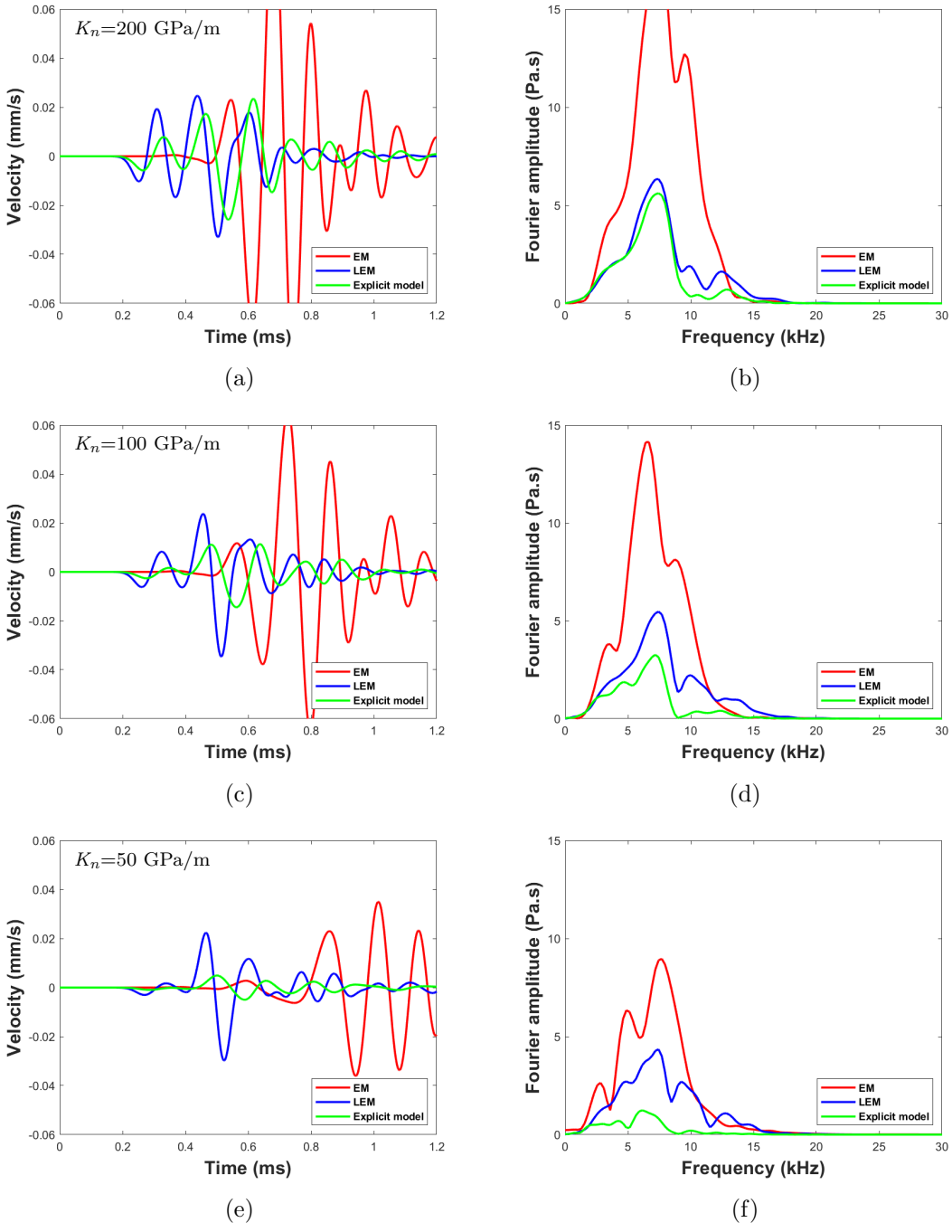

Figure 4.19: Comparison of the P-wave recordings for DFN case 2 expressed explicitly, as LEM and EM for K_n=200 GPa/m (4.19a and 4.19b), K_n=100 GPa/m (4.19c and 4.19d) and K_n=50 GPa/m (4.19e and 4.19f).

4.4.1 Discussion

As shown in Chapter 3 with parallel fractures, considering stiffness as uniform and testing different values creates a linear result, in contrast with the stress dependent stiffness which is non-linear. Similarly, when applying the stress dependent stiffness for the complex DFN fractures the same conclusion is reached. Even though the stress dependent model can be more accurate on representing natural fractures, similar to WAVE3D the stress dependent model is less efficient, in terms of computational time, than the uniform stiffness models.

Complex fracture networks was also tested for the LEM and EM approach. The LEM is based on creating zones of LEM around the he DFN discs while the EM used the Schoenberg & Sayers (1995) approach to calculate the stiffness matrix. As in Chapter 3 the EM approach is not expected to match the other two models, not even for the first DFN where the total crack density (ϵ=0.69) is close to the values Schubnel & Gueguen (2003) and Schubnel *et al.* (2003) have proposed. In contrast the ratio of wavelength to fracture diameter (λ/d) is on average 2 for DFN 1 and 0.6 for DFN 2 (4.9) which is very low compared to the threshold limit (14) Shuai *et al.* (2018) suggests. On the other hand, the LEM model produces comparable waveforms for the first DFN where the $\frac{\lambda}{d}$ is higher and the ϵ is lower. However more models need to be run to validate the balance among fracture size, fracture stiffness and source frequency that LEM and explicit fracture model perform the same for complex fracture networks.

In terms of computational efficiency of the models in 3DEC for the explicit DFN models the time-step is a function of stiffness between the contacts of the fracture surfaces, the higher the stiffness the lower the time step. The LEM and EM models where there are no such contacts the time step is much higher. For example, the DFN 1 with stiffness of 60 GPa, due to the small time step the explicit model runs for 325000 cycles with total run time of about 18000 s while the LEM and EM models runs for a higher time step for 6500 cycles with total run-time 360 s. This makes the LEM and EM model 50 times faster than the explicit model in 3DEC.

4.5 Angled fracture conversion tetrahedral versus staggered grid

WAVE3D is a very efficient numerical modelling code in terms of computational time and accuracy for orthogonal fractures, as previous work has shown. However, one of the major limitations of WAVE3D is the fact that due to the staggered grid the explicit fractures can be either horizontal or vertical. In nature though, the fractures usually appear at various angles, as a result, it becomes complicated when there is a need of modelling a less controlled, natural problem, like the one I will present in Chapter 5.
In this section, I evaluate the performance of WAVE3D for angled fractures. In this part, I use 3DEC (Itasca Consulting Group, 2019) which has been used in previous sections to examine the wave propagation in media with complex fracture network using a DFN tool. The tetrahedral element of 3DEC allows it to create fractures at various angles. At first, I create a solid block of 1 m $\times$ 1 m $\times$ 1 m with 1 cm element size for both WAVE3D and 3DEC using visco-elastic boundaries in both, applying a plane 20 kHz wave source and recording velocity histories in various positions 0.2 m, 0.5 m, 0.8 m and 0.9 m away from the source to validate that both WAVE3D and 3DEC perform the same for the same problem. The frequency of the source follows the dispersion rule explained in Chapter 2 with element size $dx = 0.01$ m. The material properties of the medium from static measurements, are presented in Table 4.10, and due to the P-wave velocity and the frequency of the source, the wavelength is λ=0.25 m. In Figure 4.20 I present the result of the solid rock for 3DEC versus WAVE3D for a 2^{nd} order accurate wave solution (Hildyard, 2001). For comparison I also include the 4^{th} accurate WAVE3D solution. Both cases perform similarly for the solid case with the cross-correlation coefficient to be 0.99. Use that value as a reference of the maximum can be reached to evaluate the performance of both codes in cases with a single fracture with dipping angles $80°, 70°, 60°, 45°, 30°, 20°, 10°$ and $0°$.
These fracture models use the same 20 kHz plane P-wave source and the velocity histories are recorded 0.9 m from the source. The centre of the fracture in all cases is the centre of the bock and the source and receiver align with the centre and create an angle with the fracture which is equal to the fracture dip angle $\theta°$.
In this section, I apply two different approaches to design a dipping fracture in the WAVE3D staggered grid code. The first approach is to simply 'pixelised' the dipping

fracture with smaller horizontal and vertical fractures following the exact same shape as shown in Figure 4.21. The second approach is based on the fracture density as described in 2, with the creation of random horizontal and vertical fractures with total fracture density as the single fracture. This approach could be considered as an equivalent discrete fractures medium (EDFM).

Property	Value
Young's modulus	55 GPa
Density	2740 kg/m^3
Poisson's ratio	0.29
P-wave velocity	5129 m/sec
S-wave velocity	2788 m/sec

Table 4.10: Mechanical properties base on static measurements of gneiss rock in Olkiluoto Finland, wave velocities have been calculated from the measured elastic parameters (Hakala, 2018; Suikkanen, 2019)

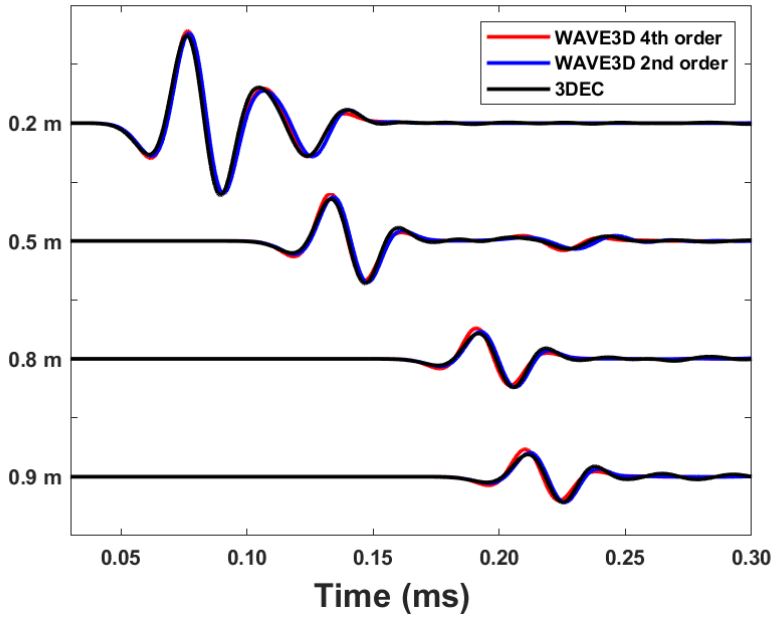

Figure 4.20: Waveforms for solid block in 3DEC and WAVE3D 4th and 2nd order wave solution, in 0.2 m, 0.5 m, 0.8 m and 0.9 m away from the source.

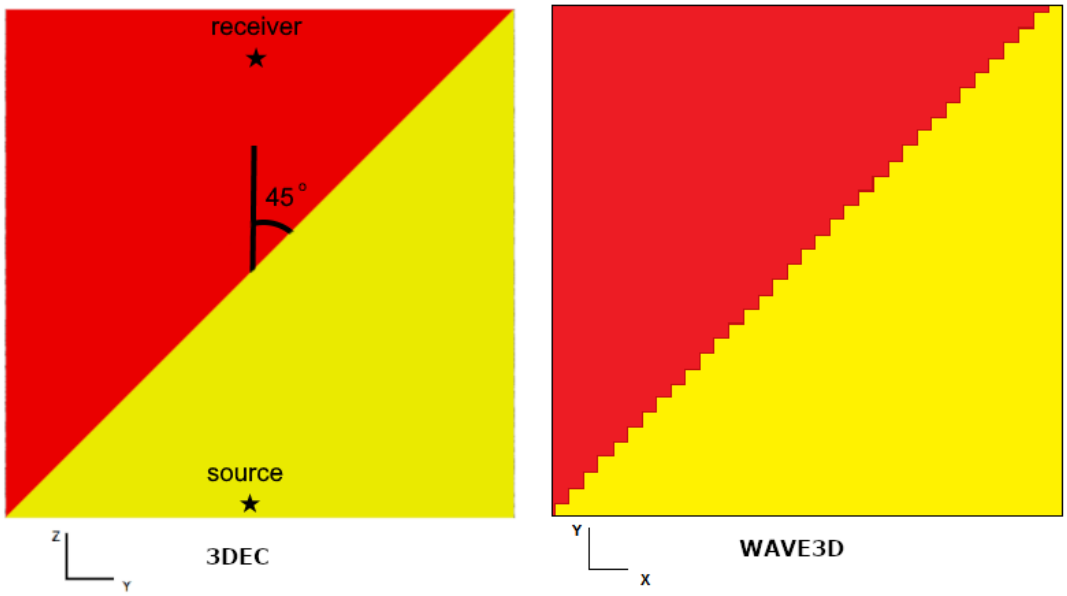

Figure 4.21: A single fracture with 45° degrees dipping in 3DEC (left) versus the 'pixelised' case in WAVE3D (right).

4.5.1 Pixelised dipping fractures

The first limitation in pixelising the fracture is the intersection points between vertical and horizontal fractures. WAVE3D currently allows limited interaction of fractures for open fractures only. Interaction of stiffness fracture is currently not supported. In order to avoid this problem, at the intersection point the vertical fracture is designed one element shorter, leaving a small gap. As a result of this limitation, the total surface of the pixelised fracture will be slightly smaller than a true dipping fracture.

The size of the horizontal and vertical fractures also need to be considered. From the above mentioned limitation, it is clear that the smaller the vertical and horizontal fractures the more fine the pixelised fracture it gets. At the same time, the intersecting points are more and this leads to larger gaps and possibly lower attenuation than the expected. From the models and the comparisons with the 3DEC waveforms, it can be concluded that when the dip is high the size of the horizontal fractures have to be smaller than the vertical and vice versa. The ratio between horizontal and vertical fractures for various angles is presented below in Table 4.11 and Figures 4.22 and 4.23. Fracture stiffness is another factor which needs to be adjusted compared to the 3DEC

fracture stiffness. Since the fracture surface in WAVE3D pixelised fracture is slightly smaller due to the gap in the intersections, the value of stiffness needs to be reduced to reach the same amplitude as in a single surface dipping fracture. The reduction in stiffness with dipping angle is summarised in Table 4.11 and Figures 4.22 and 4.23. After experimenting with various values for stiffness of the vertical fractures, it can be concluded that it has to be equal to ten times smaller than the stiffness used in the dipping fracture in order to have the same arrival, frequency and amplitude.
The smaller horizontal fractures lead to almost double the amplitude than the expected and a larger reduction of stiffness to unrealistic values would need to be used. Thus, a balance between horizontal fracture length and stiffness adjustments are needed in order to have the optimal result. Below, the waveforms of 3DEC dipping fractures versus the WAVE3D (Figures 4.22 and 4.23) for various dipping angles are presented.

Dip angle	**Max. coefficient**	**Time μs**	**Horizontal fracture size (m)**	**Horizontal fracture K_n factor**
10°	0.85	0.8	2.5×10^{-2}	1.15
20°	0.89	0.4	5×10^{-2}	0.85
30°	0.90	1.2	6.5×10^{-2}	0.70
45°	0.90	1.2	7.5×10^{-2}	0.65
60°	0.95	1.2	1×10^{-2}	0.70
70°	0.95	0.8	1.4×10^{-2}	0.80
80°	0.98	-0.4	1.65×10^{-2}	0.85

Table 4.11: Maximum cross-correlation coefficient between 3DEC and WAAVE3D waveforms and the time need to add on the second waveform to reach maximum correlation, and the adjustments needed for fracture size and stiffness K_n for the horizontal fractures for the pixelised fractures.

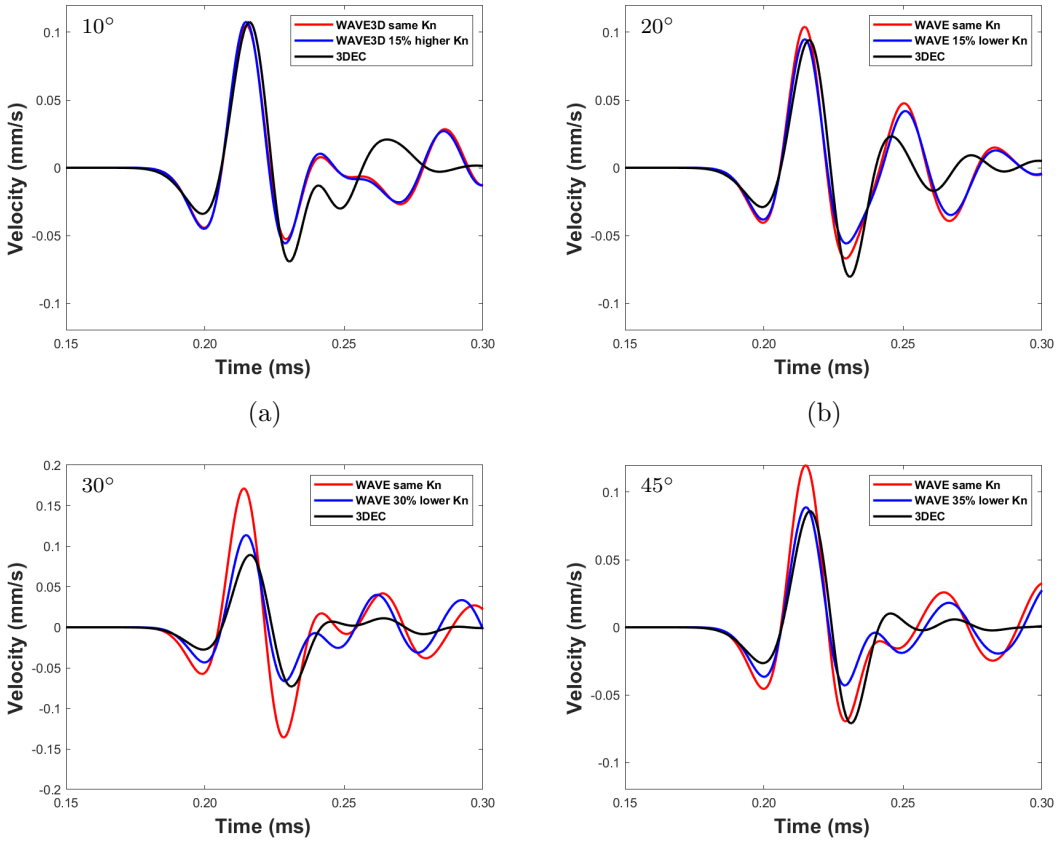

Figure 4.22: Comparison of the P-wave velocities of the waveforms for a single dipping fracture at various angles (4.22a 10°, 4.22b 20°, 4.22c 30° and 4.22d 45°) in 3DEC and "pixelised" in WAVE3D

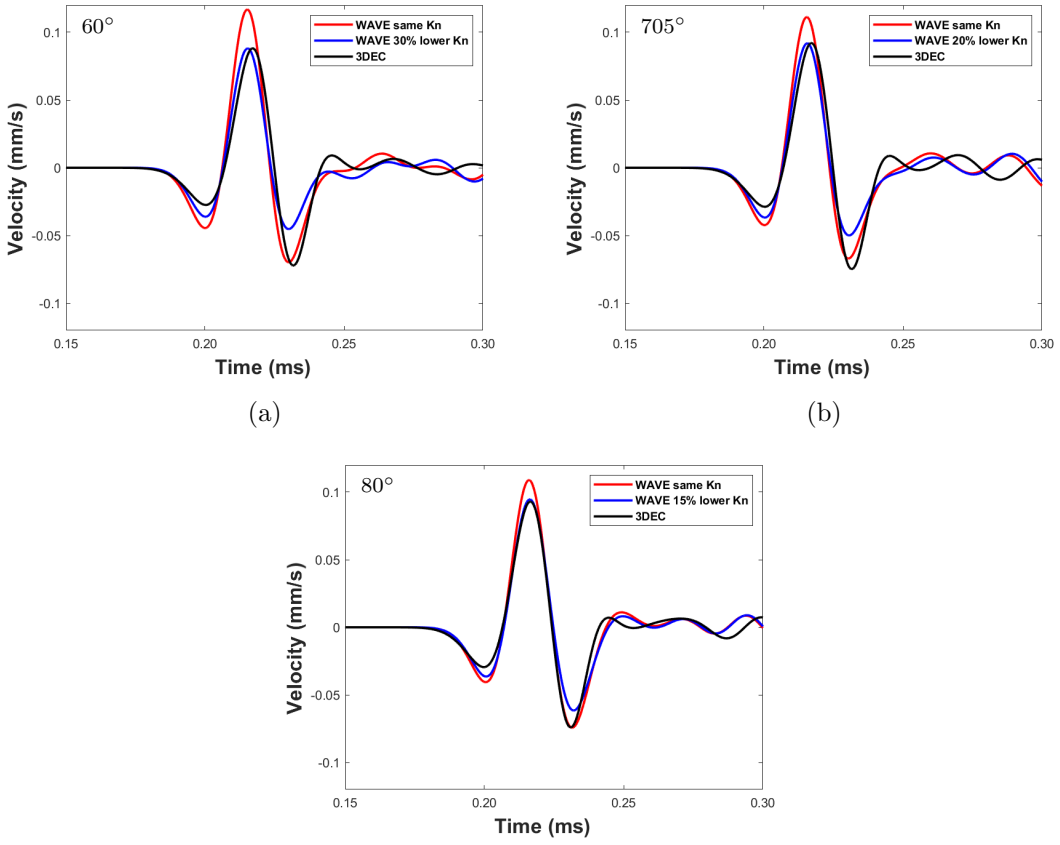

Figure 4.23: Comparison of the P-wave velocities of the waveforms for a single dipping fracture at various angles (4.23a 60°, 4.23b 70° and 4.23c 80°) in 3DEC and 'pixelised' in WAVE3D

4.5.2 Equivalent discrete fracture model (EDFM)

The equivalent discrete fracture medium (EDFM) is an explicit fracture model which, instead of mapping the exact fracture geometry and orientation, uses orthogonal vertical and horizontal fractures at random positions in the same volume as the original fracture. These random fractures have the same total crack density ϵ as the single fracture with complex geometry.

The density of the vertical and horizontal fractures depends on the total surface of the fracture and the volume of the area, as well as the angle of the fracture. The equation 2.8 gives the fracture density of a population of parallel fractures in the given

volume. In order to, convert the fracture density ϵ of a single dipping fracture, to an orthogonal staggered grid geometry, the fracture density has to be split into x- and y-components. Equations 4.6 use the $sin\theta$ and $cos\theta$ to calculate the crack density ϵ for a dipping fracture with angle θ in x- and y-axis. Then, these two values are used to create random cracks parallel to the x- and y-directions respectively:

$$\begin{aligned}\epsilon_{total} &= \frac{1}{\pi V}\frac{A^2B^2}{A+B}, \\ &= \left(\frac{1}{\pi V}\frac{(A\times\cos\theta)^2B^2}{A+B}\right)+\left(\frac{1}{\pi V}\frac{(A\times\sin\theta)^2B^2}{A+B}\right), \\ &= \epsilon_x+\epsilon_y,\end{aligned} \tag{4.6}$$

A is the length of the fracture, B is the width, V is the volume and θ° is the dip angle between the x-axis. At this stage, the azimuth angle is not considered to keep the problem and the geometry simple.

Table 4.12 below shows the calculated crack density for the dipping fracture case I use in this part. It is clear that when the dipping angle is small, the total volume around the fracture is small and the crack density is very high and vice versa. The equivalent fracture zone is at the same volume and position as the dipping fracture and the source and receiver in the models are in the same positions as in the previous models. The cracks per unit length parameter 1/L for the same volume and fracture is also presented in Table 4.12 in order to make direct comparisons of the two quantities.

Dip	**Volume m^3**	ϵ_{total}	ϵ_y	ϵ_x	$\frac{1}{L}$ **m^{-1}**
10°	0.17	0.92	0.89	0.03	5.85
20°	0.36	0.47	0.42	0.05	3.11
30°	0.57	0.34	0.25	0.09	2.31
45°	1	0.26	0.13	0.13	2.00
60°	0.57	0.34	0.09	0.25	2.31
70°	0.36	0.47	0.05	0.42	3.11
80°	0.17	0.92	0.03	0.89	5.85

Table 4.12: Crack density ϵ and 1/L for the single dipping fractures cases from 10° to 80° degrees.

The parameters can vary in the equivalent discrete fracture medium in order to have the same result as the single dipping fracture. These are the range of fracture dimensions

and the fracture stiffness. Initially, I start with fracture sizes similar to the pixelised case and then I increase and/or decrease the size of either the horizontal or vertical fractures and adjust the stiffness to match the arrival and the amplitude. The Figures 4.24, 4.25 and the Table 4.13 below summarises the results from various models used to mimic the result of a dipping fracture.

The first impression is that the results are not as well matched with the dipping fracture in 3DEC, as the pixelised fracture case. When the angle is $30^\circ < \theta^\circ$ or $\theta^\circ > 60^\circ$ the required crack density ϵ is so high that whatever the size of the fracture a much higher stiffness will be needed in order to match the results in arrival time. The high stiffness value though leads to lower attenuation and higher amplitude. On the other hand, when the angle is $30^\circ \leq \theta^\circ \geq 60^\circ$ the waveforms match better with the 3DEC results and only small adjustments to stiffness are required.

One of the reasons that the small and large dipping angles do not match so well might be due to the fact that the source and receiver are aligned with and in close touch with the fracture zone. Results may improve if the source and receiver remain aligned with the fracture, but further away from the fracture zone.

Dipping angle	**Max. coefficient**	**Time μs**	**Horizontal fracture size (m)**	**Horizontal fracture K_n factor**
10°	0.93	-4.4	3×10^{-2}	10
20°	0.75	-6.8	$7.5 - 17.5 \times 10^{-2}$	1.5
30°	0.77	1.2	$2 - 3 \times 10^{-1}$	1.5
45°	0.84	-1.2	$2 - 3 \times 10^{-1}$	-1.5
60°	0.87	2.4	$2 - 3 \times 10^{-2}$	1.5
70°	0.95	-2.4	$7.5 - 15 \times 10^{-2}$	10
80°	0.97	1.2	3×10^{-2}	10

Table 4.13: Maximum cross-correlation coefficient between 3DEC and WAAVE3D waveforms and the time need to add on the second waveform to reach maximum correlation, and the adjustments needed for fracture size and stiffness K_n for the horizontal fractures for equivalent discrete fracture medium.

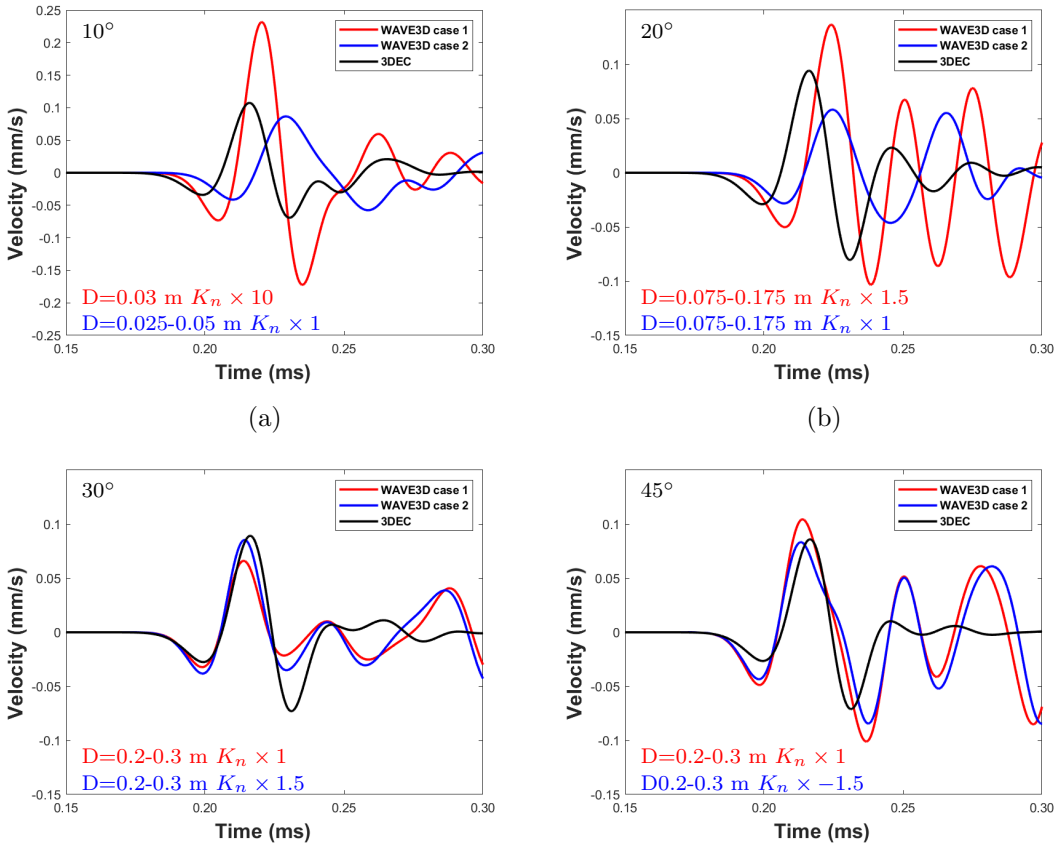

Figure 4.24: Comparison of the P-wave velocities of the waveforms for single dipping fracture at various angles (4.24a 10°, 4.24b 20°, 4.24c 30° and 4.24d 45°) in 3DEC and equivalent discrete fractures in WAVE3D, 4.24a case 1 horizontal fracture size D= 0.03 m, vertical fracture size : 0.025 - 0.035 m K_n is 10 times higher than the one for 3DEC fracture and case 2 horizontal fracture size D= 0.025 - 0.05 m vertical fracture size : 0.025 - 0.035 m, K_n is the same as in 3DEC, 4.24b case 1 horizontal fracture size D= 0.075 - 0.175 m vertical fracture size : 0.075 - 0.150 m, K_n is 1.5 times higher and case 2 horizontal fracture size D= 0.075 - 0.175 m vertical fracture size : 0.075 - 0.150 m, K_n is the same as in 3DEC for horizontal fractures and 10 times lower for vertical, 4.24c case 1 horizontal fracture size D= 0.2 - 0.3 m vertical fracture size : 0.1 - 0.2 m, K_n is the same as in 3DEC and case 2 horizontal fracture size D= 0.2 - 0.3 m vertical fracture size : 0.1 - 0.2 m, K_n is 1.5 times higher and 4.24d case 1 horizontal fracture size D= 0.2 - 0.3 m vertical fracture size : 0.2 - 0.3 m, K_n is the same as in 3DEC and case 2 horizontal fracture size D= 0.2 - 0.3 m vertical fracture size : 0.2 - 0.3 m, K_n is 1.5 times higher.

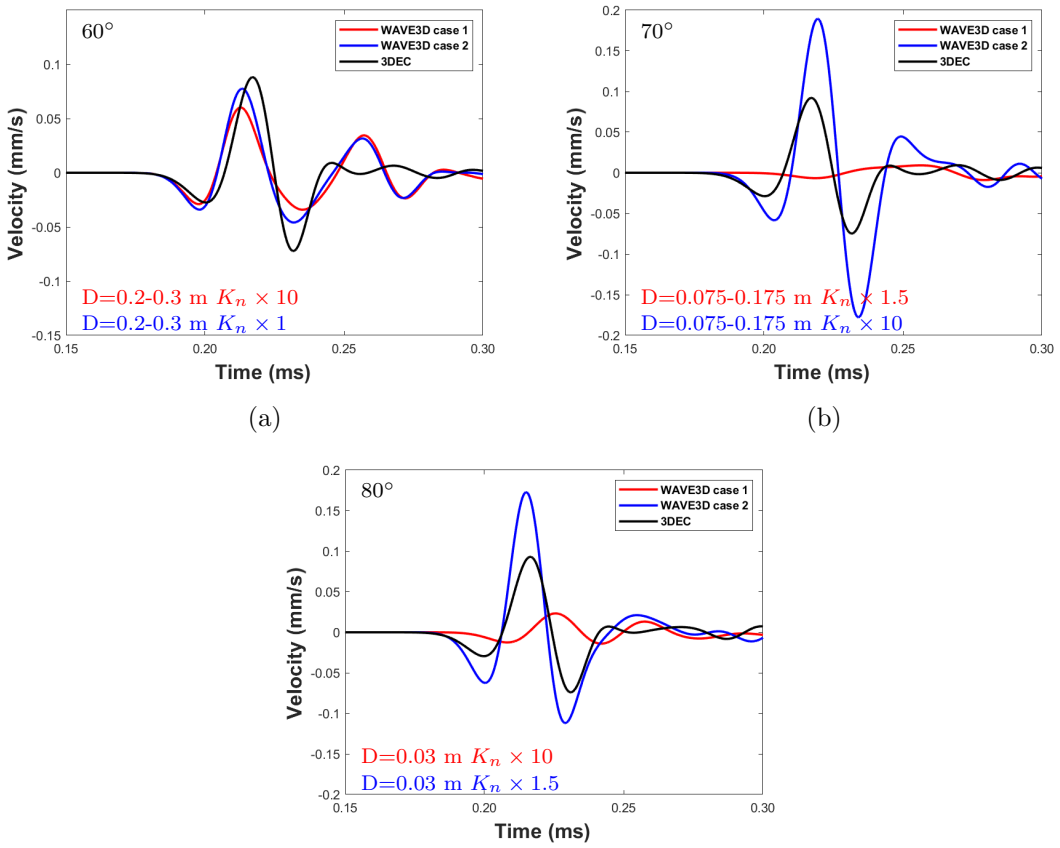

Figure 4.25: Comparison of the P-wave velocities of the waveforms for single dipping fracture at various angles 4.25a 60°, 4.25b 70° and 4.25c 80°) in 3DEC and equivalent discrete fracture in WAVE3D, 4.25a case 1 horizontal fracture size D= 0.2 - 0.3 m vertical fracture size : 0.100 - 0.200 m, K_n is 10 times higher than the one for 3DEC fracture and case 2 horizontal fracture size D= 0.2 - 0.3 m vertical fracture size : 0.100 - 0.200 m, K_n is the same as in 3DEC, 4.25b case 1 horizontal fracture size D= 0.075 - 0.175 m vertical fracture size : 0.075 - 0.150 m, K_n is 1.5 times higher and case 2 horizontal fracture size D= 0.075 - 0.175 m vertical fracture size : 0.075 - 0.150 m, K_n is the same as in 3DEC for horizontal fractures and 10 times lower for vertical, 4.25c case 1 horizontal fracture size D= 0.03 m, vertical fracture size : 0.025 - 0.035 m, K_n is the same as in 3DEC and case 2 horizontal fracture size D= 0.03 m, vertical fracture size : 0.025 - 0.035 m K_n is 1.5 times higher

4.5.3 Discussion

Due to the staggered grid limitation there is a need for converting dipping fractures into horizontal and vertical fractures.Two methods have been proposed the pixelised and the EDFM. Both approaches could be used to test the model performance in more realistic engineering problems.

The pixelised explicit model fracture can represent a dipping fracture well when following a specific ratio between horizontal and vertical fractures size. The stiffness of the horizontal part is adjusted for each case, the stiffness on the vertical fractures (parallel with the transducer-receiver couple) has to be 10 times higher than the horizontal. However, as explained, the intersecting point between vertical and horizontal fracture must not be included leaving a gap. Therefore, further development is necessary so as to overcome that limitation.

The EDFM does not perform well when the fracture density is high for a small volume because more fractures are present and the wave is attenuated and delayed further and more reflections are visible in the waveform. As a result further adjustments need to be made.

At this stage several tests and conclusions have been made for the performance of the models for both parallel and more complex fracture networks. Now the models need to be validated in real and challenging conditions.

In this chapter methods have been examined for representing complex fracture systems in alternative simplified ways. A key context is the efficiency of the model. Furthermore for context the 3DEC models take around 12 times longer to run compared to WAVE3D. For example the time needed for the models with a single dipping fracture was 15120 s, from which the 3420 s was for meshing and 11700 s was the model run time. The equivalent run time for WAVE3D was 1290 s with no need of extra time for meshing. The computational power used in both cases was a four 2.14 GHz processor and 16 GB RAM PC. The WAVE3D models could in fact have been run at lower resolution due to higher order solution reducing the run time by a further 8 fold. As a result the run time can be 96 times faster . If models are to be need within an inversion loop, they would need to be with this sort of efficiency.

4.6 Summary and conclusions

I have tested the performance of the LEM against the explicit fracture model and EM for different LEM layer thickness and for various frequencies and fracture stiffness. For high frequencies the LEM layer needs to be as thin as possible to operate similar to the explicit fracture model rather than close to the EM.

The models were scaled up for larger element size and lower frequencies, showing that there is a linear relationship between frequency, stiffness and element size.

I then tested the explicit fracture approach for complex fracture networks. I initially compared it against models with parallel fractures. The attenuation in amplitude and frequencies is higher for the parallel fracture case compared to the DFN, even though the fracture density (D in m^{-1}) is the same for both cases. I then tested DFNs with different fracture densities. Finally, I considering the fracture stiffness to be uniform. Previous work on stress dependent fracture stiffness have been done for the case of parallel fractures underling the importance of stress in understanding the mechanics of fractures and modelling wave propagation more accurately. Further development is required so that the explicit representation of the DFN could be compared with a complex anisotropic effective medium model.

When implementing the DFN effect to the EM and LEM models for small fractures, it was found that the LEM performs closer to the explicit model for smaller fracture sizes and high stiffness values.

Finally, I have applied two methods to generate a dipping fracture in a staggered grid WAVE3D and evaluated the resulting waveforms with one using the tetrahedral mesh of 3DEC. The first method of pixelizing the fracture in horizontal and vertical fractures performed well against the dipping fractures. The second method of using the the crack density ϵ to create an equivalent discrete fracture medium of vertical and horizontal fractures did not perform as well against the dipping fractures for angles $30^\circ < \theta^\circ$ or $\theta^\circ > 60^\circ$.

The conclusions made from the LEM tests and the complex fracture models are:

- The thickness of the LEM layer is important when the frequency is high, and the normal stiffness is low.

- The LEM thickness has to be as thin as 19 times the wavelength when the model is operating at its lowest possible stiffness, but when the source wavelength is about half the maximum, the LEM can be flexible in terms of thickness.
- As a result, when the frequency is high the LEM models with thick layers tend to perform similar to the EM model, and when the frequency is lower the thick LEM layer performs similar to the thinner one and the explicit model with a correlation coefficient above 0.9.
- Using a larger element size and, as a result lower 1/L value, has no impact on the waveform when using the suggested maximum frequency, creating a linear relationship between element size, maximum frequency, 1/L and stiffness. The scaling of the model leads to the conclusion that heterogeneity created by the alternation between LEM layer and homogeneous material is the one that creates an effect on the waveform similar to the explicit model.
- The differences in wave propagation for a medium with parallel fractures and DFN with the same fracture density can be explained due to the various angles the fractures in the DFN has, resulting in less waveform energy to be reflected.
- Decreasing the fracture density and the size of the fractures lead to a less attenuated and delayed waveform.
- Applying the method of stress dependence for the DFN leads to different waveforms which even if they are close to the uniform stress waveforms, have differences on arrival, amplitude and frequencies.
- The LEM and explicit models match better when the wavelength to DFN fractures diameter is below 1 and close to 0.5, but not perfectly as in the orthogonal fractures. This differences in behaviour of LEM between orthogonal and DFN fractures is due to the various angles of the fractures that suppress the higher frequencies for the explicit model.
- The dipping fractures can be modelled successfully in WAVE3D by adjusting the stiffness and splitting the fracture in smaller horizontal and vertical fractures creating a pixelised geometry with the same angle.

- A second approach, the EDFM, was only partially successful to produce a comparable result to a dipping fracture, in the range $30^\circ \leq \theta^\circ \geq 60^\circ$ with correlation coefficient between 0.77 to 0.87.

Chapter 5

Excavation Damage Zone seismic tomography modelling

In this chapter I work on modelling data from a seismic velocity survey. This velocity survey was part of a study on mapping and providing a better understanding of the fractures in the EDZ of a future GDF. The data are provided by Posiva Oy and Itasca Consulting UK. The scope of this work is to link the findings from the previous chapters and apply the same modelling techniques to an engineering problem and draw conclusions on the *in-situ* performance of the models. The first part of the chapter summarises the purpose and the design of the experiment along with some background information about the Finnish GDF. The second part gives a description of the fracture network as designed by previous studies as well as the methodology followed to invert the source wavelet for the models. Finally, I present the result of the models and compare them against the experiment's and work on optimising the fracture stiffness to achieve better coupling between the data and the models for specific ray-paths.

5.1 Introduction

Nuclear waste has to be safely disposed of in a permanent GDF when the temperature of the spent fuel drops to safe levels, as explained in Chapter 1. At the moment, all of the countries producing such HLW keep the spent fuel in cooling water pools while researching and designing a permanent GDF. One of the pioneer countries in this field is Finland. Posiva Oy is the company responsible for the design and construction of

the GDF ONKALO in Olkiluoto, Finland. Since 2004, Posiva Oy has carried out a series of tests and experiments in the future host rock in Olkiluoto, in order to have a clear view of the geology and mechanical behaviour of the rock. In 2015, the company finally obtained a licence to move forward from the testing stage to the construction of the GDF.

In 2007, Posiva Oy launched an EDZ research program to study how the excavation process itself affects the effectiveness of the rock by creating new possible paths for water flow. The key objectives of this program are to create a method for characterisation of the EDZ, improve the excavation methods to minimise damage, evaluate the flow paths for nuclear waste leaking and create solutions to eliminate such migration (e.g., Reyes-Montes & Flynn, 2015; Sinnathamby *et al.*, 2014; Siren *et al.*, 2015a,b; Suikkanen, 2019). Several methods have been tested to monitor the evolution of an EDZ such as microseismic and AE monitoring (e.g., Carlson & Young, 1993; Collins *et al.*, 2002; Young *et al.*, 2020), cross-hole tomography (e.g., Manukyan *et al.*, 2012; Marelli *et al.*, 2010) and other methods as presented in Chapter 1.3

As part of this EDZ program, Posiva Oy requested from Itasca Consulting UK Ltd. to perform a cross-hole velocity tomography survey in the testing tunnel of the future GDF ONK-TKU-3620 niche. The variations in the seismic wave velocities are used to interpret the damage in the rock due to fractures which might have been created during excavation near the tunnel surface.

My work in this part is to model the survey and use the recorded P-waves to compare the full waveforms with the models, as conducted previously for the laboratory experiment in Chapter 3. The survey concentrates on seismic velocities and not on examining the full waveforms.

5.2 Survey information

Throughout the years of the EDZ program operation, field and lab surveys and tests have taken place in the testing tunnel ONK-TKU-3620 niche. These tests include mechanical properties characterization, reflection Ground Penetrating Radar surveys, electrical resistivity tomography, core drilling and geological logging, block sawing and many more. As a result, there is a database of accurate information for the tomography studied area which is going to be used in the modelling process.

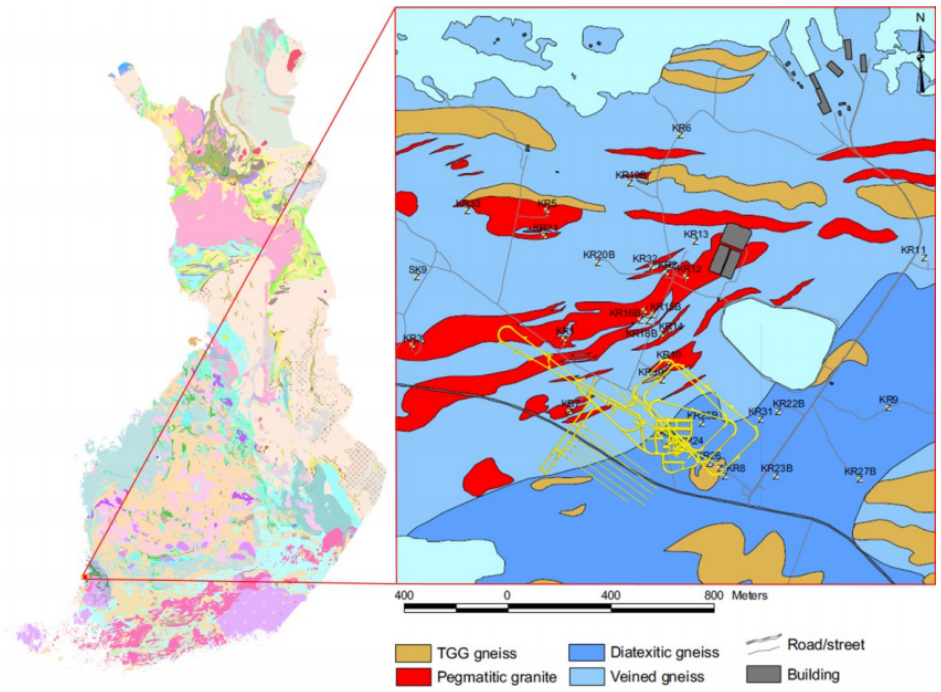

Figure 5.1: The geological map of Finland and the position of the Olkiluoto GDF (Kiuru, 2016).

5.2.1 Lithology of the area

Several reports performed by Posiva Oy include a detailed description of the geology of the surrounding area of the testing tunnel (Figure 5.1). These studies use combined methods to map the lithology, in-situ stress and fracture orientation of the tunnel such as core logging, geophysical measurements, photogrametry etc.

In terms of lithology, the main rock type in the tunnel area is veined gneiss (VGN) and pegmatitic granite (PGR), as shown in Figure 5.3. Figure 5.3 shows the mapped lithology of the testing tunnel ONK-TKU-3620 niche and Figure 5.4 shows the projection of the studied area for the P-wave velocity survey.

According to the previous studies, the average VGN dip and dip direction is $45/163^o$ (Hakala, 2018; Suikkanen, 2019). The properties of both rock types are presented in Table 5.1, which includes dynamic measurements based on P- and S-wave velocities (Alejano, 2018), the ratio between P-and S-wave velocities is 1.72. As a result any

possible S-wave is expected to be in a later part of the waveform.

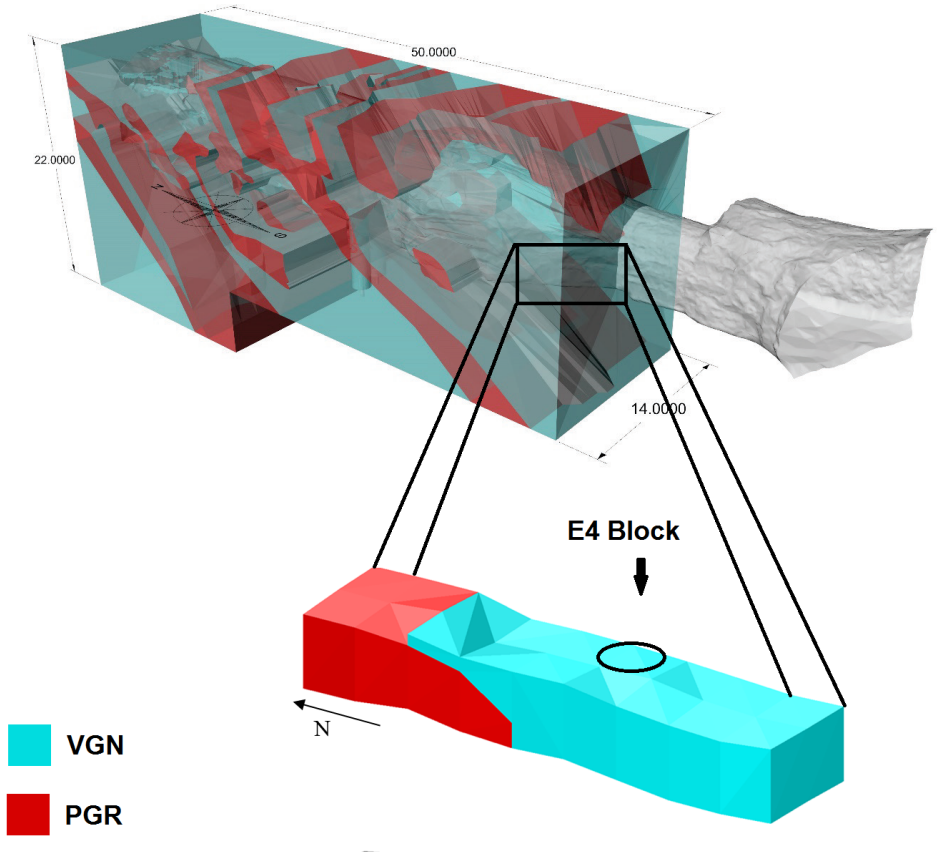

Figure 5.2: The 3D lithological model of the whole testing tunnel with the contact area between veined gneiss (VGN) and pegmatitic granite (PGR). The zoomed area is the EDZ study highlighting the modelled area and E4 block (modified from Hakala (2018); Suikkanen (2019))

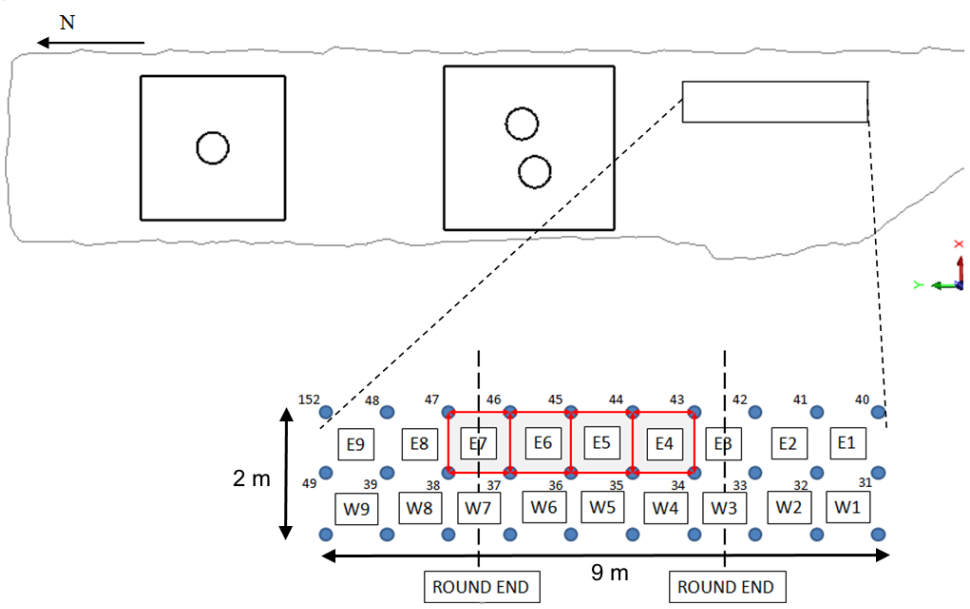

Figure 5.3: 2D projection of the testing tunnel ONK-TKU-3620 niche that the velocity survey area took place and the modelled area E4 (Reyes-Montes & Flynn, 2015; Suikkanen, 2019)

Property	Value
Young's modulus	66 GPa
Density	2740 kg/m^3
Poisson's ratio	0.24
P-wave velocity	5380 m/s
S-wave velocity	3130 m/s

Table 5.1: Mechanical properties based on dynamic measurements of granitic rock in Olkiluoto Finland. Wave velocities have been calculated from the measured elastic parameters (Alejano, 2018)

5.2.2 Fracture model and stress state

There are three sets of fractures which pre-date the excavation. The orientation of these fractures are 38/159^o, 85/267^o and 84/344^o. The area where the seismic tomography has taken place has a detailed fracture model which has been created by combining

different geophysical methods, core logging and sawing of blocks E4 to E7 as shown in Figure 5.3. Then, using the results from the sawing blocks, It was able to identify the fractures in the other geophysical data. In the current fracture model, the fractures are classified depending on their origin to Natural fracture, Natural fracture opened by excavation, EDZ fractures, possible EDZ and two unclassified fractures F1 and F2. The fracture model in the sawed area is presented in Figure 5.4a along with the classification of the fractures and the extended fracture model is presented in Figure 5.4b (Suikkanen, 2019).

The in-situ stress field inside the testing tunnel is uncertain as the measurements vary both in orientation and in magnitude. As a result, there are two different interpretations of the in-situ stress, where the first has been conducted before the expansion of the tunnel in 2010 and the second afterwards. The values for stress of the second measurement are in the following Table 5.2 (Suikkanen, 2019).

	Stress (MPa)	**Trend** (^{o})	**Plunge** (^{o})
σ_1	18.2	120	2
σ_2	15.6	210	4
σ_3	8.9	3	85

Table 5.2: In-situ stress field in the testing tunnel after expansion (Suikkanen, 2019)

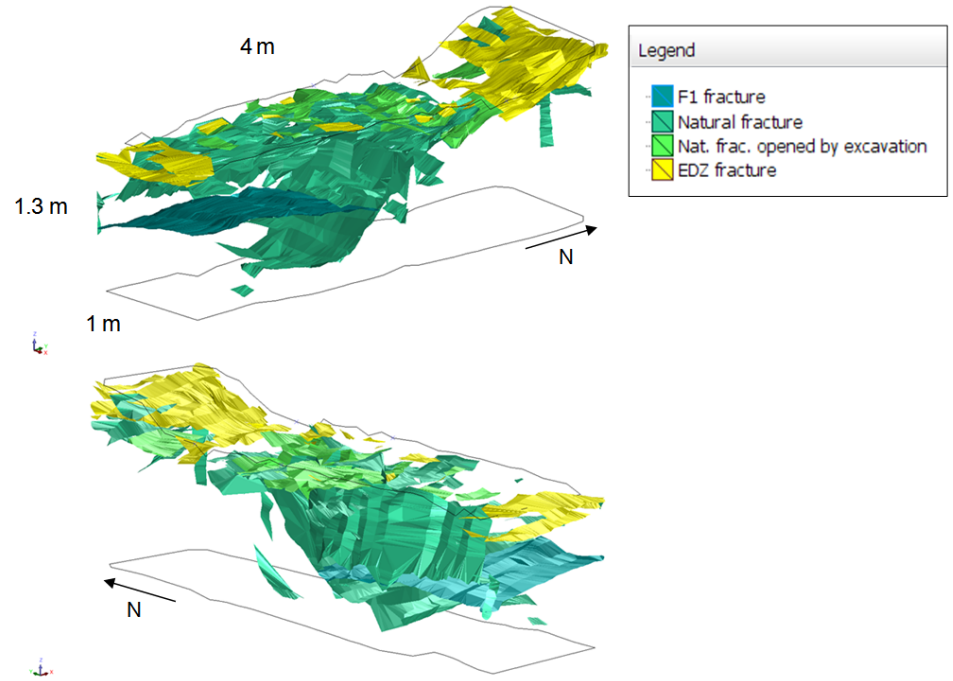

(a)

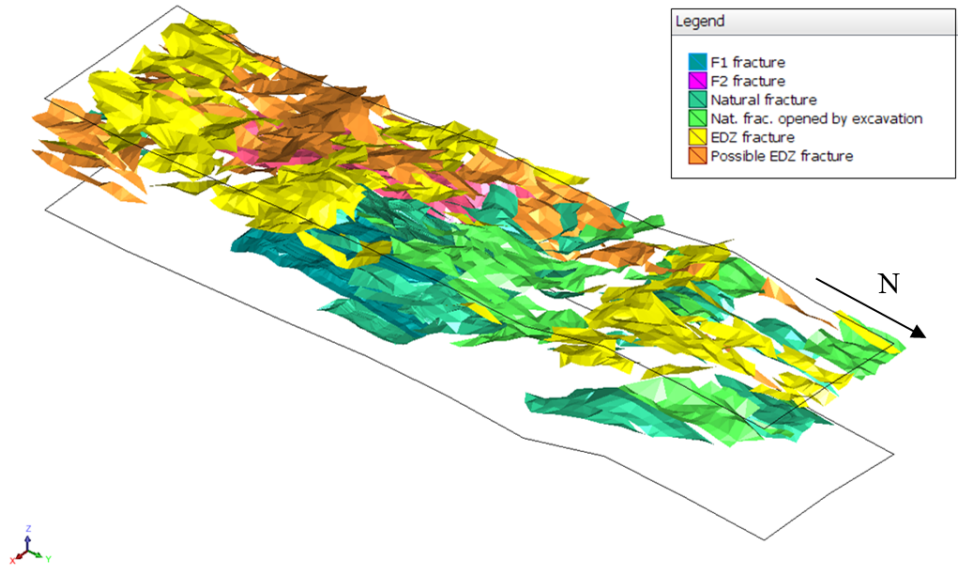

(b)

Figure 5.4: Fracture model from the sawed block area (E4 to E7 blocks) 5.4a, and extended fracture model based on reflection method 5.4b (Suikkanen, 2019)

5.2.3 Equipment and acquisition setup

For the seismic P-wave velocity survey, Acoustic Emission (AE) equipment designed by Itasca Consulting UK and owned by Posiva Oy was used. The equipment consisted of a multi-channel data acquisition system, a multi-channel trigger and hit count system, pulser amplifier system for sensor signals, AE transducers and borehole frames to fit eight transducers in centre to centre distance of 5 cm each creating an array of 40 cm length (Reyes-Montes & Flynn, 2015). In appendix C there is a brief description of the acquisition system and the properties of the sensors used for that survey as described on the Reyes-Montes & Flynn (2015) report.

The survey was carried out using an array of 24 AE sensors measuring P-wave velocities. The survey took place in the central area of the EDZ field as shown in Figure 5.3 and covers the blocks from E3 to E8. The acquisition setup of the survey is presented in Figure 5.5. Each block consists of four borehole. Two borehole frames with the eight sensors each are placed in the pre-existing boreholes in orientation N-S and E-W twice each, SW-NE and SE-NW creating a 2D plane each time. Eight more sensors are positioned on the surface of the tunnel (Reyes-Montes & Flynn, 2015).

Every time a survey is carried out there is a sensor that acts as a transducer to a high frequency signal and 23 acting as passive sensors, recording the waveforms. Each survey has 24 shots, and there are four surveys taking place on each 2D plane (Figure 5.6). This creates in total 552 waveforms per survey and 2208 waveforms per 2D frame. In the first survey, both frames are placed at a depth between 0-0.4 m. In the second survey, the first frame is placed at a depth between 0.4-0.8 m and the second frame in the initial position. The third has the same installation as the second but with a second borehole in a deeper position and the first close to the surface. The final survey has both frames at deeper depth. The data from the surface of the tunnel have a low signal to noise ratio and, as a result, are not going to be used for comparisons with the models (Reyes-Montes & Flynn, 2015).

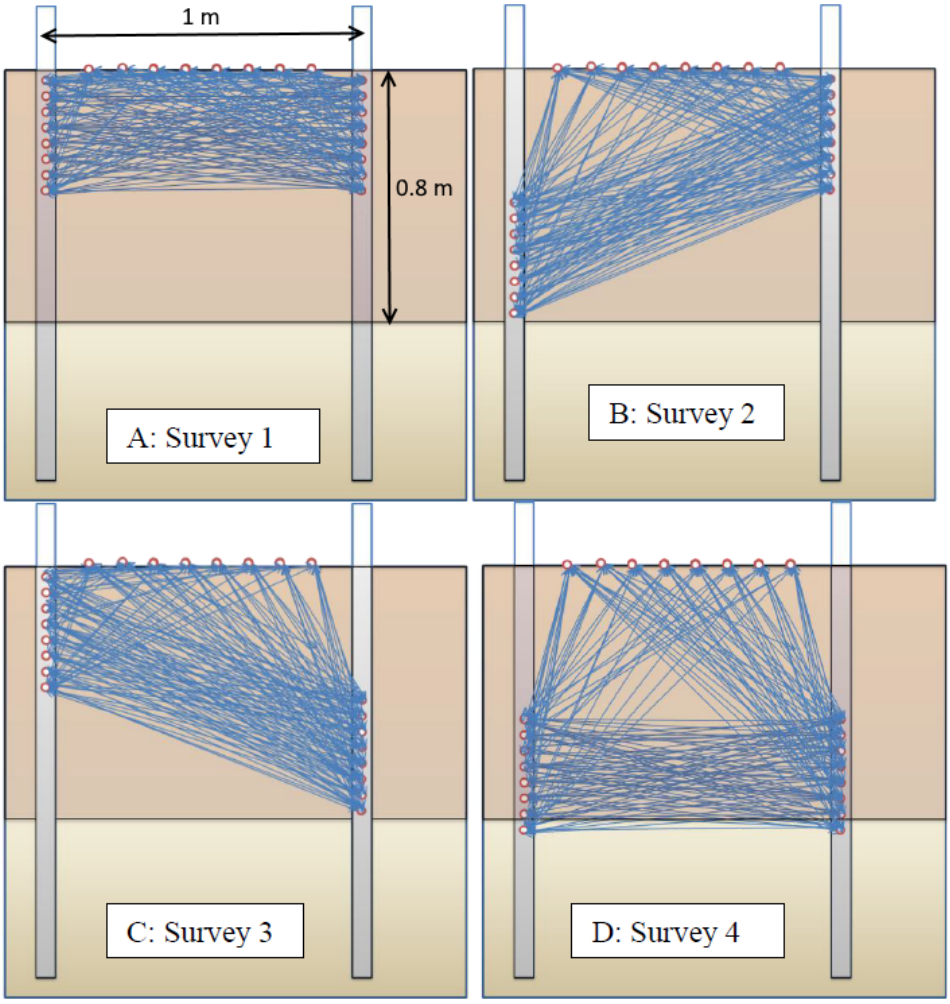

Figure 5.5: One 2D tomography plane consists of 4 surveys with 24 shots. The red circles are the position of the receiver/transducer and the blue lines are the ray-paths created when transducing from each of these positions (Reyes-Montes & Flynn, 2015)

5.3 Modelling the experiment

The scope of this work is to study wave propagation in various directions and compare the model with the survey data. Therefore, it is necessary to create a detailed and accurate representation of the modelled area. The most important information needed to have accurate models are the lithology and the rock properties based on dynamic

measurements, the stress state, an accurate fracture model and a clear seismic source representation used for the purpose of the project. From the reports provided by Posiva Oy and Itasca Consulting Ltd. Alejano (2018); Hakala (2018); Reyes-Montes & Flynn (2015); SKB (2010); Suikkanen (2019), I have a clear view of the lithology, stress state and fracture model of the studied area. The active seismic source used for the survey has to be retrieved by a source inversion technique similar to the one described in section 3.3.1.

The studied area is 6 m^2 large covering blocks E2 to E8 as shown in Figure 5.3. The seismic velocity survey data are in the size of tens of thousands of waveforms, so it is not possible to model the experiment for the full scale. As a result, I had to be more selective with the data I am going to use to compare with my model results. The area modelled in this section has been chosen based on the numerical limitations of WAVE3D in order to avoid model complexity.

5.3.1 Design of the models and limitations

The structure of the model has to expand in three directions in order to study the wave propagation in all the possible azimuths of the survey. One of the first things to consider before starting to create the models are the numerical limitations.

The first limitation relates to the wave frequency and the element size to avoid dispersion, as explained in section 3.2 with equation 2.3. Based on the frequency of the recorded waveforms, the predominant period of the wave is 0.118 μs and based on the report (Reyes-Montes & Flynn, 2015) the minimum velocity is 4800 m/sec. This leads to an element size no larger than 5.6 mm. However, in order to have a more rounded number that fully fills the dispersion criteria, the element size finally used is 5 mm. Due to the element size, a volume area of 1 m^3 will consists of at least 8,000,000 elements. Considering that padding of 100 elements on each side, around the model is going to be added makes the models significantly large.

The lithology of the survey area is close to a contact between pegmatitie Granite and veined Gneiss. Since I am working on the anisotropy of wave propagation based on the fractures, it is important to keep the lithology as simple as possible and avoid any wave anisotropy based on the lithology. Based on the report and the detailed mapping of the the lithology, the area with the minimum mixture of different rock types (Suikkanen, 2019) has been chosen. Moreover, the area has to have a detailed and verified fracture

model and such areas are the blocks E4 to E7 which have been sawed and all of the fractures have been mapped. The area which consists of veined Gneiss is block E4, as shown in Figure 5.3. This block is a 1 m^3 size and there are four boreholes on the edges of the block (Borehole number 34, 35, 43 and 44 in Figure 5.3). As described in section 5.2.3, in each block there are six surveys based on the borehole couples (34-43, 34-35, 34-44, 35-43, 35-44 and 43-44).

5.3.2 Source inversion

In the reports by Itasca and Posiva, there is a detailed description of the acquisition system and the design of the survey, but unfortunately, there is nothing describing the source itself. The only information regarding the source shape and frequency is the recording waveform from the transmitting sensor each time. The transmitted signal has a higher amplitude than the capacity of the recorded one and, as a result, the signal looks more like a square wave 'clipping' due to amplitude saturation, making any frequency analysis difficult. For each survey the same clipping is also observed on the sensors next to the one which is transducing each time. More specific the two sensors above (10 cm upwards) and the two below (10 cm below) the transducing one are clipped too. However, in this modelling project these waveforms are not considered since only waveforms from the opposite borehole from the transducer which crossing the fractures, are going to be modelled. From that recording though, I concluded that the shape of the source is not a single spike source but more of a double ricker shape with at least three full cycles.

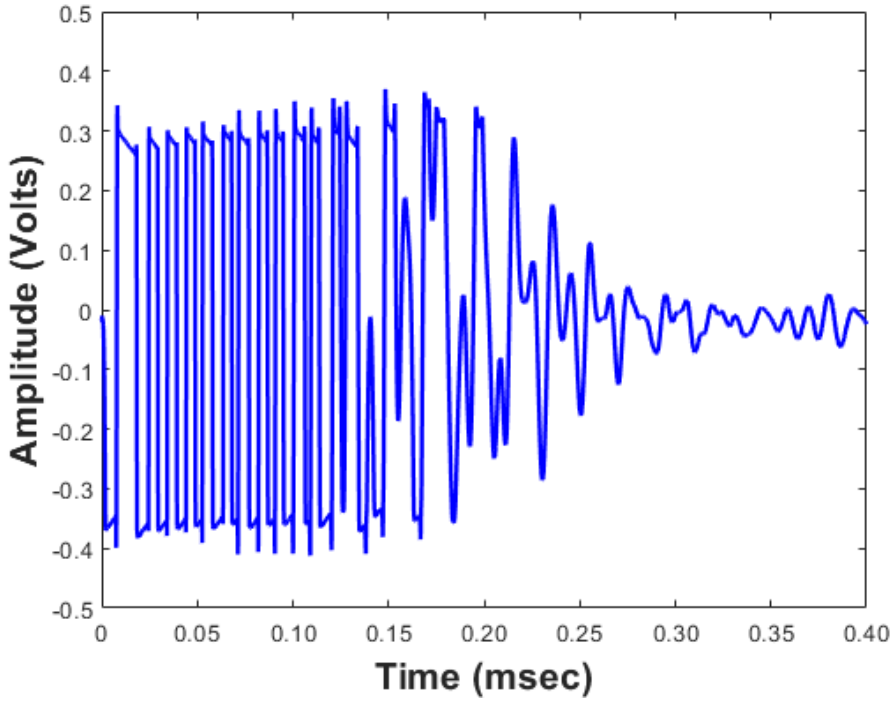

Figure 5.6: Example of the recorded signal from the transducer in borehole frame 34-43 positioned in the 0.4 m depth on borehole 34, showing the square shape wave due to due to saturation in amplitude.

In section 3.3.1 I described the source inversion process followed to model the Pyrak-Nolte *et al.* (1990) experiment. In order to invert the source for that experiment, I used the waveform from the solid homogeneous steel block. In this survey though, there is not anything equivalent to that. For that reason, I had to use the current data and invert waveforms to define a source close to the one applied in the field.

Based on the fracture model from the sawing and the mapped fractures from the boreholes in the report (Suikkanen, 2019), the deeper part of the survey below 0.5 m from the surface for the block E4 has no fractures and is considered as homogeneous. I used waveforms from the survey below that depth and inverted them using the same process as in section 3.3.1. Since the rock is not isotropic because of the crystalline structure, the source inversion process is more complex than in chapter 3 and cannot be defined by a single shot position. The source inversion process had to be repeated several

times and from different borehole pairs in the block. This was necessary in order to compare the inverted sources from different positions and define the similarities. There are seven selected positions in the non fractured area of the block, all of them are at a depth between 0.7 m to 0.8 m. The seven positions are for specific borehole pairs and the inversion was applied to both directions providing fourteen waveforms (Figure 5.7). The waveforms of the different positions used for inversion are similar in arrival time frequency and amplitude.

The waveforms chosen for that source inversion process follow some criteria. The criteria were to have no presence of high frequency noise and the receiver has to stand at the same depth as the transducer on the opposite borehole.

From the modelling side, I used a homogeneous Isotropic medium with the dynamic material properties from the report (Alejano, 2018). The model source was a 0.8 MHz frequency sinusoidal wave presented. The sources inverted from the selected positions are presented in Figure 5.8. Finally, the inverted sources from all the positions phase shifted to match one another. The fourteen phase shifted sources were combined to create a mean source (Figure 5.8). In the mean source I applied a tapering function to include only the first part of the source, as the rest might be due to reflections and ring-down count.

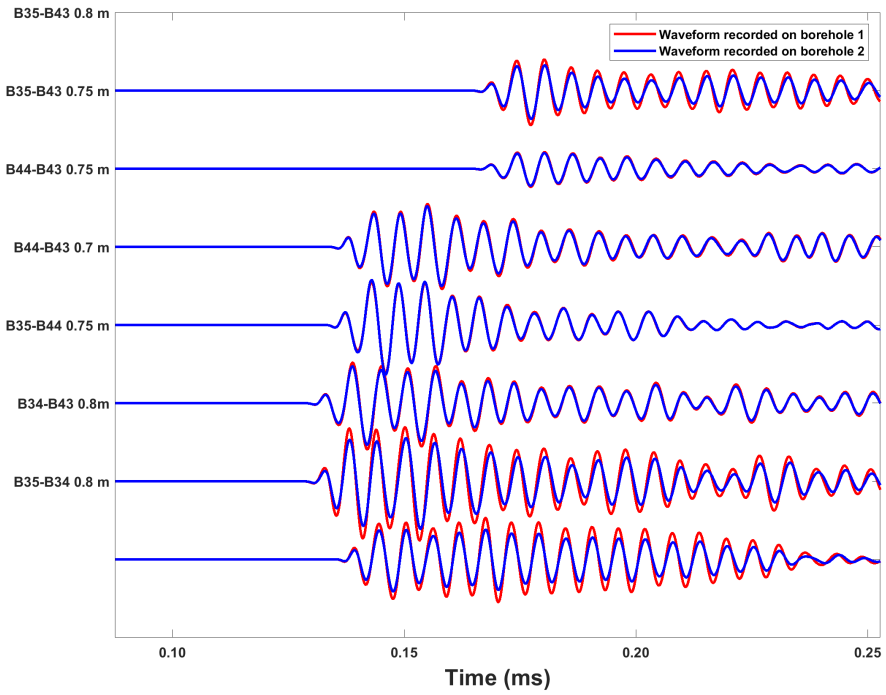

Figure 5.7: The seven pair positions selected for source inversion. On the y-axis is the borehole pair and the depth in which the recorded waveform has been chosen for the inversion. For example, B35-B43 0.8 m is the borehole frame 35 and 43 with shot and recording position at 0.8 m depth, where the red waveform was recorded in borehole 43 at 0.8 m depth when the shot was in borehole 35 at the same depth and vice versa for the blue waveform.

The mean source was then tested in homogeneous models for the same positions as the waveforms used for the inversion process. The results for the mean source are plotted on top of the survey data in Figure 5.9 and the correlation coefficient along with the time shift needed, to reach maximum correlation, is presented in Table 5.3.

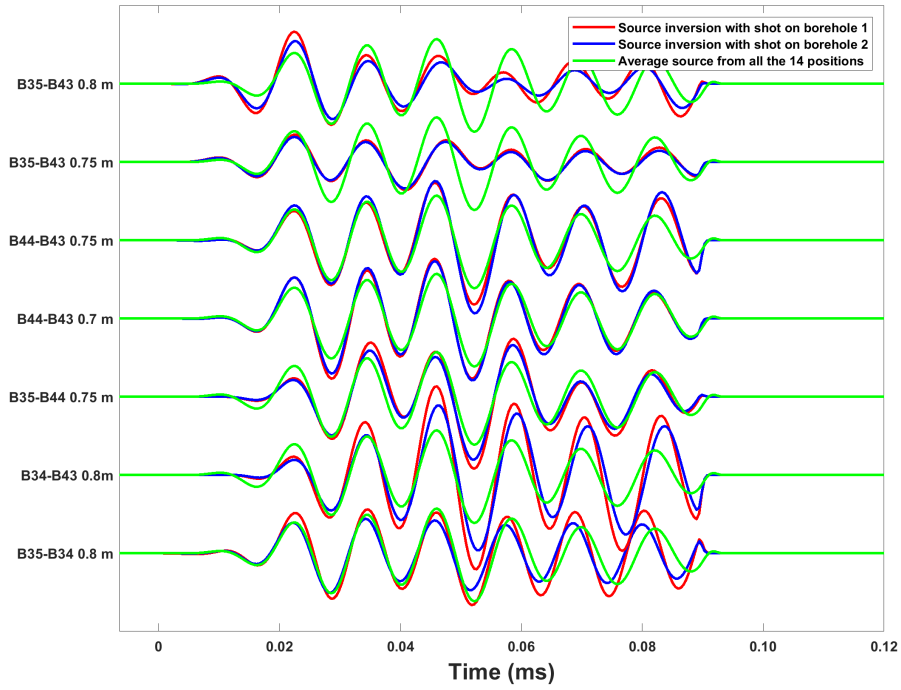

Figure 5.8: The source inversion result for all seven pairs positions along with the mean source from all the positions.

	Max. coefficient	Time ms
B35-B34 0.8 m	0.92	-4.3
B34-B43 0.8 m	0.86	7.1
B35-B44 0.75 m	0.90	6.4
B44-B43 0.7 m	0.97	-1.1
B44-B43 0.75 m	0.93	-2.5
B35-B43 0.75 m	0.96	-0.7
B35-B43 0.8 m	0.96	-0.7

Table 5.3: Maximum cross-correlation coefficient between survey and modelled data with the inverted source and the time needed to add on the second waveform to reach maximum correlation.

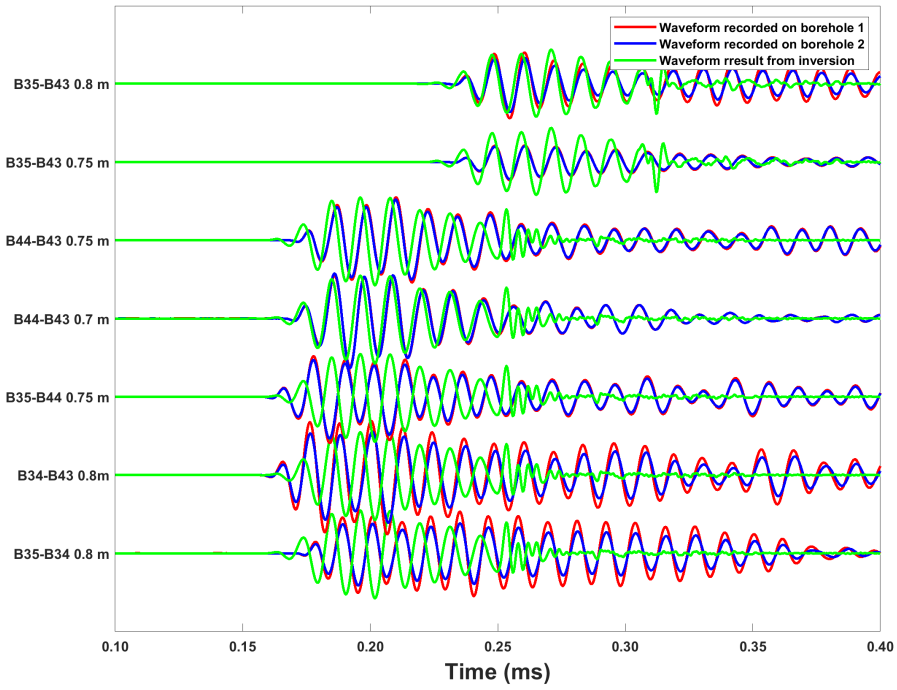

Figure 5.9: The seven pair positions selected for source inversion and the result of the mean source after the inversion.

5.3.3 Implementation of fracture zone

Posiva Oy have provided me with the design files of the detailed fracture models as presented in Figure 5.4. In Figure 5.10 an approximate sketch in 2D of the block E4 for the borehole pair B34-B43 used for the velocity survey is presented. The surface of each fracture within the area of interest has been measured separately. The fracture area was then used for the design of the models. However, most of the fracture surfaces are not planar and further information was utilised from the Report (Suikkanen, 2019) based on the stereo-nets of the measured fractures, in order to describe each fracture with only two angles (dipping and dip direction). This information is summarised in the Table 5.4. The majority of the fractures have a smooth dip angle between 6 to 20^o.

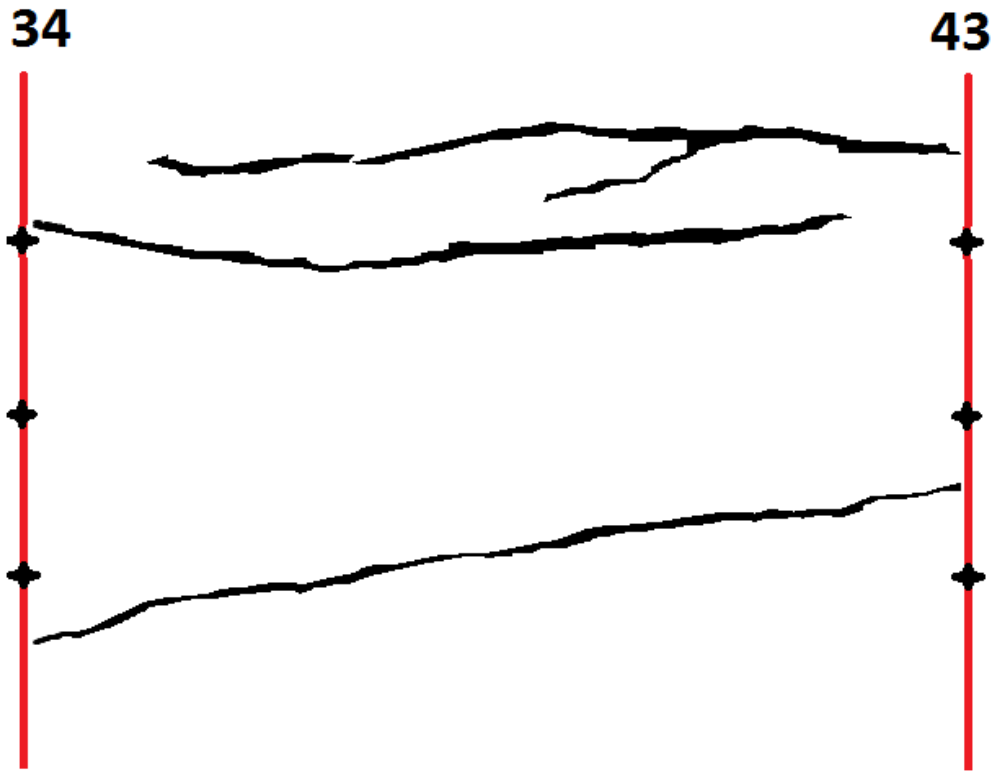

Figure 5.10: Approximate 2D cross-section of the fracture model for borehole frame 34-43 for E4 block to be modelled.

WAVE3D uses a staggered grid and this limits its ability to represent complex fracture geometries, as explained in previous sections. However, in Section 4.5.2 I have described two methods for the explicit model, to convert a dipping fracture. The first one is to pixelise the surface and the second is to create an equivalent discrete fracture medium (EDFM). Both methods have been validated and the conclusions identified, in order to approach the dipping surface for a single fracture model. These conclusions are used in this part in order to construct the explicit fracture model. As a result, there will be two cases of explicit fracture models for the same survey; the pixelised model and the

N	Fracture type	Coordinates (x,y,z)	Dip (^{o})	Dip Direction (^{o})	Area (m^2)	Volume (m^3)	Normal stiffness (Pa/m)
1	NF	(0.99,-0.05,0.60)	10	269	0.014	7.9×10^{-4}	5×10^{11}
2	NF	(0.96,0.07,0.92)	10	269	0.134	1.4×10^{-2}	1.25×10^{11}
3	NF	(1.03,0.73,0.80)	18	159	9.2×10^{-3}	8.7×10^{-4}	5×10^{11}
4	EDZ	(1.01,0.92,0.79)	9	153	7.8×10^{-3}	5.4×10^{-4}	5×10^{11}
5	NFOE	(0.53,0.90,0.74)	9	181	0.078	2.7×10^{-3}	1.67×10^{11}
6	NF	(0.03,0.52,0.15)	8	276	0.010	6.6×10^{-4}	1.67×10^{11}
7	F1	(0.57,0.42,0.59)	6	301	1.35	3.2×10^{-1}	3.3×10^{10}
8	NF	(0.54,0.84,0.63)	18	159	0.032	2.5×10^{-3}	2.5×10^{11}
9	EDZ	(0.75,0.89,0.25)	12	180	5.0×10^{-1}	4.2×10^{-2}	5×10^{12}
10	NF	(0.41,0.70,0.33)	18	159	0.12	9.8×10^{-3}	1.25×10^{11}
11	EDZ	(0.03,0.52,0.15)	6	185	1.7×10^{-2}	3.9×10^{-3}	1.25×10^{11}
12	EDZ	(0.09,0.81,0.22)	7	185	0.39	2.6×10^{-2}	5.71×10^{10}
13	NF	(0.28,0.67,0.57)	18	159	2.7×10^{-2}	1.4×10^{-3}	5×10^{13}
14	NF	(0.30,0.86,0.57)	18	159	1.1×10^{-2}	1.2×10^{-3}	2.5×10^{11}
15	EDZ	(0.28,0.91,0.27)	12	180	1.9×10^{-1}	1.7×10^{-2}	5×10^{11}
16	EDZ	(0.31,0.92,0.98)	9	126	8.6×10^{-2}	3.5×10^{-3}	1×10^{13}
17	NFOE	(0.25,0.77,0.98)	4	63	3.6×10^{-2}	4.0×10^{-3}	1.67×10^{11}
18	NF	(0.12,0.62,0.70)	70	255	5.9×10^{-1}	1.9×10^{-1}	2.5×10^{11}

Table 5.4: List of fractures and orientation. Natural fractures (NF), Natural fractures opened by excavation (NFOP), Excavation damage zone fractures (EDZ), fracture of unknown origin (F1) modified from Suikkanen (2019).

equivalent discrete fracture medium (Figure 5.11 and 5.12). The waveforms of the two models will be compared against the survey data and the waveforms from the other fracture representation models.

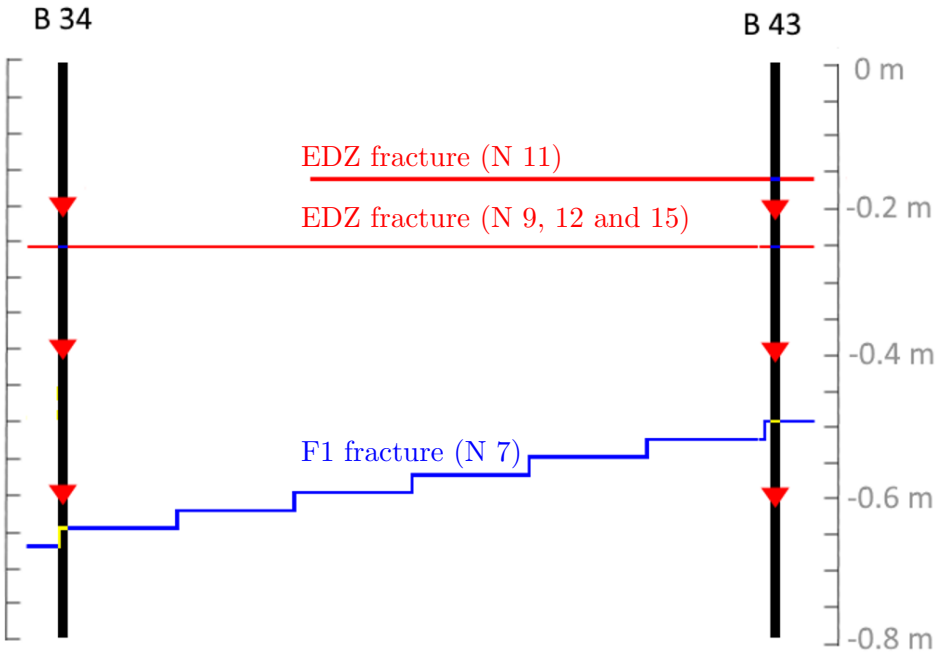

Figure 5.11: Cross-section of the pixelised fracture model for the borehole frame 34-43, fracture F1 (blue) number N 7 in table 5.4 and EDZ fractures (red) number N 9, 11, 12 and 15 in table 5.4.

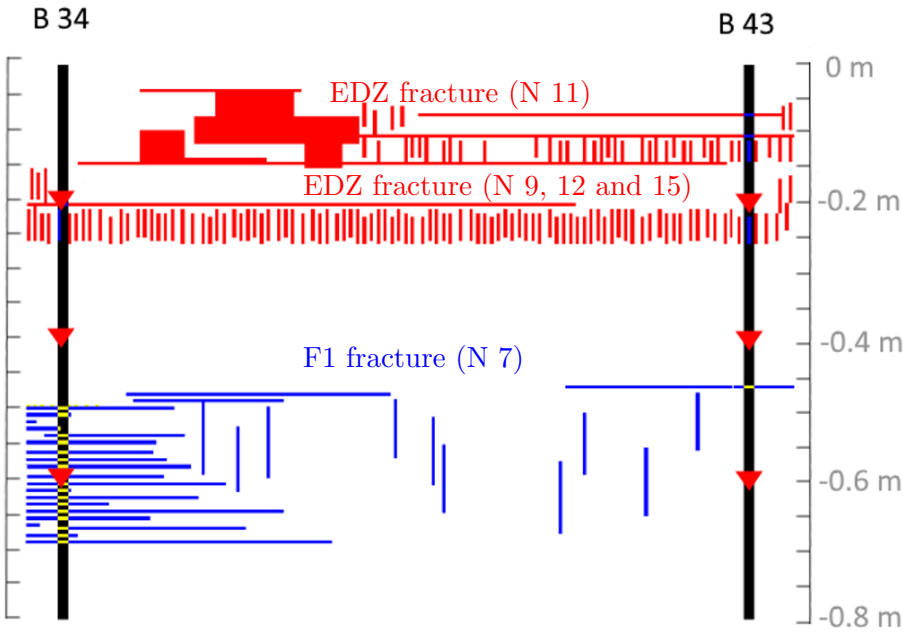

Figure 5.12: Cross-section of the equivalent discrete fracture medium model for the borehole frame 34-43, fracture F1 (blue) number N 7 in table 5.4 and EDZ fractures (red) number N 9, 11, 12 and 15 in table 5.4.

For the EM model, the total area of the fractures was calculated and the average dipping and dip direction angles presented in the Report (Suikkanen, 2019) was used. As a result, the EM model was simpler to design (Figure 5.13).

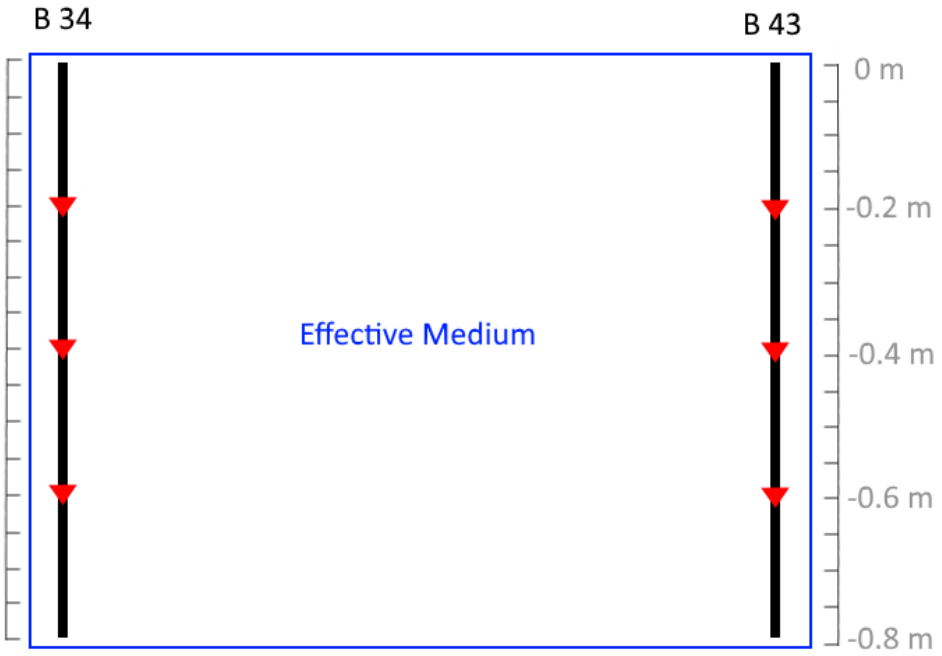

Figure 5.13: Cross-section of the EM fracture model for the borehole frame 34-43.

For the LEM, two cases were used. The first case uses a rectangular volume of LEM material around the fracture with coordinates the same as the fracture. The volume and the surface for each fracture gives a different 1/L value, the two angles are also used to rotate the stiffness matrix in the same direction as the fracture (Figure 5.14). For the second case, the input values are the four coordinates of the fracture and the two angles, then WAVE3D creates a thin LEM layer with a thickness equal to one element and the 1/L is equal to $1/\Delta x$ (Figure 5.15). The first case has lower 1/L values compared to the second case and as shown in 4 the lower the 1/L the closer to the EM model. However, the reason I used the first case of LEM is because, even though the 1/L will be low, the dipping and the dip direction angle will be different for each fracture and, thus, different from the single angle of the EM model.

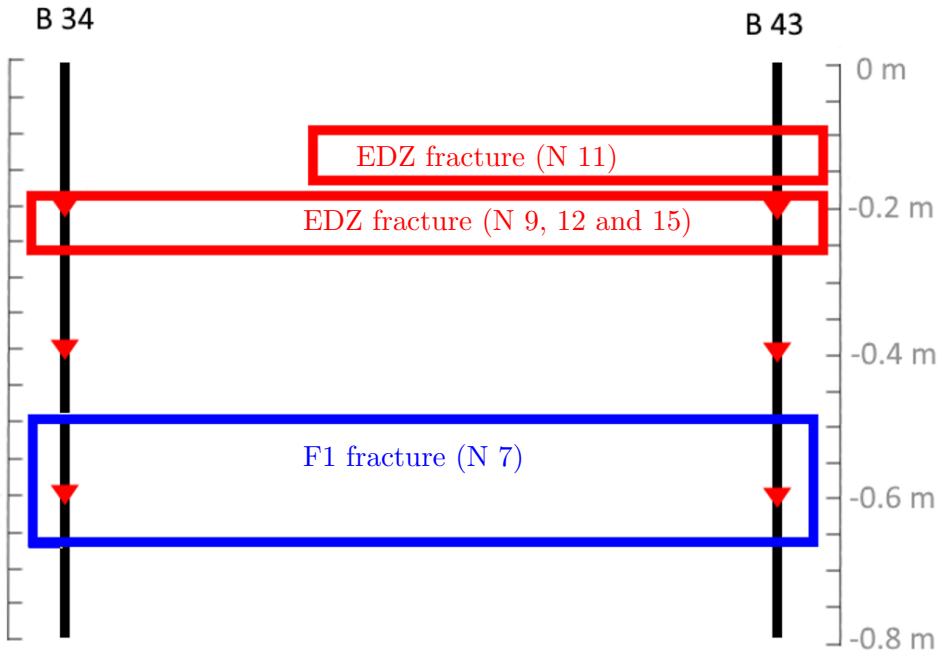

Figure 5.14: Cross-section of the thick layer LEM fracture model for the borehole frame 34-43, fracture F1 (blue) number N 7 in table 5.4 and EDZ fractures (red) number N 9, 11, 12 and 15 in table 5.4.

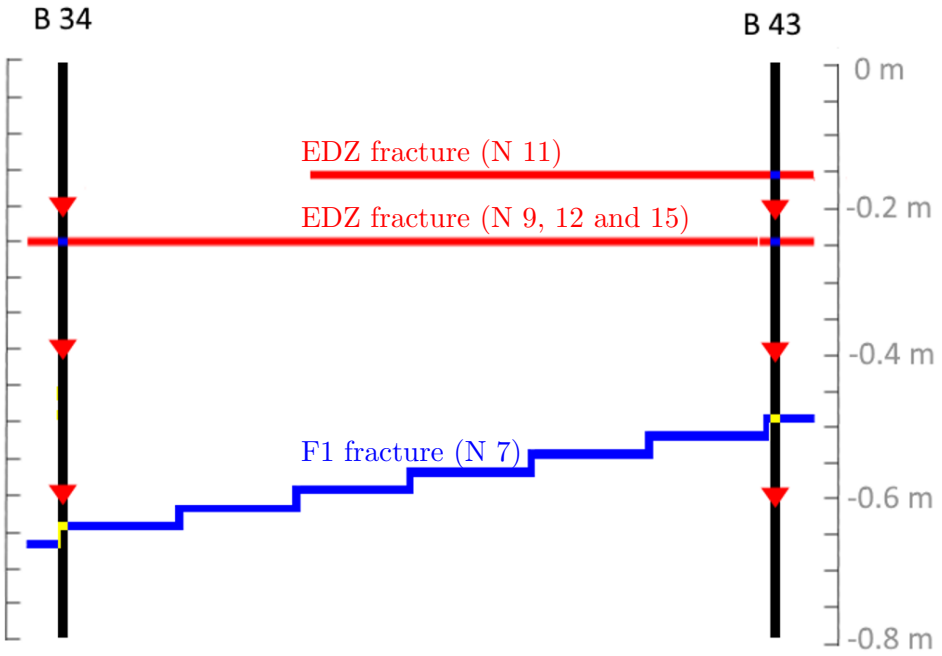

Figure 5.15: Cross-section of the fine layer LEM fracture model for the borehole frame 34-43, fracture F1 (blue) number N 7 in table 5.4 and EDZ fractures (red) number N 9, 11, 12 and 15 in table 5.4.

The fracture normal stiffness K_n used in the initial model are presented in Table 5.4. The values of stiffness were estimated according to the the size of the fracture as described by Worthington & Lubbe (2007). The shear stiffness K_s was set at one third of the normal stiffness. Based on the results of the initial models, the stiffness of some fractures will be adjusted and rerun in order to achieve better matching. For the EM model, the normal stiffness K_n was an average value of the above stiffness 1×10^{11} Pa/m. In this part, in order to model the seismic tomography survey more accurately, these five models, two explicit cases, the EM and two LEM cases will now be investigated.

5.4 Initial model evaluation

Overall, modelling the above survey poses many challenges. First of all, it is expected to have a background anisotropy in wave velocities. The VGN formation has a dipping and dip direction creating a foliation which might affect the velocities. Another factor creating uncertainty is the shape of the source used in the survey and whether the source coming out of the inversion process is representative in all cases. The issue with source inversion is linked to the next problem; the fact that some sensors of the array may have a better coupling with the surface of the borehole creating differences in amplitude. The coupling between the borehole surface and the receiver and/or transducer have an effect on the transfer function on the acquisition system (Marelli *et al.*, 2010) and can result in differences in amplitude from 5 to 25% as shown in Figure 5.7. For example in the 'B34-B43 0.8 m' case the recorded on borehole 1 (red) has 25% higher amplitude compare to the recording on borehole 2 (blue), even though both waveform are propagating through the same path but with opposite orientation and expected to have identical waveforms. In addition to the coupling, the presence of water in the boreholes covered in the report (Reyes-Montes & Flynn, 2015) creates further complexity. Attenuation and delay in wave velocities are expected due to the presence of water in the boreholes. In designing the models, some assumptions about the geometry of the fractures have been made for the different fracture representations as explained in previous sections. Finally, fracture stiffness is an unknown parameter and will need adjustment in order to approach closer the survey data is the fracture stiffness.

At this stage, only the waveforms between boreholes 34 and 43 are to be considered. The reason I do not use the data from other borehole frames is to minimise the amount of data and concentrate on specific ray-paths which I will try to optimise in the second stage to improve the model outputs.

5.4.1 Boreholes 34-43 geometry and fractures

Between boreholes 34 and 43 there are two main fracture sets. The first one is the F1 fracture which is cutting the whole block with 6^o average dipping and 301^o dip direction. The minimum and maximum depth of the fracture is at 46 cm and 70 cm respectively. The initial fracture stiffness used is 3.33×10^{10} (Table 5.4) and it is based

on the size of the fracture which is greater than 1 m^2. The second fracture set has been characterised as EDZ fractures. It has been split into four fractures, as shown in table 5.4, fractures 9,11,12 and 15. The dipping of the those fractures varies from 6^o to 12^o and dip direction of approximately 180^o. The size of the fractures is between 0.5 m^2 to 0.017 m^2 with fracture stiffness 5.71×10^{10} Pa/m to 5×10^{12} Pa/m. The dip angle of all the fractures presented between borehole 34 and 43 are almost horizontal. The two fracture sets are highlighted in Figure 5.16.
Based on the initial results, I have selected specific ray-paths to present. The selection of those ray-paths was made based on how comparable with the survey data some of the models are. The Ray-paths chosen are as follows:

- Shot on borehole 34 at 0.40 m depth and recording at depth 0.80 m, where the angle of propagation is 22^o from horizontal and crossing the F1 fracture.
- Shot on borehole 34 at 0.60 m depth and recording at depth 0.50 m, where the angle of propagation is approximately 6^o from horizontal and is almost parallel to the F1 fracture.
- Shot on borehole 34 at 0.20 m depth and recording at depth 0.40 m. This case examines a ray-path propagating at an angle of about 11^o from horizontal where the shot position is at the edge of the EDZ fractures and the recording position is in an area with no fractures. So the waveform does not cross any fracture directly.
- Shot on borehole 43 at 0.60 m depth and recording at depth 0.20 m. The angle of the ray-path is about 22^o and crossing the F1 fracture.
- Shot on borehole 43 at 0.60 m depth and recording at depth 0.55 m and 0.60 mm. The waveform in these cases propagates with 3^o angle and 0^o from horizontal crossing the F1 fracture.

On the first case, based on the travel time calculations the part of the waveform after the first 0.25 ms is the result of a strong reflection from the EDZ fractures above the F1. The wave in the third case travels between the edges of the two fracture sets. However, because waves are not simple rays but plane waves there will be attenuation and there will be changes in the waveforms even though the wave does not travel directly through the fractures as in the first two cases.

The first impression from the results of the initial models is that the pixelised explicit model and the fine LEM model perform in a similar way and in some cases very close to the survey data. The fine LEM model in some cases works better than the explicit model. The thickness of the LEM model and the low 1/L value in some cases does not affect the final result, which is close to the pixelised explicit and the fine LEM models. On the other hand, the EM model is not very comparable with the survey data.

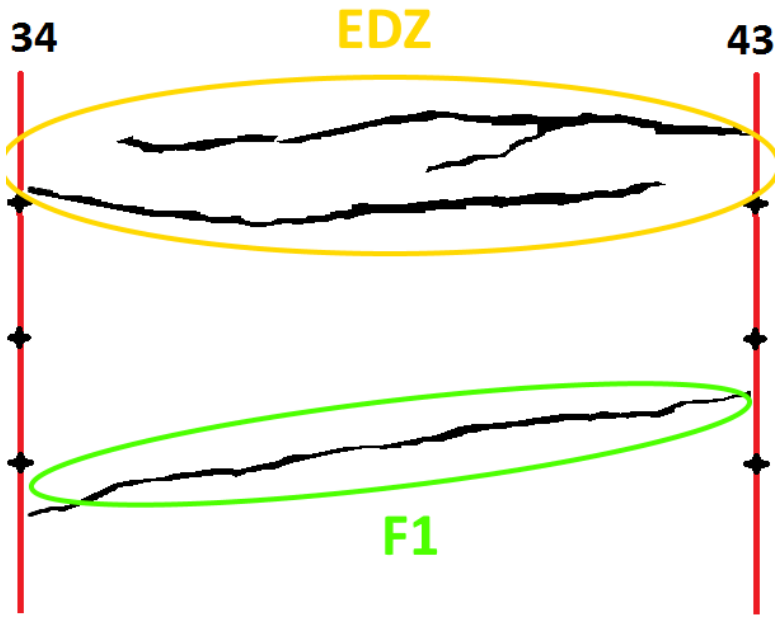

Figure 5.16: Cross-section of the fracture model between boreholes 34-43.

Effective Medium model results

The EM expands to the full size of the modelled block, which practically means that the volume of the EM is equal to the volume of the studied area. As a result, using the summary of all the fracture areas (Table 5.4) over the total volume the 1/L is then equal to 3.73 m^{-1}. The average dip and dip direction of the fractures is measured as 34^o and 163^o respectively (Suikkanen, 2019). Finally, the fracture stiffness used for the EM model was calculated as an average of the individual fractures stiffness and its size.

The amplitude of the waves in the EM model is much higher than the survey data and the other four models, in some cases the maximum amplitude of the EM model is up to twenty-five times higher than the survey (see table 5.5 ray-path 3). Furthermore, the wave velocities of the EM models are much slower compared to the survey data and the other models (Figures 5.17 to 5.18). The delay of the EM model is between 20 μsec to 100 μsec.

Overall, the EM model is not able to approach the real data since the fracture model in this survey is far more complex to be characterised by just two angles and a single stiffness value. Table 5.5 summarises in numbers the result of the presented waveforms with the minimum and maximum amplitude of the survey and the model data and the arrival time for each case.

	Normalised peak-to-peak amplitude	**Normalised first arrival**
Ray-path 1	4.31	1.26
Ray-path 2	4.25	1.65
Ray-path 3	25.09	1.45
Ray-path 4	11.00	1.26
Ray-path 5	8.39	1.58
Ray-path 6	4.43	1.61

Table 5.5: Values of peak-to-peak amplitude of the EM model waveforms normalised to the survey data, along with the normalised first arrival, for the six ray-paths presented below.

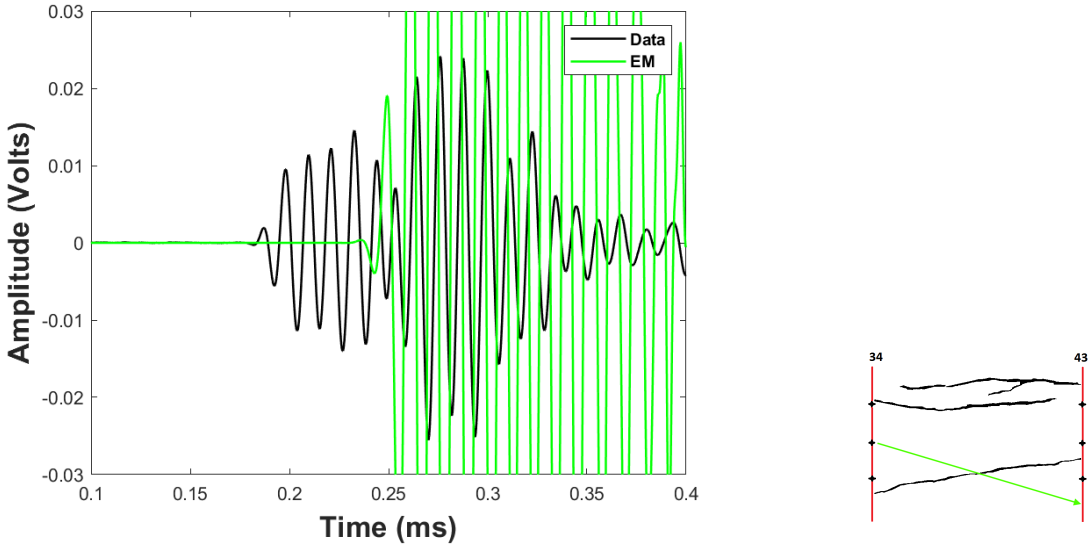

(a)

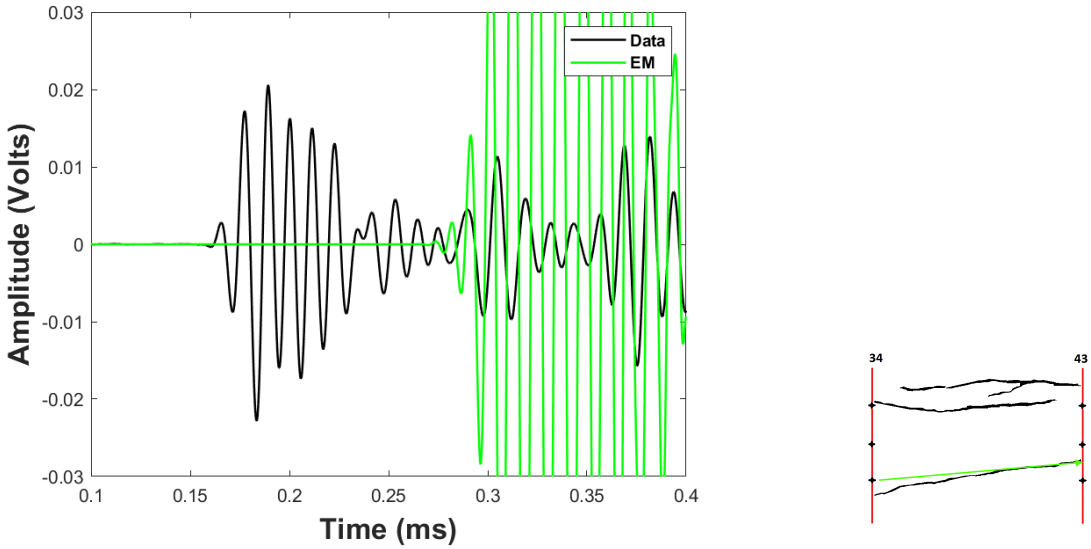

(b)

Figure 5.17: Waveforms for the frame between boreholes 34-43 for the EM model. The two shot positions are on borehole 34 and recording on borehole 43. On the side is the sketch of the ray-path of the wave. 5.17a, shot depth at 0.4 m and recording at 0.8 m and 5.17b shot depth at 0.6 m and recording at 0.5 m.

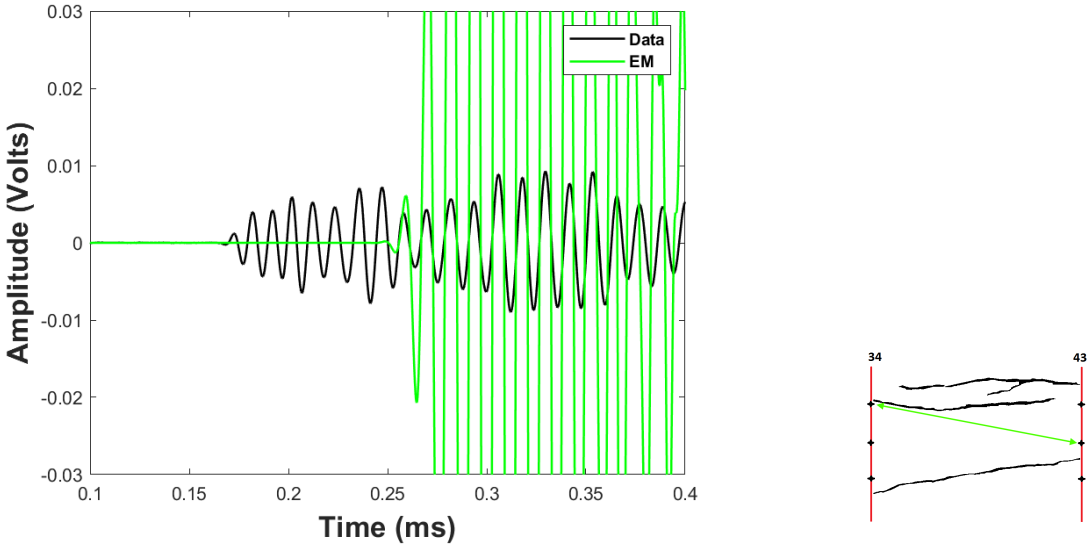

(a)

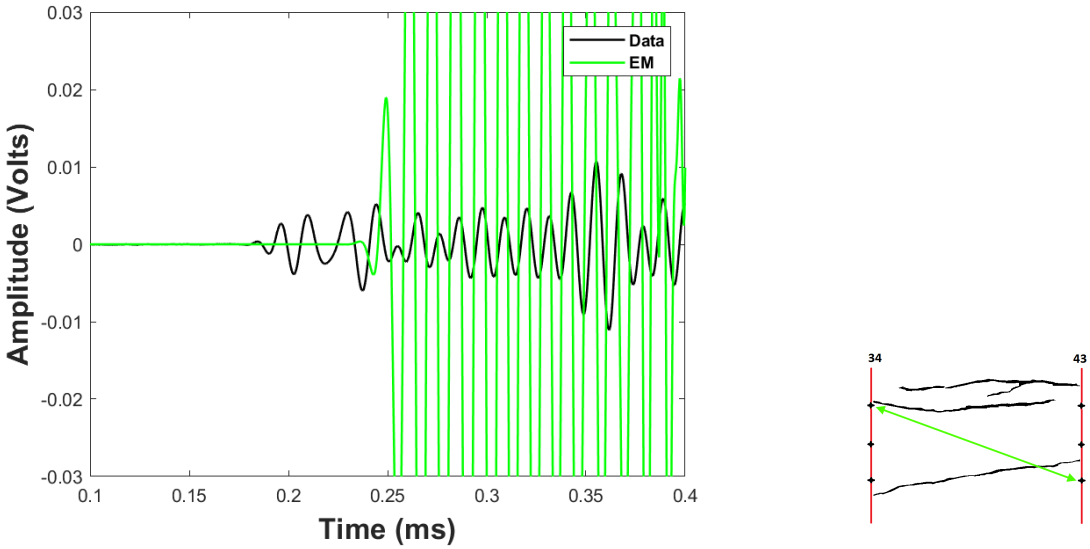

(b)

Figure 5.18: Waveforms for the frame between boreholes 34-43 for the EM model. The first shot position is on borehole 34 and the second on borehole 43 recording on 43 and 34 respectively. On the side is the sketch of the ray-path of the wave. 5.18a, shot depth at 0.2 m and recording at 0.4 m and 5.18b shot depth at 0.6 m and recording at 0.2 m.

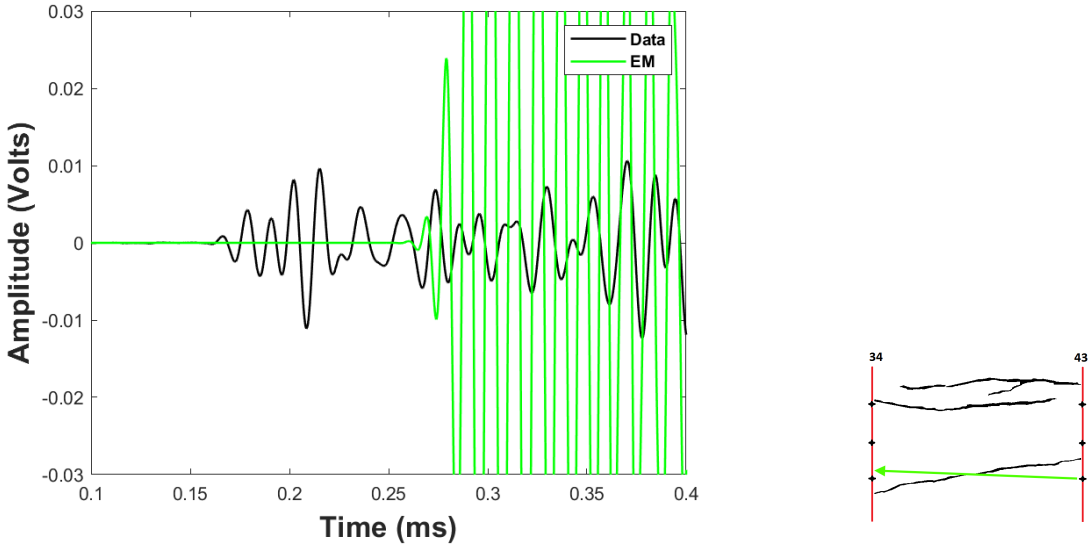

(a)

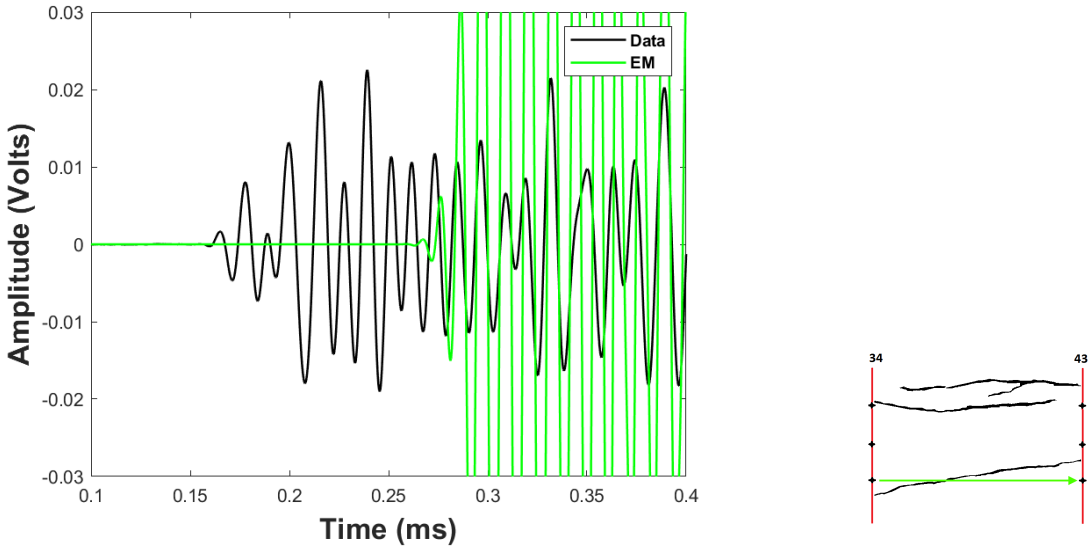

(b)

Figure 5.19: Waveforms for the frame between boreholes 34-43 for the EM model. The two shot positions are on borehole 43 and recording on borehole 43. On the side is the sketch of the ray-path of the wave. 5.19a, shot depth at 0.6 m and recording at 0.55 m and 5.19b shot depth at 0.6 m and recording at 0.6 m.

Localised Effective Medium (thick layer) model results

The LEM with thick layers uses the rectangular volume around the fracture based on minimum and maximum coordinates. The 1/L parameter is then calculated based on the total fracture surface and the volume as described above. The values for the 1/L for each fracture are presented in the Table 5.6 below, and the angles and the stiffness values used are in Table 5.4.

Fracture type	**Coordinates (x,y,z)**	**1/L (m^{-1})**
NF	(0.99,-0.05,0.60)	17.6
NF	(0.96,0.07,0.92)	9.7
NF	(1.03,0.73,0.80)	10.5
EDZ	(1.01,0.92,0.79)	14.4
NFOE	(0.53,0.90,0.74)	29
NF	(0.03,0.52,0.15)	16.2
F1	(0.57,0.42,0.59)	4.2
NF	(0.54,0.84,0.63)	12.4
EDZ	(0.75,0.89,0.25)	11.9
NF	(0.41,0.70,0.33)	10.4
EDZ	(0.03,0.52,0.15)	12.2
EDZ	(0.09,0.81,0.22)	14.6
NF	(0.28,0.67,0.57)	4.3
NF	(0.30,0.86,0.57)	19.8
EDZ	(0.28,0.91,0.27)	9.4
EDZ	(0.31,0.92,0.98)	11
NFOE	(0.25,0.77,0.98)	24.1
NF	(0.12,0.62,0.70)	8.9

Table 5.6: List of fractures and orientation

The results are more comparable with the survey data unlike the EM model. The amplitude of the waves in the LEM model is lower in some cases than the survey data. Furthermore, the wave velocities of the LEM models are slightly faster in the cases where the amplitude is similar to the data and slower in the cases where the amplitude is lower.

In Figure 5.20a, the first 1 ms of the waveform is similar to the data where later the

amplitude drops. After the first 0.25 ms the survey waveform has a two times higher amplitude while the model's is very low. Based on the calculations of the travel time this signal cannot be an S-wave since the theoretical arrival of the S-wave expected to be 1.72 times the arrival of P (in this case more than 0.31 ms). This part of the waveform with high amplitude might be a reflection from the EDZ fracture above based on the travel times. However, for the thick LEM this reflection is not that strong since the EDZ fracture is another thick layer creating a smoother reflection. The velocity is 0.01 ms faster, as the wave passes through the F1 fracture zone. In Figure 5.20b, the modelled data are more attenuated because the propagation in this case is through the zone and not at the edge of the fracture. For the ray-path in Figure 5.21 the result of the models are still good in terms of both amplitude and velocity. In contrast, the waveforms in Figure 5.22 are more attenuated than the survey data in amplitude and in arrival time.

Overall, the LEM model with thick layer is a considerably good approach to the real data since the fracture model is able to catch some of the complexity of the reality. Table 5.7 compares the maximum and minimum amplitude and the first arrival between the LEM model and the survey data for the six presented ray-paths.

	Normalised peak-to-peak amplitude	**Normalised first arrival**
Ray-path 1	0.43	0.95
Ray-path 2	0.37	1.00
Ray-path 3	2.40	0.96
Ray-path 4	0.88	0.94
Ray-path 5	1.08	1.00
Ray-path 6	0.30	1.00

Table 5.7: Values of peak-to-peak amplitude of the LEM model with thick layer waveforms normalised to the survey data, along with the normalised first arrival, for the six ray-paths presented below.

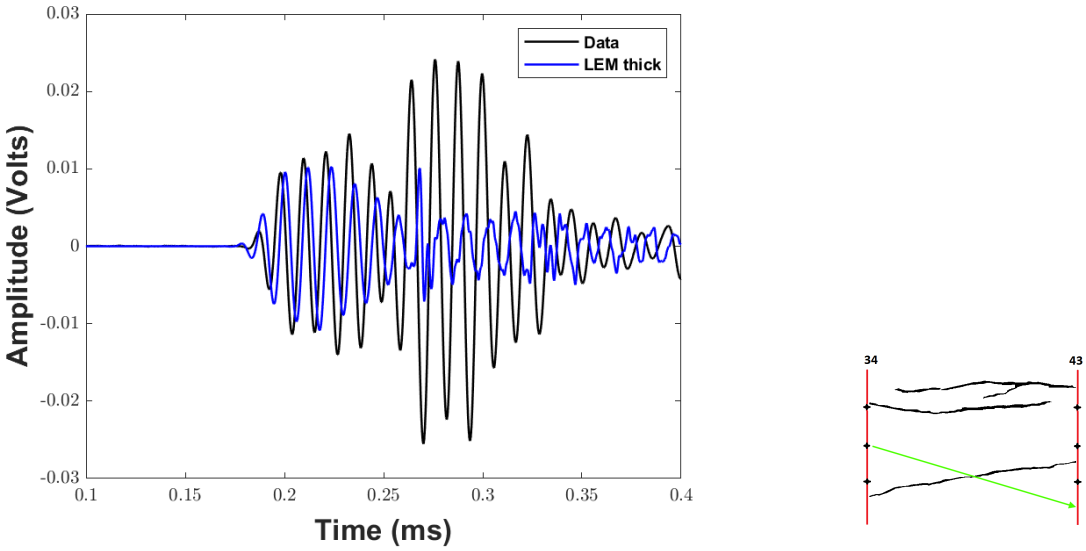

(a)

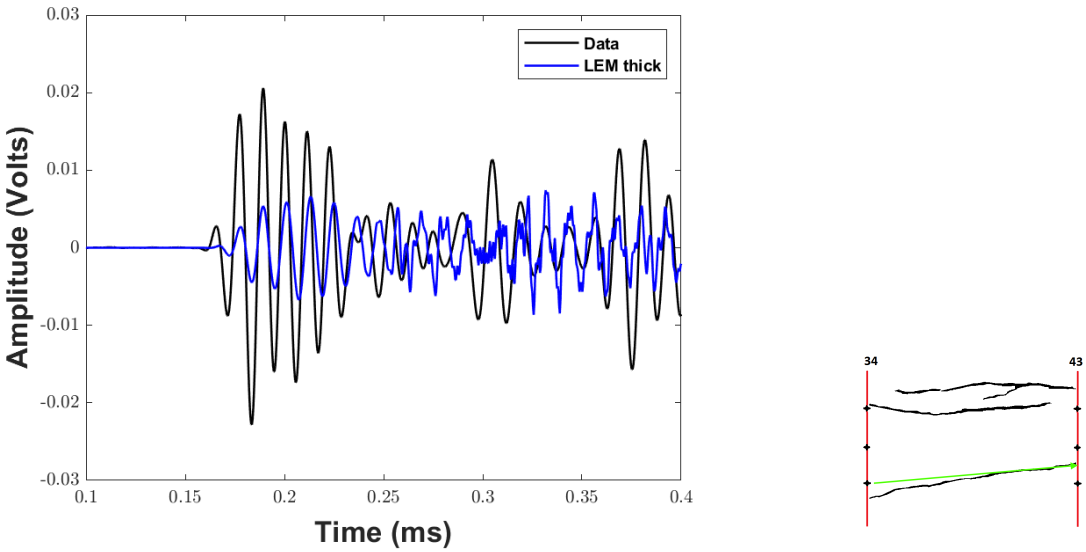

(b)

Figure 5.20: Waveforms for the frame between boreholes 34-43 for the LEM model with thick LEM layer. The two shot positions are on borehole 34 and recording on borehole 43. On the side is the sketch of the ray-path of the wave. 5.20a, shot depth at 0.4 m and recording at 0.8 m and 5.20b shot depth at 0.6 m and recording at 0.5 m.

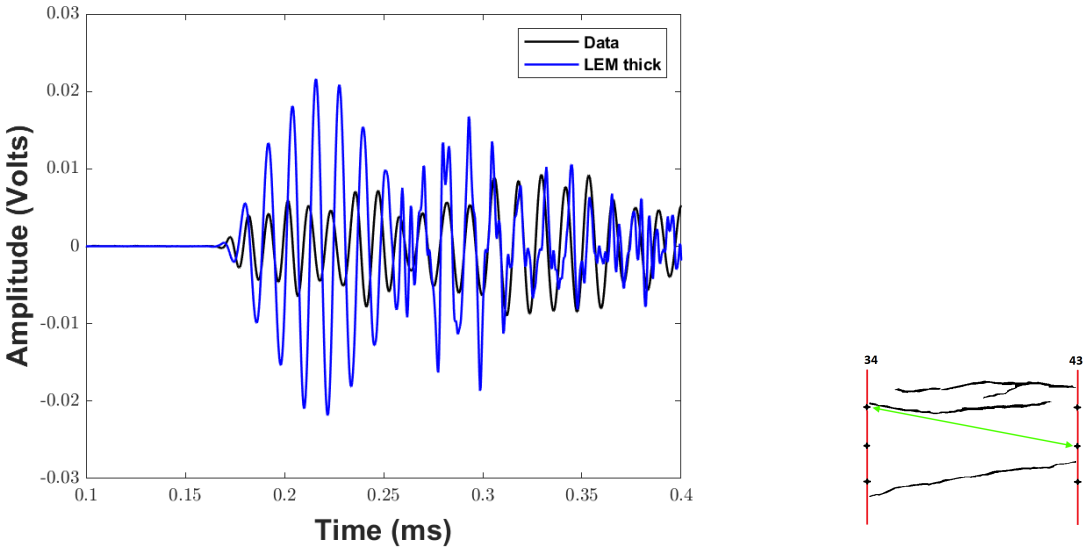

(a)

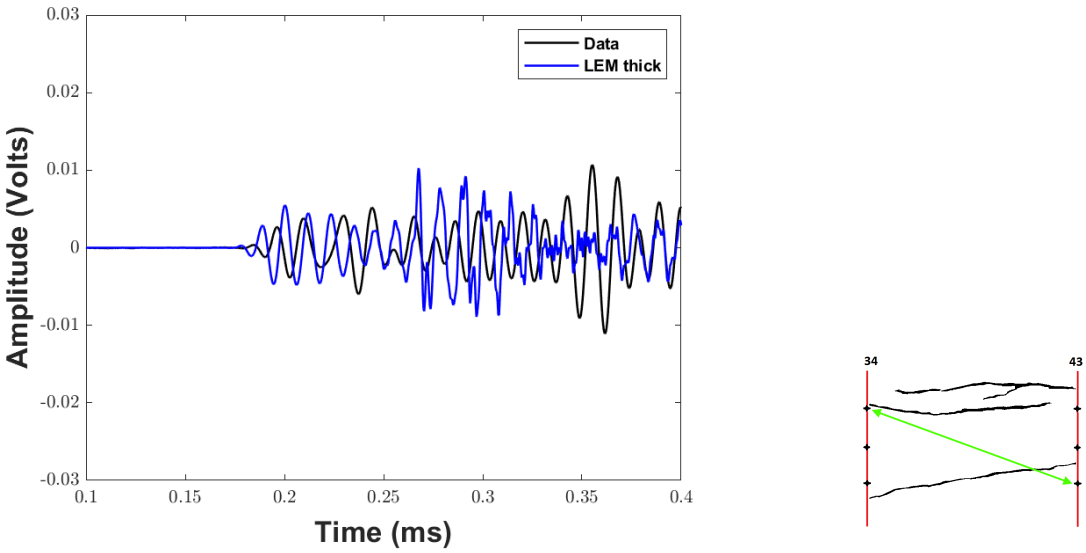

(b)

Figure 5.21: Waveforms for the frame between boreholes 34-43 for the LEM model with thick LEM layer. The first shot position is on borehole 34 and the second on borehole 43 recording on 43 and 34 respectively. On the side is the sketch of the ray-path of the wave. 5.21a, shot depth at 0.2 m and recording at 0.4 m and 5.21b shot depth at 0.6 m and recording at 0.2 m.

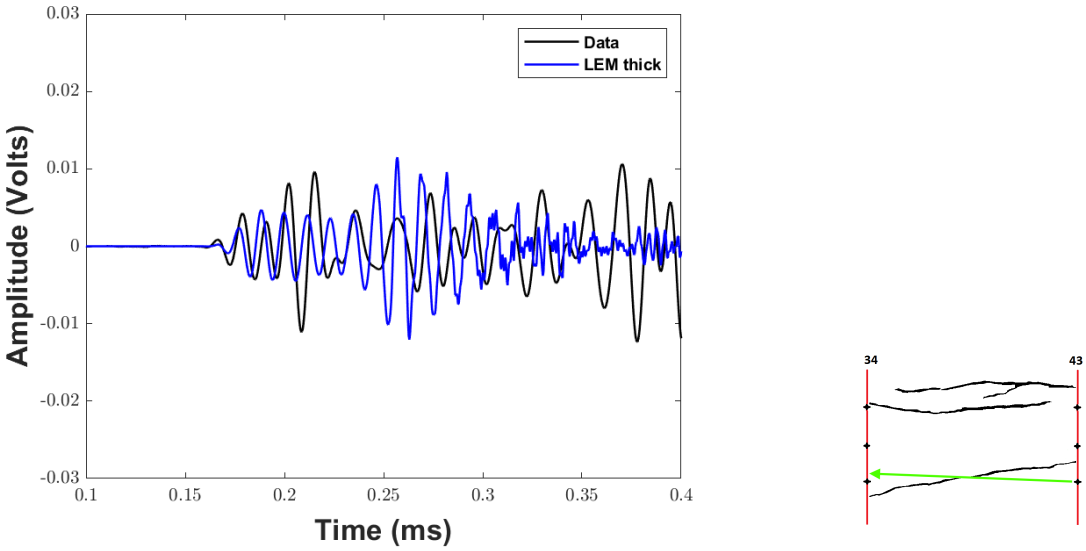

(a)

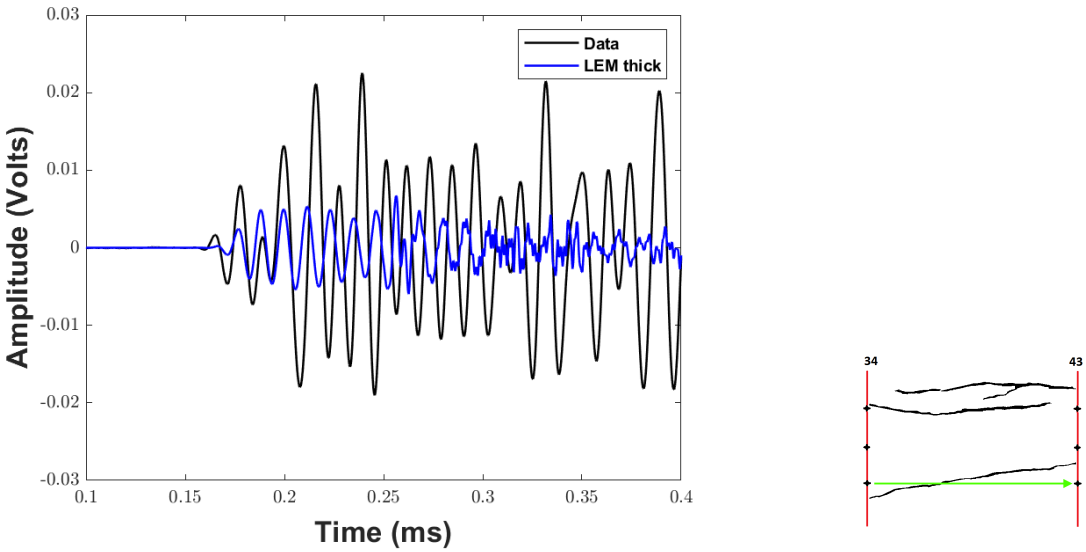

(b)

Figure 5.22: Waveforms for the frame between boreholes 34-43 for the LEM model with thick LEM layer. The two shot positions are on borehole 43 and recording on borehole 43. On the side is the sketch of the ray-path of the wave. 5.22a, shot depth at 0.6 m and recording at 0.55 m and 5.22b shot depth at 0.6 m and recording at 0.6 m.

Localised Effective Medium (fine layer) model results

LEM with thin layers uses a geometrical approach similar to the pixelised explicit model in which the dipping fractures are split into horizontal and vertical components. The thickness of each pixelised layer is equal to the element size and this gives the 1/L value to be 200 m^{-1} for all of the fractures. Similarly to the previous cases, the angles and the stiffness values used are given in Table 5.4.

The results in some cases are similar to the previous LEM case. Overall, the amplitude of the waves in this LEM model is lower than the survey data apart from some exceptions. Furthermore, the wave velocities of the LEM thin layer models approach the survey data with differences between 0.01 to 0.0006 ms (Table 5.8).

In Figure 5.23a, the waveform does not match the data where the amplitude drops significantly. The first arrival is 0.01 ms faster than the survey data as the wave passes through the F1 fracture. In Figure 5.23b, the modelled data are less attenuated and the maximum amplitude is three times higher than the survey data. For the ray-path in Figure 5.24a, the result of the models are still good both in terms of amplitude and velocity. On the other hand, the waveforms in Figure 5.25 are more attenuated than the survey data in amplitude and in arrival time, but better compared to the previous LEM model.

Overall, the LEM model with fine layer is a very good approach with good matches to the real data since the fracture model is able to catch some of the complexity of the reality. The thin layers and higher 1/L are responsible for the better velocity and slightly more attenuated waveforms compared to the LEM with a thick layer. Below, the Table 5.8 compares the amplitude and first arrival of the survey waveforms and the LEM fine layer model data.

	Normalised peak-to-peak amplitude	Normalised first arrival
Ray-path 1	0.63	0.95
Ray-path 2	2.70	0.99
Ray-path 3	3.46	0.97
Ray-path 4	0.54	0.99
Ray-path 5	1.03	1.00
Ray-path 6	0.94	1.00

Table 5.8: Values of peak-to-peak amplitude of the LEM model with fine layer waveforms normalised to the survey data, along with the normalised first arrival, for the six ray-paths presented below.

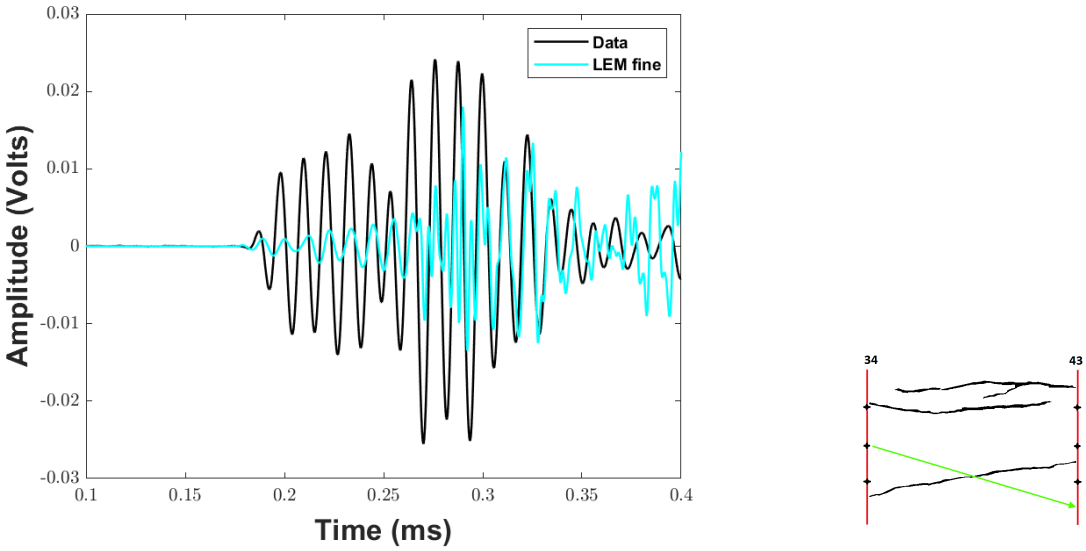

(a)

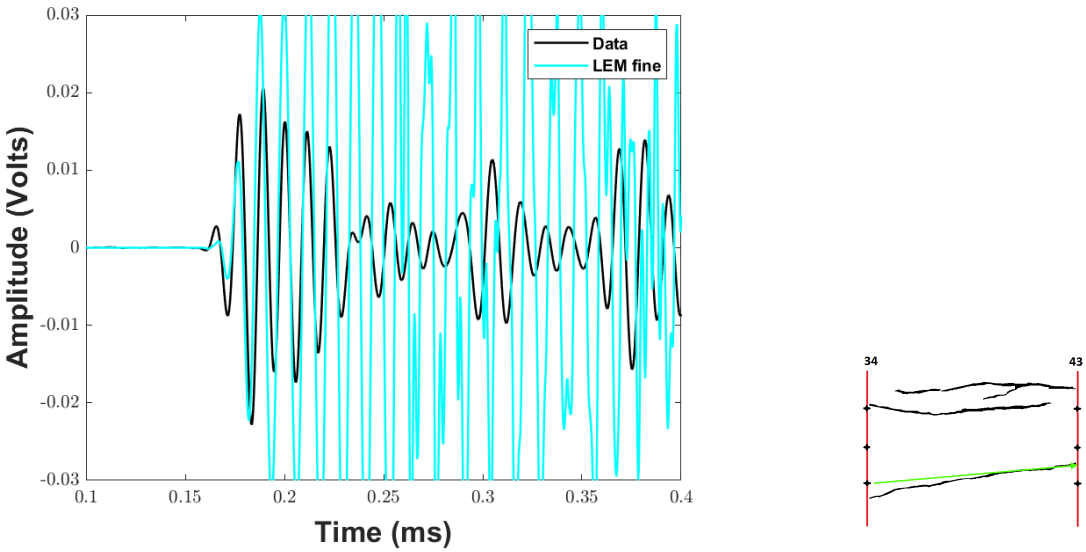

(b)

Figure 5.23: Waveforms for the frame between boreholes 34-43 for the LEM model with fine LEM layer. The two shot positions are on borehole 34 and recording on borehole 43. On the side is the sketch of the ray-path of the wave. 5.23a, shot depth at 0.4 m and recording at 0.8 m and 5.23b shot depth at 0.6 m and recording at 0.5 m.

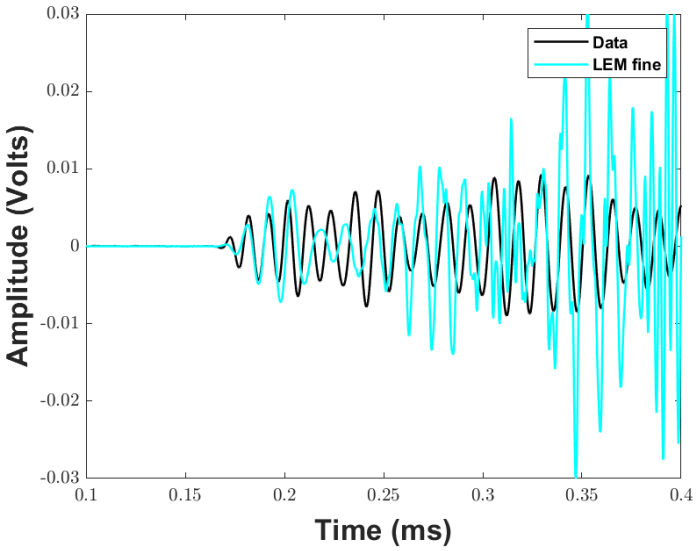

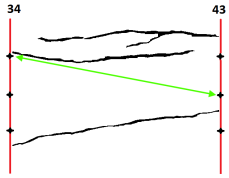

(a)

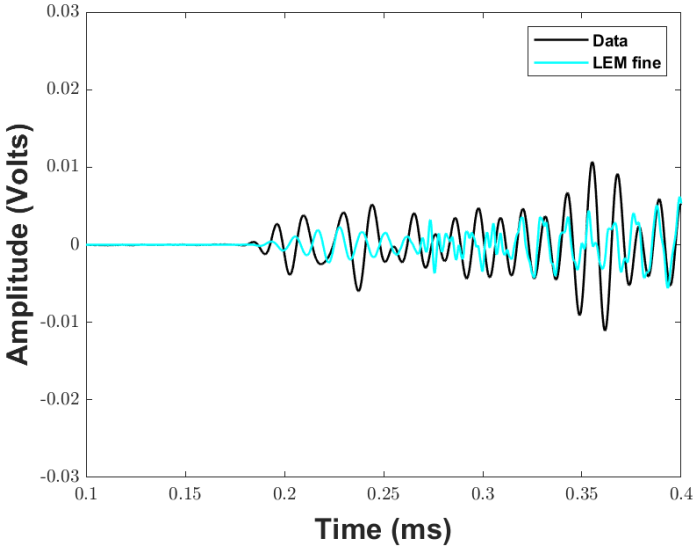

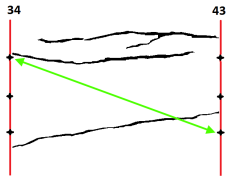

(b)

Figure 5.24: Waveforms for the frame between boreholes 34-43 for the LEM model with fine LEM layer. The first shot position is on borehole 34 and the second on borehole 43 recording on 43 and 34 respectively. On the side is the sketch of the ray-path of the wave. 5.24a, shot depth at 0.2 m and recording at 0.4 m and 5.24b shot depth at 0.6 m and recording at 0.2 m.

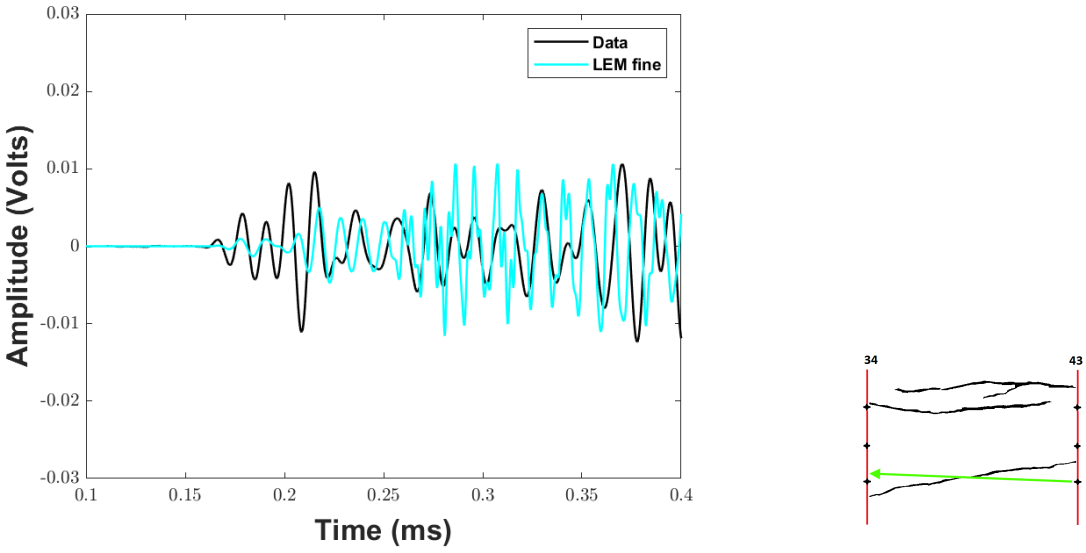

(a)

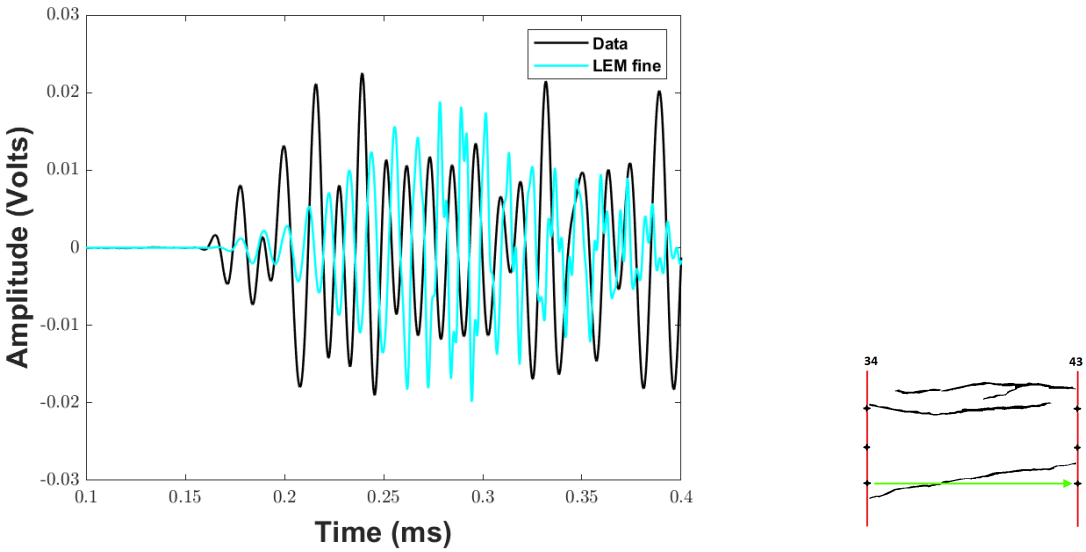

(b)

Figure 5.25: Waveforms for the frame between boreholes 34-43 for the LEM model with fine LEM layer. The two shot positions are on borehole 43 and recording on borehole 43. On the side is the sketch of the ray-path of the wave. 5.25a, shot depth at 0.6 m and recording at 0.55 m and 5.25b shot depth at 0.6 m and recording at 0.6 m.

Pixelised Explicit model results

The pixelised Explicit model converts the dipping fractures and splits them into horizontal and vertical components. The stiffness values used are in Table 5.4. The values of fracture stiffness have been modified based on the angle of each fracture as described in previous section 4.5.1.

Most of the waveforms are similar to both LEM cases. The amplitude of the waves in this explicit model is at similar level as the survey data. In addition, the wave velocities of the pixelised explicit model agrees with the survey data in most cases.

In Figure 5.26a, the waveform matches the data for the amplitude with slightly faster arrival time. In Figure 5.26b, the result of the models are good in terms of velocity, but the amplitude is about 2.7 times higher than the survey but similar to the LEM with fine layer (see Tables 5.9 and 5.8). For the ray-path in Figure 5.27a the first 1 ms are similar. The model waveform in Figure 5.27b is more attenuated compared to survey data and performs similar to the LEM with fine layer.

Overall, the pixelised explicit model is the better approach, of the two explicit models, with good matches to the real data since the fracture model is able to catch some of the complexity of the reality. The maximum time difference between explicit model and survey data is 0.0086 ms and minimum is 0.0009 ms as shown in Table 5.9 which summarises the values for amplitude and first arrival.

	Normalised peak-to-peak amplitude	**Normalised first arrival**
Ray-path 1	0.56	0.95
Ray-path 2	2.69	0.99
Ray-path 3	1.82	0.98
Ray-path 4	0.42	0.99
Ray-path 5	1.10	1.00
Ray-path 6	0.80	1.01

Table 5.9: Values of peak-to-peak amplitude of the pixelised fractures explicit model waveforms normalised to the survey data, along with the normalised first arrival, for the six ray-paths presented below.

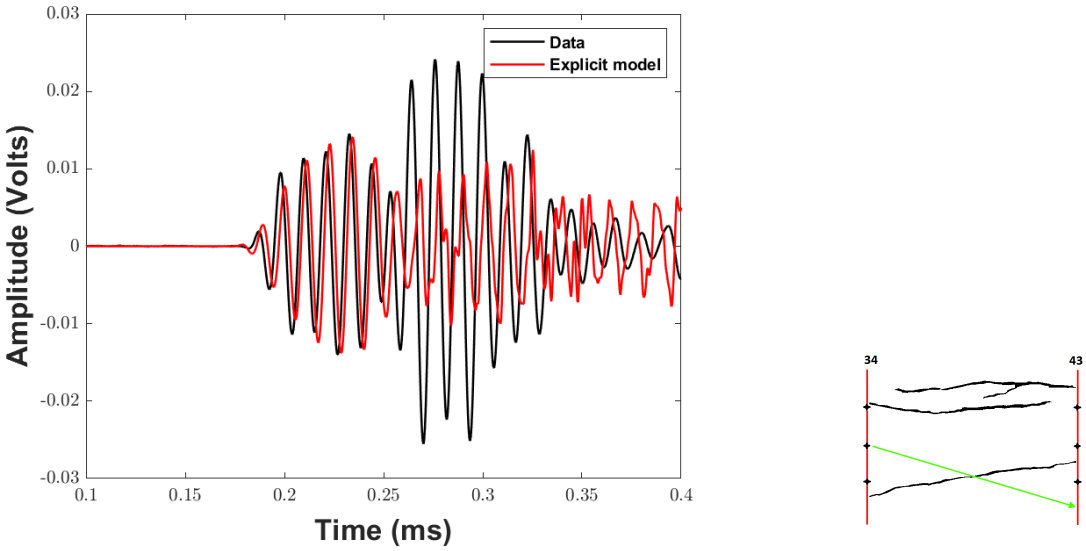

(a)

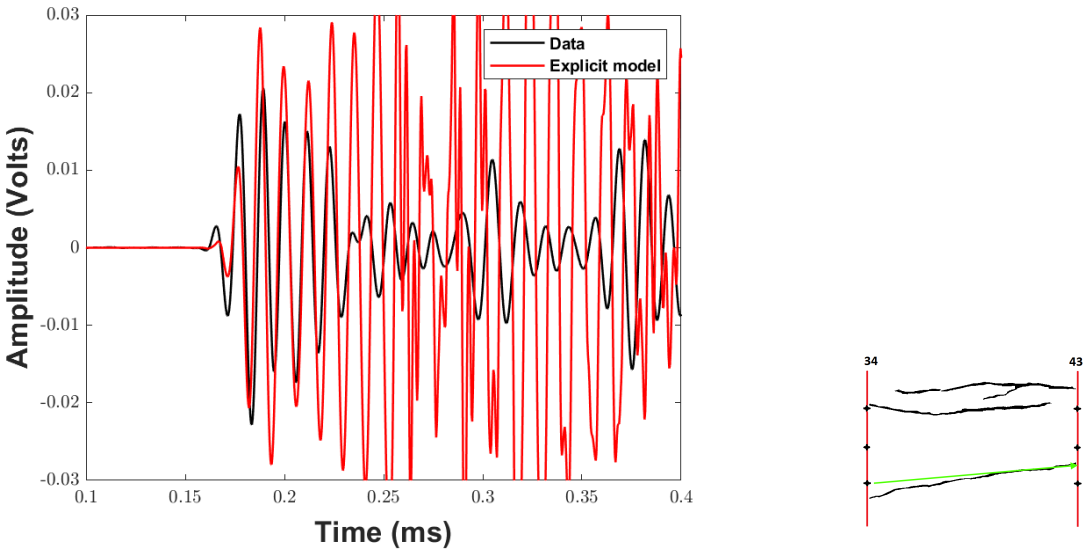

(b)

Figure 5.26: Waveforms for the frame between boreholes 34-43 for the Explicit model with pixelised fractures. The two shot positions are on borehole 34 and recording on borehole 43. On the side is the sketch of the ray-path of the wave. 5.26a, shot depth at 0.4 m and recording at 0.8 m and 5.26b shot depth at 0.6 m and recording at 0.5 m.

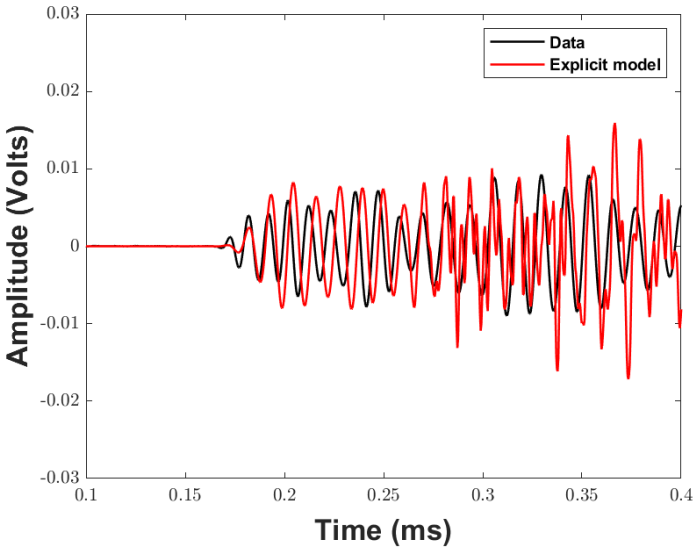

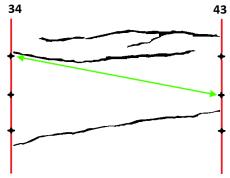

(a)

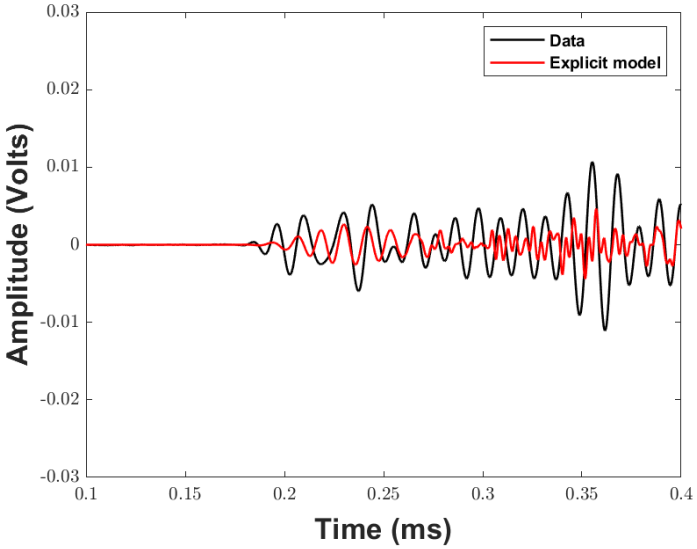

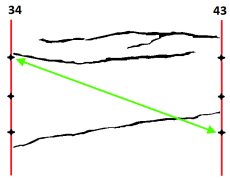

(b)

Figure 5.27: Waveforms for the frame between boreholes 34-43 for the Explicit model with pixelised fractures. The first shot position is on borehole 34 and the second on borehole 43 recording on 43 and 34 respectively. On the side is the sketch of the ray-path of the wave. 5.27a, shot depth at 0.2 m and recording at 0.4 m and 5.27b shot depth at 0.6 m and recording at 0.2 m.

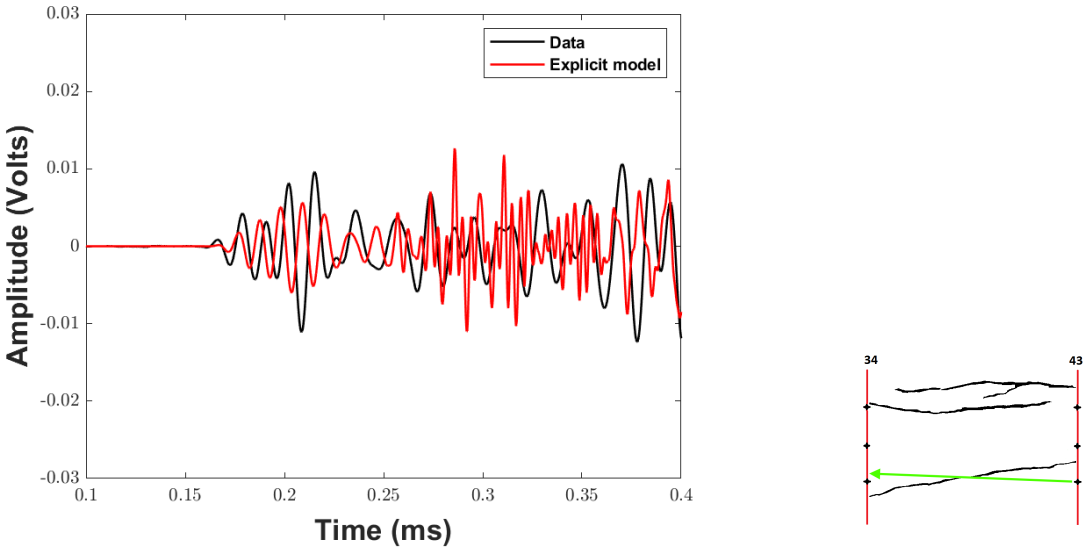

(a)

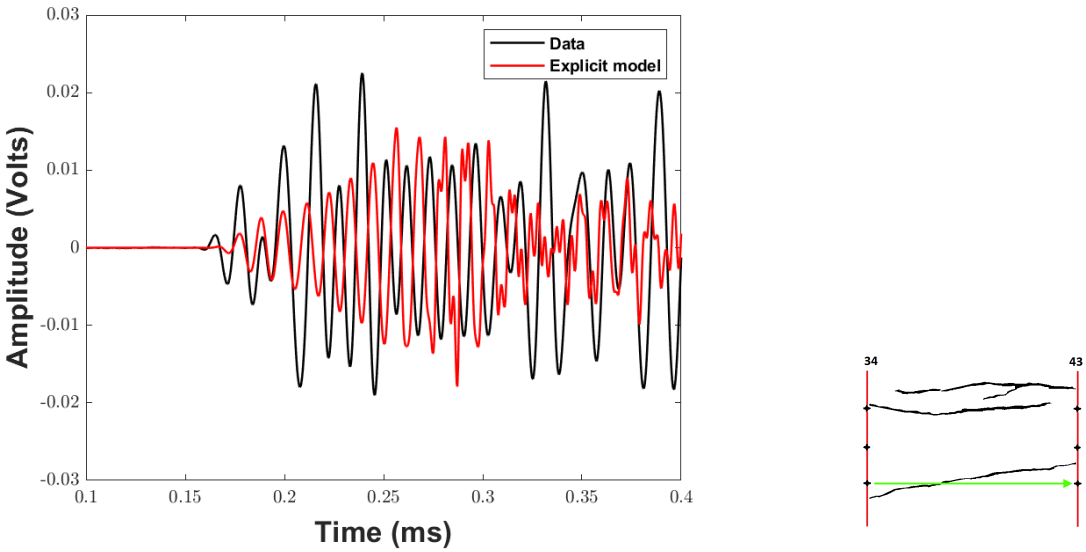

(b)

Figure 5.28: Waveforms for the frame between boreholes 34-43 for the Explicit model with pixelised fractures. The two shot positions are on borehole 43 and recording on borehole 43. On the side is the sketch of the ray-path of the wave. 5.28a, shot depth at 0.6 m and recording at 0.55 m and 5.28b shot depth at 0.6 m and recording at 0.6 m.

Equivalent Discrete Fracture Medium model results

The Equivalent Discrete Fracture Medium model converts the dipping fractures and splits them into horizontal and vertical components. I calculate the fracture density ϵ for the horizontal and vertical axes and use that as input values. Randomly placed rectangular fractures are created in a horizontal and vertical direction with the same fracture density as the original fracture. The stiffness values used are in the Table 5.4. The majority of the waveforms match neither the data nor the other model results. The amplitude of the waves in this Equivalent Discrete Fracture Medium model is much lower. Furthermore, the wave velocities of the model data do not correlate with the survey data in most cases as summarised in table 5.10.
The Equivalent Discrete Fracture Medium model has lower amplitude and slower velocities because of the high number of small fractures which create more attenuation of this high frequency signal. In order to make this model to work, further adjustments are required to balance the size of the fractures with the frequency of the signal and the fracture stiffness.

	Normalised peak-to-peak amplitude	**Normalised first arrival**
Ray-path 1	0.49	0.97
Ray-path 2	0.19	1.28
Ray-path 3	2.50	1.04
Ray-path 4	0.39	1.02
Ray-path 5	0.32	1.14
Ray-path 6	0.14	1.18

Table 5.10: Values of peak-to-peak amplitude of the equivalent discrete fracture medium model waveforms normalised to the survey data, along with the normalised first arrival, for the six ray-paths presented below.

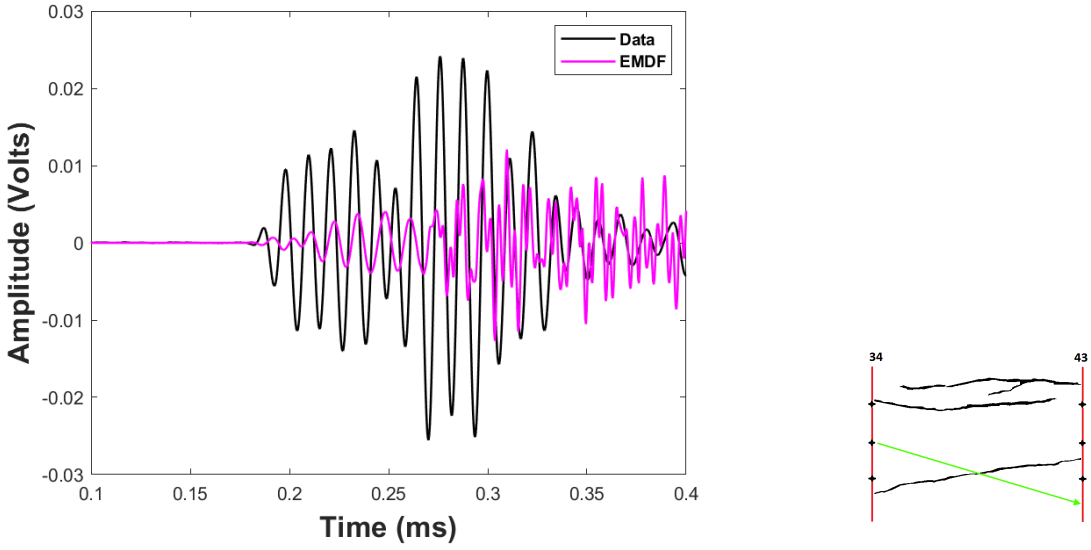

(a)

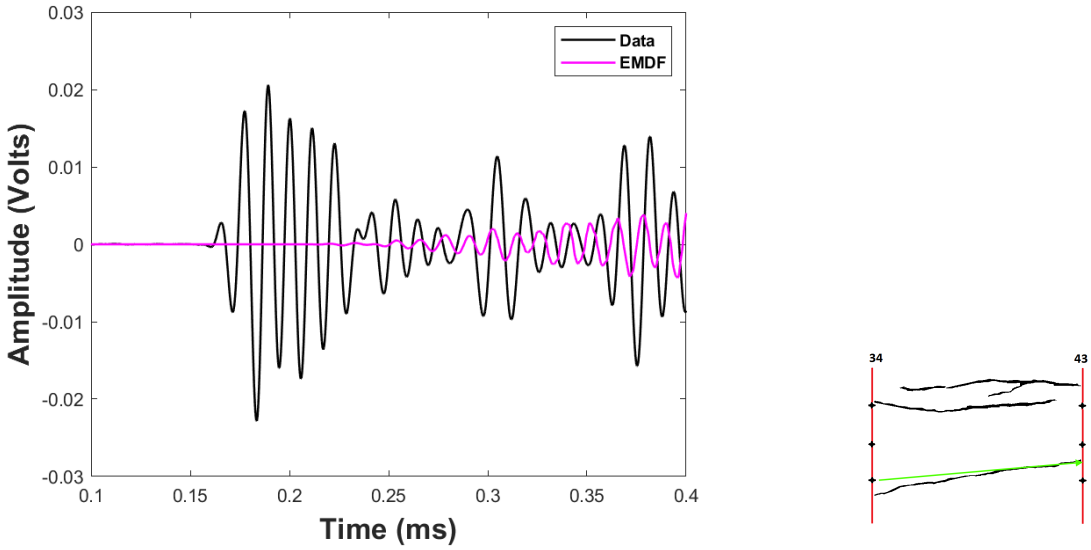

(b)

Figure 5.29: Waveforms for the frame between boreholes 34-43 for the Equivalent Discrete Fracture Medium model. The two shot positions are on borehole 34 and recording on borehole 43. On the side is the sketch of the ray-path of the wave. 5.29a, shot depth at 0.4 m and recording at 0.8 m and 5.29b shot depth at 0.6 m and recording at 0.5 m.

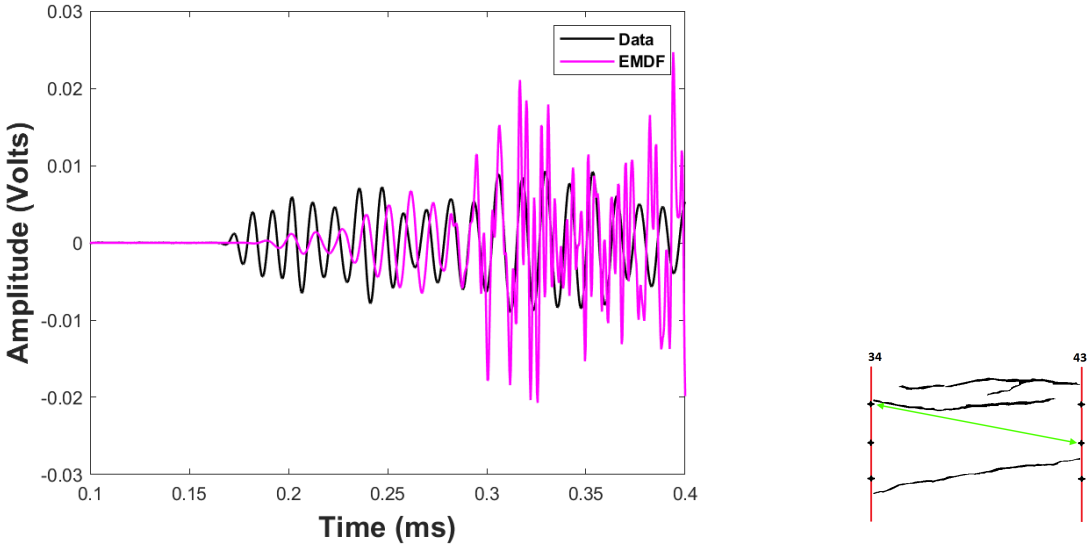

(a)

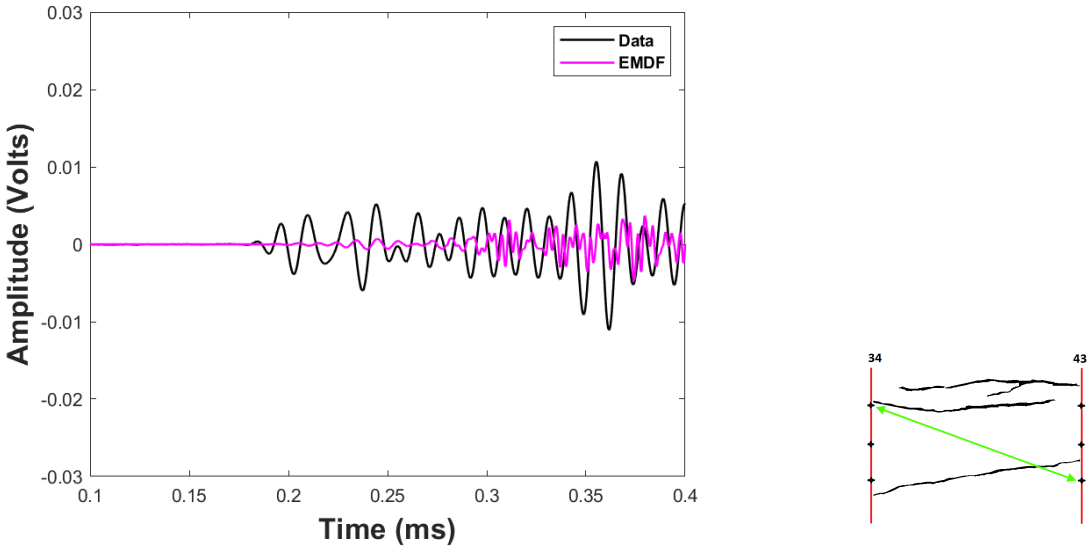

(b)

Figure 5.30: Waveforms for the frame between boreholes 34-43 for the Equivalent Discrete Fracture Medium model. The first shot position is on borehole 34 and the second on borehole 43 recording on 43 and 34 respectively. On the side is the sketch of the ray-path of the wave. 5.30a, shot depth at 0.2 m and recording at 0.4 m and 5.30b shot depth at 0.6 m and recording at 0.2 m.

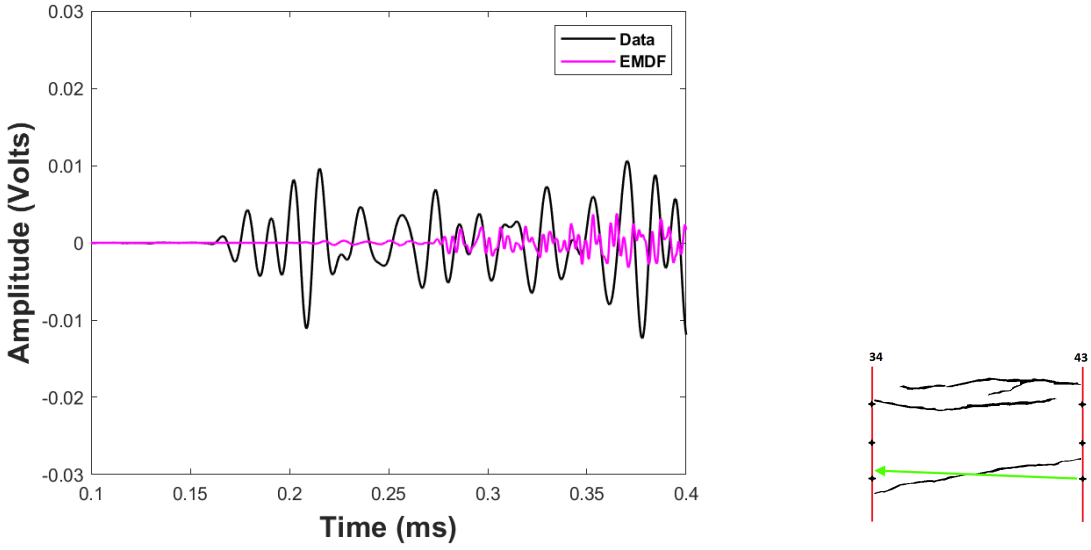

(a)

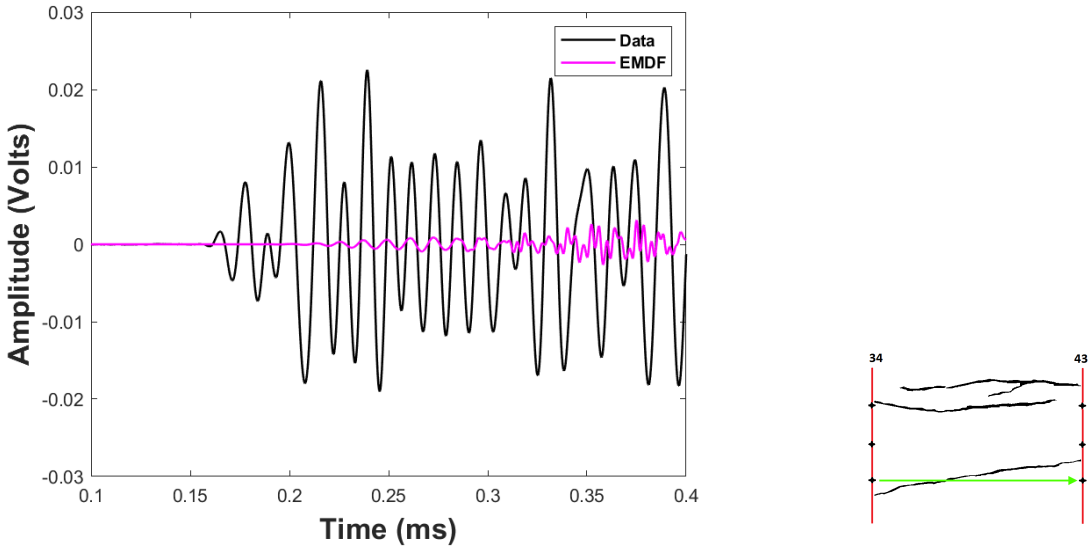

(b)

Figure 5.31: Waveforms for the frame between boreholes 34-43 for the Equivalent Discrete Fracture Medium model. The two shot positions are on borehole 43 and recording on borehole 43. On the side is the sketch of the ray-path of the wave. 5.31a, shot depth at 0.6 m and recording at 0.55 m and 5.31b shot depth at 0.6 m and recording at 0.6 m.

5.4.2 Implications

The tables 5.5 to 5.10 contain information about the first arrival, the maximum and the minimum amplitude for the models and the survey data, for all the six ray-paths presented. The first arrival for the models and the survey data has been calculated using the root mean square (RMS) amplitude with a threshold value to be just above numerical noise ($5 \times 10^{-}6$) for the models and above ambient noise ($5 \times 10^{-}4$). The reason for the tables is to summarise the output of the models using these three variables to quantify the performance of each model.
In the cases presented above, the pixelised explicit model, the fine LEM and the thick LEM models are closer to the survey data. The other two models do not perform as well. As a result, the EM and the EDFM will no longer be used further, for this particular modelling project.

5.5 Optimisation

Apart from the cases shown above where one or more waveforms from the different fracture models match with the survey, the majority suffer from either earlier or later arrival and higher or lower amplitude. Increasing or decreasing the fracture stiffness could have an effect on the final result.
Based on the comparisons of the models against the survey data, I conclude on which fractures need adjustment on stiffness. For the survey in boreholes 34 and 43 (Figure 5.10), the waves are more attenuated in terms of amplitude around the F1 fracture. F1 fracture has some unique characteristis, is large enough to cover the whole block and with a smooth dipping. The depth of the fracture is between 0.5-0.7 m and isolated from the other fractures and the free surface. The fact that it is isolated, is helpful at this stage, since the stiffness of a single fracture will need to be adjusted avoiding any complex system with more fractures which might create non-unique results.

5.5.1 Stress-dependent stiffness versus manual iterative optimisation.

In the previous chapters, I have shown that when the fracture stiffness is linked with the stress field the result from the models approach reality. For this specific case, however, I am not going to use the same stress-dependent method to optimise the fracture stiffness. Instead manual iterative optimisation for fracture stiffness will be

used.

The reasons for not using the previous method of stress-dependence are both due to physical and numerical limitations.

First of all, based on the theory (Bandis *et al.*, 1983), stiffness is calculated based on the value of stress normal to the fracture surface. Since the fractures on the borehole frame 34-43 being modelled are almost horizontal (Table 5.4 for fracture dipping), the normal stress will be the vertical stress. The stress in the tunnel surface will be equal to zero and increase with depth. As a result, the stress dependent solutions will have a small effect on the fractures linked with the EDZ. Moreover, as shown in the previous chapter, when the wave propagates parallel to the fractures, the stress dependence method barely changes the final result. In this case, the waves propagate between 0^o to 60^o from the horizontal surface and the stress dependence method will have a similar result with a manual iterative optimisation method, since most of the waves will propagate at small angles or almost parallel to the fractures.

The second reason for not using the stress dependence method at this stage is more technical. The newly developed stress dependence function for the LEM model has not been optimised in terms of computational memory use and, as a result, is a very slow process. The model I am using at the moment is 8 times larger than the models used in previous chapters and run on a special version of WAVE3D and still needs more computational time to run them (see Table 3.12 in Chapter 3). In addition, extra time will be needed to add the function of stress dependence for LEM to this WAVE3D version. On the other hand, I can run multiple models at the same time for the manual iterative optimisation so save time.

However, the stress dependent solution might be able to produce more accurate results. For that reason it would be an interesting topic for future study to compare the results with the manual iterative optimisation.

5.5.2 Demonstrate manual iterative optimisation

Based on the scale between fracture size and compliance stiffness from Worthington & Lubbe (2007) I have used the lowest stiffness value from the suggested range. For the size of F1 fractures, the suggested range of stiffness is up to a hundred times higher.

As a result, I have created thirteen cases with different stiffness. The stiffness used on each model is summarised in table 5.11 anf Figure 5.32. For the first ten cases, I

increase the normal stiffness from ten to one hundred times the initial stiffness value at intervals of ten and the shear stiffness is always calculated as a factor of 0.33 of the normal stiffness. In the last three cases, the normal fracture stiffness is constant and the factor for the shear stiffness changes as 0.5, 0.6 and 0.2.

I have selected a specific ray-path to present in this part and attempted to optimise the fracture stiffness in order to better approach the survey data. The ray-path selected goes from borehole 43 to 34 with the shot position at 0.6 m depth and recording at 0.55 m on 34 5.33. This ray-path is also presented in the previous section. One of the reasons for choosing that ray-path is because it only involves crossing one single fracture (F1) and, consequently, it will not be affected by other fractures that will complicate the optimisation process. Furthermore, both the fracture and the ray-path are relatively deep and away from any other fracture that could add extra information to the first 2 ms of the waveform, due to reflections and diffraction of the nearby fractures. Fracture F1 is a large fracture that cuts through the whole block at a smooth angle and, as a result, the chosen ray-path propagates with an angle of approximately 10^o. Finally, the specific path showed a significant change on the resulting waveform during the optimisation process.

There are a large number of waveforms and figures resulting from the optimisation process. In this section, I present only the key figures from four of the thirteen cases. The results of the three models for the chosen ray-path are presented in figures 5.34 to 5.45. Appendix D includes all the thirteen cases for the specific ray-path and for two more ray-paths crossing only fracture F1, those are the ray-path 4 and 6 presented in the previous section.

For this wave frequency and for these propagation angles relative to the fracture, the small changes in the stiffness, in the first couple of cases, were not enough to change the result for the explicit and the fine LEM models (Figures 5.34, 5.38 and 5.42). As the stiffness reaches forty times the initial stiffness, the amplitude of these two models is similar to the survey data (figures 5.35, 5.39 and 5.43). When the stiffness goes above fifty times the initial stiffness, the amplitude of the models is much higher than the data for all three models (figures 5.36, 5.40 and 5.44). The velocity of the waveforms does not change significantly for the two LEM cases with maximum differences up to 0.0022 ms. For the explicit case, the velocity remains the same for all different situations.

Cases eleven to thirteen, where the shear stiffness is the one that changes, have lower

impact on the amplitude of the waveform compared to the changes with normal stiffness (figures 5.37, 5.41 and 5.45). In this case, the amplitude of the waveform is reduced by about 5% compared to the case five with the same normal stiffness.

	Normal stiffness K_n (Pa/m)	**Shear stiffness K_s (Pa/m)**
Case 1	3.33×10^{11}	1.00×10^{11}
Case 2	6.67×10^{11}	2.00×10^{11}
Case 3	1.00×10^{12}	3.00×10^{11}
Case 4	1.33×10^{12}	4.00×10^{11}
Case 5	1.67×10^{12}	5.00×10^{11}
Case 6	2.00×10^{12}	6.00×10^{11}
Case 7	2.33×10^{12}	7.00×10^{11}
Case 8	2.67×10^{12}	8.00×10^{11}
Case 9	3.00×10^{12}	9.00×10^{11}
Case 10	3.33×10^{12}	1.00×10^{12}
Case 11	1.67×10^{12}	8.33×10^{11}
Case 12	1.67×10^{12}	1.0×10^{12}
Case 13	1.67×10^{12}	3.33×10^{11}

Table 5.11: Values used for optimising Normal K_n and Shear K_s fracture stiffness for fracture F1.

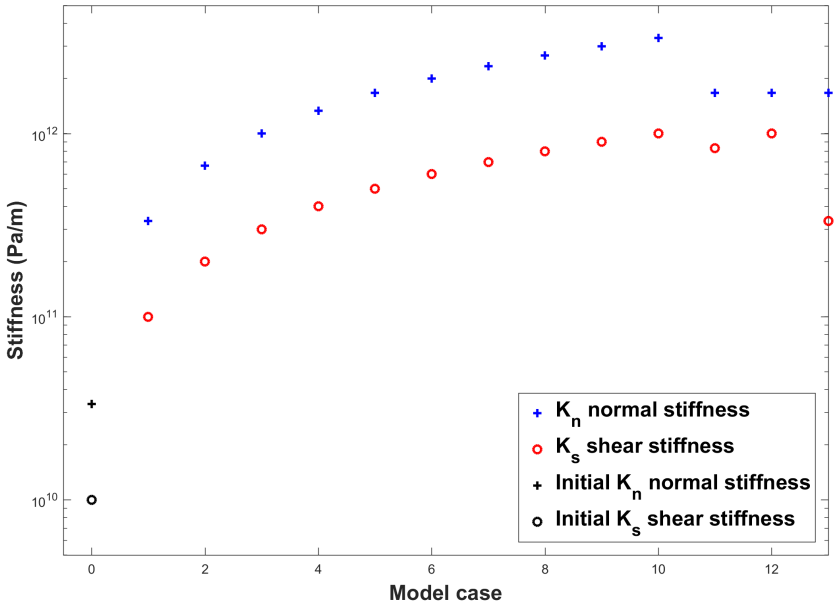

Figure 5.32: Values used for optimising Normal K_n and Shear K_s fracture stiffness for fracture F1 versus model case.

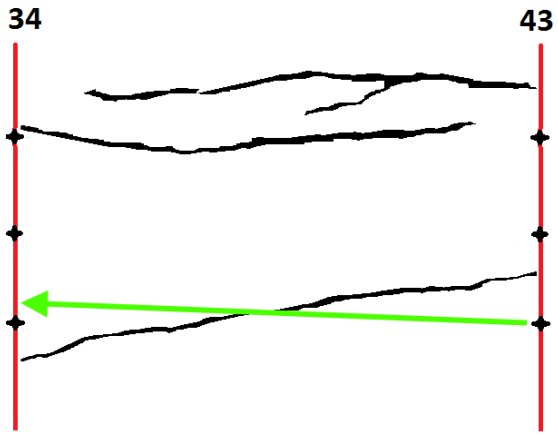

Figure 5.33: 2D cross-section between borehole 34 and 43 when the ray-path has been optimised for normal K_n and shear K_s stiffness.

LEM thick layer results for stiffness optimisation

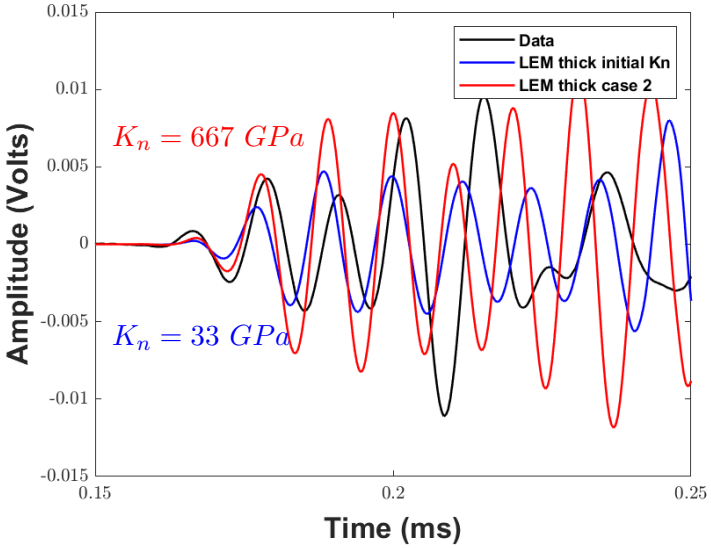

Figure 5.34: Case 2 (K_n twenty times higher than initial) waveforms for the frame between boreholes 34-43 for the LEM model with thick layer.

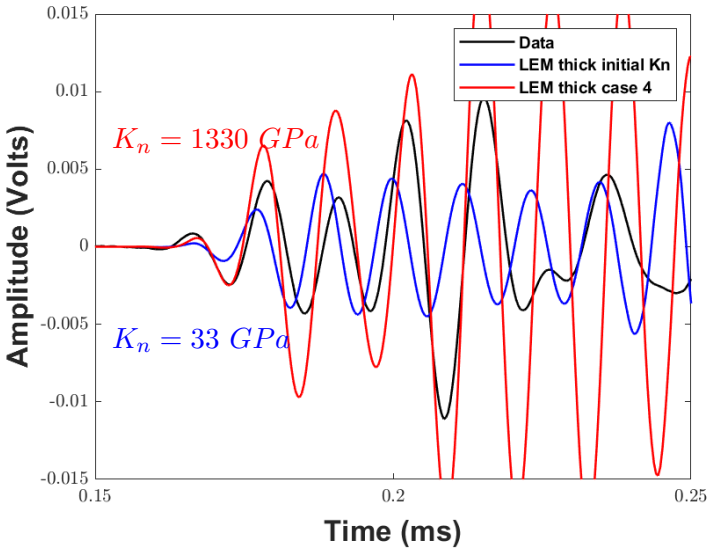

Figure 5.35: Case 4 (K_n forty times higher than initial) waveforms for the frame between boreholes 34-43 for the LEM model with thick layer.

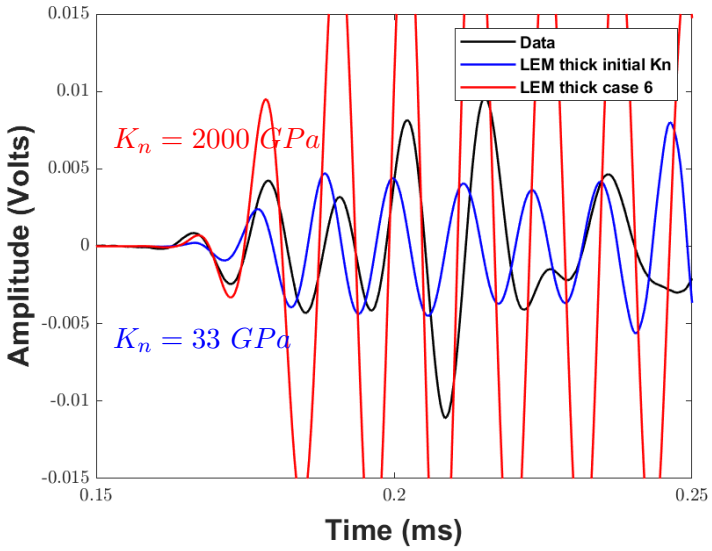

Figure 5.36: Case 6 (K_n sixty times higher than initial) waveforms for the frame between boreholes 34-43 for the LEM model with thick layer.

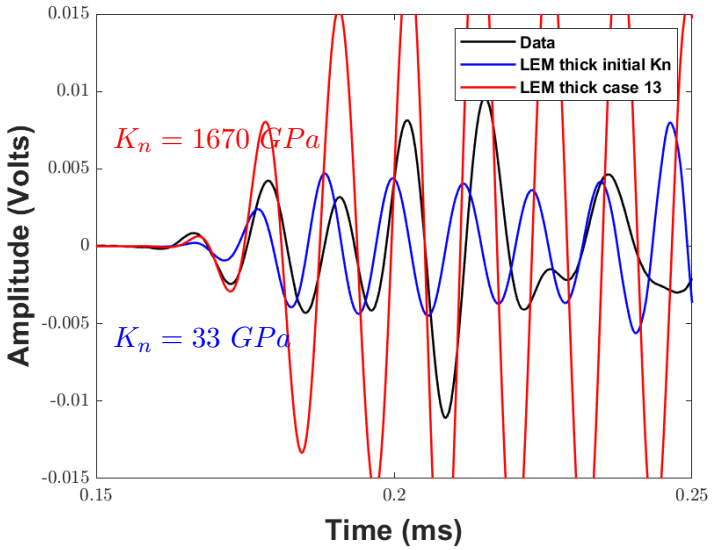

Figure 5.37: Case 13 (K_n fifty times higher than initial and K_s 0.6 of the initial) waveforms for the frame between boreholes 34-43 for the LEM model with thick layer.

LEM fine layer results for stiffness optimisation

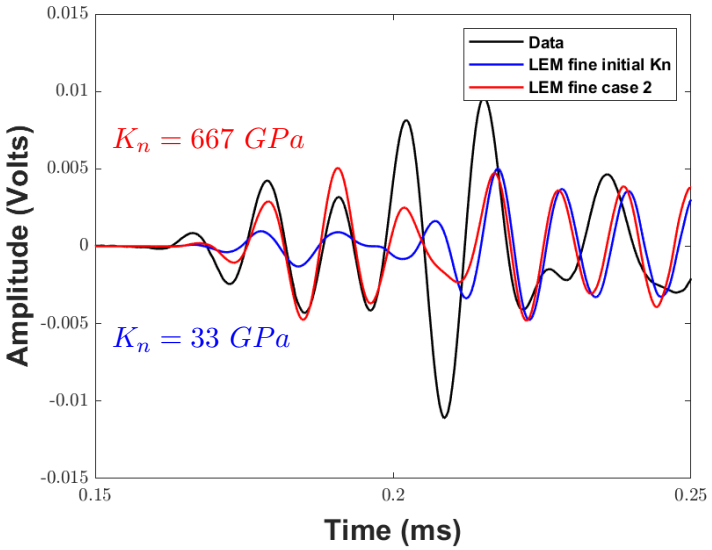

Figure 5.38: Case 2 (K_n twenty times higher than initial) waveforms for the frame between boreholes 34-43 for the LEM model with fine layer.

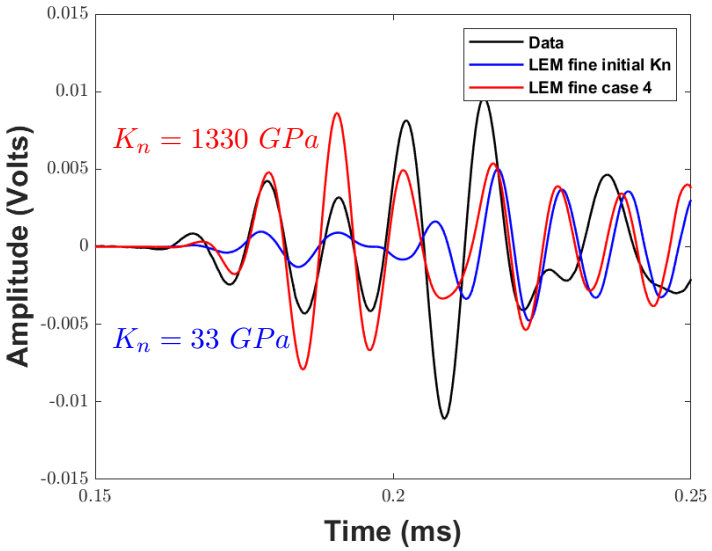

Figure 5.39: Case 4 (K_n forty times higher than initial) waveforms for the frame between boreholes 34-43 for the LEM model with fine layer.

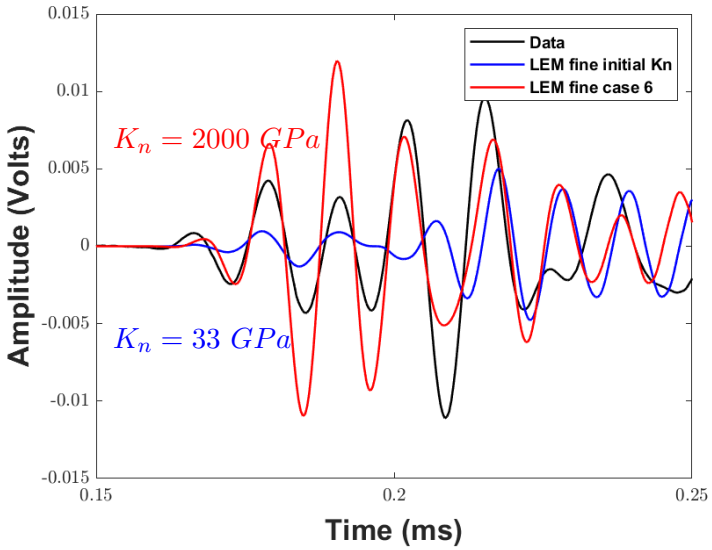

Figure 5.40: Case 6 (K_n sixty times higher than initial) waveforms for the frame between boreholes 34-43 for the LEM model with fine layer.

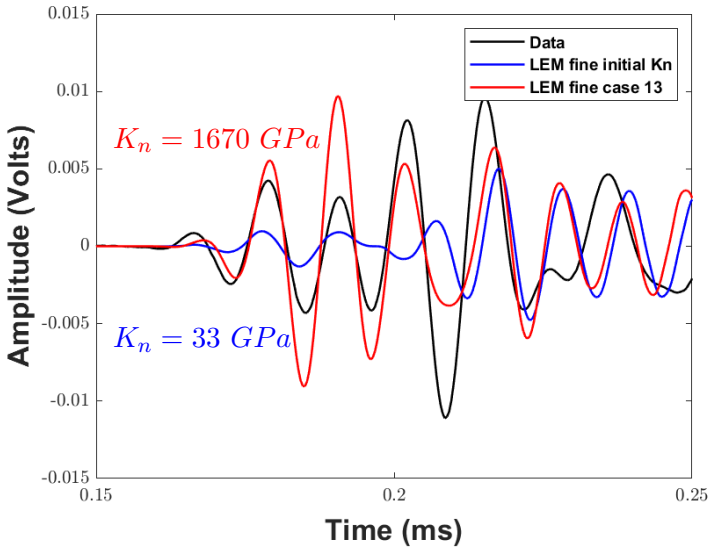

Figure 5.41: Case 13 (K_n fifty times higher than initial and K_s 0.6 of the initial) waveforms for the frame between boreholes 34-43 for the LEM model with fine layer.

Explicit model results for stiffness optimisation

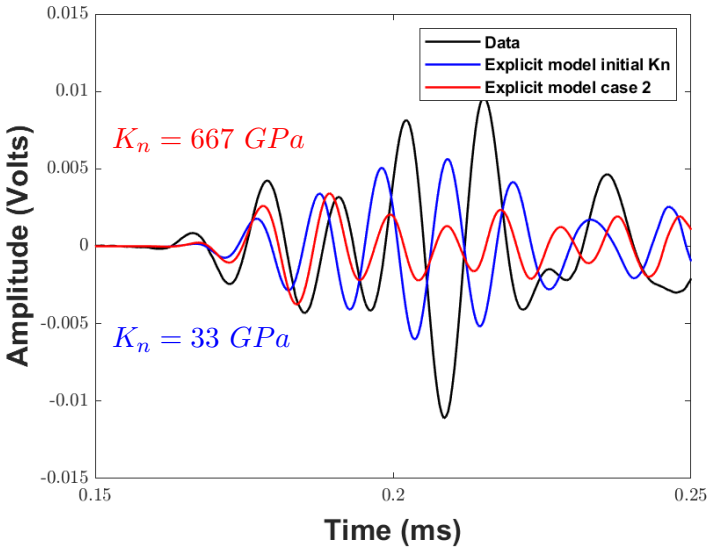

Figure 5.42: Case 2 (K_n twenty times higher than initial) waveforms for the frame between boreholes 34-43 for the LEM model with fine layer.

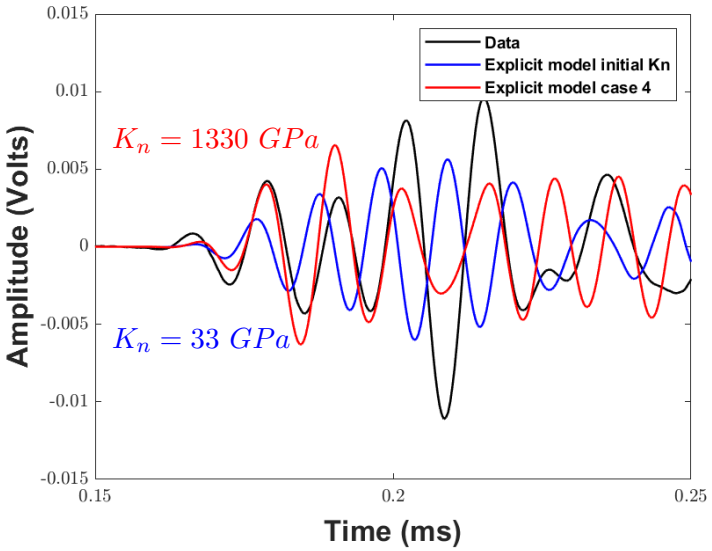

Figure 5.43: Case 4 (K_n forty times higher than initial) waveforms for the frame between boreholes 34-43 for the LEM model with fine layer.

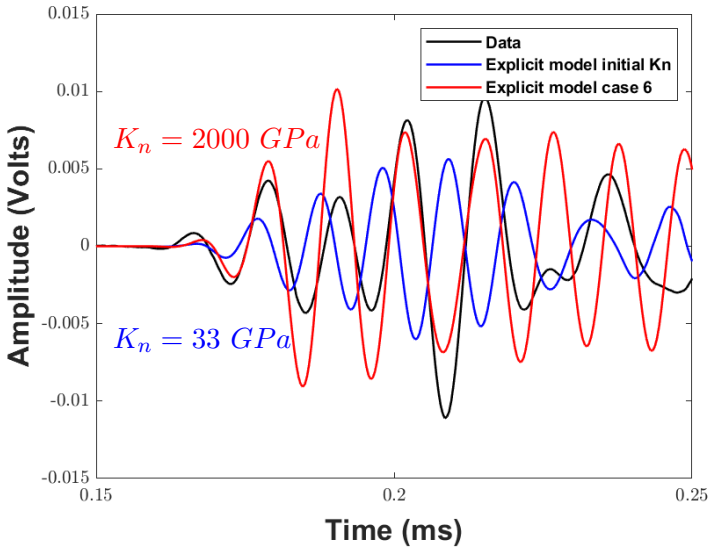

Figure 5.44: Case 6 (K_n sixty times higher than initial) waveforms for the frame between boreholes 34-43 for the LEM model with fine layer.

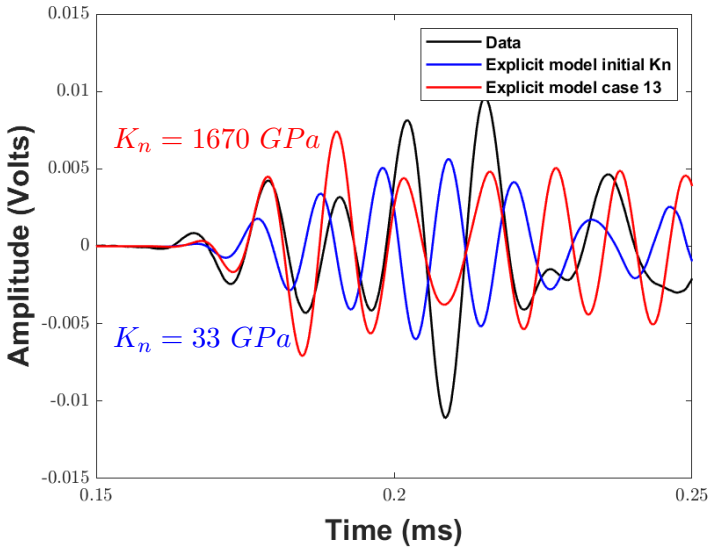

Figure 5.45: Case 13 (K_n fifty times higher than initial and K_s 0.6 of the initial) waveforms for the frame between boreholes 34-43 for the LEM model with fine layer.

Results - Initial vs "Best iterative" cases

Figure 5.46 and Tables 5.12 and 5.13 summarise the information for amplitude, maximum and minimum, and first arrival for all the thirteen cases. For the explicit model and the fine LEM, the amplitude increases up to five times in an almost linear process as the stiffness of the fracture increases. The waveforms for the thick LEM end in an amplitude which is almost double that of the other two models.

Normalised peak-to-peak amplitude			
	Explicit model	**LEM thick layer**	**LEM fine layer**
Case 1	0.37	0.75	0.47
Case 2	0.35	1.11	0.48
Case 3	0.47	1.41	0.65
Case 4	0.62	1.81	0.80
Case 5	0.78	2.48	0.97
Case 6	0.92	2.65	1.11
Case 7	1.07	2.86	1.23
Case 8	1.22	3.05	1.38
Case 9	1.37	3.20	1.49
Case 10	1.50	3.45	1.60
Case 11	0.90	2.30	1.04
Case 12	0.96	2.29	1.08
Case 13	0.70	2.37	0.91

Table 5.12: Values of peak-to-peak amplitude of for all cases used on optimising fracture stiffness for fracture F1 model waveforms normalised to the survey data.

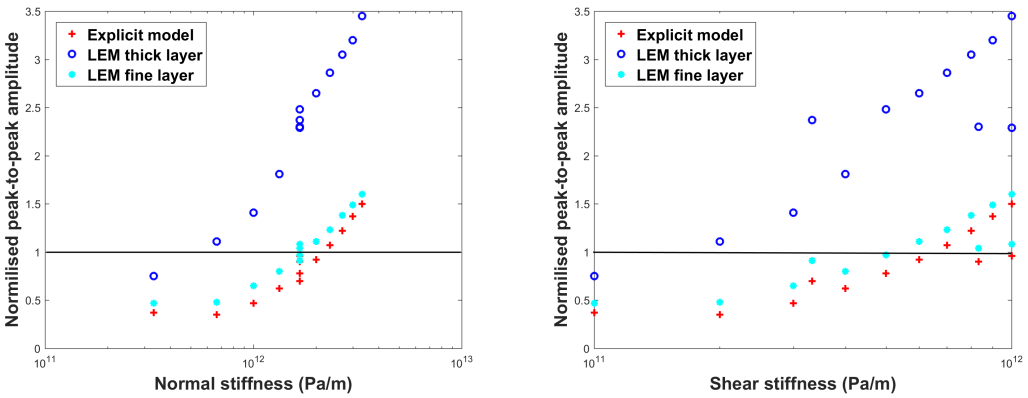

(a) (b)

Figure 5.46: Normalised peak-to-peak amplitude versus the normal 5.46a and shear 5.46b stiffness values for all 13 cases of stiffness optimisation (Table 5.11 and Figure 5.32).

Values first arrival (ms)			
	Explicit model	**LEM thick layer**	**LEM fine layer**
Case 1	1.007	0.991	1.005
Case 2	1.007	0.991	1.005
Case 3	1.007	0.991	1.007
Case 4	1.007	0.991	1.007
Case 5	1.007	0.991	1.007
Case 6	1.007	0.989	1.007
Case 7	1.007	0.989	1.009
Case 8	1.007	0.989	0.998
Case 9	1.007	0.989	0.998
Case 10	1.007	0.989	0.996
Case 11	1.007	0.991	1.007
Case 12	1.007	0.991	1.007
Case 13	1.007	0.991	1.007

Table 5.13: Values of normalised first arrival, of waveforms for all cases used on optimising fracture stiffness for fracture F1.

5.6 Discussion

Mapping and understanding the creation and evolution of the EDZ is a topic of high importance when considering the safety of a future GDF as described in Chapter 1. The P-wave velocity survey presented above is part of a series of experiments carried out in the future GDF of Finland in order to link the velocity changes with the man-made fractures as previously have been done (e.g., Collins *et al.*, 2002; Goodfellow & Young, 2014; Manukyan *et al.*, 2012; Marelli *et al.*, 2010; Young *et al.*, 2020). However the objective of this work is to use methods and conclusions made on the previous chapters and numerical models to produce comparable results.

The source inversion method based on previous work from Hildyard (2001), which was successfully used in Chapter 3, has now been enhanced to create an input source for a more modelling a far more complex velocity survey, achieving a considerably good result with correlation coefficient for intact rock between 0.86 to 0.97. The flexibility of the LEM model in terms of thickness as described and analysed in Chapter 4.1 created two subcategories of the LEM approach one with thick and one with very fine LEM layers for each fracture set. Finally, the need to run large models in the most efficient way created the pixelised and EDFM models as subcategories of the explicit approach for fracture representation.

Modelling such a survey was a challenging process from many aspects. The quality of the waveform data due to coupling (Marelli *et al.*, 2010), the complex geometry of the fracture network and the limited information of the stiffness of the fractures were some of the limitations for modelling this survey.

The initial results using EM, two LEM (thick and fine) and two explicit (pixelised and EDFM) approaches for representing fractures are in agreement with the conclusions made on the previous two chapters.

The EM did not work well. The waveforms from the EM models are delayed 1.26 to 1.65 times compared to the survey waveforms (as a reference P- to S-wave velocity ratio is 1.72, table 5.1). The direction of anisotropy, in the effective medium it has been used an average value of (34°/163°) while the azimuth of the line between borehole 34 and 43 is 90°. Taking a closer look on the snapshot of the wave propagation below in figure 5.47 can explain the delay in the arrival showing a fast direction for wave propagation parallel to the plane of anisotropy and a slow perpendicular to it. The amplitude of

the EM waveforms is 4 to 25 times higher. As previous chapters and literature suggests (e.g., de Figueiredo *et al.*, 2013; Ding *et al.*, 2014; Pyrak-Nolte *et al.*, 1990) the effective medium model cannot correctly predict the amplitude of transmitted waves. As in previous chapters the frequency is too high for that size of the fractures. Similar to chapter 3 the EM model is not expected to match the survey data for the reasons explained above, however is is used as a reference point on the compariosn of the two LEM cases.

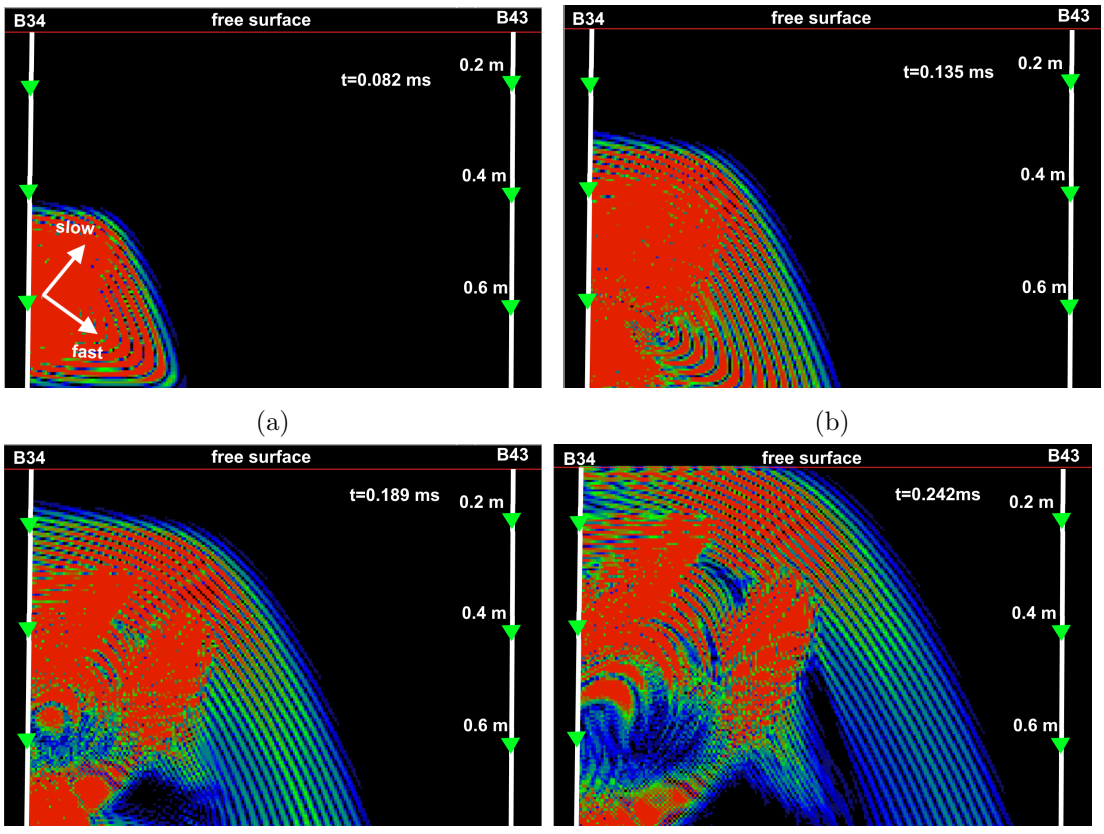

Figure 5.47: Snapshots of the wave propagation for the boreholes 34 to 43 with an example shot at 0.60 m depth at t=0.082 ms 5.47a, t=0.135ms 5.47b, t=0.189 ms 5.47c, and t=0.242 ms 5.47d showing a fast (parallel to the plane of anisotropy) and a slow (perpendicular to the plane of anisotropy) wave propagation.

The EDFM model fails to predict correctly the arrival time and the amplitude as the model waveforms are more attenuated and delayed. Similarly to Chapter 4.5 the dip

angles of the majority of the fractures are between 4° to 18°, these values are below the lower limit of 30° in which the EDFM model produces more comparable waveforms. The LEM with thick layer works well for some cases on the initial models but it is not able to predict well the part of the waveforms related to the reflections caused by the surrounding fractures. Likewise the pixelised explicit model successfully matches the arrival time and amplitude in most cases but it is underestimating the reflections too, thus, the stiffness of the EDZ fractures above must be lowered. The fine LEM model for the initial models, is successful on the arrival time but not on the amplitude.
The manual optimisation process for fracture stiffness has worked on increasing the amplitude of the waveforms, ending in more comparable results with the three models to perform more similar to the survey data. For the explicit and fine LEM, case 5 where the stiffness is K_n= 1670 GPa is the best case for uniform stiffness against the survey data. The equivalent value for the thick LEM is K_n= 667 GPa for case 2. Marelli *et al.* (2010) concluded that when comparing cross-hole tomography data against modelling it was easy to match the first two pulse cycles but the latter part becomes more unpredictable, this statement is in agreement with the current models. Even though the result has been improved, it never reaches a full match with the survey data. One possible explanation is that the stiffness used, is uniform throughout the whole fracture. As the uniform stiffness increases the amplitude of the waveform crossing the fracture increases in a linear relationship. In nature, such a fracture does not exist. Since the stress dependent stiffness is not feasible at the moment for such a large model, a different approach is needed. A possible solution for the future would be to further optimise the fracture stiffness by creating manually zones with higher and lower stiffness in order to mimic the stiffness of a natural fracture.

5.7 Summary and conclusions

Based on the findings and methodology developed in the previous section, I have modelled a seismic velocity survey which took place in the GDF ONKALO in Olkiluoto, Finland as part of a study for mapping the fractures in the EDZ. The purpose of this work was to test the performance of the models used before in a real, complex engineering problem.
The fractures of the studied area were mapped and were able to be implemented into

the models. Since the geometry of the fractures was more complex, there was a need to overcome the limitation of staggered grid. At this stage for the explicit fracture representation, two approaches were used, as presented in chapter 4; the pixelised explicit model and the EDFM model. Two versions of LEM model were applied, the first using a thick LEM layer and the second using very fine LEM layers. As a result, the initial runs were for five models for fracture representation.
The wave source used for the models was created by an inversion process using waveforms at great depth where there was no presence of fractures. The initial stiffness used in the fractures was based on the size of the fracture according to Worthington & Lubbe (2007). Due to the vast amount of waveforms (552 waveforms per survey) from the survey, I had to confine the waveforms to be used based on the fracture complexity of the ray-paths.
The EM and EDFM model did not create comparable results. The EM had a much higher amplitude and slower arrival of approximately 0.1 ms while the EDFM was more attenuated in terms of amplitude and slower velocities.
The fracture stiffness for F1 fracture has been optimised for a single ray-path for the explicit and the two LEM models.
The main conclusions of this modelling challenge are:

- The EM model cannot give a reasonable solution to a problem with such a complex fracture network as the EDZ. EM fails to create comparable data because the different fracture groups have been averaged into a single fracture group.

- The EDFM model needs further optimisation to balance the size of the equivalent discrete fractures with the fracture density and the fracture stiffness in order to create more comparable results, similar to the conclusion made in section 4.5.2.

- Using the LEM with thick layers for each fracture, the resulting waveforms are closer to the survey data compared to the EM model but not as good as the fine LEM and the explicit.

- The two LEM and the explicit models work very well for some cases in terms of velocities, amplitude and frequencies. However, further optimisation of the fracture stiffness is needed to improve the performance of the models and approach reality.

- The LEM with thick layer can give a quick and easy-to-build model (no need to write model files with complex objects) with reasonably good results, but it is not as good as the explicit and the fine LEM models.
- Optimising fracture stiffness for a single ray-path propagation through a single fracture creates better results for the three models, increasing the amplitude to a level where the first two pulses of survey and modelled data are comparable.
- The LEM with a thick layer is more sensitive to changes of fracture stiffness and can reach the survey amplitude with lower stiffness values compared to the explicit and the fine LEM models. As summarised in Table 5.12 the normalised peak-to-peak amplitude can be up to three times higher than the explicit and fine LEM models in the optimisation process.
- As in the previous chapters, it can be concluded that the explicit model and the LEM with fine layering perform similarly in terms of fracture optimisation.
- None of the models achieves 100% the survey results. This is likely due to the fact that uniform stiffness has been used for the studied fracture in the optimisation process.
- Further optimisation of the fracture stiffness is needed by either creating zones with different stiffness in the fracture or by applying stress dependent fracture stiffness. For the latter, further code development will be required.

Chapter 6

Discussion and Conclusions

6.1 Discussion

The explicit model can in most cases accurately reproduce the waveforms from experiments under known conditions (number of fractures, geometry, material properties and stress state). This is due to the fact that the explicit fractures acts like a filter for the high frequencies by reducing the amplitude and slowing the wave velocities, similar to the natural fractures. This is in agreement with previous studies such as Hildyard (2001, 2007b); Pyrak-Nolte *et al.* (1990) concluding that the explicit model is frequency and amplitude dependent and Chichinina *et al.* (2009a,b) showing that attenuation and velocities are linked. Explicit fracture models though, need high accuracy on designing the model and a good knowledge of the preexisting fracture network and geometry, something which is not always doable.

Localised effective medium (LEM) can perform similar to the explicit model when fulfilling some conditions about frequency and LEM layer thickness. This matching between the LEM and explicit model is due to the fact that the alternation between homogeneous material and thin effective medium (EM) layers are creating a frequency dependent model as proposed by Vlastos *et al.* (2003, 2007). However, when the thickness of the LEM layers, for parallel fractures, increases above a threshold value (when wavelength is < 19 time the thickness) the LEM starts to lose its frequency dependent properties. In addition when the fractures are randomly orientated the wavelength of the signal has to be at least two times larger than the diameter of the fractures to match explicit and LEM models. So far the LEM and its thickness variations have

been tested for multiple parallel fractures (Chapter 4.1), and for complex EDZ fractures as a thick and fine LEM (Chapter 5). Another interesting topic on extending the limitations of the LEM, is to test the thickness of the LEM against the explicit for grouping a population of small explicit fractures into an LEM zone in order to define how accurate the LEM can be when reducing the resolution of the model.

The last approach used for fracture representation is the EM. The EM fails to simulate the wave changes due to multiple parallel or randomly oriented fractures. The failure of the EM at this stage is something expected to happen due to the nature of experiments I have modelled. Based on previous studies (e.g., Schubnel & Gueguen, 2003; Schubnel *et al.*, 2003; Shuai *et al.*, 2018) to produce reliable data using the EM model the crack density has to be below 0.5 and the λ/d above 14. All the models I have tested, are violating these limits. The EM model is frequency independent and cannot account for the frequency dependence of these shorter wavelengths. The reason the EM model is used under these conditions is to highlight the advantage and flexibility of the LEM model. The background theory and stiffness matrix is the same for both EM and LEM, but the geometry LEM is applied creates a completely different result. With this knowledge, more models with lower frequencies and different fracture spacing could be run to link fracture spacing for EM and LEM with frequencies and transmission coefficient in a similar manner as Cai & Zhao (2000) did for explicit model.

All of the three models are sensitive to changes in fracture stiffness. When the wave travels parallel to the fractures the stiffness has low impact on the wave propagation for all the three models. Whereas, when propagating perpendicular to the fracture the stiffness has maximum effect on the waveforms. When the stiffness is higher the transmission coefficient is higher (e.g., Cai & Zhao, 2000; Hildyard, 2001; Pyrak-Nolte *et al.*, 1990) allowing more energy of the wave to propagate through the fracture resulting in lower attenuation in amplitude, frequency and velocity. A special case on the sensitivity of the stiffness is the thick LEM, where it can produce the same level of waveform amplitude for lower stiffness compared to the explicit and the fine LEM for manual stiffness optimisation. The sensitivity, to stiffness changes, for the thicker LEM is because when increasing the thickness of the LEM it is becoming less frequency sensitive. Changing the stiffness uniformly results on waveform changes in a linear manner. In contrast, fracture stiffness on natural fracture is not uniform due to stress and fracture surface roughness, in this direction manual stiffness optimisation can be used to create

areas with higher and lower stiffness in the same fracture, in order to test how close to reality such a model can be.

To overcome the above limitation stress dependent stiffness was used and produced results comparable to the experiment for all the three models. The areas with increased stress have higher stiffness from those with lower stress, where the wave propagates faster through the areas with higher stiffness creating greater scattering and dispersion. Bandis *et al.* (1983) introduced the idea of stress dependent stiffness and Hildyard (2001) applied the stress dependent stiffness to model the Pyrak-Nolte *et al.* (1990) experiment with explicit fracture representation and mentioned the non-linearity of the waveforms among the same models but with different stress dependent parameters. The stress dependent stiffness has been developed for the EM and LEM models, the last one has a similar result to the explicit model, but as explained before the EM is expected to fail in those models. For the stress dependent EM, models with lower frequencies and/or crack density need to be tested against the LEM and explicit model to validate the stress dependent stiffness for the EM.

Finally, fractures with orientation other than orthogonal, can be modelled in a staggered grid code, to save computational time (compared to tetrahedral DEM codes), as pixelised, splitting the single fracture into several horizontal and vertical fractures. To achieve the same result as the single dipping fracture, adjustments in stiffness and size of horizontal to vertical ratio, are necessary. The pixelised fracture for the staggered grid codes, creates an opportunity to study wave propagation for complex fracture systems more efficiently.

6.2 Conclusions

The GDF solution for the permanent storage of the nuclear waste has raised questions about the limitations of the design of the GDF such as permeability of the host rock, existing and induced fractures (EDZ) etc. Seismic waves carry information about the fractures which are important for the effectiveness of the GDF. To understand this information from the waveforms we first need to match results from numerical models with experiments/surveys under known conditions, so as to improve our interpretation techniques. There are two main theories creating three approaches for fracture representations the explicit, the effective medium and the localised effective medium.

The question then is, which is the most appropriate representation and what are the limitations and the applicability of each model and how can we use this information to map fracture properties.
In this project I am using numerical models to compare the resulting waveforms among the models and/or with lab/survey data for all the three approaches of fracture representations in order to define the limitations in terms of frequency, fracture stiffness, fracture size, crack density along with the applicability and efficiency for each of the approaches.
The conclusions arising from this project are grouped into the following sections:

- Performance of the fracture representation models
- Stiffness and its importance
- Techniques and methods developed

6.2.1 Performance of the fracture representation models

The three major models for fracture representation used in this project are the Explicit model, the EM model and the LEM model. There are two more subcategories of the explicit model; the pixelised explicit model and the Equivalent discrete fracture medium (EDFM) and two subcategories for the LEM with a fine and a thicker layer. All have been tested in a variety of ways and conclusions were reached about the performance of each model relative to each other and to either lab or survey data.
First of all, the explicit and the LEM fine layer models produce similar results in most of the cases tested. More specifically, when the fractures are in orthogonal orientation such as in the experiment described in Chapter 3 or the parallel fracture numerical experiments tested in Chapter 4, the two models are almost identical for wave propagation parallel or perpendicular to the fractures with correlation coefficient up to 0.96 (Figures 4.5 and 4.9). There is a clear relationship between wave frequency and LEM layer thickness. The LEM model result depends more on the frequency of the wave rather than the 1/L fracture parameter. When the wavelength is 19 times higher than the LEM layer thickness the LEM approaches explicit model and/or real data. The larger the wavelength, the more similarities between the fine LEM model and the thicker, giving the LEM a range of flexibility against the explicit model. In addition,

when the fractures are other than orthogonal (DFN) the LEM and the explicit model perform very close one another if the λ/d (λ is the wavelength and d is the diameter of the fractures) ratio ≥ 2, but not as close if the ratio is < 1.
The need to model fractures explicitly where fractures are not orthogonal in the staggered grid WAVE3D code, led to two subcategories of the explicit fracture model, the pixelised fracture and the EDFM model. The pixelised dipping fracture, can perform similar to the single dipping explicit fracture, from a tetrahedral element DEM code, with correlation coefficient up to 0.98. To achieve that result it is necessary to follow specific adjustments on stiffness values and the ratio between horizontal-vertical fracture size. On the other hand, the waveforms for the subcategory of the explicit model the EDFM, do not agree in most cases with the single dipping explicit fracture (from the DEM code). When the crack density is high, the waveform from the EDFM is more attenuated and delayed than with the simple explicit model. When representing a dipping fracture, differences in the waveform from the two models increase as the angle of the fracture gets very shallow ($\theta^\circ < 30^\circ$) or very steep ($\theta^\circ > 60^\circ$).
The EM model fails to match the other models and data in most cases. The only comparable results of the EM model for both P- and S-wave is wave propagation parallel to the parallel fractures (SH-wave). Overall, the wave travel through EM is not amplitude and frequency dependent. Also for waves travelling perpendicular to the EM anisotropy plane the travel time of the wave is further delayed.

6.2.2 Stiffness and its importance

Fracture stiffness is the major variable used for model approaches representing dry fractures. The models have been tested in a wide range of stiffness values, applying the linear solution of uniform stiffness or the non-linear stress dependent stiffness for cases where the model is under a defined stress state. In addition manual stiffness optimisation has been applied to match modelled waveforms with survey data and to test the wave transmissivity in LEM models and in models with complex fracture networks. The following are conclusions about the importance of fracture stiffness on wave propagation.
The value of fracture stiffness can have an effect on amplitude, travel time and frequency response of the wave in fractured media, and has a crucial role in matching models and recorded data. The stiffness is linked with stress. Considering the stress to

be uniform, the stiffness will be uniform in the whole fracture. When comparing different cases of uniform fracture stiffness, the major differences are in amplitude and travel time. Higher stiffness leads to higher amplitude and earlier arrival, but the shape of the waveform does not change significantly. This creates a linear relationship between uniform stiffness and wave propagation.

When the stress is not uniform, it will have an effect on the stiffness creating areas with higher and lower values of stiffness in the same fracture. The stress dependent stiffness changes the shape and frequency of the waveform as well as the amplitude and arrival time in a non-linear way. The application of a stress-dependent fracture stiffness for all three approaches for fracture representation provided waveforms much closer to the recorded data of the experiment and survey. When changing uniform stiffness the LEM and EM models have shown greater sensitivity compared to the explicit model. On the other hand, even though all three models change significantly for stress dependent stiffness, the explicit and the LEM models are more sensitive. A special case of the S-wave propagation perpendicular to the fracture where neither the explicit nor the LEM representations agree with the laboratory data (Chapter 3) for both uniform stiffness and the stress dependent stiffness models.

There is a balance between wave frequency and fracture stiffness in which the LEM model performs the same no matter the thickness, and what the value of 1/L is. When the stiffness is higher the LEM approaches the explicit for lower 1/L values for the same source frequency whereas, when the stiffness is low it is approaching the explicit model only for the highest 1/L values.

Even though the stress dependent stiffness produces more realistic results it is not always efficient and easy to apply this method. Manual stiffness optimisation can partially replace stress dependent models, to produce results faster. During the optimisation process for fracture stiffness (Chapter 5), the model data improves, approaching the survey data but never fully matching it. This is due to the linearity of the process between the stiffness and the waveform.

6.2.3 Techniques and methods developed

In order to have a comparable result between the models and the data, in Chapter 3 where the waveform from a homogeneous sample was published I have used a deconvolution method to invert for the transfer function of the receive, transducer and the

source. This same method has been also applied by Hildyard (2001) for modelling the Pyrak-Nolte *et al.* (1990) experiment with parallel fractures. This method produced a source which the models for the homogeneous sample had as high correlation coefficient as 0.99 for both cases, concluding that for such simple cases where waveforms from a homogeneous sample are available this method can be successfully used to invert for a source which will be used in the models with fractures. In a similar manner I have extended that method to use it in a survey where the direct waveforms for a homogeneous sample wasn't possible in Chapter 5. The inversion method was used for several positions, where based on the report the rock wasn't fractured and could be considered as homogeneous. The inverted source worked very well for most of the cases, expanding this method for source inversion, in cases with more complex survey designs and rock properties.

The LEM model can perform either closer to the explicit or closer to the EM model depending on the wavelength of the signal and the thickness of the LEM layer, where the first must be at least 19 times higher than the thickness. The above conclusion gives the LEM an advantage in flexibility and applicability of the model without losing the explicitness effect of the fractured medium in the wave. Wave propagation parallel perpendicular and at various angles to the fractures has been modelled. The dipping angle of a fracture is important for modelling wave propagation for waves with a wide frequency range. As the angle gets steeper, the models for fracture representation tend to mismatch both with the experiment/survey data and among the different model approaches. In order to match the different models approaches high frequency filtering methods were used and concluded that, there is a threshold frequency point in which all of the models, for fracture representation, start to perform in a similar way for frequencies below that point. The filtered model results are then comparable with both the model and the recorded experiment/survey data.

New code has been developed in WAVE3D to implement the stress dependent stiffness method to the EM and LEM models in order to provide more realistic results. The same method has also been developed for the DEM code 3DEC for applying stress dependent stiffness to the explicit DFN models. The newly developed code was used to model experimental data and improved the performance of both EM and LEM models highlighting the importance of stress when modelling wave propagation through a fractured medium.

Lastly, the efficiency of the model, in terms of computational time is equally important as the accuracy of the model itself. For that reason it was necessary to implement an explicit complex fracture network representation to LEM, to reduce the model's run time. A method to convert complex fracture geometries such as DFNs has been developed for EM and LEM and the resulting waveforms have been compared against the explicit models leading to the conclusion that, even though the LEM and explicit model waveforms are similar, they do not match as well as when the fractures are parallel and the wave propagates in an orthogonal direction. Following the same principal and converting a dipping fracture from a DEM code to a pixelised fracture or EDFM model, in a staggered grid code, reduces the model run time significantly. The pixelised dipping fracture and the EDFM are two ways to create a dipping fracture in a staggered grid numerical modelling code. Both have been tested and conclusions reached on what assumption each method needs for application to a real modelling problem. This allows us to model the same problem using a more computationally efficient method.

6.3 Recommendations for further developments

Conclusions have been reached but some questions remain which require further investigation.

- The S-wave propagation perpendicular to the fracture was less similar to the experimental data. TheS-wave needs to be studied further and the waveforms compared with other experimental/survey data with parallel and dipping fractures for both uniform and stress dependent fracture stiffness.
- For the pixelised dipping fracture and the EDFM models the adjustments needed and the limitations for the these models have been quantified to perform similar to the single explicit dipping fracture. Similar work could be conducted to define the limits and the adjustments for the thick layer LEM and the fine LEM for dipping fractures at various angles.
- LEM and explicit models work well for complex fracture networks for specific cases but further improvements are required, to define the adjustments needed to make them work better.

- Dipping fractures are harder to match with experiment/survey data, due to the pixelisiation of the fracture. There is a need to further develop the code to include fracture stiffness in the intersecting points of the vertical and horizontal fractures and to automatically produce a pixelised fracture based on the adjustments defined.

- Optimisation of the fracture stiffness has worked to a point, but in order to have more realistic results, using an inversion method to produce zones with different stiffness within the fracture could be an alternative to stress dependent stiffness.

6.4 Application to fracturing in a GDF

- I have demonstrated that specific fracture properties, size, orientations and stiffness can be obtained through modelling and optimisation. This could be extended in a full waveform inversion methodology to extract fracture parameters.

- In the evaluation of the GDF forward models are used to forecast how the EDZ evolves. These should be constrained by seismic measurements. The results from the DEM code suggest that geometrically accurate explicit models of the wave propagation are not feasible due to the size and the run time of the models. As a result complex DFN geometry can be mapped to a simpler more efficient representation using either an LEM approach or a pixelised explicit fracture method and used for comparison with full waveform seismic data.

References

Alejano, A.J.C.F.U.K.R., L.R. (2018). Scale effect of intact olkiluoto gneissic rocks through uniaxial compressive testing and geophysical measurements. Tech. rep., Posiva. 4, 163, 165, 170, 173

Bandis, S.C., Lumsden, A.C. & Barton, N.R. (1983). Fundamentals of rock joint deformation. *International Journal of Rock Mechanics and Mining Sciences*, **20**, 249–268. 67, 135, 210, 229

Biryukov, A., Tisato, N. & Grasselli, G. (2016). Attenuation of elastic waves in bentonite and monitoring of radioactive waste repositories. *GEOPHYSICAL JOURNAL INTERNATIONAL*, **205**, 105–121. 14

Blum, T.E., Snieder, R., Van Wijk, K. & Willis, M.E. (2011). Theory and laboratory experiments of elastic wave scattering by dry planar fractures. *Journal of Geophysical Research-Solid Earth*, **116**, 11. 35

Blum, T.E., van Wijk, K. & Snieder, R. (2014). Scattering amplitude of a single fracture under uniaxial stress. *Geophysical Journal International*, **197**, 875–881. 35

Budiansky, B. & Oconnell, R.J. (1976). Elastic-moduli of a cracked solid. *International Journal of Solids and Structures*, **12**, 81–97. 29, 128

Cai, J. & Zhao, J. (2000). Effects of multiple parallel fractures on apparent attenuation of stress waves in rock masses. *International Journal of Rock Mechanics and Mining Sciences*, **37**, 661 – 682. 124, 228

Carcione, J.M., Picotti, S. & Santos, J.E. (2012). Numerical experiments of fractureinduced velocity and attenuation anisotropy. *Geophysical Journal International*, **191**, 1179–1191. 33

REFERENCES

Carlson, S. & Young, R. (1993). Acoustic emission and ultrasonic velocity study of excavation-induced microcrack damage at the underground research laboratory. *International Journal of Rock Mechanics and Mining Sciences Geomechanics Abstracts*, **30**, 901 – 907. 13, 162

Chichinina, T., Obolentseva, I., Gik, L., Bobrov, B. & Ronquillo-Jarillo, G. (2009a). Attenuation anisotropy in the linear-slip model: Interpretation of physical modeling data. *Geophysics*, **74**, WB165–WB176. 22, 33, 35, 37, 40, 50, 94, 227

Chichinina, T.I., Obolentseva, I.R. & Ronquillo-Jarillo, G. (2009b). Anisotropy of seismic attenuation in fractured media: Theory and ultrasonic experiment. *Transport in Porous Media*, **79**, 1–14. 33, 35, 37, 94, 227

Coates, R.T. & Schoenberg, M. (1995). Finite-difference modeling of faults and fractures. *Geophysics*, **60**, 1514–1526. 16, 26, 32, 40, 51, 95, 247

Collins, D., Pettitt, W. & Young, R. (2002). High-resolution mechanics of a microearthquake sequence. *PURE AND APPLIED GEOPHYSICS*, **159**, 197–219. 13, 162, 222

Crampin, S. (1981). A review of wave motion in anisotropic and cracked elastic-media. *Wave Motion*, **3**, 343–391. 16, 24, 39, 50, 95

Cundall, P. & Hart, R. (1992). NUMERICAL MODELLING OF DISCONTINUA. *ENGINEERING COMPUTATIONS*, **9**, 101–113. 19, 21

Damjanac, B. & Cundall, P. (2016). Application of distinct element methods to simulation of hydraulic fracturing in naturally fractured reservoirs. *Computers and Geotechnics*, **71**, 283–294. 127

David, C., Wassermann, J., Amann, F., Klaver, J., Davy, C., Sarout, J., Esteban, L., Rutter, E.H., Hu, Q., Louis, L., Delage, P., Lockner, D.A., Selvadurai, A.P.S., Vanorio, T., Amann Hildenbrand, A., Meredith, P.G., Browning, J., Mitchell, T.M., Madonna, C., Billiotte, J., Reuschlé, T., Lasseux, D., Fortin, J., Lenormand, R., Loggia, D., Nono, F., Boitnott, G., Jahns, E., Fleury, M., Berthe, G., Braun, P., Grégoire,

D., Perrier, L., Polito, P., Jannot, Y., Sommier, A., Krooss, B., Fink, R. & Clark, A. (2018). KGB, a collaborative benchmarking exercise for estimating the permeability of the Grimsel granodiorite—Part 2: modelling, microstructures and complementary data. *Geophysical Journal International*, **215**, 825–843. 4, 8

de Figueiredo, J.J.S., Schleicher, J., Stewart, R.R., Dayur, N., Omoboya, B., Wiley, R. & William, A. (2013). Shear wave anisotropy from aligned inclusions: ultrasonic frequency dependence of velocity and attenuation. *Geophysical Journal International*, **193**, 475–488. 24, 33, 34, 37, 39, 50, 94, 95, 223

Ding, P.B., Di, B.R., Wang, D., Wei, J.X. & Li, X.Y. (2014). P and s wave anisotropy in fractured media: Experimental research using synthetic samples. *Journal of Applied Geophysics*, **109**, 1–6. 24, 33, 34, 37, 39, 50, 95, 223

Fan, L.F. & Sun, H.Y. (2015). Seismic wave propagation through an in-situ stressed rock mass. *Journal of Applied Geophysics*, **121**, 13–20. 22, 40, 50

Fang, X.D., Fehler, M.C., Zhu, Z.Y., Zheng, Y.C. & Burns, D.R. (2014). Reservoir fracture characterization from seismic scattered waves. *Geophysical Journal International*, **196**, 481–492. 36, 37

Goodfellow, S.D. & Young, R.P. (2014). A laboratory acoustic emission experiment under in situ conditions. *GEOPHYSICAL RESEARCH LETTERS*, **41**, 3422–3430. 13, 14, 222

Groenenboom, J. & Falk, J. (2000). Scattering by hydraulic fractures: Finite difference modeling and laboratory data. *Geophysics*, **65**, 612–622. 36, 38

Gu, B.L., SuarezRivera, R., Nihei, K.T. & Myer, L.R. (1996). Incidence of plane waves upon a fracture. *Journal of Geophysical Research-Solid Earth*, **101**, 25337–25346. 22

Hakala, V.J.J.J., M. (2018). Sonkalo pose experiment – 3dec back-analyses. Tech. rep., Posiva. xxi, 4, 148, 163, 164, 170

Hildyard, M. (2007a). *WAVE User Manual*. Liverpool, University of Liverpool, UK, version 5 edn. 20

Hildyard, M.W. (2001). *Wave interaction with underground openings in fractured rock*. Ph.d. thesis, University of Liverpool. xi, xii, 19, 20, 21, 31, 38, 68, 94, 95, 102, 135, 147, 222, 227, 228, 229, 233

Hildyard, M.W. (2007b). Manuel rocha medal recipient wave interaction with underground openings in fractured rock. *Rock Mechanics and Rock Engineering*, **40**, 531–561. 16, 19, 20, 21, 22, 30, 34, 39, 40, 41, 43, 50, 52, 64, 87, 102, 227

Hildyard, M.W. & Young, R.P. (2002). Modelling seismic waves around underground openings in fractured rock. *Pure and Applied Geophysics*, **159**, 247–276. 21

Hildyard, M.W., Daehnke, A. & Cundall, P.A. (1995). Wave: A computer program for investigating elastodynamic issues in mining. *Rock Mechanics - Proceedings of the 35th U.S. Symposium*, 519–524. 17, 19, 21, 40, 41, 102

Huang, X.L., Qi, S.W., Guo, S.F. & Dong, W.L. (2014). Experimental Study of Ultrasonic Waves Propagating Through a Rock Mass with a Single Joint and Multiple Parallel Joints. *Rock Mechanics and Rock Engineering*, **47**, 549–559. 33, 37

Hudson, J.A. (1981). Wave speeds and attenuation of elastic-waves in material containing cracks. *Geophysical Journal of the Royal Astronomical Society*, **64**, 133–150. 16, 24, 33, 34, 39, 50

IAEA (2016). Nuclear power and sustainable development. Tech. rep., International Atomic Energy Agency. 1, 2, 3

Itasca Consulting Group, I.. (2019). *Three-Dimensional Distinct Element Code*. Minneapolis, Itasca, USA, version 5.20. edn. 17, 35, 127, 139, 147

Kawai, K., Takeuchi, N. & Geller, R.J. (2006). Complete synthetic seismograms up to 2 hz for transversely isotropic spherically symmetric media. *Geophysical Journal International*, **164**, 411–424. 24, 39, 50

King, T., Benson, P., De Siena, L. & Vinciguerra, S. (2017). Investigating the apparent seismic diffusivity of near-receiver geology at mount st. helens volcano, usa. *GEOSCIENCES*, **7**. 38

Kiuru, R. (2016). Association analysis of petrophysical and rock mechanical data from onkalo edz study area in onk-tku-3620, olkiluoto, finland. xxi, 163

Lei, Q.H., Latham, J.P. & Tsang, C.F. (2017). The use of discrete fracture networks for modelling coupled geomechanical and hydrological behaviour of fractured rocks. *Computers and Geotechnics*, **85**, 151–176. 7

Li, J.C., Ma, G.W. & Zhao, J. (2010). An equivalent viscoelastic model for rock mass with parallel joints. *Journal of Geophysical Research-Solid Earth*, **115**. 26, 33, 36, 37, 38, 40, 51, 94

Lima, M.G., Vogler, D., Querci, L., Madonna, C., Hattendorf, B., Saar, M.O. & Kong, X.Z. (2019). Thermally driven fracture aperture variation in naturally fractured granites. *Geothermal Energy*, **7**, 1–28. 4, 11

MacQuarrie, K.T.B. & Mayer, K.U. (2005). Reactive transport modeling in fractured rock: A state-of-the-science review. *Earth-Science Reviews*, **72**, 189–227. 6

Majer, E.L., McEvilly, T.V., Eastwood, F.S. & Myer, L.R. (1988). Fracture detection using p-wave and s-wave vertical seismic profiling at the geysers. *Geophysics*, **53**, 76–84. 24, 39, 50

Manukyan, E., Maurer, H., Marelli, S., Greenhalgh, S.A. & Green, A.G. (2012). Seismic monitoring of radioactive waste repositories. *GEOPHYSICS*, **77**, EN73–EN83. 14, 162, 222

Marelli, S., Manukyan, E., Maurer, H., Greenhalgh, S.A. & Green, A.G. (2010). Appraisal of waveform repeatability for crosshole and hole-to-tunnel seismic monitoring of radioactive waste repositories. *GEOPHYSICS*, **75**, Q21–Q34. 14, 162, 184, 222, 224

Molero, M. & IturraranViveros, U. (2013). Accelerating numerical modeling of wave propagation through 2D anisotropic materials using OpenCL. *Ultrasonics*, **53**, 815–822. 33, 34, 37

Mollhoff, M. & Bean, C.J. (2009). Validation of elastic wave measurements of rock fracture compliance using numerical discrete particle simulations. *Geophysical Prospecting*, **57**, 883–895. 33, 35, 37

Nakagawa, S., Nihei, K.T. & Myer, L.R. (2002). Elastic wave propagation along a set of parallel fractures. *Geophysical Research Letters*, **29**. 22, 35, 39, 50

Napolitano, F., Siena], L.D., Gervasi, A., Guerra, I., Scarpa, R. & Rocca], M.L. (2019). cattering and absorption imaging of a highly fractured fluid-filled seismogenetic volume in a region of slow deformation. *Geoscience Frontiers*. 38

NDA (2015). An overview of nda higher activity waste. Tech. rep., Nuclear Decommissioning Authority. 1, 3

Parastatidis, E., Hildyard, M.W. & Stuart, G.W. (2017). Modelling p-wave propagation in a medium with multiple parallel fractures and direct comparison with experimental recordings. In *51st U.S. Rock Mechanics/Geomechanics Symposium*, American Rock Mechanics Association, San Francisco, California, USA. xi, xii, 23, 25, 27, 40, 41, 43, 102

Parastatidis, E., Hildyard, M.W. & Hazzard, J. (2018). Seismic waves as a tool to interpret complex fractures. In *52nd U.S. Rock Mechanics/Geomechanics Symposium*, American Rock Mechanics Association, Seattle, Washington, USA. 101, 131

Perino, A. & Barla, G. (2015). Resonant Column Apparatus Tests on Intact and Jointed Rock Specimens with Numerical Modelling Validation. *Rock Mechanics and Rock Engineering*, **48**, 197–211. 33, 35, 37, 94

Perino, A., Zhu, J.B., Li, J.C., Barla, G. & Zhao, J. (2010). Theoretical methods for wave propagation across jointed rock masses. *Rock Mechanics and Rock Engineering*, **43**, 799–809. 22, 37, 38, 40, 50

Perino, A., Orta, R. & Barla, G. (2012). Wave Propagation in Discontinuous Media by the Scattering Matrix Method. *Rock Mechanics and Rock Engineering*, **45**, 901–918. 33, 36, 37, 38

Pyrak-Nolte, L.J., Myer, L.R. & Cook, N.G.W. (1990). Anisotropy in seismic velocities and amplitudes from multiple parallel fractures. *Journal of Geophysical Research-Solid Earth and Planets*, **95**, 11345–11358. xiii, 16, 17, 22, 34, 35, 39, 40, 41, 42, 46, 48, 49, 50, 52, 53, 94, 98, 102, 124, 172, 223, 227, 228, 229, 233

Rathore, J.S., Fjaer, E., Holt, R.M. & Renlie, L. (1995). P-wave and s-wave anisotropy of a synthetic sandstone with controlled crack geometry. *Geophysical Prospecting*, **43**, 711–728. 24, 33, 37, 38, 39, 50

Reyes-Montes, J. & Flynn, W. (2015). Edz study area in onk-tku-3620: Seismic cross-hole tomography. Tech. rep., Posiva. xxi, xxvi, 15, 162, 165, 168, 169, 170, 184, 267, 269, 270, 271

Rutqvist, J. (2015). Fractured rock stress-permeability relationships from in situ data and effects of temperature and chemical-mechanical couplings. *Geofluids*, **15**, 48–66. 7

Saadati, M., Forquin, P., Weddfelt, K., Larsson, P. & Hild, F. (2014). Granite rock fragmentation at percussive drilling – experimental and numerical investigation. *International Journal for Numerical and Analytical Methods in Geomechanics*, **38**, 828–843. 128

Schoenberg, M. (1980). Elastic wave behavior across linear slip interfaces. *Journal of the Acoustical Society of America*, **68**, 1516–1521. 15, 16, 22, 102

Schoenberg, M. (1983). Reflection of elastic-waves from periodically stratified media with interfacial slip. *Geophysical Prospecting*, **31**, 265–292. 24

Schoenberg, M. & Sayers, C.M. (1995). Seismic anisotropy of fractured rock. *Geophysics*, **60**, 204–211. 139, 146

Schubnel, A. & Gueguen, Y. (2003). Dispersion and anisotropy of elastic waves in cracked rocks. *JOURNAL OF GEOPHYSICAL RESEARCH-SOLID EARTH*, **108**. 34, 51, 95, 128, 146, 228

Schubnel, A., Nishizawa, O., Masuda, K., Lei, X., Xue, Z. & Gueguen, Y. (2003). Velocity measurements and crack density determination during wet triaxial experiments on oshima and toki granites. *PURE AND APPLIED GEOPHYSICS*, **160**, 869–887. 34, 51, 95, 128, 146, 228

Shao, S., Petrovitch, C.L. & Pyrak-Nolte, L.J. (2015). *Wave guiding in fractured layered media*, vol. 406 of *Geological Society Special Publication*, 375–400. 22, 40, 50

REFERENCES

Shuai, D., Wei, J., Di, B., Yuan, S., Xie, J. & Yan, S. (2018). Experimental study of fracture size effect on elastic-wave velocity dispersion and anisotropy. *GEOPHYSICS*, **83**, C49–C59. 34, 51, 95, 128, 146, 228

Sinnathamby, G., Korkiala-Tanttu, L. & Fores, J.G. (2014). Interface shear behaviour of tunnel backfill materials in a deep-rock nuclear waste repository in finland. *Soils and Foundations*, **54**, 777–788. xi, 4, 11, 162

Siren, T., Hakala, M., Valli, J., Kantia, P., Hudson, J. & Johansson, E. (2015a). In situ strength and failure mechanisms of migmatitic gneiss and pegmatitic granite at the nuclear waste disposal site in olkiluoto, western finland. *International Journal of Rock Mechanics and Mining Sciences*, **79**, 135 – 148. 3, 4, 11, 162

Siren, T., Kantia, P. & Rinne, M. (2015b). Considerations and observations of stress-induced and construction-induced excavation damage zone in crystalline rock. *International Journal of Rock Mechanics and Mining Sciences*, **73**, 165–174. 4, 8, 10, 162

SKB (2010). Choice of method - evaluation of strategies and systems for disposal of spent nuclear fuel. Tech. rep., Svensk Kärnbränslehantering AB. 1, 2, 3, 4, 170

Sovacool, B.K. (2011). *Contesting the Future of Nuclear Power*. WORLD SCIENTIFIC. xi, 1, 2

Suikkanen, J. (2019). Edz study area in onk-tku-3620: Integrated modelling. Tech. rep., Posiva. xxi, 4, 148, 162, 163, 164, 165, 166, 167, 170, 172, 176, 178, 180, 186

Thomsen, L. (1986). Elastic anisotropy due to aligned cracks; theoretical models. *EOS Transactions of the American Geophysical Union*, **67**, 1207. 33, 47

Tillotson, P., Chapman, M., Best, A.I., Sothcott, J., McCann, C., Shangxu, W. & Li, X.Y. (2011). Observations of fluid-dependent shear-wave splitting in synthetic porous rocks with aligned penny-shaped fractures. *Geophysical Prospecting*, **59**, 111–119. 24, 33, 37, 38, 39, 50

Tillotson, P., Chapman, M., Sothcott, J., Best, A.I. & Li, X.Y. (2014). Pore fluid viscosity effects on p- and s-wave anisotropy in synthetic silica-cemented

sandstone with aligned fractures. *Geophysical Prospecting*, **62**, 1238–1252. 24, 33, 37, 39, 50

Tsang, C.F., Bernier, F. & Davies, C. (2005). Geohydromechanical processes in the excavation damaged zone in crystalline rock, rock salt, and indurated and plastic clays - in the context of radioactive waste disposal. *International Journal of Rock Mechanics and Mining Sciences*, **42**, 109–125. 4, 6, 9, 10

Tsang, C.F., Neretnieks, I. & Tsang, Y. (2015). Hydrologic issues associated with nuclear waste repositories. *Water Resources Research*, **51**, 6923–6972. xi, 4, 6, 7

Vlastos, S., Liu, E., Main, I.G. & Li, X.Y. (2003). Numerical simulation of wave propagation in media with discrete distributions of fractures: effects of fracture sizes and spatial distributions. *Geophysical Journal International*, **152**, 649–668. 26, 33, 36, 37, 40, 51, 94, 95, 227

Vlastos, S., Liu, E., Main, I.G. & Narteau, C. (2007). Numerical simulation of wave propagation in 2D fractured media: scattering attenuation at different stages of the growth of a fracture population. *Geophysical Journal International*, **171**, 865–880. 36, 94, 124, 227

Wang, D., Qu, S.L., Zhao, Q., Yin, X.Y. & Zhou, F. (2017). Laboratory studies of ultrasonic wave response of fractures with different lengths: Anisotropy characteristics and coda analysis. *ULTRASONICS*, **80**, 101–112. 38

Wenning, Q.C., Madonna, C., de Haller, A. & Burg, J.P. (2018). Permeability and seismic velocity anisotropy across a ductile–brittle fault zone in crystalline rock. *Solid Earth*, **9**, 683–698. 4

Worthington, M.H. & Lubbe, R. (2007). The scaling of fracture compliance. *Fractured Reservoirs*, **270**, 73–+. 127, 130, 131, 183, 210, 225

Wu, C.L., Harris, J.M., Nihei, K.T. & Nakagawa, S. (2005). Two-dimensional finite-difference seismic modeling of an open fluid-filled fracture: Comparison of thin-layer and linear-slip models. *Geophysics*, **70**, T57–T62. 26, 37, 38, 40, 51

REFERENCES

Yil, W., Nihei, J.W., K. T.and Rector, Nakagawa, S., Myer, L.R. & Cook, N.G.W. (1997). Frequency-dependent seismic anisotropy in fractured rock. *International Journal Rock Mechanics and Mining Science*, **34**. 33, 35, 37, 94

Young, R.P., Nasseri, M.H.B. & Sehizadeh, M. (2020). Mechanical and seismic anisotropy of rocks from the onkalo underground rock characterization facility. *INTERNATIONAL JOURNAL OF ROCK MECHANICS AND MINING SCIENCES*, **126**. 14, 162, 222

Zhang, J.F. & Gao, H.W. (2009). Elastic wave modelling in 3-d fractured media: an explicit approach. *Geophysical Journal International*, **177**, 1233–1241. 26, 37, 40, 51, 94

Appendix A

Appendix

In this appendix I present the functions used for calculating stress dependent stiffness. In the first section A.1 is the FORTRAN subroutine which calculates the stress dependent stiffness for the EM and LEM models looping through the stiffness matrix (Coates & Schoenberg, 1995), in WAVE3D. This code have been used for the stress dependent models in Chapter 3.
The second section A.2 is the same function as in the first section, but this time is written in FISH for 3DEC explicit model. This code have been used for the stress dependent model in Chapter 4.

A.1 WAVE3D Function for stress-dependence stiffness on the EM and LEM.

```
subroutine sd_crackmat3d (imat,crrat,snn,crka,crkb,crkc,ipmat)
c crka value for \textit{a} see equation 4.1
c    -- scan for a stress dependence crack material,
c       create new material if not found --
 real c(6,6),rot(6,6),roti(6,6),ctmp(6,6),r1(6,6),r2(6,6)
c   -- calulate kn and ks due to stress values
c     Kn calculation see equation \ref{eq:36}
      crkn = ((1+crkb*(-snn))**2)/crka

c    Ks calculation see equation \ref{eq:37}
```

```
      crks = crkn*crkc
c     -- calculate the stiffness matrix \citep{Coates}
c          (e2 = $\lambda$ , e1 = $\lambda$ + 2G)
c          (1/L = crrat, ZN=1/kn, ZS=1/ks)
      blk = bulk(imat)
      shr = shear(imat)
      e1  = blk + 4.0 * shr / 3.0
      e2  = blk - 2.0 * shr / 3.0
      if (crkn .le. 1e-16) then
          crkn_i = 1e16
         else
          crkn_i = 1.0 / crkn
      endif
      if (crks .le. 1e-16) then
          crks_i = 1e16
         else
          crks_i = 1.0 / crks
      endif
      r   = e2/e1
      dlt = (crks_i*shr*crrat) / (crks_i*shr*crrat+1.0)
      dln = (crkn_i*e1*crrat)  / (crkn_i*e1*crrat+1.0)
      rdln    = r*dln
      rsqdln  = r**2*dln

      c(1,1) = e1*(1.0-rsqdln)
      c(1,2) = e2*(1.0-dln)
      c(1,3) = e2*(1.0-rdln)
      c(1,4) = 0.0
      c(1,5) = 0.0
      c(1,6) = 0.0
      c(2,1) = e2*(1.0-dln)
      c(2,2) = e1*(1.0-dln)
      c(2,3) = e2*(1.0-dln)
      c(2,4) = 0.0
      c(2,5) = 0.0
      c(2,6) = 0.0
```

```
      c(3,1) = e2*(1.0-rdln)
      c(3,2) = e2*(1.0-dln)
      c(3,3) = e1*(1.0-rsqdln)
      c(3,4) = 0.0
      c(3,5) = 0.0
      c(3,6) = 0.0

      c(4,1) = 0.0
      c(4,2) = 0.0
      c(4,3) = 0.0
      c(4,4) = shr*(1.0-dlt)
      c(4,5) = 0.0
      c(4,6) = 0.0
      c(5,1) = 0.0
      c(5,2) = 0.0
      c(5,3) = 0.0
      c(5,4) = 0.0
      c(5,5) = shr
      c(5,6) = 0.0
      c(6,1) = 0.0
      c(6,2) = 0.0
      c(6,3) = 0.0
      c(6,4) = 0.0
      c(6,5) = 0.0
      c(6,6) = shr*(1.0-dlt)
c     -- store --
      ip = ipmat+ncrmat
      do i=1,6
       do j=1,6
          a(ip) = c(i,j)
          ip = ip+1
       enddo
      enddo
      return
      end
```

A.2 3DEC FISH Function for explicit model stress-dependence stiffness.

```
def set\_properties
ka =  ; value for \textit{a} see equation \ref{eq:36a}
kb = ; value for \textit{b} see equation \ref{eq:36b}
kc = ; value for \textit{c} see equation \ref{eq:37}
ci = contact\_head ; contacts between elements
loop while ci \# 0 ; loop for every contact
  if c\_type(ci)\# 7 ; contact type 7 is the joint area
    cxi = c\_cx(ci) ; sub-contacts
    loop while cxi \# 0 ; loop for every sub-contact
     if cx\_area(cxi) > 0 ;sub-contact area larger than 0
      ; calculate stress using force value over area
      nstress = cx\_nforce(cxi)/cx\_area(cxi)
      ; calculate Kn equation \ref{eq:36}
      cx\_prop(cxi , "jkn") = ((1 + $kb \times nstress)^2$)/ka
      ; calculate Ks equation \ref{eq:37}
      cx\_prop(cxi , "jks") = cx\_prop(cxi , "jkn")*kc
     endif ; close loops
    cxi = cx\_next(cxi) ;go to next sub-contact
   endloop       ; close loops
  endif   ; close loops
  ci = c\_next(ci) ;go to next contact
 endloop  ; close loops
end
@set\_properties
```

Appendix B

Appendix

B.1 Cross-correlation coefficient results for LEM models in Chapter 4

Parallel K_n=60000 GPa		
	0.62 MHz	
	Explicit $\star$ LEM	
	Max. coefficient	Time (μs)
1/L=2000 m^{-1}	0.96871	0.0368
1/L=1000 m^{-1}	0.852116	0.0368
1/L=667 m^{-1}	0.699824	0.0368
1/L=500 m^{-1}	0.566569	0
1/L=400 m^{-1}	0.484103	0
	EM $\star$ LEM	
	Max. coefficient	Time (μs)
1/L=2000 m^{-1}	0.438829	0.0736
1/L=1000 m^{-1}	0.681389	0.0368
1/L=667 m^{-1}	0.837134	0.0368
1/L=500 m^{-1}	0.904982	0
1/L=400 m^{-1}	0.936937	-0.0368

Table B.1: Maximum cross-correlation coefficient between explicit with LEM and EM with LEM for K_n=0000 GPa.

Parallel K_n=60000 GPa		
	0.50 MHz	
	Explicit $\star$ LEM	
	Max. coefficient	Time (μs)
1/L=2000 m^{-1}	0.986871	0.0368
1/L=1000 m^{-1}	0.940415	0.0368
1/L=667 m^{-1}	0.852519	0.0368
1/L=500 m^{-1}	0.746178	0.0368
1/L=400 m^{-1}	0.647043	0.0368
	EM $\star$ LEM	
	Max. coefficient	Time (μs)
1/L=2000 m^{-1}	0.514455	0.0368
1/L=1000 m^{-1}	0.667774	0.0368
1/L=667 m^{-1}	0.802084	0.0368
1/L=500 m^{-1}	0.890652	0.0368
1/L=400 m^{-1}	0.938399	0

Table B.2: Maximum cross-correlation coefficient between explicit with LEM and EM with LEM for K_n=60000 GPa.

Parallel K_n=60000 GPa		
	0.42 MHz	
	Explicit $\star$ LEM	
	Max. coefficient	Time (μs)
1/L=2000 m^{-1}	0.992946	0.0368
1/L=1000 m^{-1}	0.970426	0.0368
1/L=667 m^{-1}	0.922294	0.0736
1/L=500 m^{-1}	0.847975	0.0368
1/L=400 m^{-1}	0.761913	0.0368
	EM $\star$ LEM	
	Max. coefficient	Time (μs)
1/L=2000 m^{-1}	0.571502	0
1/L=1000 m^{-1}	0.673347	0.0368
1/L=667 m^{-1}	0.775684	0.0368
1/L=500 m^{-1}	0.860165	0.0368
1/L=400 m^{-1}	0.911446	0.0368

Table B.3: Maximum cross-correlation coefficient between explicit with LEM and EM with LEM for K_n=60000 GPa.

Parallel K_n=60000 GPa		
	0.36 MHz	
	Explicit $\star$ LEM	
	Max. coefficient	Time (μs)
1/L=2000 m^{-1}	0.996396	0
1/L=1000 m^{-1}	0.982567	0.0368
1/L=667 m^{-1}	0.954786	0.0736
1/L=500 m^{-1}	0.90822	0.0736
1/L=400 m^{-1}	0.849565	0.0736
	EM $\star$ LEM	
	Max. coefficient	Time (μs)
1/L=2000 m^{-1}	0.613698	-0.0368
1/L=1000 m^{-1}	0.688398	0
1/L=667 m^{-1}	0.759302	0
1/L=500 m^{-1}	0.825966	0.0368
1/L=400 m^{-1}	0.876243	0.0368

Table B.4: Maximum cross-correlation coefficient between explicit with LEM and EM with LEM for K_n=60000 GPa.

Parallel K_n=60000 GPa		
	Explicit $\star$ LEM	
	0.31 MHz	
	Max. coefficient	Time (μs)
1/L=2000 m^{-1}	0.997405	0
1/L=1000 m^{-1}	0.988977	0.0368
1/L=667 m^{-1}	0.971551	0.0736
1/L=500 m^{-1}	0.94426	0.0736
1/L=400 m^{-1}	0.90814	0.0736
	EM $\star$ LEM	
	Max. coefficient	Time (μs)
1/L=2000 m^{-1}	0.627979	-0.0368
1/L=1000 m^{-1}	0.687412	0
1/L=667 m^{-1}	0.739787	0
1/L=500 m^{-1}	0.791442	0
1/L=400 m^{-1}	0.837912	0.0368

Table B.5: Maximum cross-correlation coefficient between explicit with LEM and EM with LEM for K_n=60000 GPa.

Perpendicular K_n=60000 GPa		
	0.62 MHz	
	Explicit $\star$ LEM	
	Max. coefficient	Time (μs)
1/L=2000 m^{-1}	0.955743	0.0368
1/L=1000 m^{-1}	0.429959	0.0736
1/L=667 m^{-1}	0.283355	0.1472
1/L=500 m^{-1}	0.268435	0.1472
1/L=400 m^{-1}	0.263081	2.576
	EM $\star$ LEM	
	Max. coefficient	Time (μs)
1/L=2000 m^{-1}	0.288218	-2.3552
1/L=1000 m^{-1}	0.519764	0.6624
1/L=667 m^{-1}	0.746455	0.5152
1/L=500 m^{-1}	0.84111	0.4048
1/L=400 m^{-1}	0.897461	0.3312

Table B.6: Maximum cross-correlation coefficient between explicit with LEM and EM with LEM for K_n=60000 GPa.

Perpendicular K_n=60000 GPa		
	0.50 MHz	
	Explicit ⋆ LEM	
	Max. coefficient	Time (μs)
1/L=2000 m^{-1}	0.979229	0
1/L=1000 m^{-1}	0.69948	0.1104
1/L=667 m^{-1}	0.485694	0.1472
1/L=500 m^{-1}	0.402818	0.1104
1/L=400 m^{-1}	0.351815	0.0736
	EM ⋆ LEM	
	Max. coefficient	Time (μs)
1/L=2000 m^{-1}	0.359404	-2.4288
1/L=1000 m^{-1}	0.498827	-2.3184
1/L=667 m^{-1}	0.74839	0.5152
1/L=500 m^{-1}	0.863384	0.4048
1/L=400 m^{-1}	0.923843	0.3312

Table B.7: Maximum cross-correlation coefficient between explicit with LEM and EM with LEM for K_n=60000 GPa.

Perpendicular K_n=60000 GPa		
	0.42 MHz	
	Explicit ⋆ LEM	
	Max. coefficient	Time (μs)
1/L=2000 m^{-1}	0.990266	-0.0368
1/L=1000 m^{-1}	0.877737	0.1104
1/L=667 m^{-1}	0.693669	0.1472
1/L=500 m^{-1}	0.5546	0.1472
1/L=400 m^{-1}	0.473604	0.1104
	EM ⋆ LEM	
	Max. coefficient	Time (μs)
1/L=2000 m^{-1}	0.399375	-2.5024
1/L=1000 m^{-1}	0.530275	-2.3552
1/L=667 m^{-1}	0.717928	0.5152
1/L=500 m^{-1}	0.853164	0.4048
1/L=400 m^{-1}	0.923097	0.3312

Table B.8: Maximum cross-correlation coefficient between explicit with LEM and EM with LEM for K_n=60000 GPa.

Perpendicular K_n=60000 GPa		
	0.36 MHz	
	Explicit $\star$ LEM	
	Max. coefficient	Time (μs)
1/L=2000 m^{-1}	0.993966	-0.0368
1/L=1000 m^{-1}	0.94113	0.1104
1/L=667 m^{-1}	0.832323	0.184
1/L=500 m^{-1}	0.697486	0.184
1/L=400 m^{-1}	0.603321	0.184
	EM $\star$ LEM	
	Max. coefficient	Time (μs)
1/L=2000 m^{-1}	0.45664	0.1472
1/L=1000 m^{-1}	0.531335	0.4048
1/L=667 m^{-1}	0.697236	0.4784
1/L=500 m^{-1}	0.834964	0.4048
1/L=400 m^{-1}	0.909297	0.3312

Table B.9: Maximum cross-correlation coefficient between explicit with LEM and EM with LEM for K_n=60000 GPa.

Perpendicular K_n=60000 GPa		
	0.31 MHz	
	Explicit $\star$ LEM	
	Max. coefficient	Time (μs)
1/L=2000 m^{-1}	0.99495	-0.0736
1/L=1000 m^{-1}	0.964544	0.1104
1/L=667 m^{-1}	0.900313	0.184
1/L=500 m^{-1}	0.801482	0.184
1/L=400 m^{-1}	0.71435	0.184
	EM $\star$ LEM	
	Max. coefficient	Time (μs)
1/L=2000 m^{-1}	0.534671	0.1104
1/L=1000 m^{-1}	0.605572	0.2944
1/L=667 m^{-1}	0.710551	0.4048
1/L=500 m^{-1}	0.81954	0.368
1/L=400 m^{-1}	0.891052	0.3312

Table B.10: Maximum cross-correlation coefficient between explicit with LEM and EM with LEM for K_n=60000 GPa.

Parallel K_n=100000 GPa		
	0.62 MHz	
	Explicit ⋆ LEM	
	Max. coefficient	Time (μs)
1/L=2000 m^{-1}	0.975692	0.0368
1/L=1000 m^{-1}	0.922687	0.0368
1/L=667 m^{-1}	0.817805	0.0368
1/L=500 m^{-1}	0.72243	0.0368
1/L=400 m^{-1}	0.667237	0.0368
	EM ⋆ LEM	
	Max. coefficient	Time (μs)
1/L=2000 m^{-1}	0.641632	0.0368
1/L=1000 m^{-1}	0.825993	0.0368
1/L=667 m^{-1}	0.920971	0.0368
1/L=500 m^{-1}	0.953003	0
1/L=400 m^{-1}	0.970305	0

Table B.11: Maximum cross-correlation coefficient between explicit with LEM and EM with LEM for K_n=100000 GPa.

Parallel K_n=100000 GPa		
	0.50 MHz	
	Explicit ⋆ LEM	
	Max. coefficient	Time (μs)
1/L=2000 m^{-1}	0.991896	0.0368
1/L=1000 m^{-1}	0.968315	0.0368
1/L=667 m^{-1}	0.914718	0.0368
1/L=500 m^{-1}	0.854567	0.0368
1/L=400 m^{-1}	0.805201	0.0368
	EM ⋆ LEM	
	Max. coefficient	Time (μs)
1/L=2000 m^{-1}	0.723409	0
1/L=1000 m^{-1}	0.835001	0.0368
1/L=667 m^{-1}	0.907007	0.0368
1/L=500 m^{-1}	0.948115	0.0368
1/L=400 m^{-1}	0.968748	0

Table B.12: Maximum cross-correlation coefficient between explicit with LEM and EM with LEM for K_n=100000 GPa.

Parallel K_n=100000 GPa		
	0.42 MHz	
	Explicit $\star$ LEM	
	Max. coefficient	Time (μs)
1/L=2000 m^{-1}	0.995086	0.0368
1/L=1000 m^{-1}	0.985567	0.0368
1/L=667 m^{-1}	0.956841	0.0368
1/L=500 m^{-1}	0.920887	0.0368
1/L=400 m^{-1}	0.88414	0.0368
	EM $\star$ LEM	
	Max. coefficient	Time (μs)
1/L=2000 m^{-1}	0.778525	0
1/L=1000 m^{-1}	0.853901	0
1/L=667 m^{-1}	0.904428	0
1/L=500 m^{-1}	0.940403	0.0368
1/L=400 m^{-1}	0.963738	0

Table B.13: Maximum cross-correlation coefficient between explicit with LEM and EM with LEM for K_n=100000 GPa.

Parallel K_n=100000 GPa		
	0.36 MHz	
	Explicit $\star$ LEM	
	Max. coefficient	Time (μs)
1/L=2000 m^{-1}	0.997529	0
1/L=1000 m^{-1}	0.99249	0.0368
1/L=667 m^{-1}	0.976163	0.0368
1/L=500 m^{-1}	0.954341	0.0368
1/L=400 m^{-1}	0.929921	0.0368
	EM $\star$ LEM	
	Max. coefficient	Time (μs)
1/L=2000 m^{-1}	0.819841	0
1/L=1000 m^{-1}	0.874093	0
1/L=667 m^{-1}	0.909944	0
1/L=500 m^{-1}	0.937164	0
1/L=400 m^{-1}	0.957265	0

Table B.14: Maximum cross-correlation coefficient between explicit with LEM and EM with LEM for K_n=100000 GPa.

Parallel K_n=100000 GPa		
	0.31 MHz	
	Explicit ⋆ LEM	
	Max. coefficient	Time (μs)
1/L=2000 m^{-1}	0.998098	0
1/L=1000 m^{-1}	0.995637	0.0368
1/L=667 m^{-1}	0.986496	0.0368
1/L=500 m^{-1}	0.973605	0.0368
1/L=400 m^{-1}	0.958535	0.0368
	EM ⋆ LEM	
	Max. coefficient	Time (μs)
1/L=2000 m^{-1}	0.845737	-0.0368
1/L=1000 m^{-1}	0.885553	0
1/L=667 m^{-1}	0.91151	0
1/L=500 m^{-1}	0.932614	0
1/L=400 m^{-1}	0.94996	0

Table B.15: Maximum cross-correlation coefficient between explicit with LEM and EM with LEM for K_n=100000 GPa.

Perpendicular K_n=100000 GPa		
	0.62 MHz	
	Explicit ⋆ LEM	
1/L=2000 m^{-1}	Max. coefficient	Time (μs)
1/L=1000 m^{-1}	0.973248	0.0368
1/L=667 m^{-1}	0.717802	0.0736
1/L=500 m^{-1}	0.533473	0.0368
1/L=400 m^{-1}	0.479036	-0.0368
	0.478076	-0.0736
	EM ⋆ LEM	
	Max. coefficient	Time (μs)
1/L=2000 m^{-1}	0.477433	-2.576
1/L=1000 m^{-1}	0.707011	0.368
1/L=667 m^{-1}	0.879324	0.2576
1/L=500 m^{-1}	0.93739	0.2208
1/L=400 m^{-1}	0.956885	0.184

Table B.16: Maximum cross-correlation coefficient between explicit with LEM and EM with LEM for K_n=100000 GPa.

Perpendicular K_n=100000 GPa		
	0.50 MHz	
	Explicit $\star$ LEM	
	Max. coefficient	Time (μs)
1/L=2000 m^{-1}	0.988913	0
1/L=1000 m^{-1}	0.900606	0.0736
1/L=667 m^{-1}	0.740023	0.0368
1/L=500 m^{-1}	0.645704	0.0368
1/L=400 m^{-1}	0.615649	0
	EM $\star$ LEM	
	Max. coefficient	Time (μs)
1/L=2000 m^{-1}	0.547499	0.1472
1/L=1000 m^{-1}	0.696135	0.2944
1/L=667 m^{-1}	0.863864	0.2576
1/L=500 m^{-1}	0.933434	0.2208
1/L=400 m^{-1}	0.96369	0.1472

Table B.17: Maximum cross-correlation coefficient between explicit with LEM and EM with LEM for K_n=100000 GPa.

Perpendicular K_n=100000 GPa		
	0.42 MHz	
	Explicit $\star$ LEM	
	Max. coefficient	Time (μs)
1/L=2000 m^{-1}	0.994557	-0.0368
1/L=1000 m^{-1}	0.96083	0.0736
1/L=667 m^{-1}	0.874562	0.0736
1/L=500 m^{-1}	0.783038	0.0736
1/L=400 m^{-1}	0.730402	0.0368
	EM $\star$ LEM	
	Max. coefficient	Time (μs)
1/L=2000 m^{-1}	0.646031	0.0736
1/L=1000 m^{-1}	0.740232	0.2208
1/L=667 m^{-1}	0.850654	0.2208
1/L=500 m^{-1}	0.921343	0.2208
1/L=400 m^{-1}	0.960422	0.1472

Table B.18: Maximum cross-correlation coefficient between explicit with LEM and EM with LEM for K_n=100000 GPa.

Perpendicular K_n=100000 GPa		
	0.36 MHz	
	Explicit ⋆ LEM	
	Max. coefficient	Time (μs)
1/L=2000 m^{-1}	0.99697	-0.0368
1/L=1000 m^{-1}	0.982449	0.0368
1/L=667 m^{-1}	0.937825	0.0736
1/L=500 m^{-1}	0.874103	0.0736
1/L=400 m^{-1}	0.821052	0.0736
	EM ⋆ LEM	
	Max. coefficient	Time (μs)
1/L=2000 m^{-1}	0.727183	0.0368
1/L=1000 m^{-1}	0.793842	0.1472
1/L=667 m^{-1}	0.862076	0.184
1/L=500 m^{-1}	0.920215	0.184
1/L=400 m^{-1}	0.958221	0.1472

Table B.19: Maximum cross-correlation coefficient between explicit with LEM and EM with LEM for K_n=100000 GPa.

Perpendicular K_n=100000 GPa		
	0.31 MHz	
	Explicit ⋆ LEM	
	Max. coefficient	Time (μs)
1/L=2000 m^{-1}	0.997693	-0.0368
1/L=1000 m^{-1}	0.991005	0.0368
1/L=667 m^{-1}	0.966814	0.0736
1/L=500 m^{-1}	0.927592	0.0736
1/L=400 m^{-1}	0.888207	0.0736
	EM ⋆ LEM	
	Max. coefficient	Time (μs)
1/L=2000 m^{-1}	0.793157	0
1/L=1000 m^{-1}	0.841574	0.1104
1/L=667 m^{-1}	0.885762	0.1472
1/L=500 m^{-1}	0.926656	0.1472
1/L=400 m^{-1}	0.957639	0.1472

Table B.20: Maximum cross-correlation coefficient between explicit with LEM and EM with LEM for K_n=100000 GPa.

Parallel K_n=30000 GPa		
	0.62 MHz	
	Explicit $\star$ LEM	
	Max. coefficient	Time (μs)
1/L=2000 m^{-1}	0.941279	0.0736
1/L=1000 m^{-1}	0.672343	0.0368
1/L=667 m^{-1}	0.521103	-0.0368
1/L=500 m^{-1}	0.439309	-0.0368
1/L=400 m^{-1}	0.326903	-0.1104
	EM $\star$ LEM	
	Max. coefficient	Time (μs)
1/L=2000 m^{-1}	0.265999	0.2208
1/L=1000 m^{-1}	0.536231	0.1104
1/L=667 m^{-1}	0.748238	0.0368
1/L=500 m^{-1}	0.84492	0
1/L=400 m^{-1}	0.889776	-0.0368

Table B.21: Maximum cross-correlation coefficient between explicit with LEM and EM with LEM for K_n=30000 GPa.

Parallel K_n=30000 GPa		
	0.50 MHz	
	Explicit $\star$ LEM	
	Max. coefficient	Time (μs)
1/L=2000 m^{-1}	0.966444	0.0368
1/L=1000 m^{-1}	0.835792	0.0368
1/L=667 m^{-1}	0.723467	0
1/L=500 m^{-1}	0.593578	-0.0368
1/L=400 m^{-1}	0.463157	-0.0368
	EM $\star$ LEM	
	Max. coefficient	Time (μs)
1/L=2000 m^{-1}	0.326092	0.1472
1/L=1000 m^{-1}	0.505731	0.1104
1/L=667 m^{-1}	0.69906	0.0736
1/L=500 m^{-1}	0.816193	0.0368
1/L=400 m^{-1}	0.869452	0

Table B.22: Maximum cross-correlation coefficient between explicit with LEM and EM with LEM for K_n=30000 GPa.

Parallel K_n=30000 GPa		
	0.42 MHz	
	Explicit ⋆ LEM	
	Max. coefficient	Time (μs)
1/L=2000 m^{-1}	0.970769	-0.184
1/L=1000 m^{-1}	0.909987	0.0368
1/L=667 m^{-1}	0.835087	0.0368
1/L=500 m^{-1}	0.732452	0.0368
1/L=400 m^{-1}	0.628519	0.0368
	EM ⋆ LEM	
	Max. coefficient	Time (μs)
1/L=2000 m^{-1}	0.364135	-0.1472
1/L=1000 m^{-1}	0.49005	0.1104
1/L=667 m^{-1}	0.634808	0.0736
1/L=500 m^{-1}	0.749958	0.0736
1/L=400 m^{-1}	0.817377	0.0368

Table B.23: Maximum cross-correlation coefficient between explicit with LEM and EM with LEM for K_n=30000 GPa.

Parallel K_n=30000 GPa		
	0.36 MHz	
	Explicit ⋆ LEM	
	Max. coefficient	Time (μs)
1/L=2000 m^{-1}	0.992928	0
1/L=1000 m^{-1}	0.946445	0.0368
1/L=667 m^{-1}	0.901455	0.0368
1/L=500 m^{-1}	0.841617	0.0736
1/L=400 m^{-1}	0.775515	0.0736
	EM ⋆ LEM	
	Max. coefficient	Time (μs)
1/L=2000 m^{-1}	0.401412	0.0368
1/L=1000 m^{-1}	0.477934	0.0736
1/L=667 m^{-1}	0.574171	0.0736
1/L=500 m^{-1}	0.668491	0.0736
1/L=400 m^{-1}	0.741348	0.0736

Table B.24: Maximum cross-correlation coefficient between explicit with LEM and EM with LEM for K_n=30000 GPa.

Parallel K_n=30000 GPa		
	Explicit ⋆ LEM	
	0.31 MHz	
	Max. coefficient	Time (μs)
1/L=2000 m^{-1}	0.996164	0
1/L=1000 m^{-1}	0.967737	0.0736
1/L=667 m^{-1}	0.941671	0.0736
1/L=500 m^{-1}	0.906047	0.0736
1/L=400 m^{-1}	0.863094	0.0736
	EM ⋆ LEM	
	Max. coefficient	Time (μs)
1/L=2000 m^{-1}	0.390509	0.0368
1/L=1000 m^{-1}	0.445931	0.0736
1/L=667 m^{-1}	0.510148	0.0736
1/L=500 m^{-1}	0.583589	0.0736
1/L=400 m^{-1}	0.657147	0.0736

Table B.25: Maximum cross-correlation coefficient between explicit with LEM and EM with LEM for K_n=30000 GPa.

Perpendicular K_n=30000 GPa		
	0.62 MHz	
	Explicit ⋆ LEM	
	Max. coefficient	Time (μs)
1/L=2000 m^{-1}	0.961656	0.0368
1/L=1000 m^{-1}	0.195091	0.1472
1/L=667 m^{-1}	0.142307	0.6992
1/L=500 m^{-1}	0.21958	0.552
1/L=400 m^{-1}	0.207197	0.2208
	EM ⋆ LEM	
	Max. coefficient	Time (μs)
1/L=2000 m^{-1}	0.119093	0.368
1/L=1000 m^{-1}	0.354985	0.2208
1/L=667 m^{-1}	0.57764	-1.6192
1/L=500 m^{-1}	0.574013	0.9568
1/L=400 m^{-1}	0.667374	0.8096

Table B.26: Maximum cross-correlation coefficient between explicit with LEM and EM with LEM for K_n=30000 GPa.

Perpendicular K_n=30000 GPa		
	0.50 MHz	
	Explicit ⋆ LEM	
	Max. coefficient	Time (μs)
1/L=2000 m^{-1}	0.976957	0
1/L=1000 m^{-1}	0.321146	0.1472
1/L=667 m^{-1}	0.232534	0.4784
1/L=500 m^{-1}	0.287468	0.4784
1/L=400 m^{-1}	0.280232	0.2208
	EM ⋆ LEM	
	Max. coefficient	Time (μs)
1/L=2000 m^{-1}	0.153485	0.4784
1/L=1000 m^{-1}	0.344118	0.2208
1/L=667 m^{-1}	0.643571	-1.656
1/L=500 m^{-1}	0.656506	0.9568
1/L=400 m^{-1}	0.719063	0.8096

Table B.27: Maximum cross-correlation coefficient between explicit with LEM and EM with LEM for K_n=30000 GPa.

Perpendicular K_n=30000 GPa		
	0.42 MHz	
	Explicit ⋆ LEM	
	Max. coefficient	Time (μs)
1/L=2000 m^{-1}	0.982136	0
1/L=1000 m^{-1}	0.536343	0.184
1/L=667 m^{-1}	0.37601	0.4048
1/L=500 m^{-1}	0.356706	0.4048
1/L=400 m^{-1}	0.343418	0.2576
	EM ⋆ LEM	
	Max. coefficient	Time (μs)
1/L=2000 m^{-1}	0.195283	0.5888
1/L=1000 m^{-1}	0.280322	0.2944
1/L=667 m^{-1}	0.622686	-1.6928
1/L=500 m^{-1}	0.682526	0.9568
1/L=400 m^{-1}	0.755386	0.7728

Table B.28: Maximum cross-correlation coefficient between explicit with LEM and EM with LEM for K_n=30000 GPa.

Perpendicular K_n=30000 GPa		
	0.36 MHz	
	Explicit $\star$ LEM	
	Max. coefficient	Time (μs)
1/L=2000 m^{-1}	0.982914	0
1/L=1000 m^{-1}	0.770511	0.2208
1/L=667 m^{-1}	0.553377	0.368
1/L=500 m^{-1}	0.441011	0.368
1/L=400 m^{-1}	0.409891	0.2944
	EM $\star$ LEM	
	Max. coefficient	Time (μs)
1/L=2000 m^{-1}	0.23629	0.6256
1/L=1000 m^{-1}	0.253612	-1.84
1/L=667 m^{-1}	0.585596	-1.7296
1/L=500 m^{-1}	0.677526	0.9936
1/L=400 m^{-1}	0.769945	0.8096

Table B.29: Maximum cross-correlation coefficient between explicit with LEM and EM with LEM for K_n=30000 GPa.

Perpendicular K_n=30000 GPa		
	0.31 MHz	
	Explicit $\star$ LEM	
	Max. coefficient	Time (μs)
1/L=2000 m^{-1}	0.983154	-0.0368
1/L=1000 m^{-1}	0.895352	0.2208
1/L=667 m^{-1}	0.713293	0.3312
1/L=500 m^{-1}	0.539531	0.3312
1/L=400 m^{-1}	0.486219	0.2944
	EM $\star$ LEM	
	Max. coefficient	Time (μs)
1/L=2000 m^{-1}	0.268451	0.6624
1/L=1000 m^{-1}	0.353695	-1.7664
1/L=667 m^{-1}	0.552632	-1.7296
1/L=500 m^{-1}	0.659524	0.9936
1/L=400 m^{-1}	0.758773	0.8464

Table B.30: Maximum cross-correlation coefficient between explicit with LEM and EM with LEM for K_n=30000 GPa.

Appendix C

Appendix

C.1 Acquisition system properties for EDZ cross-hole tomography in Chapter 5

The AE acquisition equipment was used for this study was designed and constructed by Itasca Consulting Ltd UK. At this part attached the technical properties of the equipment as described in the Reyes-Montes & Flynn (2015) report. The junction boxes containing the 24 Pulser Amplifier Desktop units (PADs) were moved and mounted on the wall of the niche close to the EDZ area. All cabling between the junction boxes and instrument rack was reconnected. The AE and ultrasonic equipment previously installed for POSE3 at POSIVA which was also used for the EDZ study included:

- 1 x 24-channel ASC Milne data acquisition system, providing simultaneous multi-channel16-bit full waveform acquisition, at sampling rates of up to 10 MS/s per channel;
- 1 x 24-channel ASC Trigger-hit-count (THC) unit, providing multi-channel trigger and hit count logic;
- 1 x 24-channel ASC Pulser Amplifier System (PAS), consisting of 24 x Pulser Amplifier Desktop units (PADs) which provide amplification (30 dB to 70 dB) of sensor signals and 1 x Pulser Interface Unit (PIU) which provides power to the PADs;
- 24 x 10 m cable assemblies between each PAD and the PIU for signal transmission and power supply;

- 2 wall-mounted EMI junction boxes with screened sensor cable glands for housing of the 24 PADs; In addition to the above equipment, the following equipment was purchased specifically for the EDZ study.
- 30 acoustic emission transducers (PAC's ISR6 sensor Figure C.1, with a resonant frequency of 50 kHz, frequency response of 35 kHz to 100 kHz frequency range) and integrated 10 m waterproof cable assemblies;
- 2 (plus 1 spare) borehole frame assemblies for mounting 16 AE transducers (8 transducers per borehole frame as in Figures C.3 and C.4);
- 8 surface mounts for mounting 8 AE transducers (via bolts acting as waveguides) to the rock surface.

The AE transducer used for this project is the ISR6 model transducer from Physical Acoustics Corporation (PAC) Figures C.1. The AE transducer model is a sealed sensor with integral waterproof cable for underwater use. This sensor does not have an integral pre-amplifier in order to enable its use as a pulsing source during the velocity surveying. The pulsing and amplification is provided by the PADs as previously described. The general data-sheet characteristics of the sensor are as follows (PAC ISR6 data-sheet):

- Peak Sensitivity V/(m/s); [V/μbar]: 76 [-63] dB;
- Operating Frequency Range: (35 to 80) kHz;
- Resonant Freq. V/(m/s); [V/μbar]: 50 [85] kHz;
- Shock limit: 1000 g;
- Temperature Range: (-45 to 125) $^{\circ}C$;
- Dimensions (Height x Outer Diameter): (19.2 x 22.6) mm;
- Waterproof: IP66
- Weight: 33 gr.

Figure C.1: ISR6 model AE transducer (PAC) (Reyes-Montes & Flynn, 2015).

To optimise coupling of the sensor to the borehole, a sensor coupling cap has been designed and attached C.2 (using silicone grease to increase coupling) to the sensing face of each transducer. This brass cap has a profile matching that of the borehole (38 mm radius) (Reyes-Montes & Flynn, 2015).

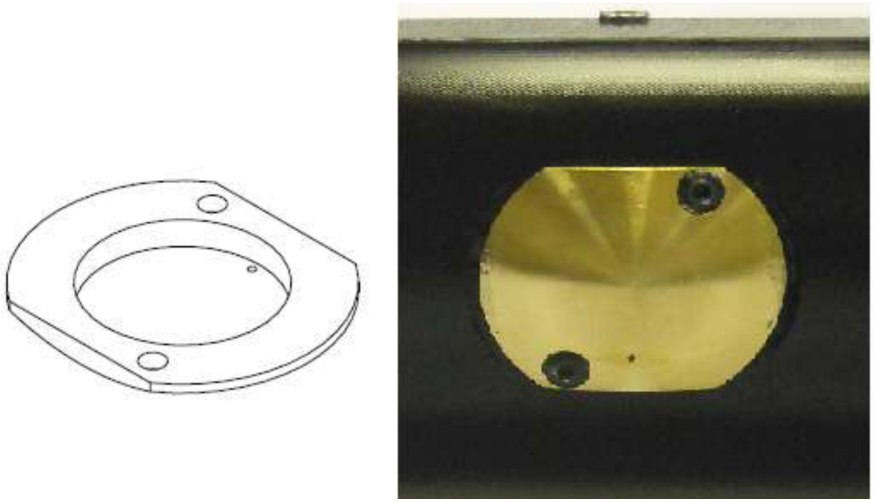

Figure C.2: AE sensor cap design (left) and AE sensor cap (right) (Reyes-Montes & Flynn, 2015).

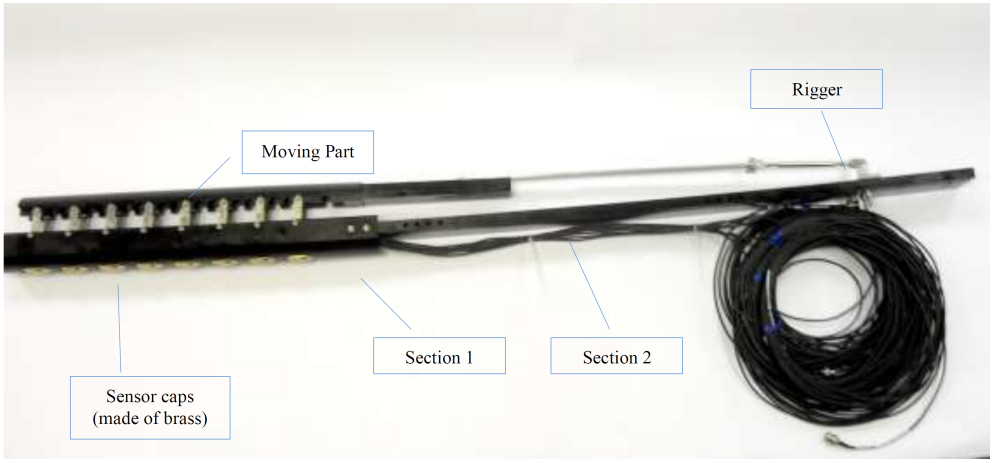

Figure C.3: Full set up of the borehole frame design (Reyes-Montes & Flynn, 2015).

Figure C.4: Example survey during the EDZ study showing the setup of the borehole and surface frames. (Reyes-Montes & Flynn, 2015).

Appendix D

Appendix

D.1 Stiffness optimisation results for Chapter 5

This appendix provides the waveforms for three ray paths from the optimisation process including all ten cases with different fracture stiffness. The ray paths presented are : The ray-path presented are all in shout depth at 0.6 m in borehole 43 for all the three models (thick LEM, fine LEM and pixelised explicit model) and recording at borehole 34 at 0.2 m, 0.55 m and 0.6 m depth. Some of the Figures have been also presented in in chapter 5 for the ray path recording at 0.55 m depth.

D.1.1 LEM thick layer results for stiffness optimisation

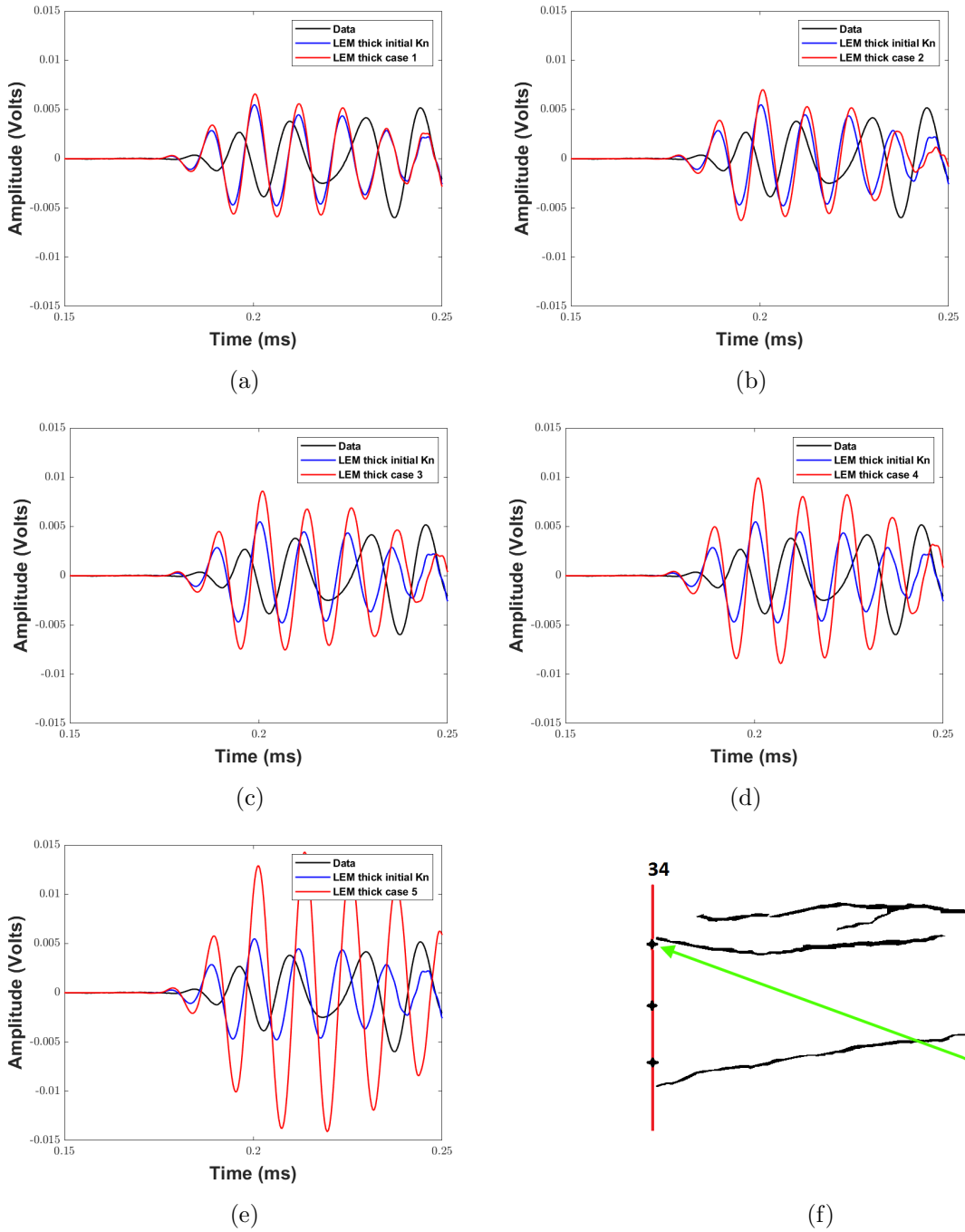

Figure D.1: Waveforms for the frame between boreholes 34-43 for the LEM model with thick layer. Shot in borehole 43 at depth 0.6 m and recordings at 0.2 m D.1f. Case 1 D.1a to 5 D.1e (K_n 10 to 50 times higher than initial).

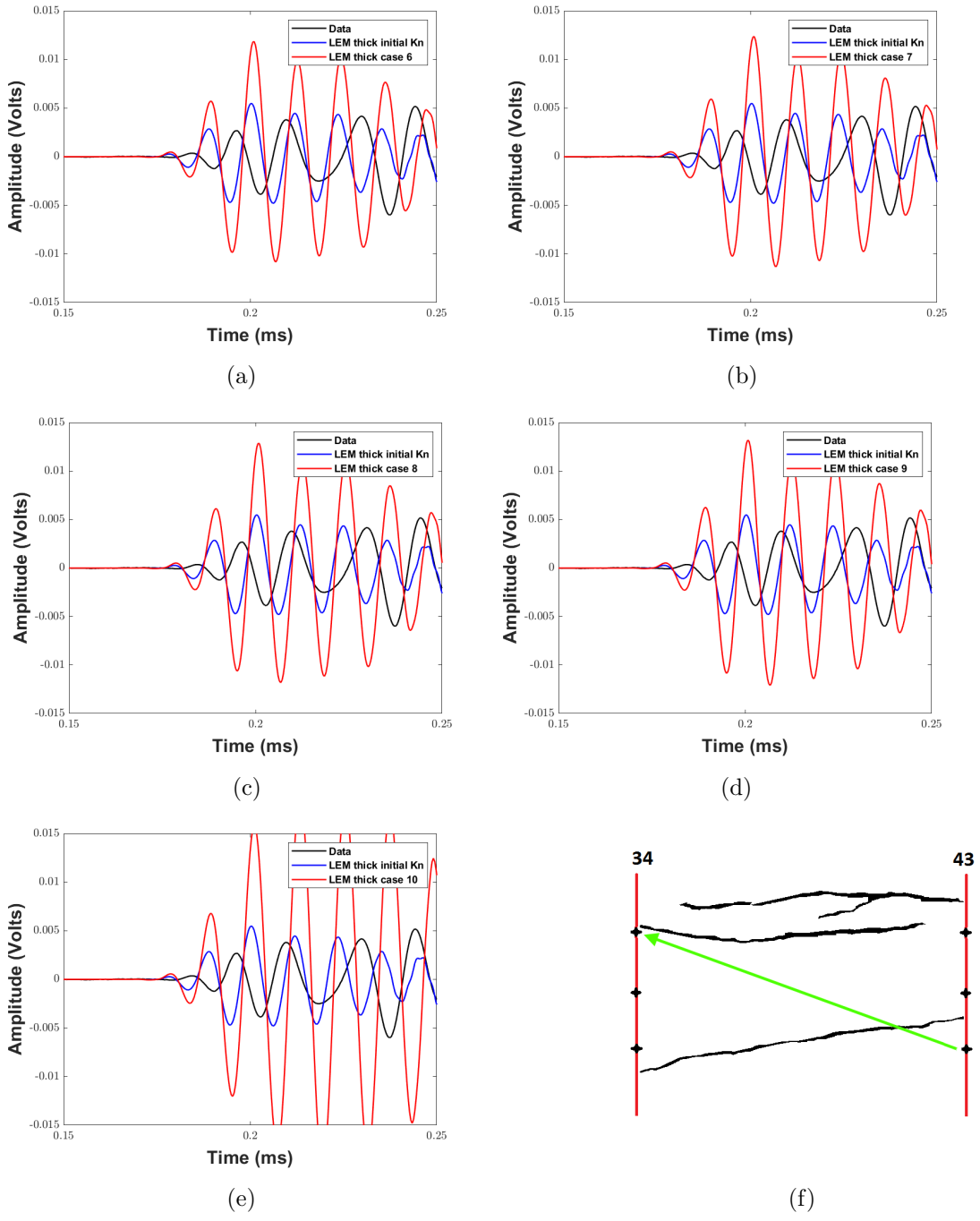

Figure D.2: Waveforms for the frame between boreholes 34-43 for the LEM model with thick layer. Shot in borehole 43 at depth 0.6 m and recordings at 0.2 m D.2f. Case 6 D.2a to 10 D.2e (K_n 60 to 100 times higher than initial).

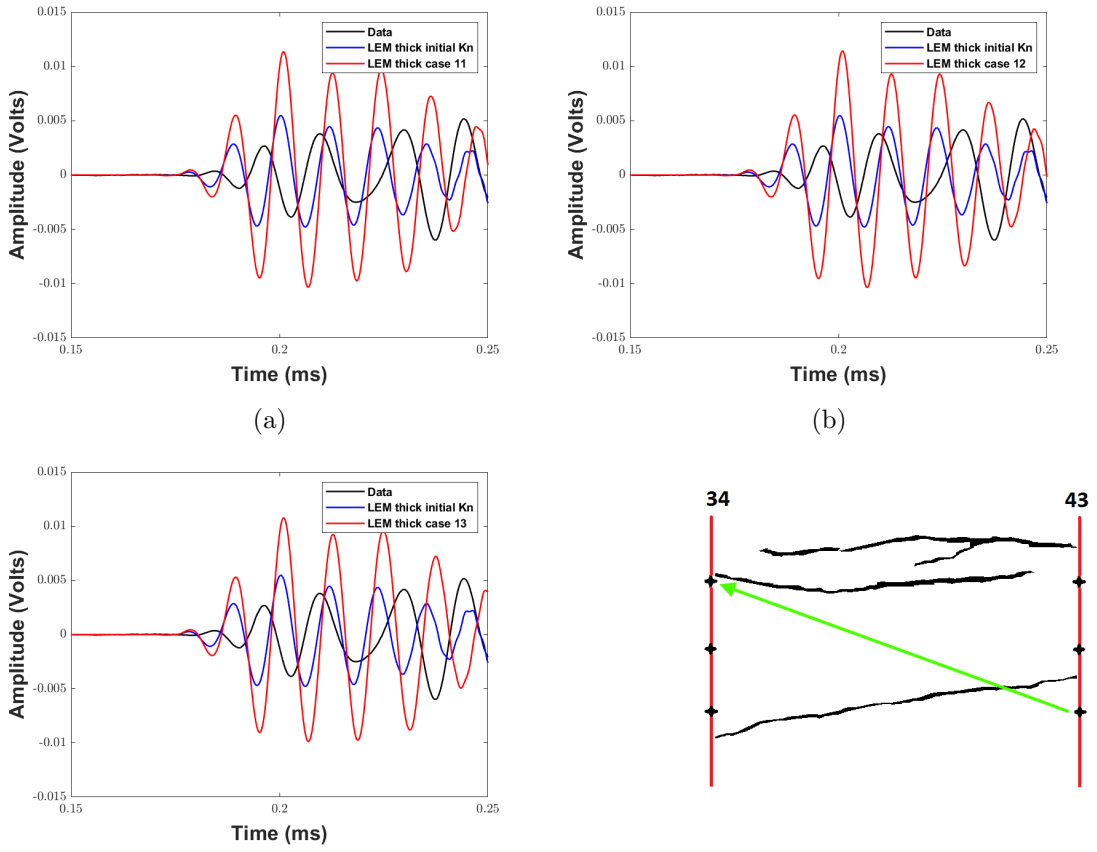

Figure D.3: Waveforms for the frame between boreholes 34-43 for the LEM model with thick layer. Shot in borehole 43 at depth 0.6 m and recordings at 0.2 m D.3d. Case 11 D.3a to 13 D.3c (K_s 0.5, 0.6 and 0.2 the normal fracture stiffness $K_n = 1.67 \times 10^{12}$ to 100 times higher than initial).

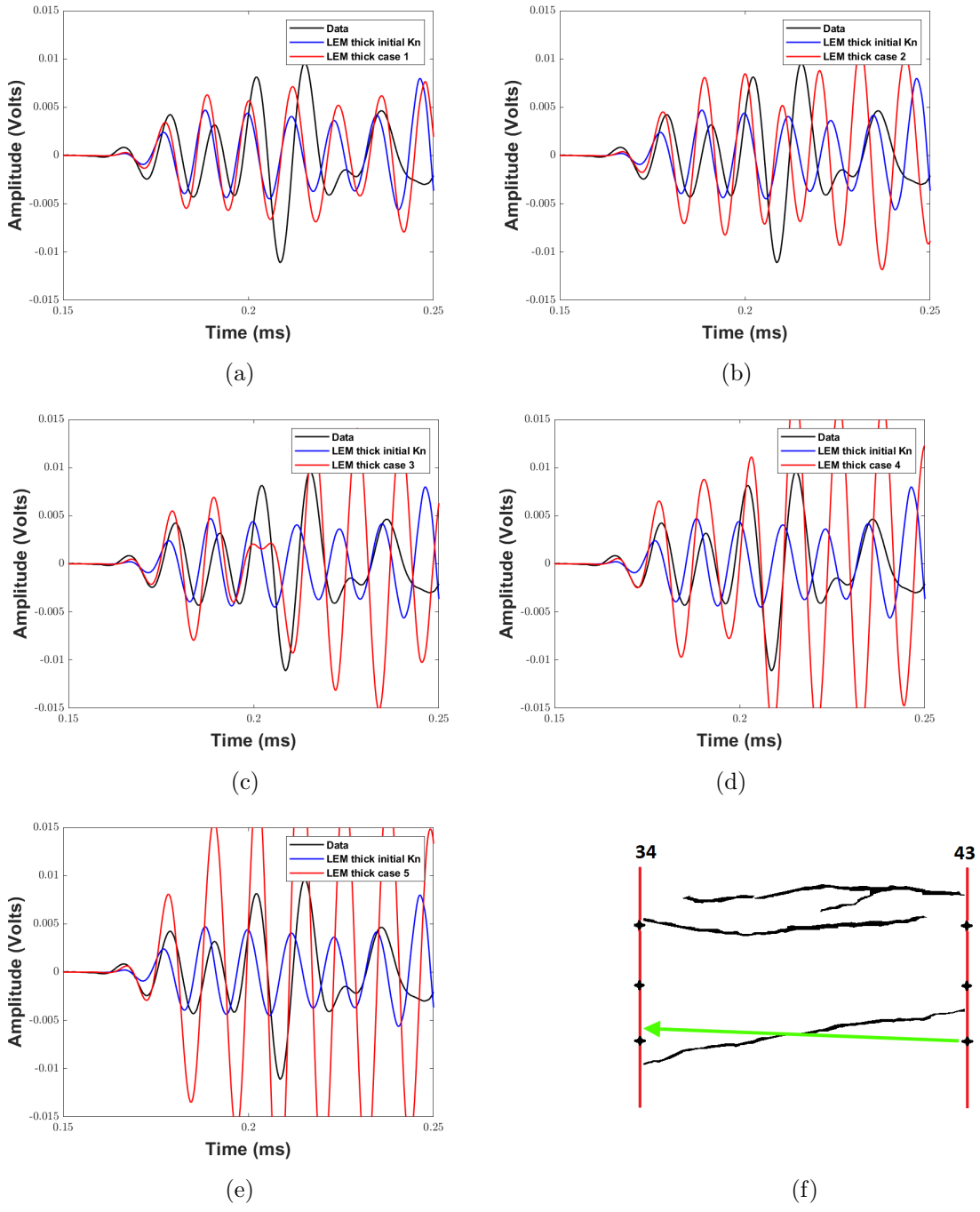

Figure D.4: Waveforms for the frame between boreholes 34-43 for the LEM model with thick layer. Shot in borehole 43 at depth 0.6 m and recordings at 0.55 m D.4f. Case 1 D.4a to 5 D.4e (K_n 10 to 50 times higher than initial).

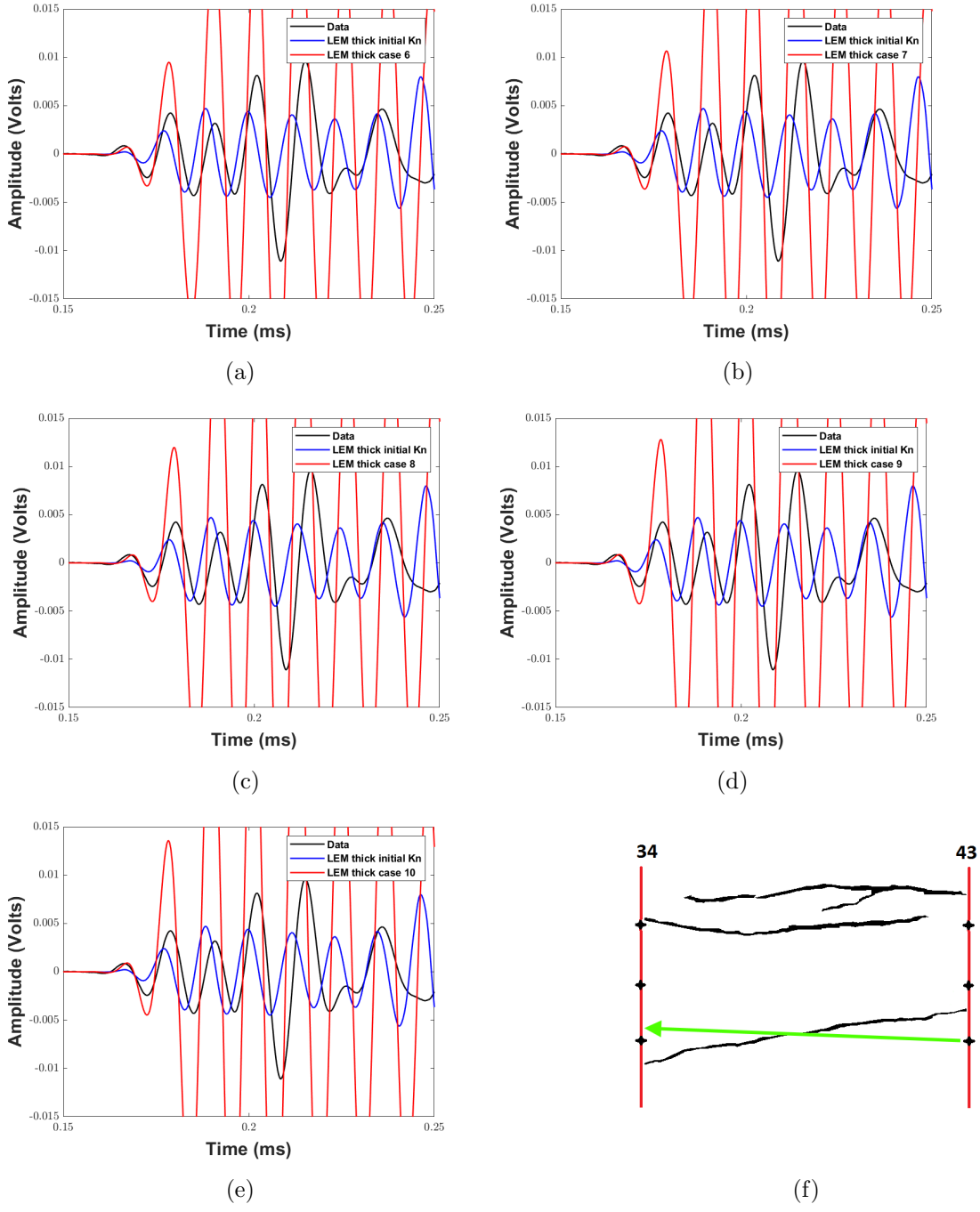

Figure D.5: Waveforms for the frame between boreholes 34-43 for the LEM model with thick layer. Shot in borehole 43 at depth 0.6 m and recordings at 0.55 m D.5f. Case 6 D.5a to 10 D.5e (K_n 60 to 100 times higher than initial).

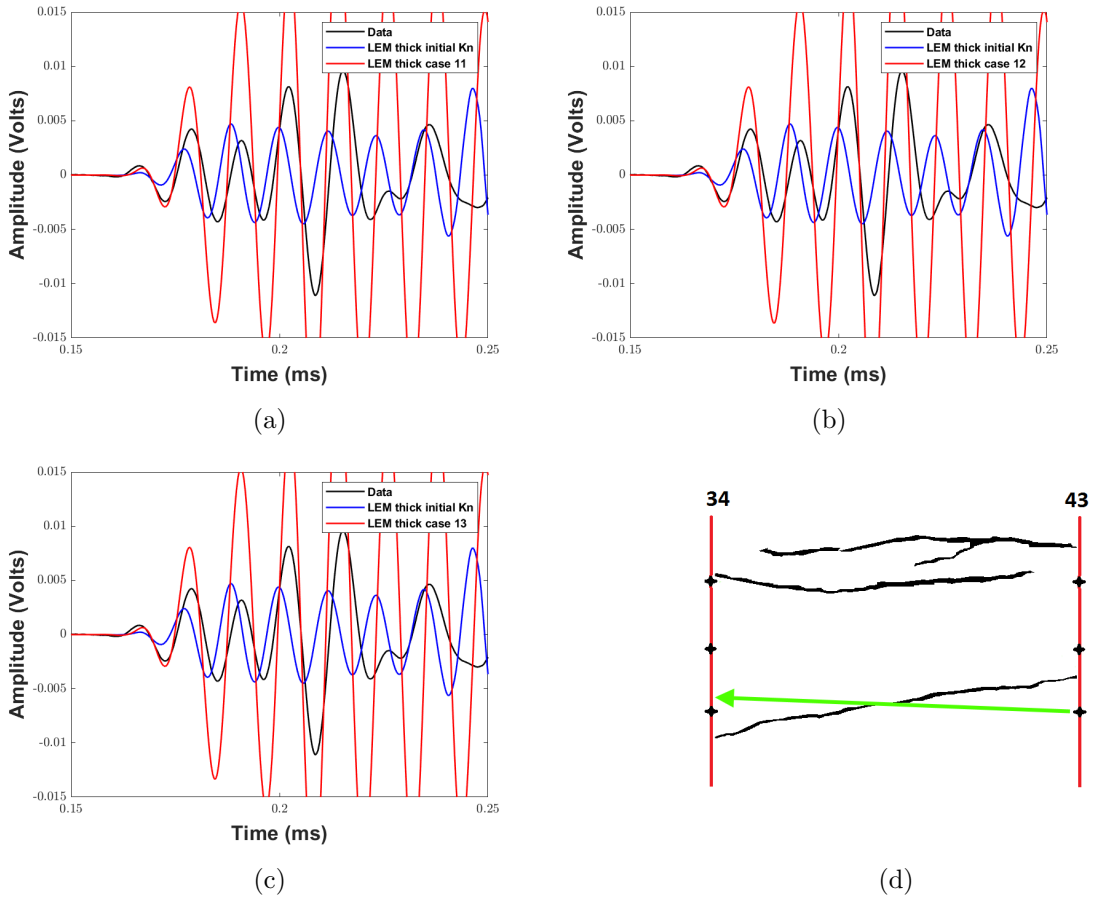

Figure D.6: Waveforms for the frame between boreholes 34-43 for the LEM model with thick layer. Shot in borehole 43 at depth 0.6 m and recordings at 0.55 m D.6d. Case 11 D.6a to 13 D.6c (K_s 0.5, 0.6 and 0.2 the normal fracture stiffness $K_n = 1.67 \times 10^{12}$ to 100 times higher than initial).

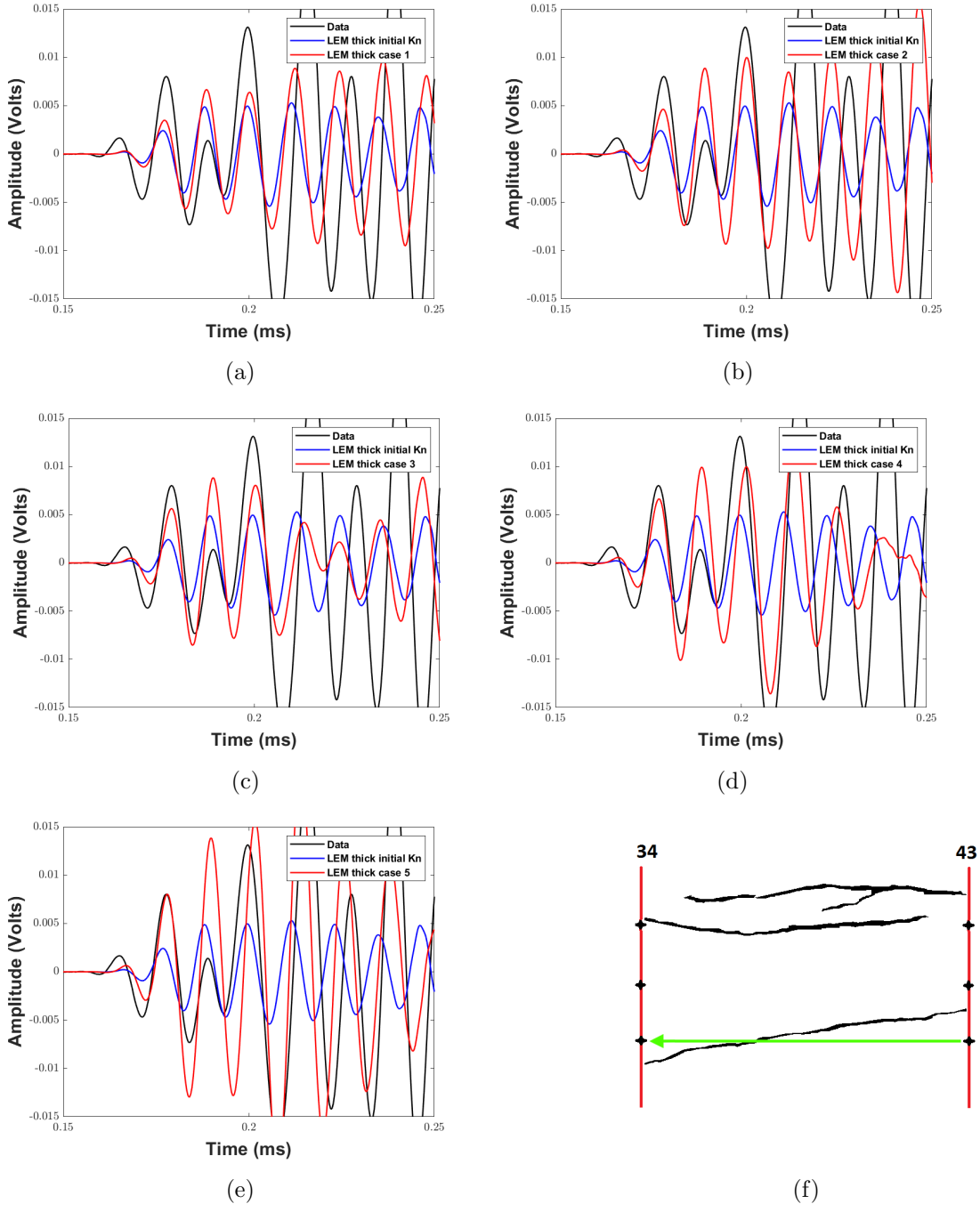

Figure D.7: Waveforms for the frame between boreholes 34-43 for the LEM model with thick layer. Shot in borehole 43 at depth 0.6 m and recordings at 0.6 m D.7f. Case 1 D.7a to 5 D.7e (K_n 10 to 50 times higher than initial).

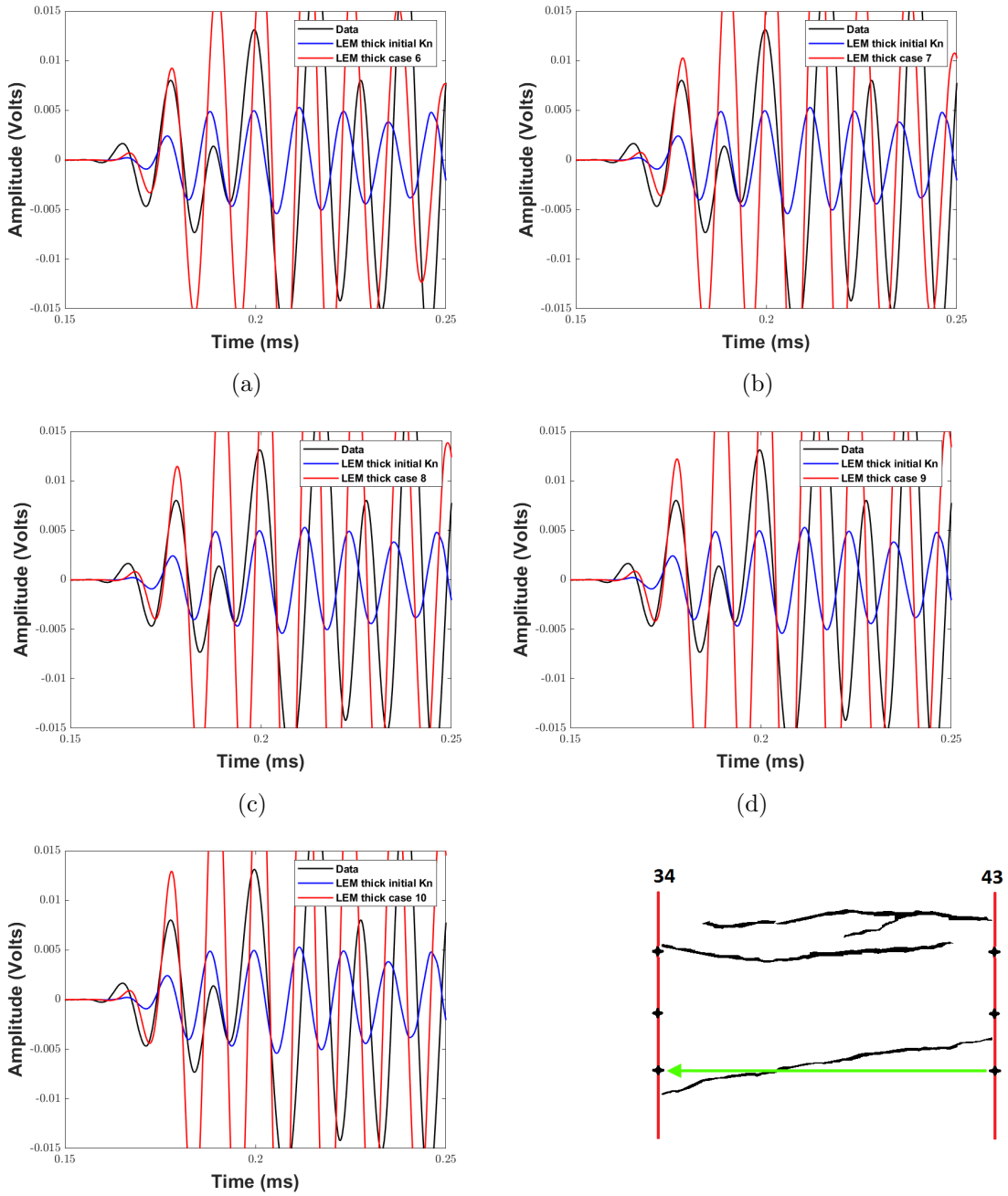

Figure D.8: Waveforms for the frame between boreholes 34-43 for the LEM model with thick layer. Shot in borehole 43 at depth 0.6 m and recordings at 0.6 m D.8f. Case 6 D.8a to 10 D.8e (K_n 60 to 100 times higher than initial).

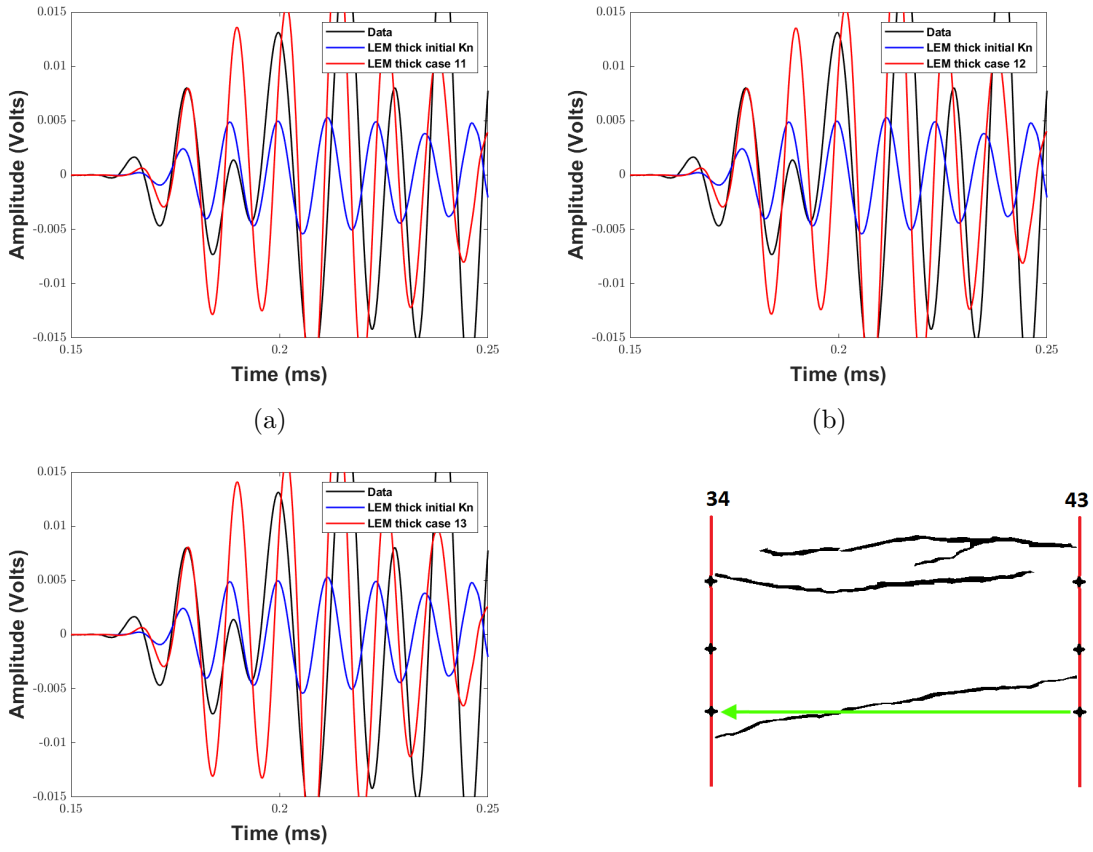

Figure D.9: Waveforms for the frame between boreholes 34-43 for the LEM model with thick layer. Shot in borehole 43 at depth 0.6 m and recordings at 0.6 m D.9d. Case 11 D.9a to 13 D.9c (K_s 0.5, 0.6 and 0.2 the normal fracture stiffness $K_n = 1.67 \times 10^{12}$ to 100 times higher than initial).

D.1.2 LEM fine layer results for stiffness optimisation

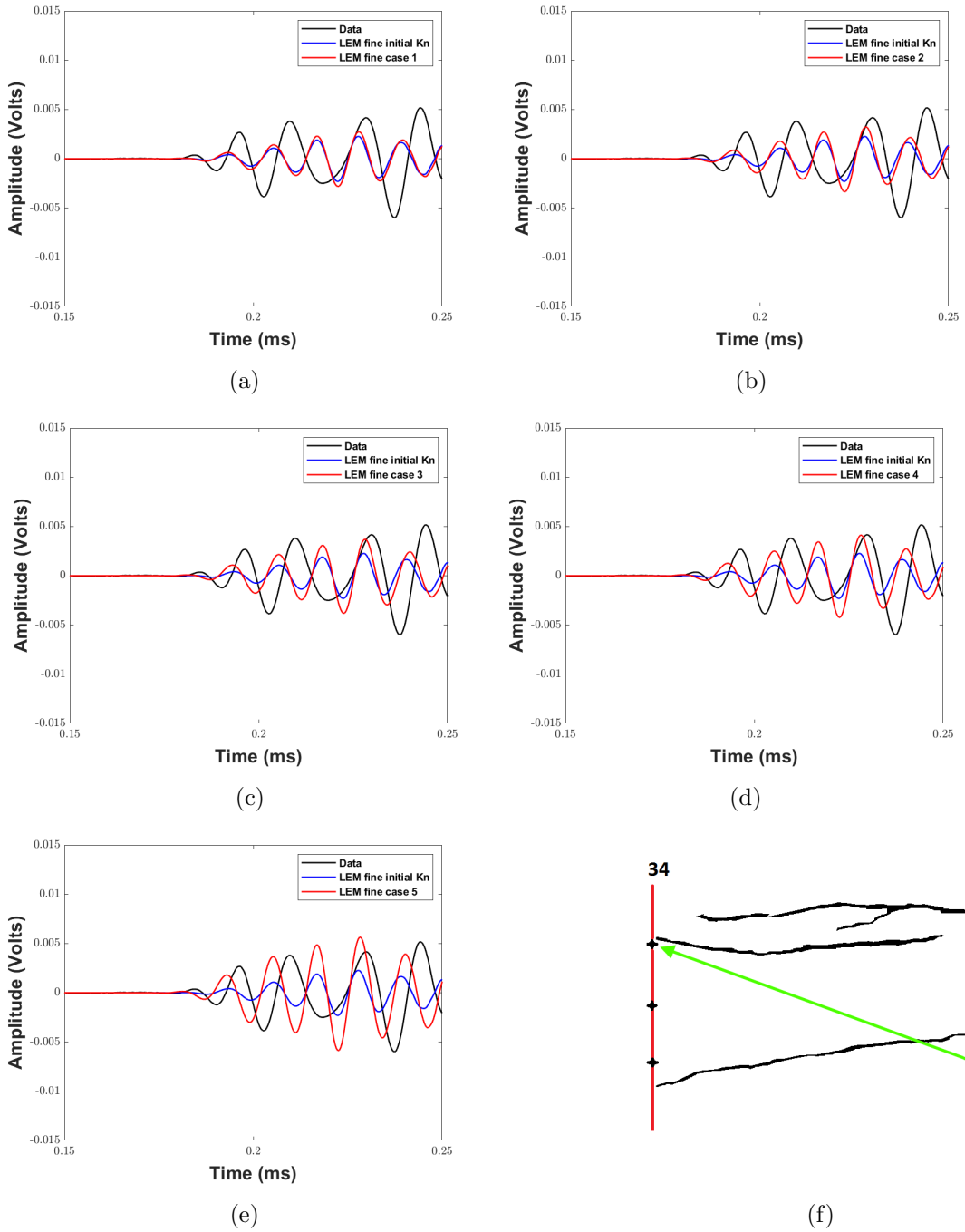

Figure D.10: Waveforms for the frame between boreholes 34-43 for the LEM model with fine layer. Shot in borehole 43 at depth 0.6 m and recordings at 0.2 m D.10f. Case 1 D.10a to 5 D.10e (K_n 10 to 50 times higher than initial).

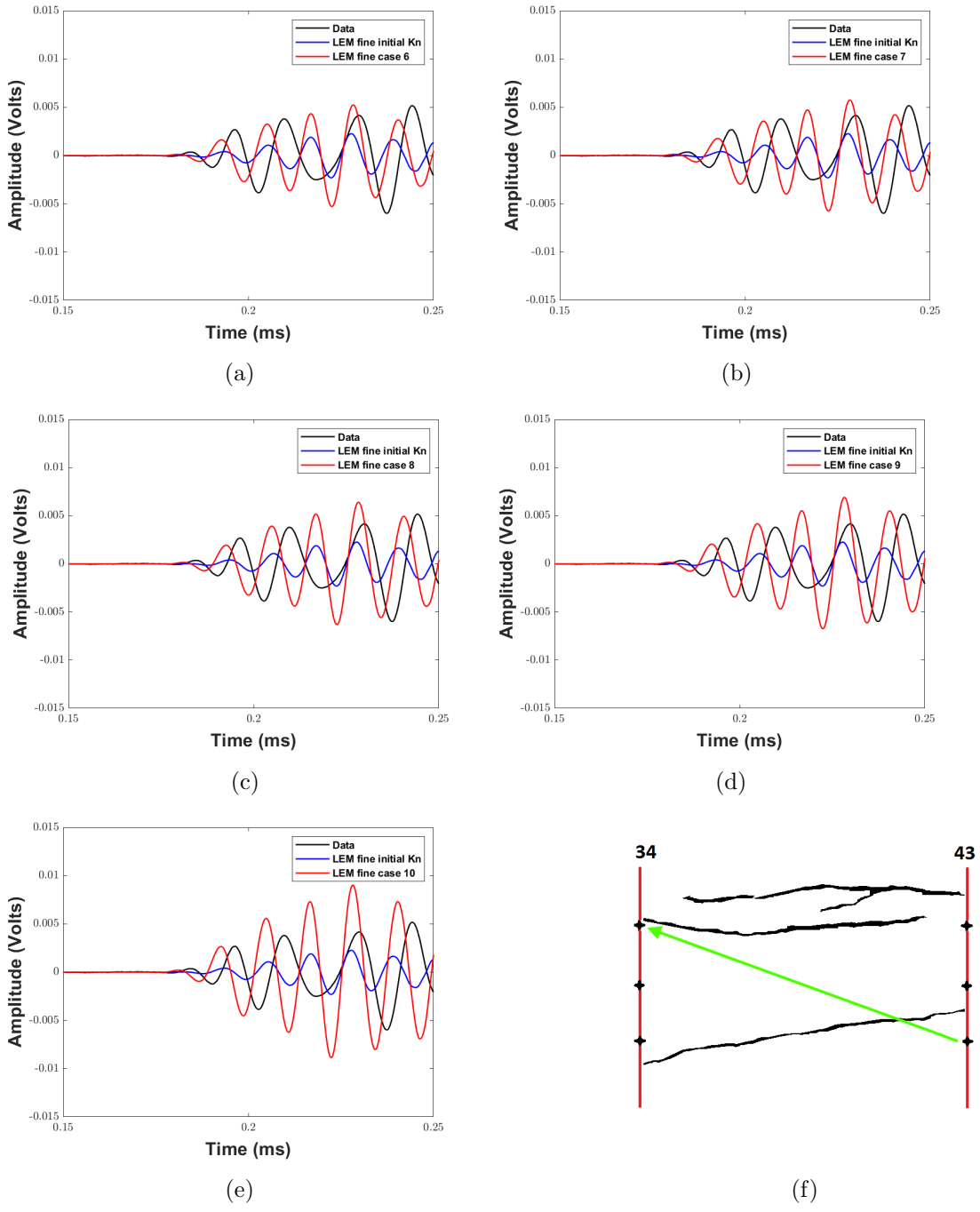

Figure D.11: Waveforms for the frame between boreholes 34-43 for the LEM model with fine layer. Shot in borehole 43 at depth 0.6 m and recordings at 0.2 m D.11f. Case 6 D.11a to 10 D.11e (K_n 60 to 100 times higher than initial).

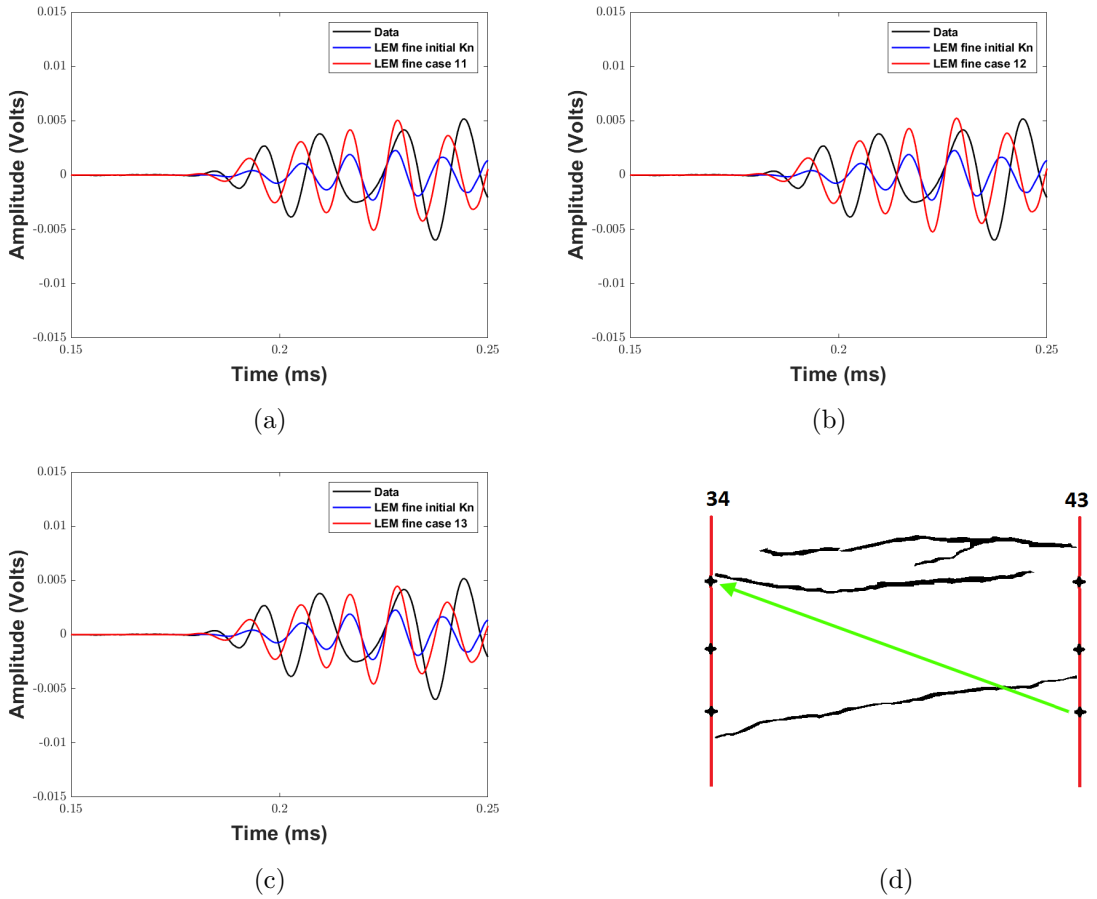

Figure D.12: Waveforms for the frame between boreholes 34-43 for the LEM model with fine layer. Shot in borehole 43 at depth 0.6 m and recordings at 0.2 m D.12c. Case 11 D.12a to 13 D.12d (K_s 0.5, 0.6 and 0.2 the normal fracture stiffness $K_n = 1.67 \times 10^{12}$ to 100 times higher than initial).

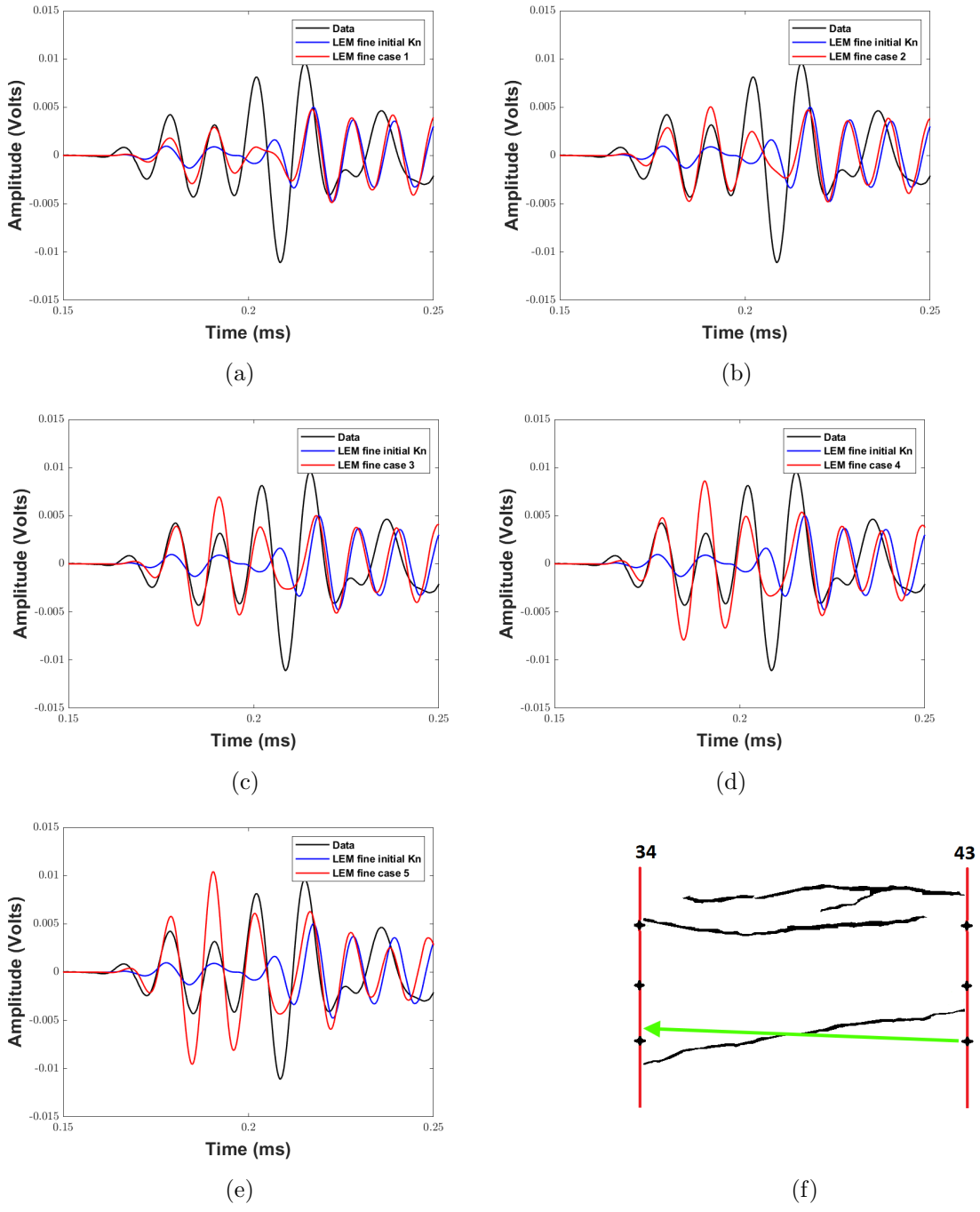

Figure D.13: Waveforms for the frame between boreholes 34-43 for the LEM model with fine layer. Shot in borehole 43 at depth 0.6 m and recordings at 0.55 m D.13f. Case 1 D.13a to 5 D.13e (K_n 10 to 50 times higher than initial).

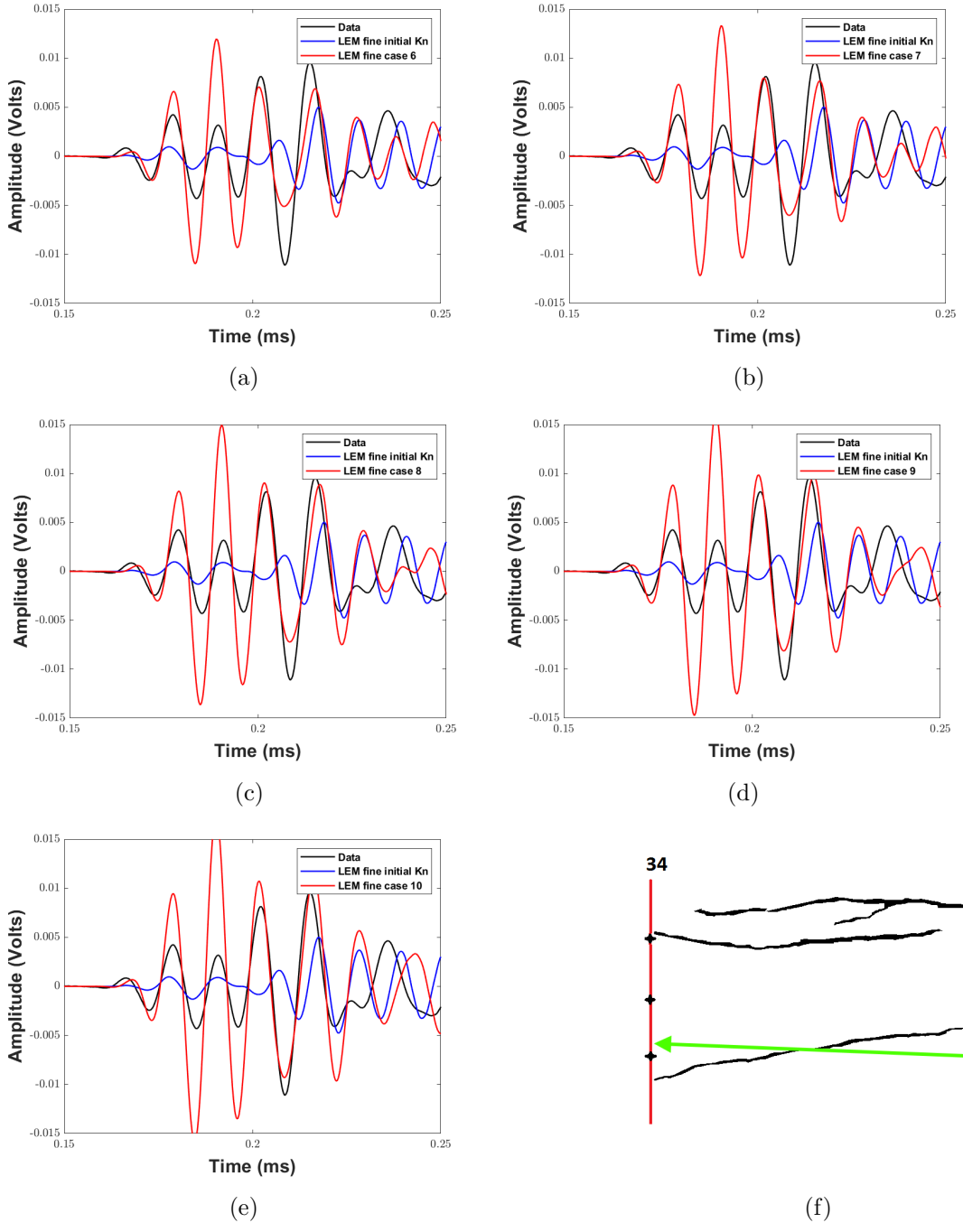

Figure D.14: Waveforms for the frame between boreholes 34-43 for the LEM model with fine layer. Shot in borehole 43 at depth 0.6 m and recordings at 0.55 m D.14f. Case 6 D.14a to 10 D.14e (K_n 60 to 100 times higher than initial).

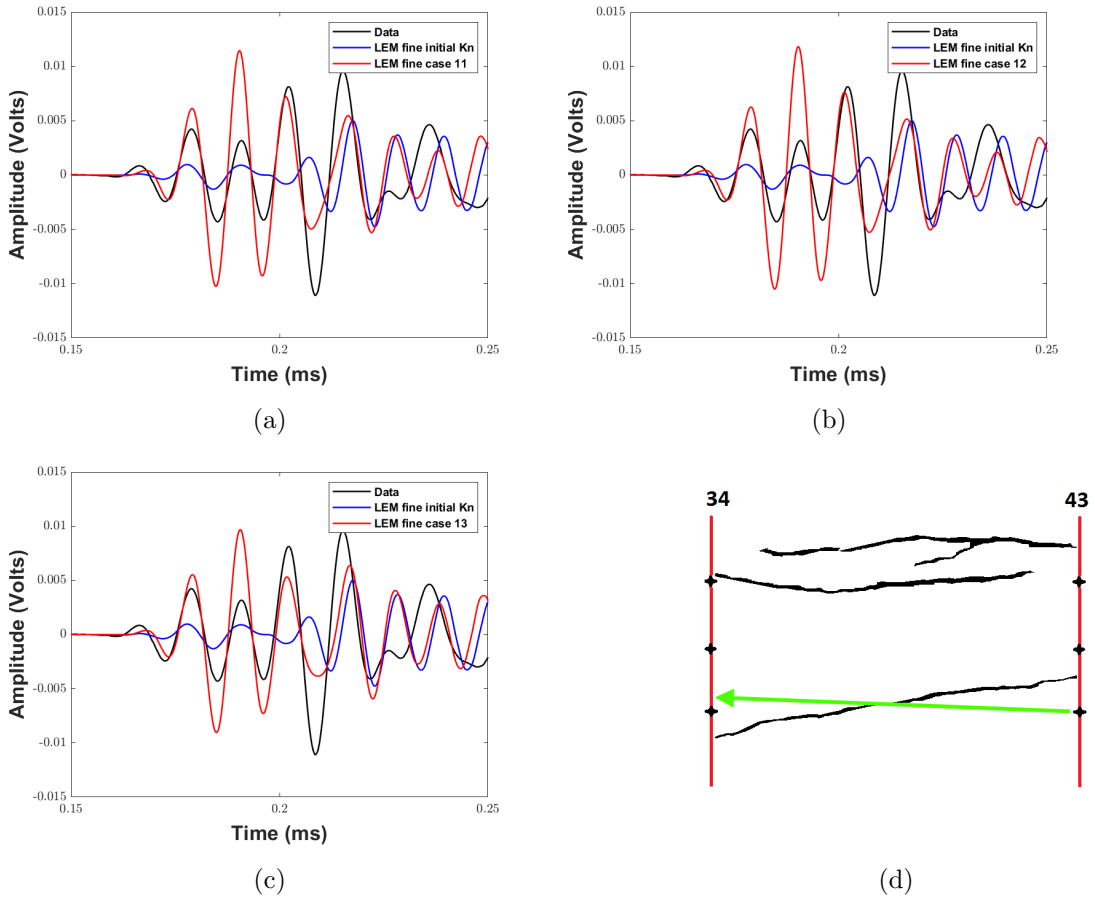

Figure D.15: Waveforms for the frame between boreholes 34-43 for the LEM model with fine layer. Shot in borehole 43 at depth 0.6 m and recordings at 0.55 m D.15d. Case 11 D.15a to 13 D.15c (K_s 0.5, 0.6 and 0.2 the normal fracture stiffness $K_n = 1.67 \times 10^{12}$ to 100 times higher than initial).

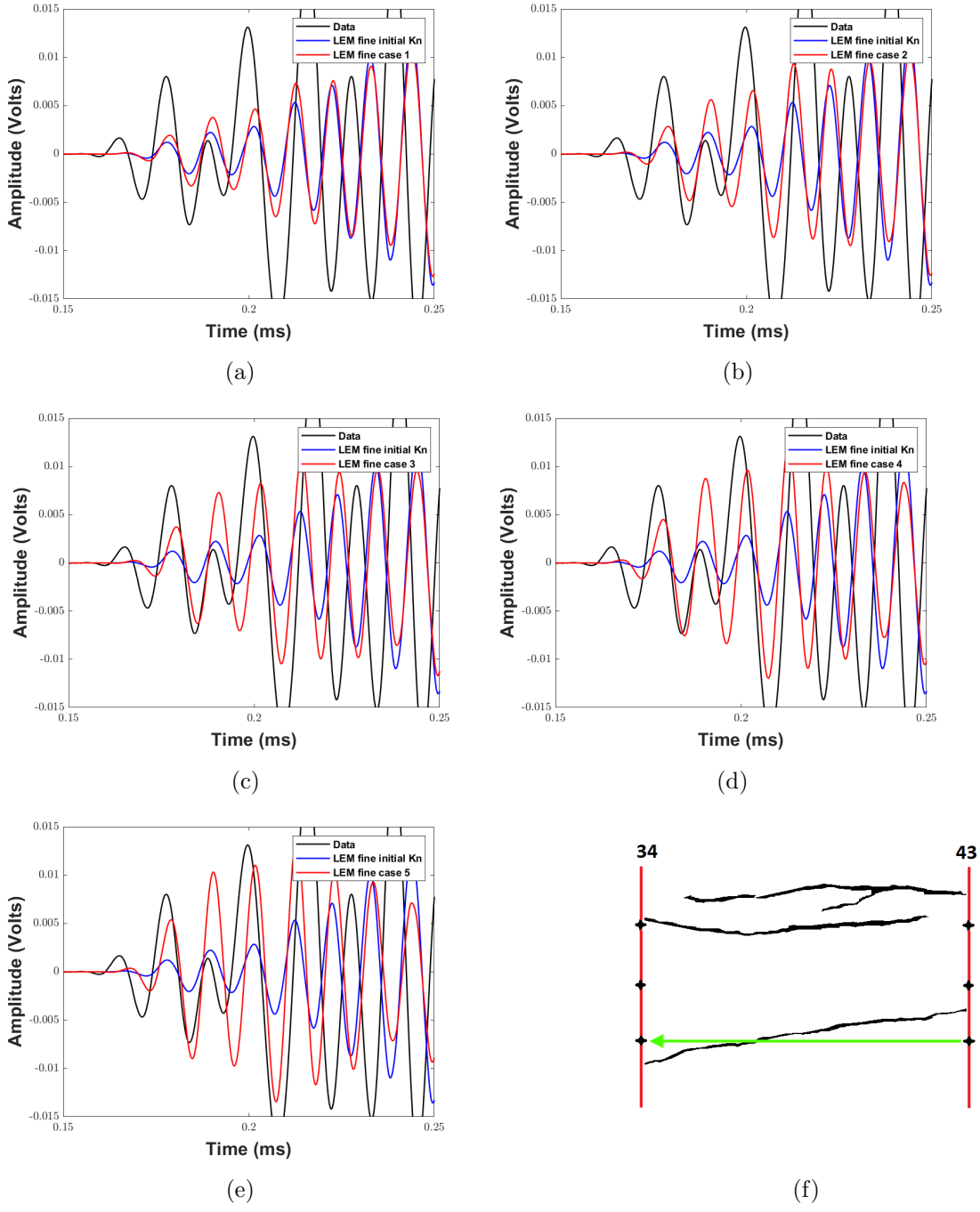

Figure D.16: Waveforms for the frame between boreholes 34-43 for the LEM model with fine layer. Shot in borehole 43 at depth 0.6 m and recordings at 0.6 m D.16f. Case 1 D.16a to 5 D.16e (K_n 10 to 50 times higher than initial).

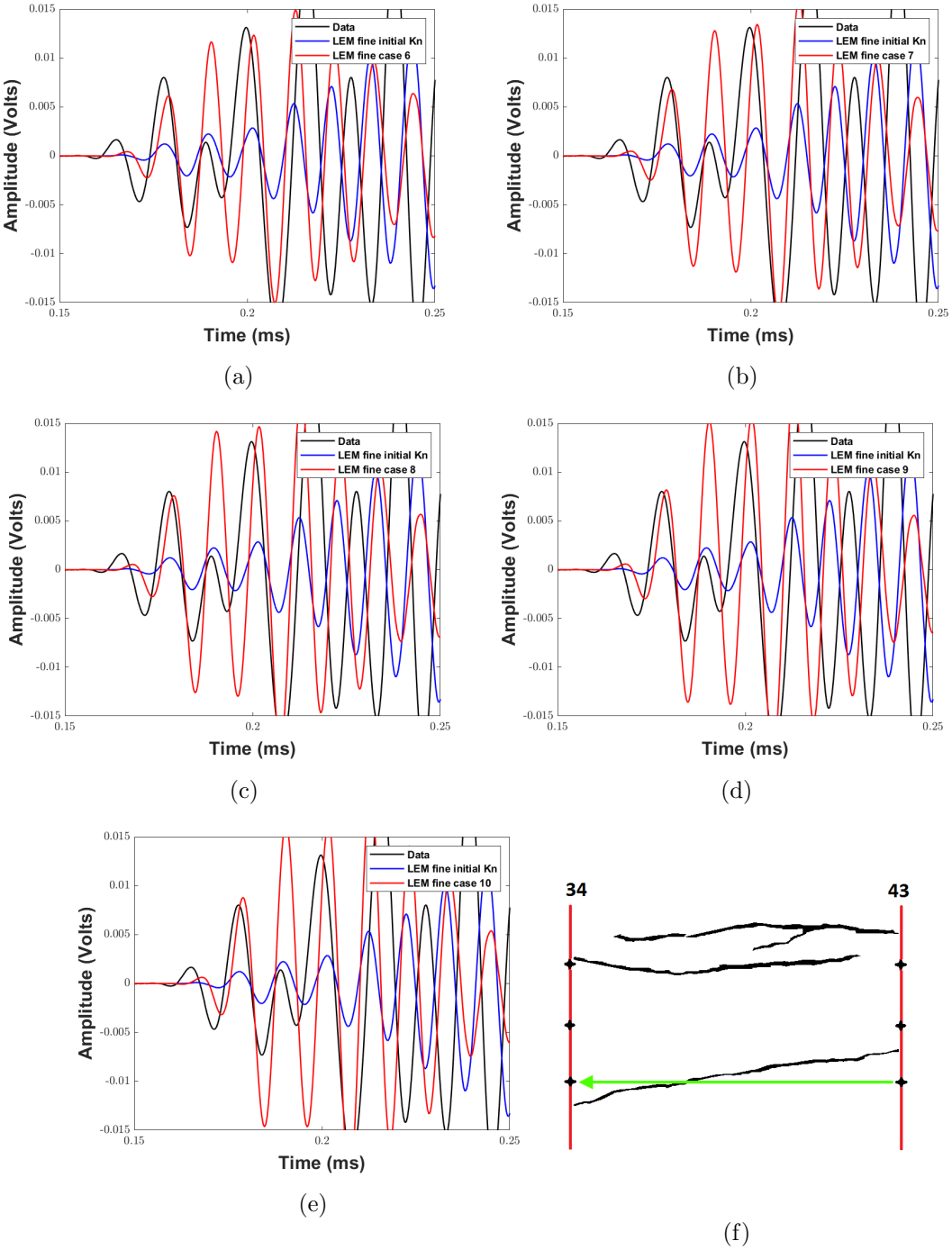

Figure D.17: Waveforms for the frame between boreholes 34-43 for the LEM model with fine layer. Shot in borehole 43 at depth 0.6 m and recordings at 0.6 m D.17f. Case 6 D.17a to 10 D.17e (K_n 60 to 100 times higher than initial).

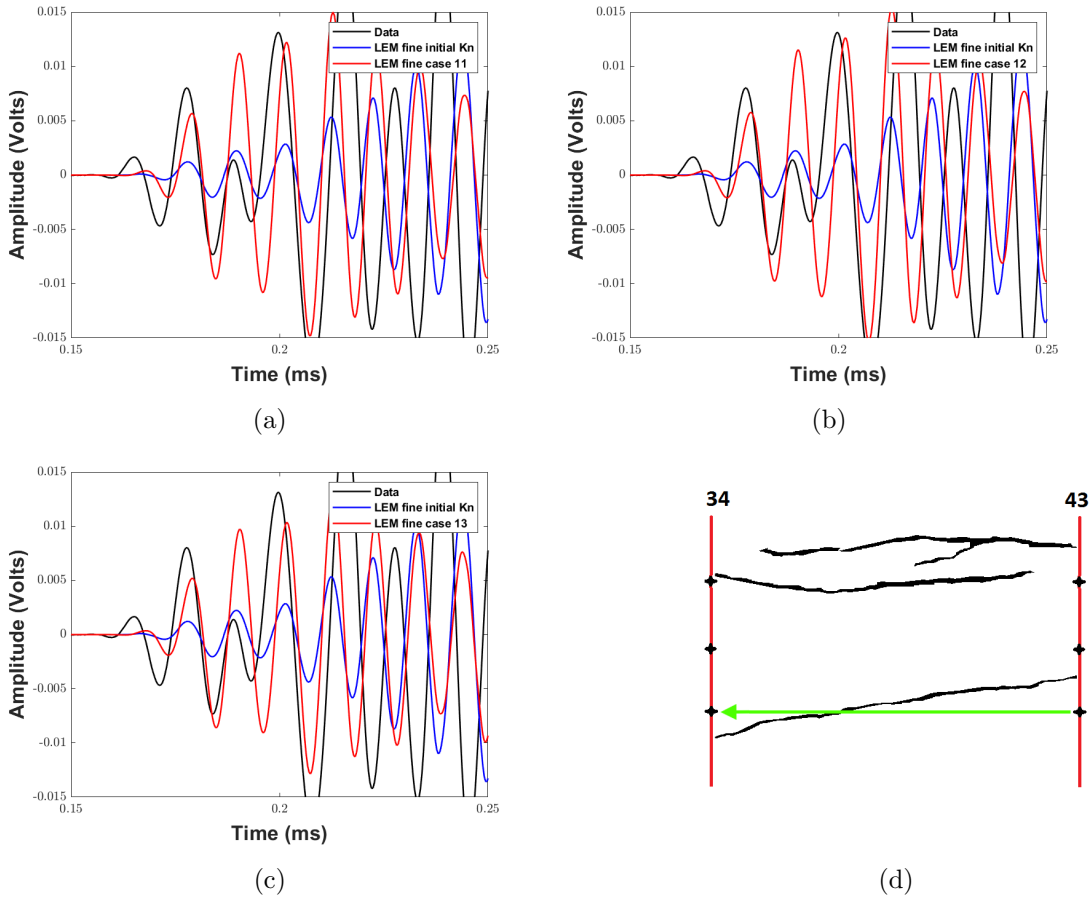

Figure D.18: Waveforms for the frame between boreholes 34-43 for the LEM model with fine layer. Shot in borehole 43 at depth 0.6 m and recordings at 0.6 m D.18d. Case 11 D.18a to 13 D.18c (K_s 0.5, 0.6 and 0.2 the normal fracture stiffness $K_n = 1.67 \times 10^{12}$ to 100 times higher than initial).

D.1.3 Explicit model results for stiffness optimisation

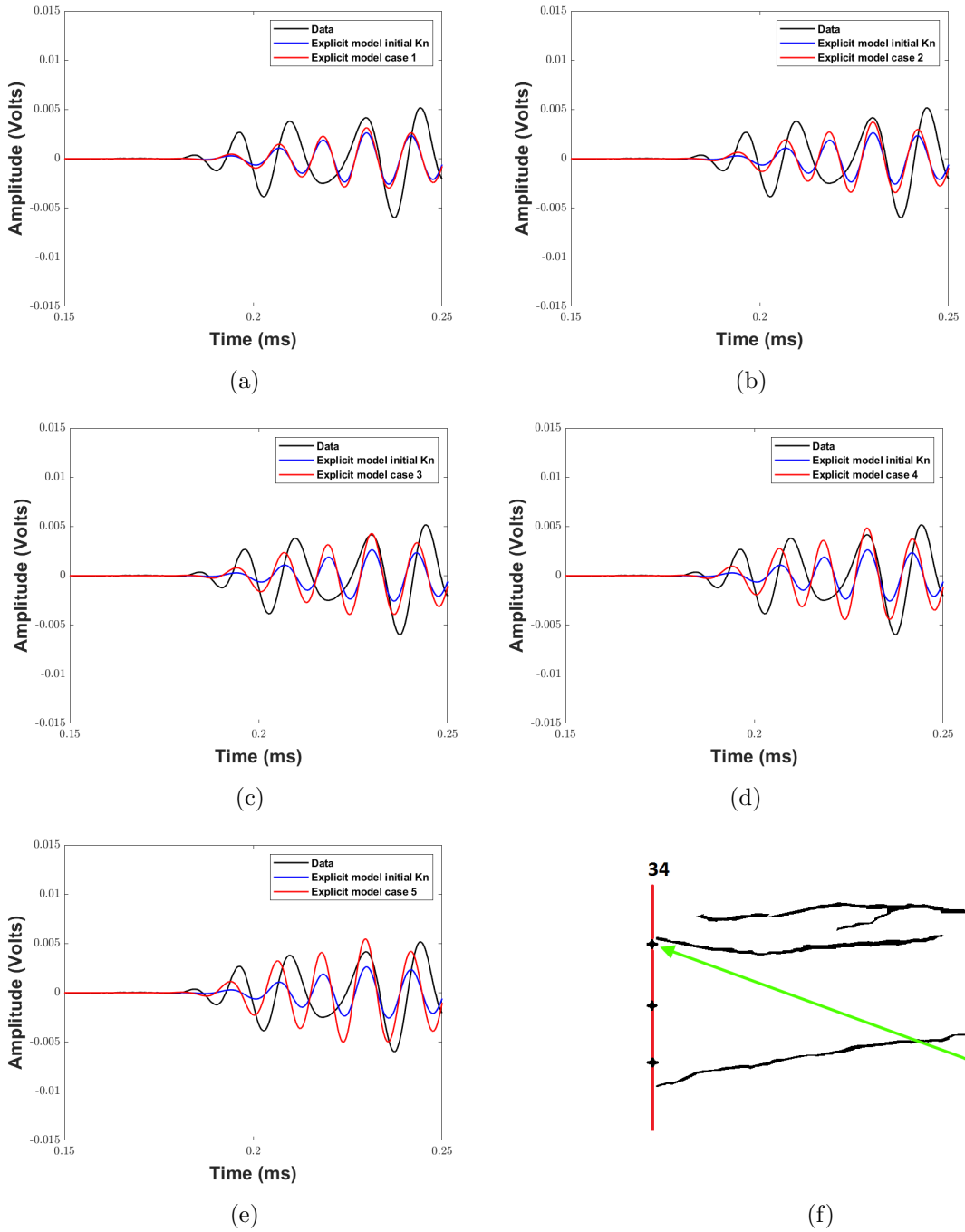

Figure D.19: Waveforms for the frame between boreholes 34-43 for the pixelised explicit model. Shot in borehole 43 at depth 0.6 m and recordings at 0.2 m D.19f. Case 1 D.19a to 5 D.19e (K_n 10 to 50 times higher than initial).

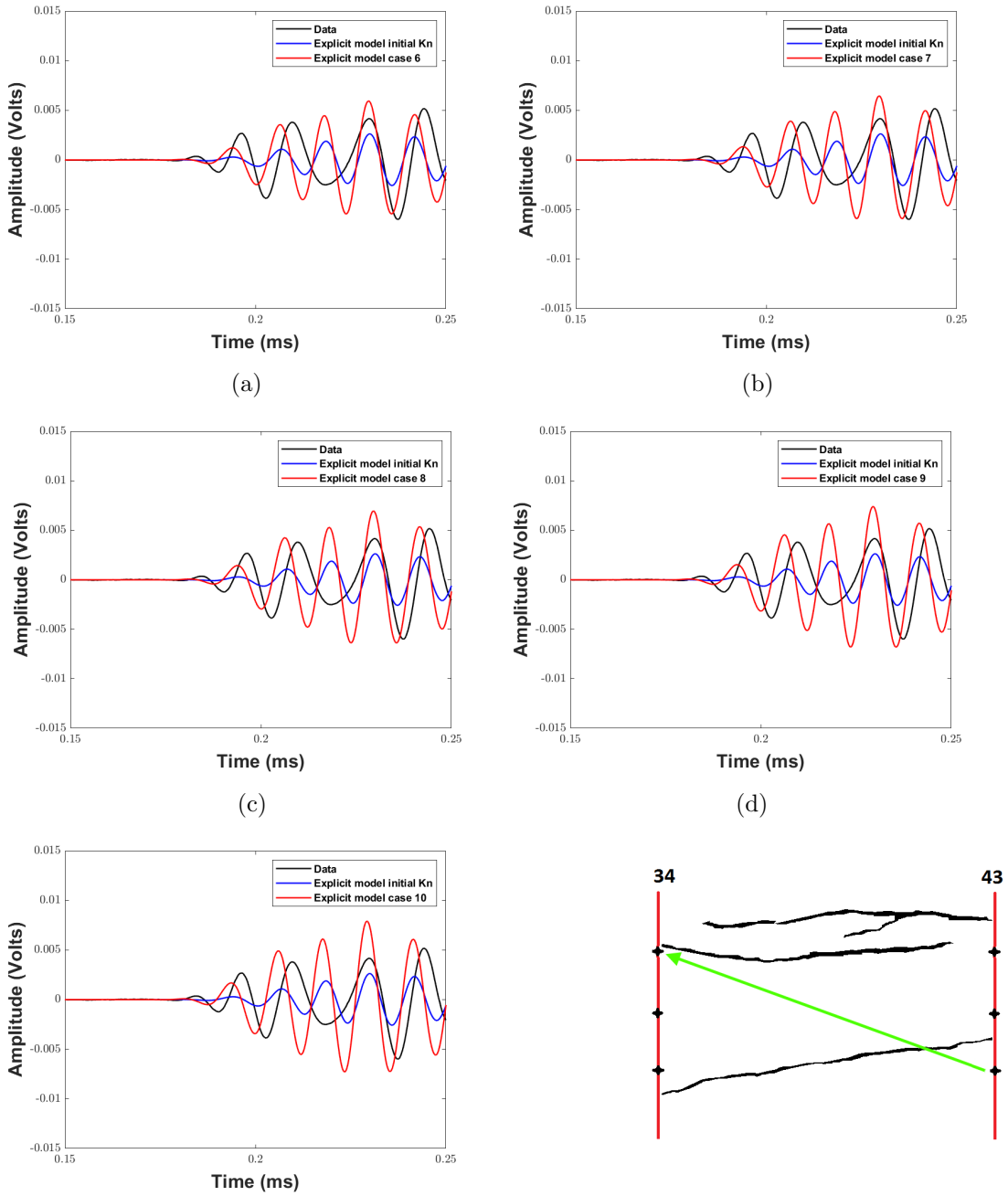

Figure D.20: Waveforms for the frame between boreholes 34-43 for the pixelised explicit model. Shot in borehole 43 at depth 0.6 m and recordings at 0.2 m D.20f. Case 6 D.20a to 10 D.20e (K_n 60 to 100 times higher than initial).

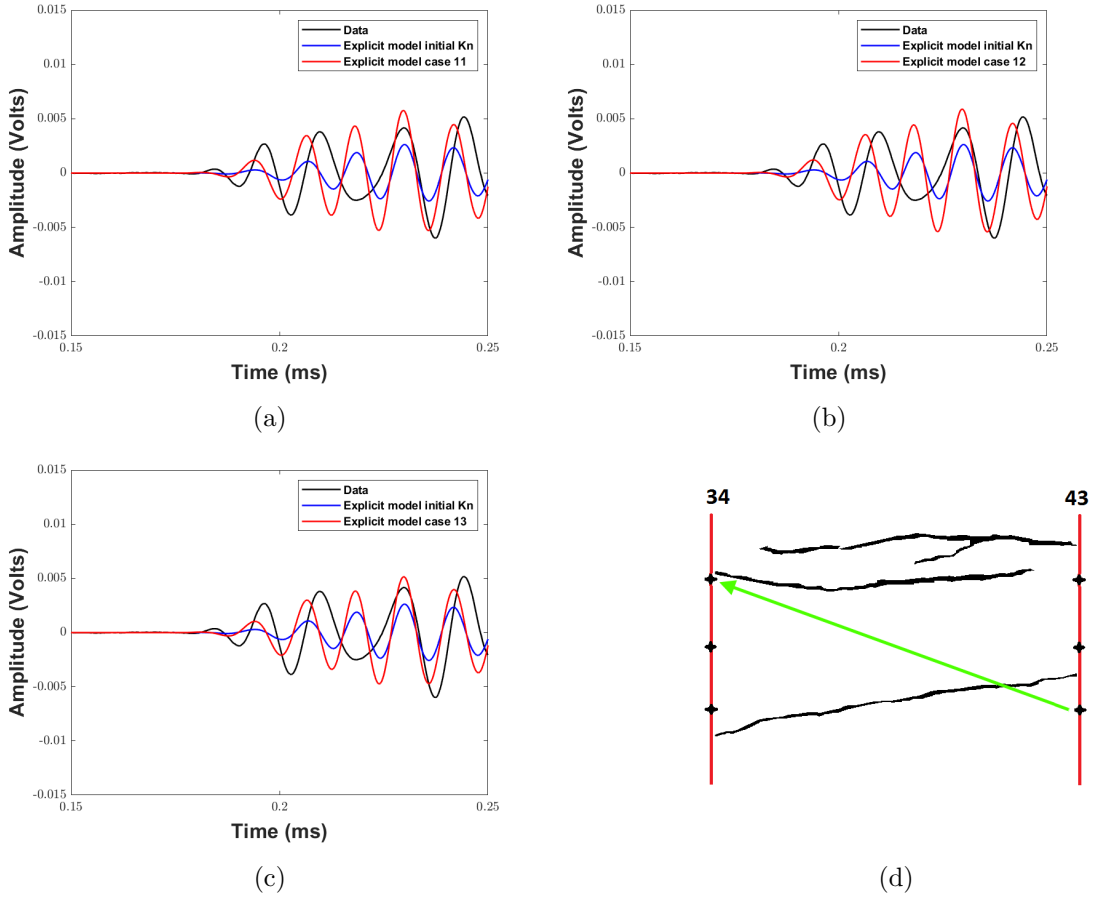

Figure D.21: Waveforms for the frame between boreholes 34-43 for the pixelised explicit model. Shot in borehole 43 at depth 0.6 m and recordings at 0.2 m D.21d. Case 11 D.21a to 13 D.21c (K_s 0.5, 0.6 and 0.2 the normal fracture stiffness $K_n = 1.67 \times 10^{12}$ to 100 times higher than initial).

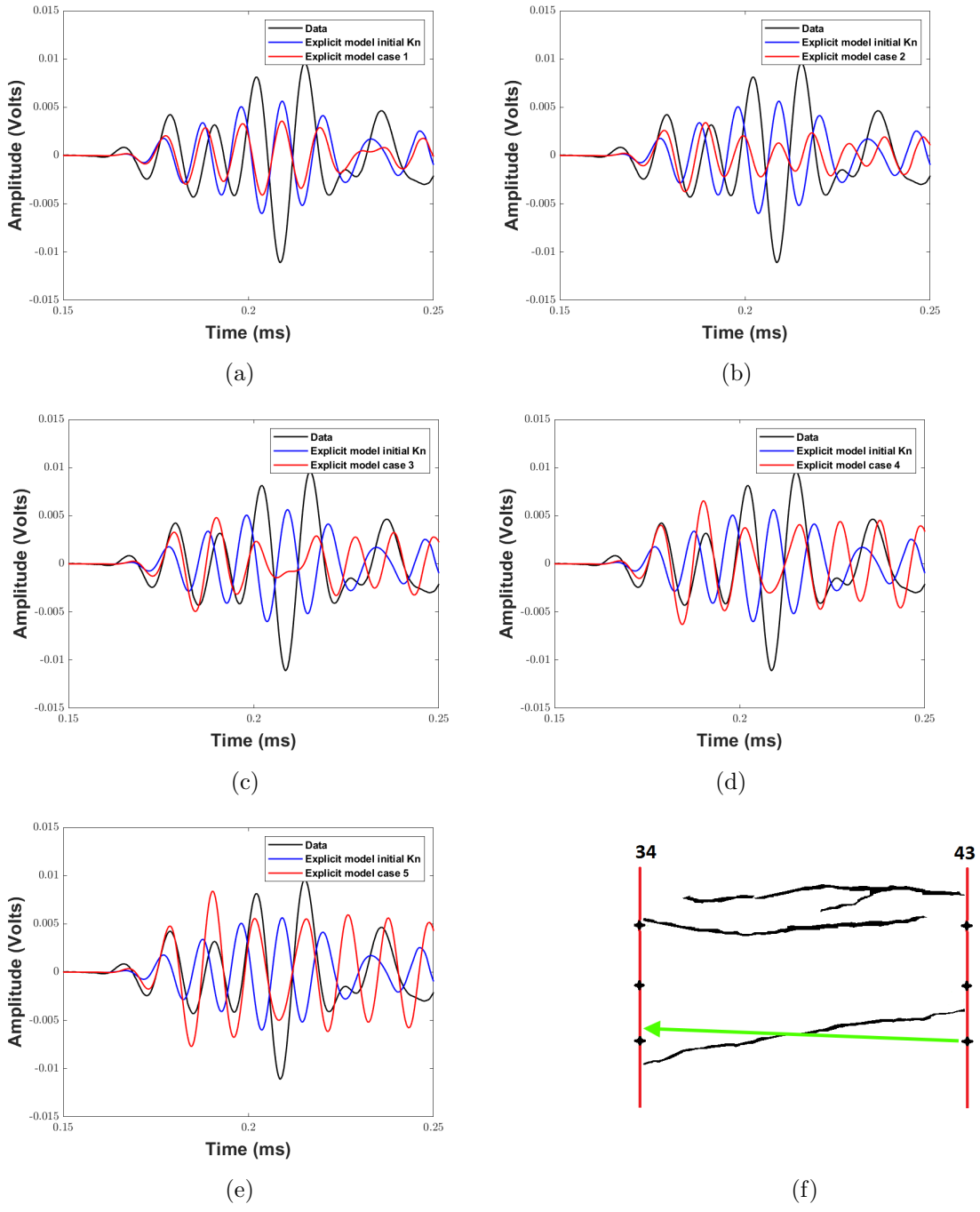

Figure D.22: Waveforms for the frame between boreholes 34-43 for the pixelised explicit modelr. Shot in borehole 43 at depth 0.6 m and recordings at 0.55 m D.22f. Case 1 D.22a to 5 D.22e (K_n 10 to 50 times higher than initial).

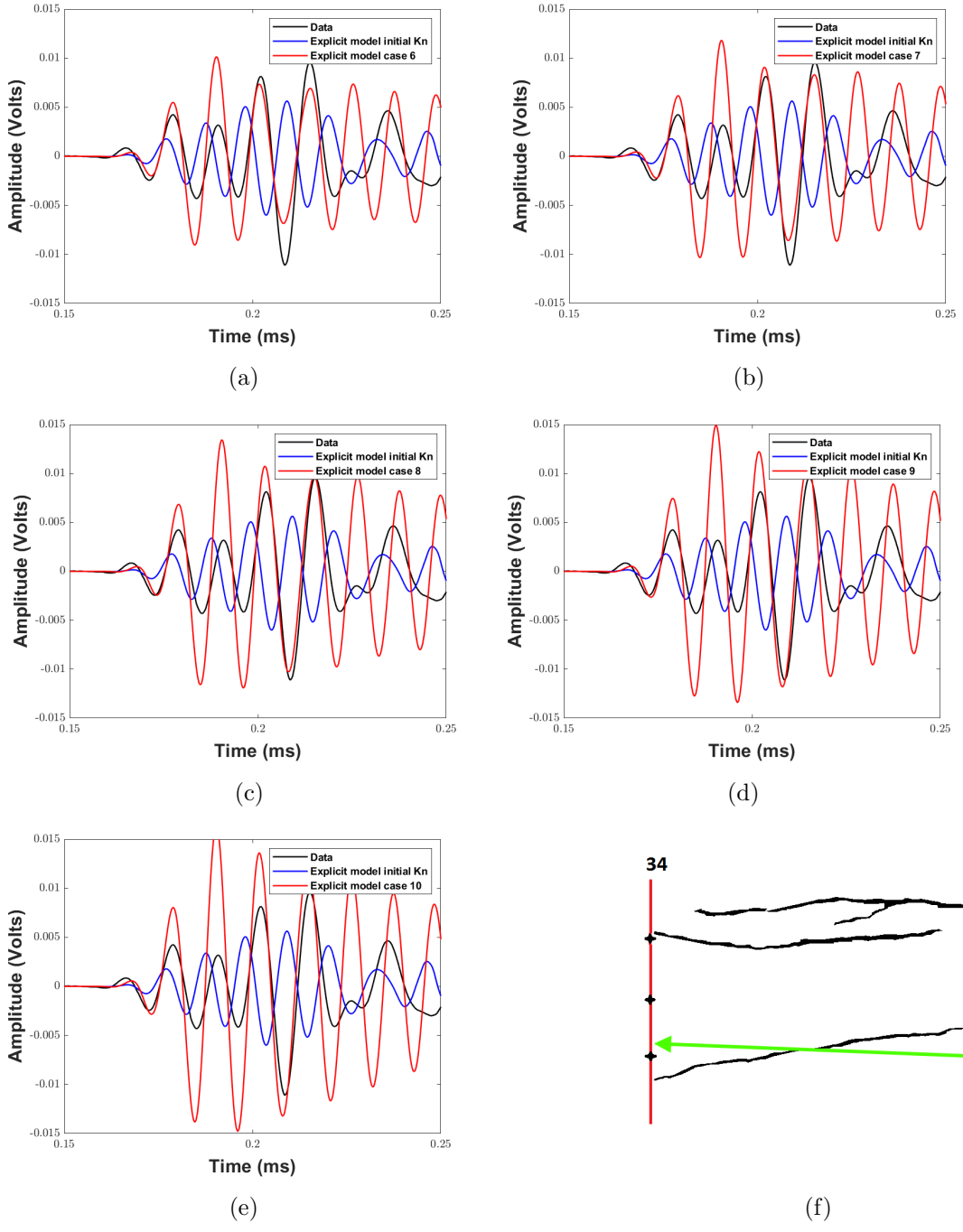

Figure D.23: Waveforms for the frame between boreholes 34-43 for the pixelised explicit model. Shot in borehole 43 at depth 0.6 m and recordings at 0.55 m D.23f. Case 6 D.23a to 10 D.23e (K_n 60 to 100 times higher than initial).

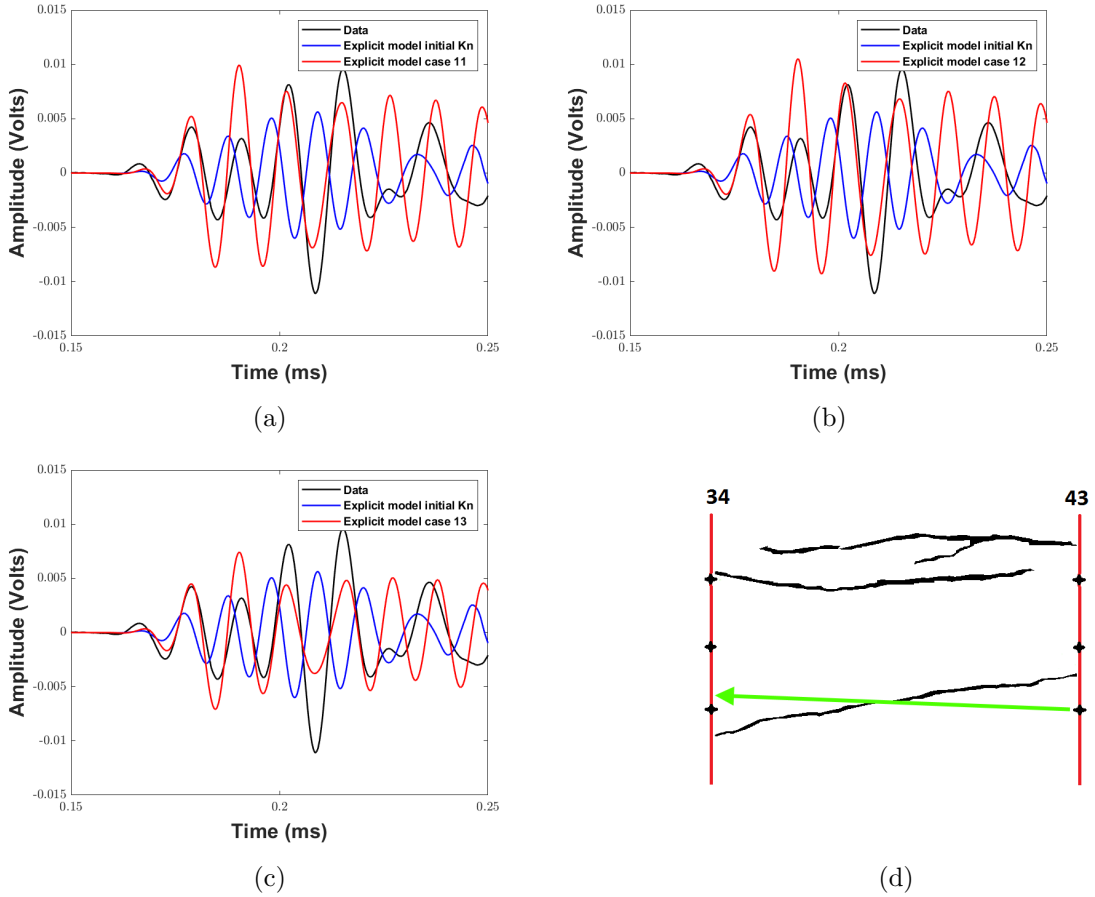

Figure D.24: Waveforms for the frame between boreholes 34-43 for the pixelised explicit model. Shot in borehole 43 at depth 0.6 m and recordings at 0.55 m D.24d. Case 11 D.24a to 13 D.24c (K_s 0.5, 0.6 and 0.2 the normal fracture stiffness $K_n = 1.67 \times 10^{12}$ to 100 times higher than initial).

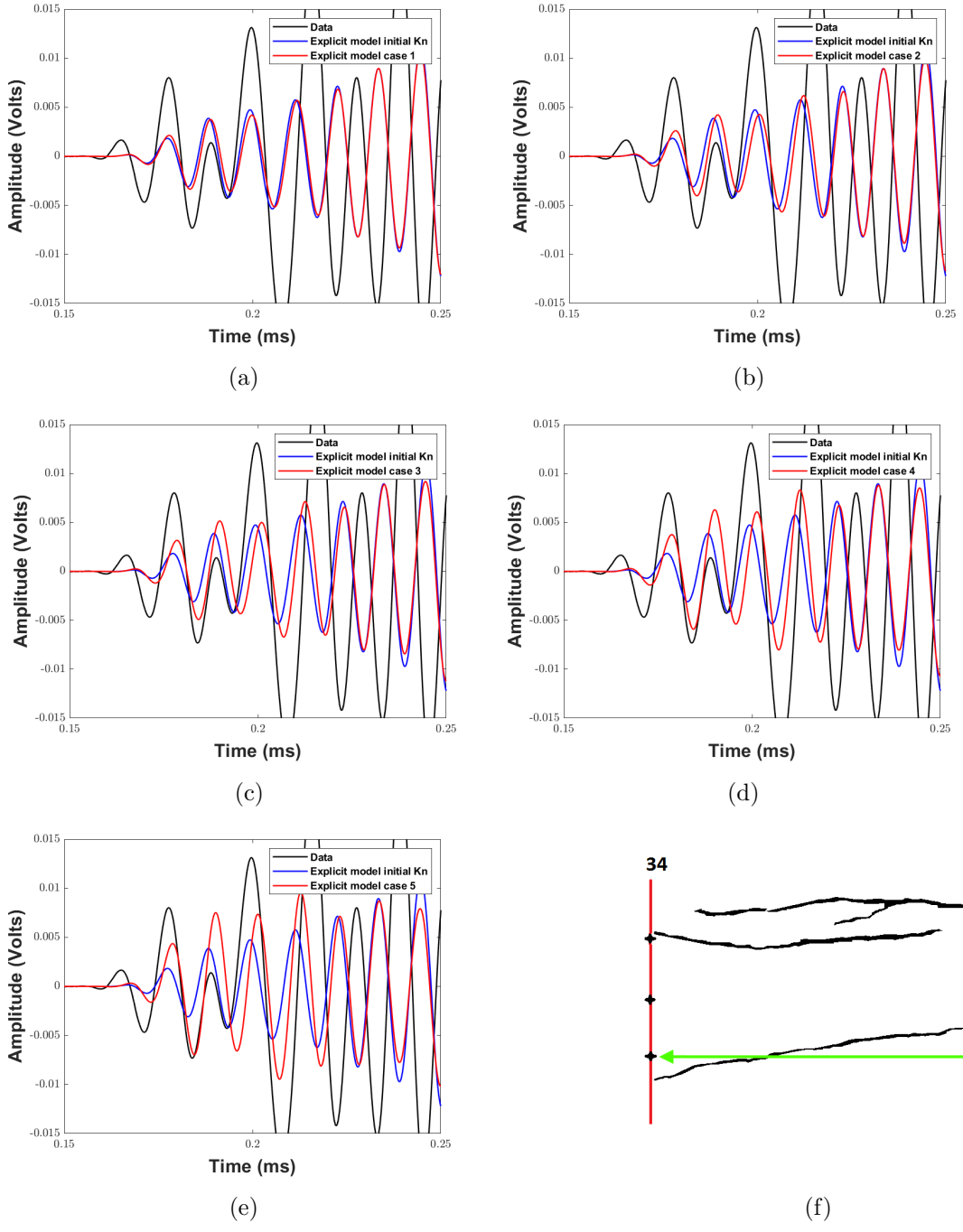

Figure D.25: Waveforms for the frame between boreholes 34-43 for the pixelised explicit model. Shot in borehole 43 at depth 0.6 m and recordings at 0.6 m D.25f. Case 1 D.25a to 5 D.25e (K_n 10 to 50 times higher than initial).

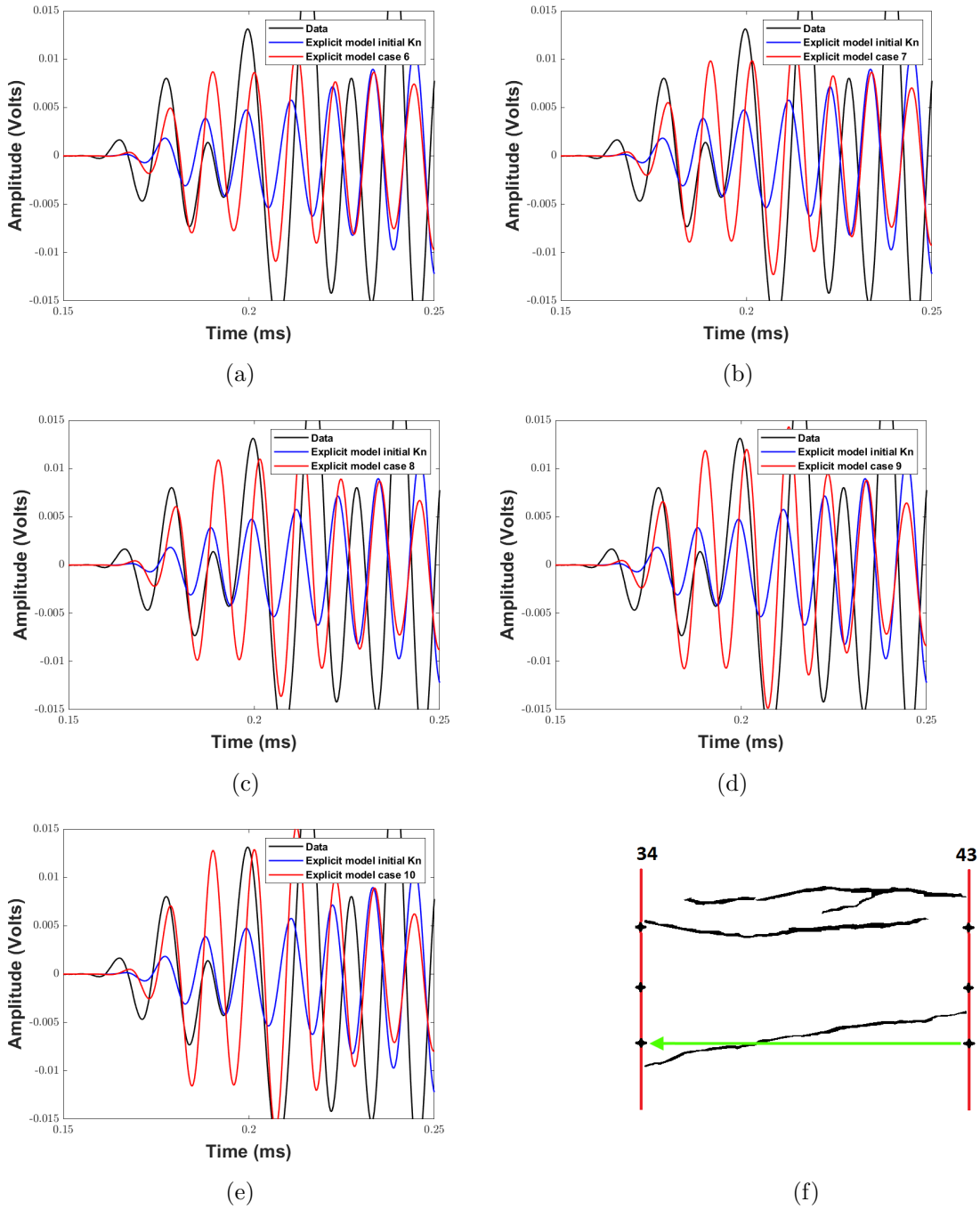

Figure D.26: Waveforms for the frame between boreholes 34-43 for the pixelised explicit model. Shot in borehole 43 at depth 0.6 m and recordings at 0.6 m D.26f. Case 6 D.26a to 10 D.26e (K_n 60 to 100 times higher than initial).

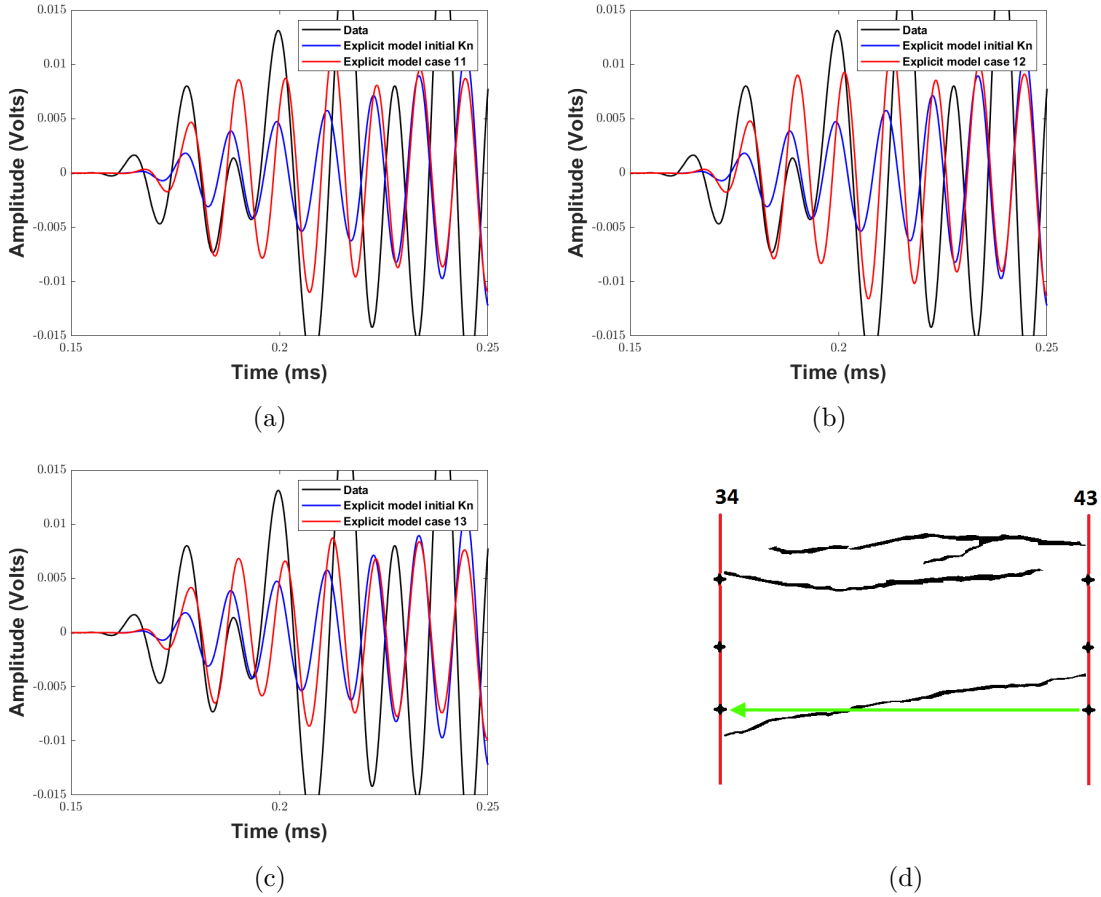

Figure D.27: Waveforms for the frame between boreholes 34-43 for the pixelised explicit model. Shot in borehole 43 at depth 0.6 m and recordings at 0.6 m D.27d. Case 11 D.27a to 13 D.27c (K_s 0.5, 0.6 and 0.2 the normal fracture stiffness $K_n = 1.67 \times 10^{12}$ to 100 times higher than initial).